Tunnelling effects on framed buildings



Jingmin Xu

Department of Civil Engineering

University of Nottingham, UK

A dissertation submitted for the degree of

Doctor of Philosophy

November 2020

Declaration

I hereby declare that except where specific reference is made to the work of others, the contents of this dissertation are original and have not been submitted in whole or in part for consideration for any other degree or qualification in this, or any other university. This dissertation is my own work and contains nothing which is the outcome of work done in collaboration with others, except as specified in the text.

Jingmin Xu

November 2020

Acknowledgement

The research of this dissertation was done at the University of Nottingham Centre for Geomechanics (NCG) with the help of numerous people, whom I would like to express my thanks to.

First, I would like to sincerely thank my primary supervisor, Dr Alec M Marshall, for his help, encouragement, support and guidance during my time in Nottingham. Dr Marshall not only guided me to do high-quality research, but also taught me to deal with the difficulties encountered from work and life. I am lucky to be one of his students.

Many thanks also to my supervisor, Dr Andrea Franza, who provided me with lots of valuable suggestions and guidance for the testing, data interpretation and paper writing. Thanks also to my supervisor, Dr Charlie Heron, for his constructive suggestions during my experimental preparation.

I am very grateful to many of the technicians in the NCG research group. In particular, I would like to thank Dr Mir Hashemi Afrapoli, Mr Luke Bedford, Mr Steven Lawton, Mr Jim Meakin, Mr Steve Gange and Mr Andrew Maddison, for their professional help, support and suggestions.

I am also grateful to all of my fellow researchers within the NCG, whom I was fortunate to get to know. In particular, I would like to sincerely thank Dr Geyang Song for his endless guidance and help for my study and life in Nottingham. Thanks also to Mr Kunkun Cheng and Mr Ge Cui, for their friendship.

For financial support, I would like to thank the China Scholarship Council (CSC) and the University of Nottingham joint research scholarship.

Last but not least, I wish to thank my parents and family, for their endless support, love and trust throughout this challenging period of my life.

Abstract

The ever-increasing population in the urban environment requires continuous improvement for infrastructure, which often involves tunnel construction. To predict/mitigate tunnelling-induced damage of nearby structures, for instance, surface buildings, engineers need to be able to understand the complex soil-structure interaction mechanisms caused by excavation. Nevertheless, due to the complexity of the problem, simplifications have to be made; for instance, the frequent use of an equivalent isotropic plate to represent the surface structure, which brings a high level of uncertainty within risk assessments.

This dissertation investigates the response of framed buildings with shallow foundations (rafts or separate strip footings) to tunnelling through using data obtained from 44 plane-strain geotechnical centrifuge tests. The research considered 8 elastic framed building models with varying configuration, with tunnelling- and structure-related parameters also varied during tests. The response of the frames on raft foundations was contrasted against results obtained using an equivalent isotropic plate.

Results indicate that, in contrast to equivalent isotropic plates, framed buildings primarily exhibit shear behaviour and a semi-flexible response with both sagging and hogging deformation modes. Regardless of the foundation configuration, buildings with a greater width (transverse to the tunnel) showed increased structural distortions, whereas building eccentricity reduced deformations because of the freedom to tilt. Tunnels with a greater cover depth resulted in a lower level of building distortion. The structure self-weight and stiffness also played a role, particularly in relation to the formation of a gap beneath the building. The relative density of sand determined the soil shear and volumetric behaviour, resulting in a greater structural deformation in loose sand than in dense sand for a given tunnel volume loss; whereas for a similar soil volume loss (equal volume of surface settlement trough), a lower level of distortion was obtained in loose sand than in dense sand, particularly for separate footings. On the other hand, the foundation configuration plays an important role in determining the ground response to tunnelling, affecting soil displacement fields as well as the distribution of soil shear and volumetric strains. Furthermore, foundation settlements and differential horizontal displacements are experimentally confirmed to be larger for separate footings compared to raft foundations.

The results also highlighted the role of footing embedment on soil-foundation interaction, with the potential of causing greater horizontal displacements and strains between footings.

The obtained building deformed shapes indicate that angular/shear distortions within each bay or panel are more appropriate for quantifying framed building distortions than deflection ratios. Based on this, a relative stiffness parameter is suggested to relate maximum angular distortions to the slope of the greenfield settlement profile. Linear trends of angular distortion modification factors with relative soil-building shear stiffness were observed (in semi-log scale), and for buildings with similar values of relative stiffness, the level of distortion within framed buildings is lower for separate footings than raft foundations. Upper and lower empirical envelopes for preliminary damage assessment considering building eccentricity and foundation configuration are suggested. In addition, the efficiency of available relative stiffness parameters for the deflection ratio modification factors is confirmed. Finally, limitations of the equivalent plate approach and practical implications of the results for framed buildings are discussed.

Keywords: tunnelling, soil-structure interaction, settlement/deformation, raft & footings, framed building, centrifuge modelling

Contents

Declaration i

Acknowledgement iii

Abstract v

Contents xi

List of Figures xx

List of Tables xxii

List of Notations xxiii

1 Introduction **1**

1.1 Background 1

1.2 Aims and objectives 3

1.3 Thesis outline 4

2 Literature review **6**

2.1 Greenfield tunnelling 7

2.1.1 Ground deformation and volume loss 7

2.1.2 Tunnelling-induced transverse settlement 9

2.1.2.1 Surface settlement 9

2.1.2.2 Subsurface settlement 11

2.1.3 Ground transverse horizontal movement 12

2.1.4 Ground longitudinal settlement 14

2.1.5 Tunnelling in sandy ground 15

2.1.5.1 Empirical methods 15

2.1.5.2 Ground displacement patterns . . . 18
2.1.5.3 Tunnel and soil volume losses . . . 21
2.2 The effects of tunnelling on buildings . . . 23
2.2.1 Building damage parameters . . . 23
2.2.2 Evaluation of building damage . . . 27
2.2.2.1 Empirical damage criteria . . . 27
2.2.2.2 Limiting tensile strain method . . . 28
2.2.2.3 Staged risk assessment for buildings . . . 33
2.2.3 Soil-structure interaction . . . 34
2.2.3.1 Modification factor approach and relative stiffness . . . 34
2.2.3.2 Estimation of building stiffness . . . 39
2.2.3.3 Tunnel-building interaction: centrifuge modelling . . . 44
2.2.3.4 Tunnelling effects on framed structures . . . 49
2.3 Summary and research gap . . . 52

3 Methodology and experimental equipment 54
3.1 Geotechnical centrifuge technique . . . 55
3.1.1 Centrifuge principles and scaling factors . . . 55
3.1.2 Limitations in centrifuge modelling . . . 57
3.2 Experimental package . . . 59
3.2.1 Geotechnical centrifuge at the University of Nottingham . . . 59
3.2.2 Strongbox . . . 60
3.2.3 Model tunnel and volume control system . . . 60
3.2.4 Soil . . . 63
3.3 Framed building models . . . 65
3.4 Data acquisition methods . . . 69
3.4.1 Particle image velocimetry (PIV) technique . . . 69
3.4.2 Other instruments . . . 72
3.5 Experimental testing plan . . . 72
3.6 Experimental setup and testing procedure . . . 75

3.6.1 Model preparation . . . 75
3.6.2 Testing procedure . . . 77
3.7 Evaluation of building stiffness . . . 78
3.7.1 Shear and bending stiffness . . . 78
3.7.2 Issue related to welding . . . 82
3.7.3 Equivalent bending stiffness . . . 84
3.8 Summary . . . 85

4 Response of buildings on raft foundations 86
4.1 Considered tests . . . 88
4.2 Model spin-up . . . 89
4.2.1 Effect of the building presence on soil movements . . . 89
4.2.2 Response of the foundations . . . 91
4.3 Tunnel pressure . . . 93
4.4 Frame foundation displacements . . . 94
4.4.1 Comparison against equivalent plates . . . 94
4.4.2 Effect of building weight . . . 97
4.4.3 Effect of soil relative density . . . 100
4.4.4 Effect of relative tunnel-building location . . . 101
4.5 Soil volume losses . . . 103
4.5.1 Soil volume losses against tunnel volume losses . . . 103
4.5.2 Soil volume loss with varying depths . . . 104
4.6 Ground deformation affected by building . . . 108
4.6.1 Greenfield tunnelling . . . 108
4.6.2 Effect of building weight . . . 110
4.6.3 Effect of soil density . . . 114
4.6.4 Effect of building width and eccentricity . . . 116
4.7 Structural distortion . . . 119
4.7.1 Deformation parameters and modification factor approach . . . 119
4.7.2 Level of damage based on strain theory . . . 125

4.7.3 Modification factor against relative soil-building stiffness 129
4.7.3.1 Estimation of soil stiffness 129
4.7.3.2 Modification factor of deflection ratio 131
4.7.3.3 Modification factor of angular distortion 133
4.8 Summary 137

5 Comparison between rafts and separate footings 140
5.1 Considered tests 142
5.2 Evaluation of footing capacity 143
5.2.1 Experimental setup 143
5.2.2 Loading test results 145
5.3 Model spin-up 147
5.3.1 Effect of the building presence on soil movements 147
5.3.2 Response of the separate footings 148
5.4 Foundation and ground displacements 149
5.4.1 Consideration of the welding issue 149
5.4.2 Centrifuge results 150
5.5 Soil volume losses 155
5.5.1 Soil volume losses against tunnel volume losses 155
5.5.2 Soil volume loss with varying depths 157
5.6 Ground deformations affected by buildings 159
5.6.1 Comparison between rafts and separate footings 159
5.6.2 Effects of building weight, width and soil density 161
5.7 Superstructure deformation parameters 163
5.8 Level of building damage 165
5.9 Modification factor against relative soil-building stiffness 168
5.10 Summary 172

6 Influence of footing embedment and tunnel depth 175
6.1 Considered tests 177

6.2 Effects of footing embedment and soil density 178
6.2.1 Foundation and underlying soil displacements 178
6.2.2 Ground movements 183
6.2.3 Structural distortion and modification factor 184
6.3 Effect of tunnel cover depth 190
6.3.1 Foundation and underlying soil displacements 190
6.3.2 Ground movements 194
6.3.3 Soil volume losses 196
6.3.4 Structural distortion and modification factor 197
6.4 Summary 200

7 Conclusions and Recommendations 202
7.1 Conclusions 204
7.1.1 The response of framed buildings on raft foundations 204
7.1.2 Comparison between raft foundations and separate footings 207
7.1.3 The roles of footing embedement and tunnel cover depth 209
7.1.4 Implications for engineering practice 210
7.2 Recommendations for further research 211
7.2.1 Limitations of the research 211
7.2.2 Recommendations for further research 211

References 214

Appendix A 226
A1 Optimisation of the welding parameter 226
A2 Instrumentation details 229
A3 Effect of centrifuge radius on the gravity field 233
A4 Soil movements after centrifuge spin-up 235
A5 Foundation and underlying soil displacements at $V_{l,t}$ =1% 238

List of Figures

2.1 Ground settlement caused by tunnelling (reproduced from Attewell et al. (1986); Franza (2016)) . . . 8
2.2 Vertical ground settlement shape described by a Gaussian curve (after Ritter (2018)) . . . 10
2.3 Vertical ground settlement, horizontal displacement and strain (after (Franzius, 2003)) . . . 13
2.4 Longitudinal surface settlement trough (after Mair and Taylor (1997)) . . . 15
2.5 Normalised displacements at $V_{l,t}$ = 3% for varying C/D_t (left) and I_d (right) (Franza et al., 2019) . . . 19
2.6 Soil arching mechanism governing the ground displacements (Franza et al., 2019) . . . 20
2.7 Contours of shear strain from centrifuge tests (Marshall et al., 2012) . . . 21
2.8 Illustration of soil volumetric behaviour under shear (Marshall et al., 2012) . . . 22
2.9 Relationship between soil and tunnel volume losses (Franza et al., 2019) . . . 22
2.10 Building deformation parameters defined (after Burland et al. (1977)) . . . 23
2.11 (a) and (b) bay distortion modes; (c) parameter definition . . . 25
2.12 Wall deformation by applying displacement at frame corners (after Elkayam and Klar (2019)) . . . 26
2.13 Cracking of a simple beam in bending and in shear (after Burland et al. (1977)) 30
2.14 Damage levels of buildings from field observations, physical and numerical model tests (after Son and Cording (2005)) . . . 32
2.15 Damage assessment framework according to Mair et al. (1996) . . . 33

2.16 Definition of parameters in modification factor approach (after Franza (2016)) . 35
2.17 Modified design curves proposed by Franzius et al. (2006) (after Farrell (2010)) 37
2.18 Modification factors of DRs of the buildings in the field monitoring (Mair, 2013) 38
2.19 Relationship between normalised angular distortion and relative soil-structure shear stiffness (Son and Cording, 2005) 40
2.20 Estimation of bending and shear stiffness (Son and Cording, 2005) 41
2.21 Laminate beam model for the representation of a building (Finno et al., 2005) . 42
2.22 Schematic of the simple portal frame (Goh and Mair, 2014) 44
2.23 Model aluminium beam building (STR-2) (Farrell, 2010) 44
2.24 Settlement profile for structures STR-1 to STR-4 (Farrell et al., 2014) 45
2.25 Observed cracking of building (Farrell et al., 2014) 45
2.26 Three-dimensional printed building model (Ritter, 2018) 46
2.27 Centrifuge results: the effects of building width and opening ((a) 20% opening; (b) 40% opening; and (c) centrifuge results) (Ritter et al., 2020) 47
2.28 Experimental results of piled structures (after Franza and Marshall (2018)) . . . 48
2.29 Deflection ratio modification factors against bending stiffness calculated using different approaches (Goh and Mair, 2014) 50
2.30 Horizontal strain modification factors against frame stiffness factors (Goh and Mair, 2014) 51
2.31 Deformed shapes of a frame to (a) vertical and (b) horizontal displacements (Franza and DeJong, 2019) 52

3.1 Normalised crater volume against normalised cavity diameter (after Kutter et al. (1994); Marshall (2009)) 58
3.2 Geotechnical centrifuge at the University of Nottingham Centre for Geomechanics (Ellis et al., 2006) 59
3.3 Components of the strongbox (after Zhou (2014)) 60
3.4 Components of model tunnel and its installation (Zhou, 2014) 62
3.5 Tunnel volume loss control system components (Zhou, 2014) 63
3.6 Sketch of the tunnel volume loss control system (Zhou, 2014) 64

3.7 Framed building models: (a) raft foundation; (b) separate footings 65
3.8 Illustration of the welding process of the framed building on raft foundation (F5t5b6L) 66
3.9 Manufacture process of the separate footings (F2t3b6L) 66
3.10 Illustration of the configuration of the framed building models 67
3.11 Illustration of the new frame (F2t3b6LN) with separate footings: (a) illustration of node connection; (b) sketch of the frame; (c) top removed; (d) node connection detail 69
3.12 Illustration of the image-based deformation measurement equipment: (a) camera field of view; (b) setup of the cameras; (c) relative camera-model position . 71
3.13 Example of the same picture (at the corner) taken with (a) white LEDs, and (b) monochromatic amber LEDs 72
3.14 Experimental layout and parameter definition 73
3.15 Illustration of the sand pouring for buried separate footings 76
3.16 Set up of the centrifuge model with buried footings 77
3.17 Setup of the loading tests: (a) four-point test; (b) three-point test 79
3.18 Configuration of experimental tests to evaluate building stiffness 80
3.19 Deformed shape of F2t3b6L on the raft in the load-deflection tests (scale factor: 50) 82
3.20 Deformed shapes of the frames with separate footings in the loading tests (scale factor=100) 83
3.21 Deformed shapes of the frames with rigid connections from finite element modelling 83
3.22 Definition of bay, panel and footing number 84

4.1 Considered tests with framed building models on raft foundations 88
4.2 Horizontal U_x and vertical U_z displacements of the dense (I_d = 90%) soil in selected tests after centrifuge spin-up (data outside the contour thresholds were set equal to the closest limit value) 90

4.3 Settlements of the rafts and surface soil in selected tests during centrifuge spin-up from 1 to 68 g 91
4.4 Illustration of the boundary effect 92
4.5 Illustration of the foundation deflection during centrifuge spin-up 93
4.6 Tunnel pressure at axis level against tunnel volume loss in selected tests 94
4.7 Comparison of t_{eq} (prototype scale) between framed buildings on raft foundations and plates from Farrell (2010) 95
4.8 Displacements of model frame foundations and equivalent plates for $e/B = 0$ and $V_{l,t} = 1\%$ 96
4.9 Displacement of model frame foundations and underlying soil at $V_{l,t}$ =2 % . . . 98
4.10 Maximum gap height against tunnel volume loss 99
4.11 Displacements of selected model foundations ($e/B = 0$, SW) at identical $V_{l,s}$ = 1.6%: (a) $I_d = 90\%$ and (b) $I_d = 30\%$ 101
4.12 Displacement of model frame foundations and underlying soil at $V_{l,t} = 2\%$ with $e/B = 0.2$ in loose soil 102
4.13 Variation of surface ($z/z_t = 0$) soil volume loss with tunnel volume loss 103
4.14 Variation of subsurface ($z/z_t = 0.5$) soil volume loss with tunnel volume loss . 105
4.15 Soil volume loss with varying depths at $V_{l,t} = 1\%$ 106
4.16 Soil volume loss with varying depths at $V_{l,t} = 2\%$ 107
4.17 Variation of relative dilatancy index against the pressure change 107
4.18 Soil movements normalised by the tunnel diameter, engineering shear and volumetric strains ($\epsilon_v < 0$ indicates dilation) in greenfield tests (data outside the contour thresholds were set equal to the closest limit value) 109
4.19 Soil movements normalised by the tunnel diameter, engineering shear and volumetric strains ($\epsilon_v < 0$ indicates dilation) at $V_{l,t} = 2\%$ for frame F2t3b3L (data outside the contour thresholds were set equal to the closest limit value) 111
4.20 Soil movements normalised by the tunnel diameter, engineering shear and volumetric strains ($\epsilon_v < 0$ indicates dilation) at $V_{l,t} = 2\%$ for frame F2t5b6L (data outside the contour thresholds were set equal to the closest limit value) 112

4.21 Soil movements normalised by the tunnel diameter, engineering shear and volumetric strains ($\epsilon_v < 0$ indicates dilation) at $V_{l,t} = 2\%$ for frame F5t5b6L (data outside the contour thresholds were set equal to the closest limit value) 113
4.22 Soil movements normalised by the tunnel diameter, engineering shear and volumetric strains ($\epsilon_v < 0$ indicates dilation) in central short frame F2t3b3S (SW) tests: effect of soil density (data outside the contour thresholds were set equal to the closest limit value) 115
4.23 Soil movements normalised by the tunnel diameter, engineering shear and volumetric strains ($\epsilon_v < 0$ indicates dilation) at $V_{l,t} = 2\%$: effect of building width and eccentricity (data outside the contour thresholds were set equal to the closest limit value) 116
4.24 Soil movements normalised by the tunnel diameter, engineering shear and volumetric strains ($\epsilon_v < 0$ indicates dilation) at $V_{l,t} = 2\%$: F5t5b6L in the loose soil (the direction of the horizontal displacement is denoted by the arrows; data outside the contour thresholds were set equal to the closest limit value) 118
4.25 Building deflection ratios against tunnel volume loss in selected tests 120
4.26 Building modification factors of deflection ratios against tunnel volume loss in selected tests 121
4.27 Building deflection ratios and angular distortions against tunnel/soil volume loss in selected tests (SW) 122
4.28 Building distortion parameters (DR, M^{DR}, β) against tunnel volume loss 123
4.29 Building angular distortion against soil volume loss 124
4.30 Post-tunnelling frame deformed shapes and level of damage (scale factor: 100); left column is dense sand tests, right column is loose sand tests 126
4.31 (a) Vertical and (b) shear stiffness degradation with strains, (c) average shear strain and (d) soil stiffness with volume loss 131
4.32 Modification factors of DR against relative stiffness ($V_{l,t} = 1$ and 2%): (a) $\rho_{sag/hog}$ (Mair, 2013), and (b) $\eta_{sag/hog}$ (Franza et al., 2020a) 132
4.33 Modification factors of β against tunnel volume loss $V_{l,t}$ 134

4.34 Modification factors of β against relative soil-building shear stiffness (numbers beneath markers indicate $V_{l,t}$) 135

5.1 Illustration of the 20 considered tunnel-frame interaction tests 143
5.2 Setup and configuration of the footing loading tests 144
5.3 The response of the footing models to vertical loading (dimension in prototype) 146
5.4 Horizontal and vertical displacements (normalised by the tunnel diameter D_t) of the dense (I_d = 90%, 2SW) soil in selected footing tests during centrifuge spin-up from 1 to 68 g (data outside the contour thresholds were set equal to the closest limit value) 147
5.5 Settlements of the foundations and surface soil in selected tests during spin-up: comparison between rafts and separate footings 148
5.6 Foundation and underlying soil displacements for loose and dense soil at $V_{l,t}$ = 2% (SW) 152
5.7 Foundation and underlying soil displacements with different building weights for dense soil at $V_{l,t}$ = 2% (I_d = 90%) 153
5.8 Foundation displacements for central buildings founded on dense soil at $V_{l,t}$ = 2% 154
5.9 Surface soil volume loss against tunnel volume loss: (a) central structures with self-weight SW in dense soil cases; (b) central structures with double self-weight 2SW in dense soil cases; (c) central structures with self-weight SW in loose soil cases; (d) eccentric structures with self-weight SW in loose soil cases 156
5.10 Subsurface (z/z_t = 0.5) soil volume loss against tunnel volume loss: (a) central structures with self-weight SW in dense soil cases; (b) central structures with double self-weight 2SW in dense soil cases; (c) central structures with self-weight SW in loose soil cases; (d) eccentric structures with self-weight SW in loose soil cases 157
5.11 Soil volume loss with varying depths at $V_{l,t}$ = 1.0% 158
5.12 Soil volume loss with varying depths at $V_{l,t}$ = 2.0% 159

5.13 Soil movements normalised by the tunnel diameter, engineering shear and volumetric strains ($\epsilon_v < 0$ indicates dilation) at $V_{l,t} = 2\%$: comparison between raft and separate footings foundations (data outside the contour thresholds were set equal to the closest limit value) . . . 160
5.14 Soil movements normalised by the tunnel diameter, engineering shear and volumetric strains ($\epsilon_v < 0$ indicates dilation) at $V_{l,t} = 2\%$ with varying length and soil density (data outside the contour thresholds were set equal to the closest limit value) . . . 162
5.15 Maximum shear distortion of the framed buildings with tunnel volume loss $V_{l,t}$ 164
5.16 Maximum shear distortion of the framed buildings with soil volume loss $V_{l,s}$: effect of soil density . . . 165
5.17 Framed building deformed shapes and level of damage at $V_{l,t} = 1\%$ (scale factor: 200) . . . 166
5.18 Framed building deformed shapes and level of damage at $V_{l,t} = 2\%$ (scale factor: 100) . . . 167
5.19 Modification factors of β against tunnel volume loss $V_{l,t}$ . . . 169
5.20 Modification factors of β against relative soil-building shear stiffness at $V_{l,t}$ =1 and 2% ($V_{l,t}$ indicated by numbers below markers); (a) central structure cases; (b) eccentric structure cases . . . 171

6.1 Illustration of the considered centrifuge tests . . . 177
6.2 Foundation and underlying soil displacements of frame F2t3b6LN at soil volume loss $V_{l,s}$ = 1.4-1.5% . . . 179
6.3 Footing displacements and horizontal strains ($\epsilon_h > 0$ indicates tension) against tunnel volume loss in the dense soil ($I_d = 90\%$) . . . 181
6.4 Footing displacements and horizontal strains ($\epsilon_h > 0$ indicates tension) against tunnel volume loss in the loose soil ($I_d = 30\%$) . . . 182

6.5 Soil movements normalised by the tunnel diameter, engineering shear and volumetric strains at $V_{l,t}$ = 2.0% of dense soil ($\epsilon_v < 0$ indicates dilation, data outside the contour thresholds were set equal to the closest limit value): effect of footing embedment depth 184
6.6 Maximum frame angular distortion against (a) tunnel and (b) soil volume loss . 185
6.7 Deformed shape and damage levels of the framed buildings at $V_{l,t}$ =2.0% (scale: 150) 186
6.8 Modification factors of (a) angular distortion and (b) horizontal strain against tunnel volume loss $V_{l,t}$ 187
6.9 Modification factors of (a) angular distortion and (b) horizontal strain against relative stiffness (numbers near markers indicate $V_{l,t}$) 188
6.10 Illustration of the horizontal displacements of the footings 189
6.11 Foundation and underlying soil displacements at $V_{l,t}$ = 2.0%: effect of tunnel cover depth 191
6.12 Foundation and underlying soil displacements at identical soil volume loss ($V_{l,s}$ = 1.4% for I_d = 90% and $V_{l,s}$ = 2.8% for I_d = 30%): effect of tunnel cover depth 193
6.13 Footing displacements and horizontal strains ($\epsilon_h > 0$ indicates tension) against tunnel volume loss in the dense soil (I_d = 90%): effect of tunnel cover depth . . 194
6.14 Soil movements normalised by the tunnel diameter, engineering shear and volumetric strains at $V_{l,t}$ = 2.0% ($\epsilon_v < 0$ indicates dilation, data outside the contour thresholds were set equal to the closest limit value): effect of tunnel cover depth 195
6.15 Variation of soil volume loss with tunnel volume loss: effect of tunnel cover depth 196
6.16 Maximum building angular distortion against tunnel/soil volume loss: effect of tunnel cover depth 197
6.17 Frame deformed shape and level of damage at tunnel volume loss $V_{l,t}$ = 2.0%: effect of tunnel cover depth 198
6.18 Modification factors of (a) angular distortion and (b) horizontal strain against tunnel volume loss: effect of tunnel cover depth 199

6.19 Modification factors of (a) angular distortion and (b) horizontal strain against relative stiffness (numbers near markers indicate $V_{l,t}$): effect of tunnel cover depth 200

A1 Illustration of the welding parts 226
A2 Illustration of the considered welding plan (example of frame F5t5b6L) 227
A3 The effect of the welding percentage on the frame total stiffness 228
A4 The effect of the distribution of welding parts on the frame total stiffness 228
A5 Illustration of the gravity field in the centrifuge 233
A6 Horizontal U_x and vertical U_z displacements of the dense (I_d = 90%) soil in selected tests (2SW) after centrifuge spin-up (data outside the contour thresholds were set equal to the closest limit value) 235
A7 Horizontal U_x and vertical U_z displacements of the dense (I_d = 90%) soil in selected tests (2-storey, e/B =0, SW) after centrifuge spin-up (data outside the contour thresholds were set equal to the closest limit value) 236
A8 Settlements of the rafts and surface soil in selected tests (2SW) during centrifuge spin-up from 1 to 68 g 236
A9 Horizontal and vertical displacements (normalised by the tunnel diameter D_t) of the dense (I_d = 90%, SW) soil in selected footing tests during centrifuge spin-up from 1 to 68 g (data outside the contour thresholds were set equal to the closest limit value) 237
A10 Settlements of the foundations and surface soil in selected tests (2SW) during spin-up: comparison between rafts and separate footings 237
A11 Displacement of model frame foundations and underlying soil at $V_{l,t}$ =1 % . . . 238
A12 Displacement of model frame foundations and underlying soil at $V_{l,t}$ = 1% with e/B = 0.2 in loose soil 239
A13 Foundation and underlying soil displacements for loose and dense soil at $V_{l,t}$ = 1% (SW) 240
A14 Foundation and underlying soil displacements with different building weights for dense soil at $V_{l,t}$ = 1% (I_d = 90%) 241
A15 Foundation displacements for central buildings founded on dense soil at $V_{l,t}$ = 1% 242

List of Tables

1.1 Publications corresponding to the chapters 5

2.1 Curves to fit surface settlement trough, summarised by Marshall et al. (2012) . 16
2.2 Damage criterion based on angular distortion (Skempton and MacDonald, 1956) 27
2.3 Damage criterion based on deflection ratio (Polshin and Tokar, 1957) 28
2.4 Critical tensile strain and categories of damage (Boscardin and Cording, 1989) 29

3.1 Centrifuge scaling laws (after Taylor (1995a)) 56
3.2 The properties of Leighton Buzzard Fraction E silica sand 64
3.3 Framed building configurations 68
3.4 Centrifuge testing plan (dimension in model scale) 74
3.5 Experimental results of bending and shear stiffness (per running meter) of building models (at model scale) 81
3.6 Equivalent EI of structures on rafts and pressure beneath the foundations (prototype scale) 85

4.1 Greenfield settlement trough characteristics (prototype scale) 100
4.2 Maximum building angular distortion ($\gamma = \beta$) at $V_{l,t}$=2% 127

5.1 Considered centrifuge tests in Chapter 5 142
5.2 Footing loading test results (prototype scale) 145
5.3 Greenfield settlement trough characteristics (prototype scale) 150

6.1 Considered centrifuge tests (model scale) 178

6.2 Greenfield settlement trough characteristics (prototype scale) 179
6.3 Greenfield settlement trough characteristics (prototype scale) 190

A1 The module for each sensor/device 229
A2 Servo motor (Linear Actuator L03 DC) specification 229
A3 Hydraulic piston (SMC CP96SDB50-320C) specification 230
A4 LVDT specification 230
A5 Load cell specification 231
A6 Druck UNIK 5000 Pressure Sensor specification 231
A7 Stepper motro specification 232

List of Notations

Roman

2SW	doubled self-weight of the building
a	dimensionless factor of $\eta_{sag/hog}$ (Franza et al., 2020a)
a_{ratio}	percentage opening in a wall (Finno et al., 2005)
A	area of cross section
A_E	constant value depending on the material property
A_i	area of cross section of each slab in the laminate beam (Finno et al., 2005)
$A_{slab,i}$	area of cross section of each slab of a building (Potts and Addenbrooke, 1997)
b	building wall thickness (Son and Cording, 2005)
b_{bay}	width of the bay
b_{foot}	width of the footing
B	building width transverse to the tunnel
$B_{1/2/3}$	span length in the load-deflection test
B_{sag}	length of the building in sagging zone
B_{hog}	length of the building in hogging zone
C	cover depth of the tunnel crown
C	column stiffening factor (Goh and Mair, 2014)
d_f	embedment depth of the foundation
d_i	vertical distance between the structure's and the slab's neutral axes (Potts and Addenbrooke, 1997)
DOF	degree of freedom
D_{50}	average grain size diameter

D_{ci}	cavity diameter (Kutter et al., 1994)
D_t	diameter of the tunnel
DR	deflection ratio ($= \Delta/L$)
$DR_{hog,bldg}$	building DR in the hogging zone
$DR_{hog,gf}$	DR of the greenfield settlement trough in the hogging zone
$DR_{sag,bldg}$	building DR in the sagging zone
$DR_{sag,gf}$	DR of the greenfield settlement trough in the sagging zone
e	building eccentricity with respect to the tunnel
e	void ratio of sand
E	Young's modulus
EA	axial stiffness
EI	bending stiffness
EI^*	bending stiffness per metre run
EI_{exp}	experimental bending stiffness
EI^*_{exp}	experimental bending stiffness per metre run
$EI^*_{exp,avg}$	average value of experimental bending stiffness per metre run
$EI_{EB,eq}$	equivalent bending stiffness
EI_{frame}	frame bending stiffness (Goh and Mair, 2014)
$EI^*_{parallel}$	bending stiffness per metre run obtained using parallel axis theory
EI^*_{sum}	bending stiffness per metre run obtained using algebraic sum method
EPB	earth pressure balance
E_s	representative Young's modulus of the soil
E_{v0}	maximum soil stiffness at low axial strain
E'_v	secant axial stiffness
$E_{v,sec}$	secant axial stiffness
F	force
$F_{sag/hog}$	dimensionless factor of $\eta_{sag/hog}$ (Franza et al., 2020a)
$F(e)$	function of void ratio, e, used to determine stiffness (Lehane and Cosgrove, 2000)
g	gravity
G	shear modulus

G_{build}	shear modulus of a building (Son and Cording, 2005)
G_{sec}	secant shear stiffness
GA_s	building shear stiffness
GA_s^*	building shear stiffness per meter run
$GA_{s,exp}$	experimental building shear stiffness
$GA_{s,exp}^*$	experimental building shear stiffness per metre run
$GA_{s,exp,avg}^*$	average value of experimental building shear stiffness per metre run
$\overline{GS}$	average greenfield slope (Son and Cording, 2005)
$\overline{GS}_{max}$	maximum average slope of the greenfield surface settlement trough corresponding to b_{bay}
GA_v	equivalent shear stiffness of the laminate beam (Finno et al., 2005)
$GA_{v,column}$	shear stiffness of the column (Finno et al., 2005)
$GA_{v,i}$	total shear stiffness of each floor (Finno et al., 2005)
$GA_{v,wall}$	shear stiffness of the wall (Finno et al., 2005)
GF	greenfield
h_i	distance from the floor to the bottom of the laminate beam (Finno et al., 2005)
h_m	total height of the model
h_{storey}	height of the building storey
H	height of the building
i	distance to the inflection point of the settlement trough
i	number of floor slabs (Potts and Addenbrooke, 1997)
I	second moment of area of the equivalent beam
I_c	relative grain strength
I_d	relatively density of sand
I_R	relative dilatancy index (Bolton, 1986)
$I_{slab,i}$	second moment of area of each slab (Potts and Addenbrooke, 1997)
K	trough width parameter
K^*	trough width parameter based on x^* (Marshall et al., 2012)
K^{**}	trough width parameter based on x^{**} (Marshall et al., 2012)

K_b	average stiffness of the beam line (= $(EI/b_{bay})_b$)
K_c	average stiffness of the footing column (= $(EI/b_{bay})_c$)
K_{LC}	average stiffness of the lower column (= $(EI/h_{storey})_{LC}$)
K_s	trough width parameter for surface displacements based on i (Marshall et al., 2012)
K_s^*	trough width parameter for surface displacements based on x^* (Marshall et al., 2012)
K_s^{**}	trough width parameter for surface displacements based on x^{**} (Marshall et al., 2012)
$K_{s,C/D_t}^{*int}$	intercept of K_{s,V_l}^{*slope} values with C/D_t (Marshall et al., 2012)
$K_{s,C/D_t}^{*slope}$	slope of K_{s,V_l}^{*slope} with C/D_t line (Marshall et al., 2012)
K_{s,V_l}^{*slope}	slope of K^* against $V_{l,t}$ (Marshall et al., 2012)
$K_{s,V_{l,t}}^{*slope,ln}$	slope of K^* (Franza et al., 2019)
$K_{s,V_{l,t}}^{**slope,ln}$	slope of K^{**} (Franza et al., 2019)
$K_{s,V_{l,t}}^{*int,ln}$	intercept of $K_{s,V_{l,t}}^{*slope,ln}$ values (Franza et al., 2019)
$K_{s,V_{l,t}}^{**int,ln}$	intercept of $K_{s,V_{l,t}}^{**slope,ln}$ values (Franza et al., 2019)
K_{UC}	average stiffness of the upper column (= $(EI/h_{storey})_{UC}$)
L	length of the building in the longitudinal direction of the tunnel
LVDT	linear variable differential transformer
M	bending moment
M^{DR}	DR modification factor
$M^{DR,sag}$	DR modification factor in sagging
$M^{DR,hog}$	DR modification factor in hogging
M^{β}	modification factor of angular distortion
$M^{\epsilon,h}$	modification factor of horizontal strain
$M^{\epsilon h,c}$	modification factor of horizontal strain in compression mode
$M^{\epsilon h,t}$	modification factor of horizontal strain in tension mode
n	number of storeys
N	centrifuge acceleration scale
PIV	particle image velocimetry
p_{atm}	atmospheric pressure
p'	the mean effective stress at failure (Bolton, 1986)

p_c	a parameter relating to the crushing strength of the grain (Bolton, 1986)
P	load
q_0	initial pressure beneath the footing
q_p	peak resistance of the footing
q_c	stress at which a significant change in the tangent stiffness occurred
R_e	effective centrifuge radius
R_t	distance between the model top and rotation axis
s	rotation of a straight line connecting two points on the structure
S	foundation slope
S_c	footing settlement at q_p or q_c
SW	self-weight of the building
t	thickness of the building element
t_{axis}	location of the neutral axis
t_{eq}	thickness of the equivalent plate
$U_{i,j}$	corner point displacement; i is the displacement direction, and j is the location of the bay corner
U_x	horizontal displacement
$U_{x,max}$	maximum horizontal displacement
U_z	vertical displacement
$U_{z,max}$	maximum vertical displacement
V	total shear force in the beam (Finno et al., 2005)
V_0	nominal cross-sectional area per metre run of the tunnel
V_{ci}	cavity volume (Kutter et al., 1994)
V_{cr}	crater volume (Kutter et al., 1994)
V_i	shear force in a storey (Finno et al., 2005)
$V_{l,s}$	soil volume loss
$V_{l,t}$	tunnel volume loss
V_s	volume of the ground surface settlement trough per metre length
V_t	volume loss of the soil around the tunnel periphery per metre length

w	bay/local tilt
w'	total tilt
w_1	left edge tilt
w_2	right edge tilt
x^*	horizontal distance of the point of $0.606U_{x,max}$ (Marshall et al., 2012)
x^{**}	horizontal distance of the point of $0.303U_{x,max}$ (Marshall et al., 2012)
z	depth of interest
z_t	depth of the tunnel axis

Greek

α	angular strain
α^*	relative soil-building axial stiffness (Potts and Addenbrooke, 1997)
α^*_{mod}	modified relative soil-building axial stiffness (Franzius et al., 2006)
α_f	frame stiffness factor (Goh and Mair, 2014)
β	building angular distortion
β_{max}	maximum building angular distortion
χ	curvature
δ	deflection
$\delta_{bending}$	frame bending deflection in loading tests
δ_{shear}	frame shear deflection in loading tests
δ_x	in-plane horizontal displacements of any point within a panel (Elkayam and Klar, 2019)
δ_{total}	total deflection in loading tests
δ_z	in-plane vertical displacements of any point within a panel (Elkayam and Klar, 2019)
Δ	relative deflection
ΔGS	greenfield ground slope (Son and Cording, 2005)
Δ_h	a unit differential footing displacement (Goh and Mair, 2014)
ΔI_d	change of sand relative density
ΔL	change of the building length
ΔU_{bend}	building settlement due to bending

ΔU_{shear}	building settlement due to shear distortion
ΔU_{tilt}	building settlement due to tilt
ΔU_{tot}	total building settlement
ΔU_z	relative/differential settlement
$\Delta U_{z,gf,max}$	maximum differential settlement of greenfield settlement trough corresponding to b_{bay}
ϵ	axial strain
$\epsilon_{b,max}$	maximum bending strain
$\epsilon_{b,t}$	total bending strain
ϵ_d	diagonal strain
$\epsilon_{d,max}$	maximum diagonal strain
ϵ_{el}	strain when the soil stiffness-strain relationship becomes non-linear
ϵ_h	horizontal strain
$\epsilon_{h,c,bldg}$	maximum building compressive strain
$\epsilon_{h,t,bldg}$	maximum building tensile strain
$\epsilon_{h,c,gf}$	maximum greenfield compressive strain
$\epsilon_{h,t,gf}$	maximum greenfield tensile strain
ϵ_{max}	maximum strains of any point within a panel (Elkayam and Klar, 2019)
ϵ_r	reference strain
ϵ_t	tensile strain
ϵ_v	soil volumetric strain
ϵ'_v	vertical effective stress
ϵ_{xx}	horizontal strains of any point within a panel (Elkayam and Klar, 2019)
ϵ_{zz}	vertical strains of any point within a panel (Elkayam and Klar, 2019)
ϵ_{xz}	diagonal strains of any point within a panel (Elkayam and Klar, 2019)
ϵ_θ	tension strain at any angle θ from the horizontal
$\epsilon_{\theta,max}$	maximum value of ϵ_θ
ϵ_{crit}	maximum value of ϵ_θ, equal to $\epsilon_{\theta,max}$
$\eta_{sag/hog}$	modified relative stiffness considering shear in the sagging/hogging zone (Franza et al., 2020a)
γ	building shear strain

γ_0	building shear strain at the foundation level
γ_1	building shear strain within the superstructure
γ_{avg}	average soil shear strain
γ_s	soil engineering shear strain
κ	relative soil-building shear stiffness
λH	distance between the neutral axis and the bottome of the beam (Finno et al., 2005)
ν	Poisson's ratio
ω	centrifuge rotational velocity
ρ^*	relative soil-building bending stiffness (Potts and Addenbrooke, 1997)
ρ^*_{mod}	modified relative soil-building bending stiffness (Franzius et al., 2006)
$\rho_{sag/hog}$	relative soil-building bending stiffness in the sagging/hogging zone (Goh and Mair, 2011)
θ	tilt
θ_{max}	the angle determined by $\tan(2\theta_{max}) = \beta/\varepsilon_h$ (Son and Cording, 2005)
τA	shear force (Son and Cording, 2005)

Chapter 1

Introduction

1.1 Background

Human society highly relies on the existence of infrastructure. The surface space in an increasingly congested urban environment is becoming more and more limited due to the rapid development of urbanisation. This has to lead to the construction of underground space, such as tunnelling, for the development of new infrastructure. However, tunnel construction inevitably gives rise to ground movements due to stress relief/disturbance, which may have detrimental effects on nearby structures (e.g. surface buildings, buried pipelines and various forms of foundations). Therefore, engineers need to be able to assess the potential damage that tunnelling may have on adjacent infrastructure.

While reliable predictions of tunnelling-induced greenfield ground movements in both vertical and horizontal planes can be achieved (Mair and Taylor, 1997; Marshall et al., 2012; Franza et al., 2020b), an accurate prediction of damage of structures caused by tunnel construction is still full of challenges because of the highly non-linear behaviour of the soil and the structures, as well as the complex soil-structure interaction mechanisms. When considering the effect of tunnelling on buildings, a method commonly used in practice is a three-stage process, with increasing detail at each stage (Mair et al., 1996). First, greenfield ground movements along the tunnel route are predicted using empirical methods (Mair and Taylor, 1997; Marshall et al., 2012; Franza et al., 2020b). Then, the buildings falling into the zones that settlements

that exceed defined thresholds are selected for assessment; at this stage, the maximum tensile strains of buildings are conservatively estimated by assuming that buildings deform according to the greenfield ground movement, neglecting the structure's ability to resist ground deformation, i.e., the stiffness of structures; building distortion level is then assessed using the limiting tensile strain method (Burland and Wroth, 1974; Boscardin and Cording, 1989). Finally, soil-structure interaction needs to be accounted for if serviceability limits are exceeded, either using the modification factor method (Potts and Addenbrooke, 1997; Franzius et al., 2006) or modelling the entire domain of soil and structure (Goh and Mair, 2014; Fargnoli et al., 2015; Boldini et al., 2018; Fu et al., 2018; Franza and DeJong, 2019).

However, extensive studies have simplified the building as an equivalent plate/beam (Franzius et al., 2006; Pickhaver et al., 2010; Maleki et al., 2011; Namazi and Mohamad, 2013; Farrell et al., 2014; Bilotta et al., 2017; Franza and Marshall, 2018). This simplification involves uncertainties that have not yet been sufficiently investigated for realistic buildings with full details. For instance, when estimating the total structure stiffness, most researchers have adopted a pure bending stiffness (Franzius et al., 2006; Goh and Mair, 2014; Haji et al., 2018) despite the evidence that shear flexibility can have an important role (Potts and Addenbrooke, 1997; Finno et al., 2005; Franza et al., 2020a). Furthermore, the local deformations of infill walls in frames is potentially not well described by equivalent beams or plates (Goh and Mair, 2014; Boldini et al., 2018).

Urban tunnel construction projects frequently take place in proximity to buildings. For instance, in the Crossrail project, at least 1200 buildings were possibly affected by the tunnel construction (Torp-Petersen and Black, 2001). Therefore, protective measures, such as compensation grouting (Mair and Taylor, 1997; Lee, 2002; Farrell, 2015) and the use of buried structures (rows of piles, diaphragm walls) (Bilotta, 2008; Bilotta and Russo, 2011; Ledesma and Alonso, 2017; Song, 2019), have to be adopted where the predicted building damage would be serious. Consequently, the cost of preventing the building damage can account for a significant proportion of the total cost of the tunnelling project (Clarke and Laefer, 2014). However, if the reliable prediction of building response to tunnelling cannot be achieved due to the lack of understanding of tunnel-building interaction, overly conservative or insufficient evaluations could

be made. This would result in either high tunnelling project costs (due to the unnecessary protective measures), or unexpected damage of adjacent structures. Therefore, to reduce the overall project costs while still preventing buildings being damaged, it is necessary to understand the soil-structure interaction mechanisms considering entire superstructure and foundation details. While several studies have considered realistic (framed) building characteristics (Boldini et al., 2018; Fu et al., 2018; Franza and DeJong, 2019; Son, 2015), there is a lack of experimental evidence to substantiate many of the findings reported by the above numerical analyses.

1.2 Aims and objectives

This project aims to, through scaled-down physical models, experimentally investigate the effects of tunnel construction on framed buildings resting either on rafts or separate footings. Geotechnical centrifuge modelling, which provides an approach for reproducing full-scale soil stress and soil/structure behaviour in a controlled laboratory environment, is the main tool for this research. The project considers a tunnel with a low cover-to-diameter ratio (≤ 2.0) constructed in sandy ground beneath a linear framed structure. The main objectives of this project are to:

- study the response of framed structures on raft foundations to tunnel construction, and compare the results against the data obtained in the scenario in which an equivalent plate model was used (Farrell, 2010);
- investigate the effects of building configurations (including the number of storeys, the thickness of building elements, building transverse length and the width of each bay) on tunnelling-induced structural deformation;
- consider the influences of external parameters of interest, including ground condition (relative density of the sand), building weight/load, and the horizontal position of the building with respect to the tunnel, on the building response to tunnelling;
- compare the difference of the response of the buildings with raft foundations and separate footings to tunnel construction;

- discuss the effects of tunnel cover depth and footing embedment on the excavation-induced framed building deformation; and
- explore the impact of the presence of buildings on the tunnelling-induced ground deformation.

1.3 Thesis outline

The structure of the thesis is listed as follows.

- Chapter 2 summarises the existing literature dealing with the problems of tunnelling in the urban environment and the assessment of building damage caused by underground excavations;
- Chapter 3 describes the methodology adopted in this research, the developed experimental equipment, the designed framed building models, and the centrifuge testing plan and procedure;
- Chapter 4 illustrates the response of framed buildings on raft foundations to tunnel excavation; framed building data are compared against the results collected in the scenario in which an equivalent plate was used (Farrell, 2010); the effects of building configuration, weight, eccentricity, and soil density on the building response to tunnelling are assessed; the influence of the presence of surface buildings with raft foundations on tunnelling-induced ground movements is discussed;
- Chapter 5 compares the difference of the response of the frame with either a raft or separate footings; building eccentricity, weight and the relative density of the soil were also varied;
- Chapter 6 investigates the effects of tunnel cover depth and footing embedment on tunnelling-induced structural and ground distortion; and
- Chapter 7 summarises the most significant findings of the research and some suggestions on where further research in this area could be carried out.

Some of the findings of the research have been published in international conference or journal papers (Xu et al., 2019, 2020a,b), listed in Table 1.1.

Table 1.1. Publications corresponding to the chapters

Publications	Chapter
J Xu, A Franza, A M Marshall, N Losacco. D Boldini (2020). Tunnel-framed building interaction: comparison between raft and separate footing foundations. *Géotechnique (in press, doi: 10.1680/jgeot.19.P.393)*	3,5
J Xu, A Franza, A M Marshall (2020). The response of framed buildings on raft foundations to tunneling. *ASCE - Journal of Geotechnical and Geoenvironmental Engineering (in press, doi: 10.1061/(ASCE)GT.1943-5606.0002376)*	3,4
J Xu, A Franza, A M Marshall, N Losacco (2020). Experimental study on the role of footing embedment depth on tunnel-foundation interaction. *ASCE - Journal of Geotechnical and Geoenvironmental Engineering (under review)*	3,6
J Xu, A M Marshall, A Franza, D Boldini, A Amorosi, M J DeJong (2019). The response of framed buildings on raft foundations to tunnelling: a centrifuge and numerical modelling study, *Proceedings of the 17th European Conference on Soil Mechanics and Geotechnical Engineering, Iceland. (doi: 10.32075/17ECSMGE-2019-0134)*	3,4
J Xu, A Franza, A M Marshall (2020). A centrifuge modelling study on the effect of foundation configuration on tunnel-frame interaction. *10th International Symposium on Geotechnical Aspects of Underground Construction in Soft Ground, Cambridge, UK. (in press)*	3,5
J Xu, A Franza, A M Marshall (2020). Centrifuge modelling of tunnel-soil-pile interaction considering the presence of rigid caps. *4th European Conference on Physical Modelling in Geotechnics, Sweden.*	-
A Hashemi, **J Xu**, C Heron, A M Marshall (2020). Chromatic aberration when using white LEDs for PIV: issues and remedies. *4th European Conference on Physical Modelling in Geotechnics, Sweden.*	3
D Boldini, N Losacco, A Franza, M J DeJong, **J Xu**, A M Marshall (2020). Tunnelling-induced deformation of framed structures: a numerical study. *ASCE - Journal of Geotechnical and Geoenvironmental Engineering (under review)*	4,5

Chapter 2

Literature review

This chapter summarises the existing works related to tunnelling and its effects on nearby structures. First, ground movement characteristics caused by greenfield tunnelling in the urban environment and their prediction methods are presented. Then, building deformation parameters and the assessment of damage category due to ground movements are illustrated. Finally, existing studies on the prediction of the tunnelling-induced structural distortion considering soil-structure interaction are reviewed and discussed.

2.1 Greenfield tunnelling

This section presents a summary of the works related to greenfield tunnelling induced ground displacements. The terminology of "greenfield" refers to the tunnel construction scenario where no structure exists around the tunnel. In this section, the concepts of the parameters commonly used to describe the ground deformation caused by tunnelling are first illustrated; then, works related to centrifuge modelling on greenfield tunnelling in sand are presented.

2.1.1 Ground deformation and volume loss

Tunnelling is common in increasingly congested urban environments. Two tunnel construction methods are practically implemented in soft ground, namely, open-faced excavation, and closed-face methods using tunnel boring machines (Mair and Taylor, 1997), depending on the construction and ground conditions. Closed-face tunnel boring machines, which are often used in unstable ground conditions, operate on the principle of a pressurised face. The development of the earth pressure balance (EPB) machines is a great improvement for tunnelling in all types of unstable ground. As an alternative method, the slurry shield machine is mainly used in water bearing granular soils.

However, no matter which construction method is used, tunnelling inevitably causes stress disturbance/relief, which results in the movement of the surrounding soil. A qualitative description of surface greenfield settlements due to tunnel construction is shown in Figure 2.1. In particular, Mair and Taylor (1997) summarised that ground movement generally includes the following components:

1. ground movement towards the tunnel opening due to stress disturbance;
2. ground deformation due to the advancement of the shield (presence of the over-cutting edge, and the tendency to plough or yaw);
3. gap existing between the shield tailskin and lining;
4. deformation of lining caused by ground loading; and

5. consolidation effect of the ground.

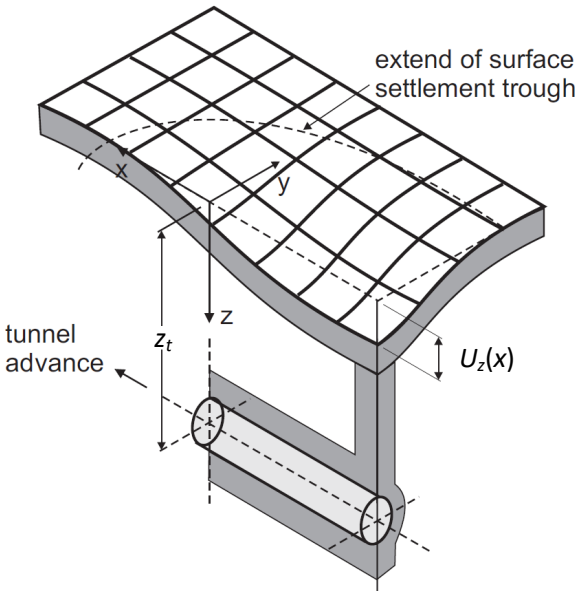


Fig. 2.1. Ground settlement caused by tunnelling (reproduced from Attewell et al. (1986); Franza (2016))

Among these components, component 1 is the most important reason for the majority of tunnelling cases, especially for open-face tunnelling. However, this aspect can be significantly reduced if pressurised face tunnelling techniques are adopted.

Ground treatment techniques are important in the control of the surface settlement. For open-face tunnelling, face reinforcement is achieved by soil nailing, which has become an effective approach to control both face stability and ground movements. On the other hand, the use of slurry and earth pressure balance shield techniques plays an important role in controlling ground deformation. When tunnelling in an urban area, compensation grouting has been frequently adopted to control ground movements, thus helping reduce the possible effect of tunnelling on nearby structures.

Ground deformation caused by tunnelling can be simplified as a two-dimensional problem in either a longitudinal or transverse plane with respect to the tunnel. Considering the transverse direction, a quantitative measure of the amount of disturbance caused by tunnelling is given by ground loss V_s (the volume of the ground surface settlement trough per metre length). To evaluate the ground settlement caused by tunnelling, the parameter of soil volume loss $V_{l,s}$ is

used, which is given by the ratio between ground loss V_s and the nominal cross-sectional area per metre run of the tunnel (V_0):

$$V_{l,s} = \frac{V_s}{V_0} \times 100\% \tag{2.1}$$

Alternatively, the term of tunnel volume loss $V_{l,t}$ is also frequently used in experimental, analytical or numerical studies. Tunnel volume loss $V_{l,t}$ can be obtained by the ratio of the volume loss of the soil around the tunnel periphery V_t to the actual excavation volume (area) of the tunnel V_0:

$$V_{l,t} = \frac{V_t}{V_0} \times 100\% \tag{2.2}$$

Importantly, for undrained conditions (e.g. tunnelling in clay in the short term), $V_{l,t}$ is equal to $V_{l,s}$. However tunnelling in sandy ground (drained condition) generates a complex relationship between $V_{l,t}$ and $V_{l,s}$ due to the contraction or dilation behaviour of the soil (Marshall et al., 2012; Franza et al., 2020b). By reviewing the settlement data reported in the existing literature about bored tunnelling, Mair and Taylor (1997) estimated that: for open-face tunnelling, tunnel volume losses in stiff clay are normally between 1% and 2%; if sprayed concrete linings are used during tunnel construction, the volume losses can be decreased to 0.5%-1.5%; for tunnelling using close-face tunnelling method, for instance, EPB or slurry shields machines, very good ground settlement control can be achieved, often giving a volume loss below 0.5% for sandy ground or stiff clays, and 1%-2% for soft clays.

2.1.2 Tunnelling-induced transverse settlement

2.1.2.1 Surface settlement

The tunnelling-induced ground surface settlement trough was first empirically described as the form of a standard Gaussian curve by Peck (1969), as shown in Equation 2.3:

$$U_z(x) = U_{z,max} \cdot \exp\left(-\frac{x^2}{2i^2}\right) \tag{2.3}$$

where U_z is ground surface settlement, $U_{z,max}$ is the maximum ground surface settlement (occurs at the tunnel centreline), x is the horizontal distance from the tunnel centreline, and i

defines the horizontal distance between the point of inflexion of the settlement trough and the tunnel centreline, as shown in Figure 2.2.

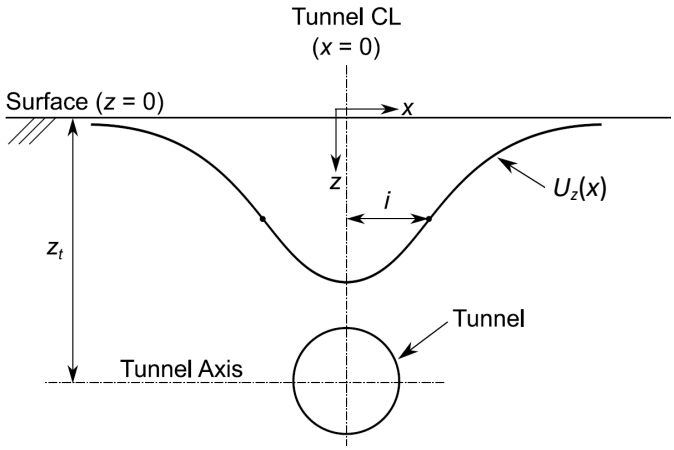


Fig. 2.2. Vertical ground settlement shape described by a Gaussian curve (after Ritter (2018))

Based on this assumption, the volume of transverse ground settlement trough per metre of tunnel, V_s, can be obtained by integrating Equation 2.3:

$$V_s = \sqrt{2\pi} i U_{z,max} \tag{2.4}$$

Equation 2.3 shows that the shape of tunnelling-induced ground surface settlement trough is defined by i and $U_{z,max}$. For parameter i, O'Reilly and New (1982) found that, based on the monitoring data of settlements above tunnels constructed in the United Kingdom, i increases approximately linearly with the depth of tunnel axis, z_t, as shown in Equation 2.5:

$$i = K z_t \tag{2.5}$$

where K is the trough width parameter. It was suggested that values of K are between 0.4 and 0.6 for tunnelling in clay, and 0.25 and 0.45 for tunnelling in sands and gravels (O'Reilly and New, 1982; Mair and Taylor, 1997).

2.1.2.2 Subsurface settlement

Tunnels are also frequently excavated in proximity to the buried structures, for example, pile foundations and buried pipelines. Therefore, in order to assess the effect of tunnelling on buried structures, it is important to predict tunnelling-induced subsurface settlement movements.

It is generally assumed that the subsurface settlement trough profiles are also characterised by a Gaussian curve (Mair et al., 1993) (Equation 2.3). To predict the value of the parameter i, using centrifuge test data and limited field measurement data of subsurface settlement profiles, Mair et al. (1993) proposed a proportional relationship between i and the depth of interest with a gradient of K, where the parameter K is a non-linear relationship of the ratio between the depth of interest and tunnel axis, z/z_t, as shown in Equations 2.6 and 2.7:

$$i = K(z_t - z) \tag{2.6}$$

$$K = \frac{0.175 + 0.325(1 - z/z_t)}{1 - z/z_t} \tag{2.7}$$

Reasonable agreement for the fit to centrifuge data of tunnelling in clay was obtained (Grant and Taylor, 2000). However, Moh et al. (1996) suggested that Equation 2.6 gave much steeper and narrower subsurface settlement troughs compared with monitoring data from an EPB tunnelling project in silty sands and clays, whereas Jones (2010) reported an overestimated width parameter K calculated using Equation 2.6 in deep tunnel scenarios. Alternatively, some new forms of equations were also suggested (Moh et al., 1996; Lee et al., 1999; Jones, 2010). In particular, by referring to the framework from Clough and Schmidt (1981), Moh et al. (1996) suggested that the tunnel diameter D_t may affect the settlement trough width, and proposed Equation 2.8 based on the settlement data collected from the construction of Taipei Rapid Transit Systems:

$$i = \left(\frac{D_t}{2}\right)\left(\frac{z_t}{D_t}\right)^{0.8}\left(\frac{z_t - z}{z_t}\right)^m \tag{2.8}$$

where the additional parameter m depends on the ground condition; for sandy ground, $m = 0.4$ was suggested, whereas $m = 0.8$ tended to fit better the data from the clayey ground. Neverthe-

less, for clays, example data were limited to the single case (Moh et al., 1996). It is also noted that Equation 2.8 was derived using field monitoring data, and thus the equation may have its limitation.

Using the monitoring data from field sites, Jones (2010) proposed the following logarithmic equation:

$$K = -0.25\ln[z_t - z] + 1.234 \tag{2.9}$$

Equation 2.9 suggests that the settlement trough shape depends on both depth of interest z and tunnel axis depth z_t.

On the other hand, Lee et al. (1999) performed a series of centrifuge tests investigating the soil movements around a tunnel in soft clays. By examining the centrifuge data, the authors suggested a simplified Equation 2.10 illustrating the relationship between tunnel diameter D_t and i:

$$2\frac{i}{D_t} = 1 + 0.58\frac{z}{D_t} \tag{2.10}$$

To further evaluate the effectiveness of the proposed equation, Lee et al. (1999) also considered the relationships suggested by Clough and Schmidt (1981) ($i = \left(\frac{D_t}{2}\right)\left(\frac{z_t}{D_t}\right)^{0.8}$, similar to Equation 2.8) and O'Reilly and New (1982) (Equation 2.5). The authors examined these equations using their centrifuge data and the centrifuge model test results obtained by Mair et al. (1981), as well as the monitoring data from the field sites (Hwang et al., 1995). It was shown that Equation 2.10 fitted reasonably well the data points, whereas the equation from Clough and Schmidt (1981) underestimated the trough width, and an overestimated trough width was obtained for deeper tunnel cases using the O'Reilly and New (1982) relationship.

2.1.3 Ground transverse horizontal movement

Horizontal ground displacements are usually very small so that few field data measured in tunnelling projects have been reported. However, the prediction of tunnelling-induced horizontal displacements is also important for the scenarios in which tunnels are excavated beneath flexi-

ble pipelines or structures with discontinuous foundations (for example, separate strip footings). Assuming that the directions of the soil displacement vectors point to a specific point, the horizontal displacements of the soil at any position, $U_x(x)$, can be derived from the predicted surface and subsurface settlement profiles (O'Reilly and New, 1982):

$$U_x(x) = \frac{x}{z - z_t} \cdot U_z(x) \tag{2.11}$$

Combining Equations 2.3 and 2.11, the horizontal strain, $\varepsilon_h(x)$, can be obtained by taking the derivative of $U_x(x)$:

$$\varepsilon_h(x) = \frac{U_{z,max}}{z_t - z} \cdot \exp(-\frac{x^2}{2i^2}) \cdot (1 - \frac{x^2}{i^2}) \tag{2.12}$$

Tunnelling-induced vertical ground surface settlements, horizontal displacements and horizontal strains can, therefore, be plotted in Figure 2.3 (Franzius, 2003).

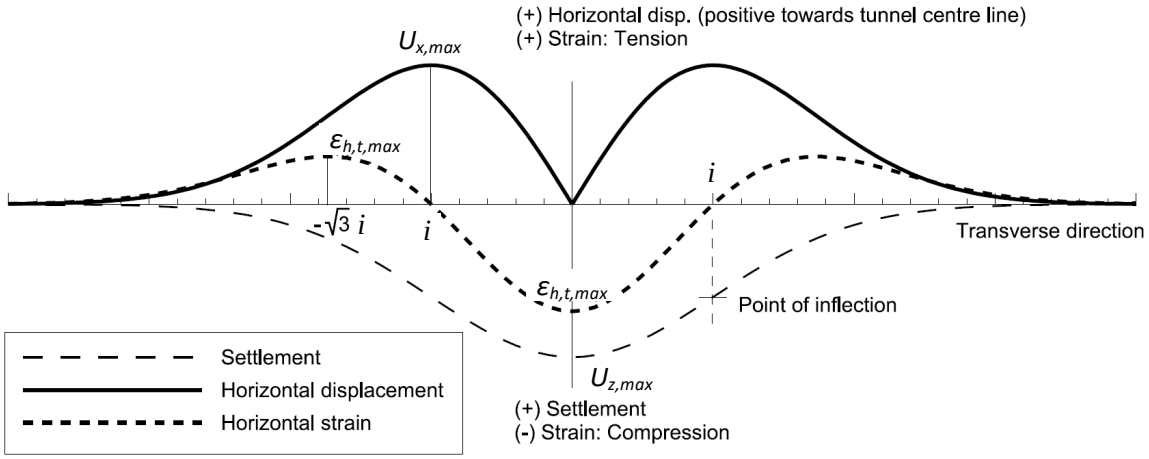


Fig. 2.3. Vertical ground settlement, horizontal displacement and strain (after (Franzius, 2003))

Alternatively, Attewell and Yeates (1984) theoretically derived the following equation for the estimation of tunnelling-induced subsurface soil horizontal displacements.

$$U_x(x) = U_z(x)\frac{nx}{z - z_t} \tag{2.13}$$

It was suggested by the authors that for cohesive soils, $n = 1.0$, which is same as Equation 2.11. On the other hand, $n < 1.0$ was suggested for granular soil, indicating that displacement vectors

point to a position below the tunnel axis.

Based on case history data for clays, it is suggested that assuming soil displacement vectors pointing towards the tunnel axis may not give a precise prediction for horizontal ground displacements induced by tunnel construction (Mair and Taylor, 1997; Taylor, 1995b). For undrained conditions, based on theoretical analysis, Taylor (1995b) proposed an alternative equation considering the variation of K with depth (shown in Equation 2.7), given as:

$$U_x(x) = U_z(x)\frac{x}{(1+0.175/0.325)z_t} \tag{2.14}$$

According to Equation 2.14, the soil displacement vectors direct toward a point with a depth of $0.175z_0/0.325$ lower than the tunnel axis (O'Reilly and New, 1982). Data obtained from the centrifuge test for tunnelling in clay (Grant and Taylor, 2000) agreed well with Equation 2.14, through the focal point may show a considerable scatter.

For tunnelling in sands, studies (Cording and Hansmire, 1975; Cording, 1991) have shown that the horizontal deformations at the edge of the settlement trough are much larger than the predicted values by Equations 2.11 and 2.13, and a greater horizontal displacement than the vertical displacement may be observed near the settlement trough edge (Cording and Hansmire, 1975). Recently, Marshall (2009) reported that, based on the results obtained from centrifuge modelling of tunnelling in sands, the direction of the displacement vectors varies not only with the offset from the tunnel centreline, but also with the depth of interest. On the other hand, Farrell (2010) suggested the use of modified Gaussian curve (for predicting $U_z(x)$) in Equation 2.13 to obtain a better prediction for the horizontal displacements of tunnelling in sandy ground.

2.1.4 Ground longitudinal settlement

The progressive longitudinal ground settlement during tunnel construction could severely damage the structures that are located directly above the tunnel face. Following the assumption that the greenfield settlement trough profile has a Gaussian curve shape, Attewell and Woodman (1982) proposed the cumulative probability curve to fit the longitudinal ground settlement

trough above the tunnel face, as shown in Figure 2.4. This approach is only applicable for the scenario that tunnels are constructed in clays, in which soil volume loss $V_{l,s}$ is equal to tunnel volume loss $V_{l,t}$ (New and O'Reilly, 1991). Based on the data obtained from a series of field sites, Attewell and Woodman (1982) found that ground surface settlement directly above the tunnel face approximately equals to $0.5U_{z,max}$ for tunnelling in stiff clays. However, this conclusion only applies to open-face tunnelling techniques in clays (Mair and Taylor, 1997), in which face support is not provided. For the tunnel excavated using EPB or slurry shield machines, where effective face support is provided, the longitudinal ground settlement trough would lag the tunnel face a certain distance (Figure 2.4), and thus the measured settlement directly above the tunnel face is significantly less than $0.5U_{z,max}$.

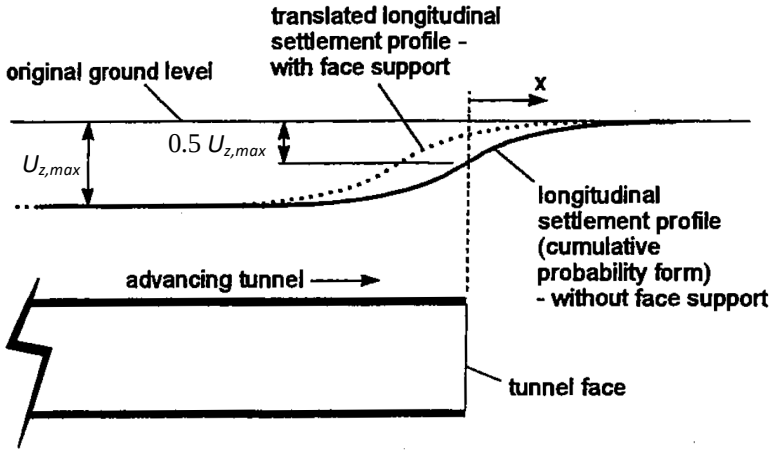


Fig. 2.4. Longitudinal surface settlement trough (after Mair and Taylor (1997))

2.1.5 Tunnelling in sandy ground

2.1.5.1 Empirical methods

Empirical methods have been widely used for the prediction of tunnelling-induced ground movement because of their reliability. Good prediction for the tunnelling-induced ground surface settlement can be empirically achieved by using standard Gaussian curve (Peck, 1969) in some cases, especially for tunnelling in clays (undrained conditions) (O'Reilly and New, 1982; Mair et al., 1993; Mair and Taylor, 1997). However, it has been frequently reported that the

standard Gaussian curve does not always provide a good fit to settlement trough data (Celestino et al., 2000; Jacobsz et al., 2004; Vorster et al., 2005), particularly for tunnels in sands (drained conditions) (Marshall et al., 2012). Furthermore, despite the poor fit for some data sets, numerous studies (Mair and Taylor, 1997; Sugiyama et al., 1999; Jacobsz, 2002; Vorster et al., 2005) also highlighted that the value of settlement trough width may be affected by additional factors, such as tunnel cover depth and volume loss, suggesting the complexity of tunnelling-induced displacements in sandy ground. Consequently, alternative curves, including yield-density type curves (Celestino et al., 2000), a slightly different form of Gaussian curve (Jacobsz et al., 2004), and modified Gaussian curve (Vorster et al., 2005) were introduced to obtain a better fit to tunnelling induced settlement data in drained conditions. These curves, along with the standard Gaussian curves, are summarised in Table 2.1 by Marshall et al. (2012).

Table 2.1. Curves to fit surface settlement trough, summarised by Marshall et al. (2012)

Curve types	Equation	Detail
Gaussian curve (Peck, 1969)	$U_z(x) = U_{z,max}\exp\left(-\frac{x^2}{2i^2}\right)$	$U_z(i) = 0.606U_{z,max}$
Jacobsz curve (Jacobsz et al., 2004)	$U_z(x) = U_{z,max}\exp\left[-\frac{1}{3}\left(\frac{\lvert x\rvert}{i}\right)^{1.5}\right]$	$U_z(i) = 0.717U_{z,max}$
Yield density curve (Celestino et al., 2000)	$U_z(x) = \frac{U_{z,max}}{1+(\lvert x\rvert/a)^b}$	$i = aB; B = \left(\frac{b-1}{b+1}\right)^{1/b}$
Modified Gaussian curve (Vorster et al., 2005)	$U_z(x) = \frac{nU_{z,max}}{(n-1)+\exp[\alpha(x^2/i^2)]}$	$n = \exp(\alpha)\frac{2\alpha-1}{2\alpha+1} + 1$

Using the data from field site monitoring (Dyer et al., 1996) and centrifuge testing, Marshall et al. (2012) evaluated the goodness of fit of the existing curves in Table 2.1. It was confirmed that the Gaussian curve cannot always provide an excellent fit to the greenfield settlement data. On the other hand, it had been shown that the modified Gaussian and Yield density curves illustrated a better fit than the standard Gaussian curve (Marshall et al., 2012), in which the goodness of the fit of the latter curve decreased with the increase of volume loss $V_{l,t}$, or the depth of interest. For instance, when fitting the curves to the greenfield surface settlement data obtained from centrifuge modelling (C/D = 1.3, I_d = 90%, Leighton Buzzard Fraction E silica sand), the values of coefficient of determination R^2 for the standard and modified Gaussian curves at $V_{l,t}$ = 1% are 0.9870 and 0.9952, respectively. However, at $V_{l,t}$ = 2.5%, the value of R^2 for the

standard Gaussian curve decreased to 0.9776 (for the modified Gaussian curve, $R^2 = 0.9966$). It is likely that the chimney-like displacement pattern results in the poor fit of the Gaussian curve (Cording, 1991; Marshall et al., 2012). Importantly, the modified Gaussian and Yield density curves are determined by three parameters, and thus they are not as user-friendly as the standard Gaussian curve. Furthermore, it is also suggested that for similar shapes of the settlement troughs, the value of i in standard and modified Gaussian curves can vary considerably (Vorster et al., 2005; Marshall et al., 2012). This would bring confusion for engineers, as the settlement trough width is an important factor within soil-structure interaction problems.

To address this issue, Marshall et al. (2012) suggested using two points, x^*, corresponding to $0.606U_{z,max}$, and x^{**}, corresponding to $0.303U_{z,max}$, where $U_{z,max}$ is the maximum settlement, to define the shape of the settlement trough. Importantly, $0.606U_{z,max}$ is also the settlement value of the inflection point of the standard Gaussian curve, thus facilitating the comparison of the shapes between two different curves. The corresponding trough width parameters, K^* and K^{**} can also be defined using Equation 2.7. Considering the effects of tunnel cover depth C/D_t and volume loss $V_{l,t}$, Marshall et al. (2012) proposed the following equations to determine the settlement trough shapes:

$$\begin{aligned} K^* &= \frac{K_s^* + (\partial x^*/\partial z)\,(z/z_t)}{1 - z/z_t} \\ K_s^* &= K_{s,C/D_t}^{*int} + K_{s,C/D_t}^{*slope}\,(C/D_t) + K_{s,V_l}^{*slope}\left(V_{l,t}\right) \end{aligned} \tag{2.15}$$

where $K_{s,C/D_t}^{*int} = 0.440$; $K_{s,C/D_t}^{*slope} = 0.055$; $K_{s,V_l}^{*slope} = -0.041$; $\partial x^*/\partial z = -0.436$;

Furthermore, the position of point x^{**} can be empirically determined using $K_s^{**} = K_s^* + 0.29$, as well as $(\partial x^{**}/\partial z) = (\partial x^*/\partial) z - 0.20$. It should be noted that the values of parameters in Equation 2.15 were determined using centrifuge testing results of tunnelling in a specific ground condition (dense dry silica sand). As a consequence, care should be taken when using the values of parameters of Equation 2.15 in scenarios with different soil properties. However, Equation 2.15 does provide a useful framework to define the settlement trough shapes above tunnelling in sand or gravels.

Using a vast database of centrifuge tests (with varying soil density I_d and a wider range of tunnel relative depth C/D_t than Marshall et al. (2012)), Franza et al. (2019) found that the

parameters used in Equation 2.15 change non-linearly with C/D_t, and thus the prediction for shallow tunnels (for instance, $C/D_t = 1.3$) is less good. To overcome this issue, and to consider the effect of soil density, Franza et al. (2019) proposed a new set of equations:

$$\begin{aligned}
\partial x^*/\partial z &= \frac{(+0.81I_d - 0.93)\ln[C/D_t] - 0.60I_d - 0.07}{1 + z/z_t} \\
\partial x^{**}/\partial z &= \frac{(+1.50I_d - 1.55)\ln[C/D_t] - 0.96I_d - 0.28}{1 + z/z_t} \\
K_{s,V_{l,t}}^{*slope,ln} &= (+0.35I_d - 0.30)\ln[C/D_t] - 0.22I_d + 0.07 \\
K_{s,V_{l,t}}^{**slope,ln} &= (+0.41I_d - 0.35)\ln[C/D_t] - 0.22I_d - 0.01 \\
K_{s,V_{l,t}}^{*int,ln} &= (-0.84I_d + 0.95)\ln[C/D_t] + 0.45I_d + 0.07 \\
K_{s,V_{l,t}}^{**int,ln} &= (-1.16I_d + 1.36)\ln[C/D_t] + 0.47I_d + 0.42
\end{aligned} \tag{2.16}$$

Franza et al. (2019) verified the proposed Equation 2.16 against the centrifuge data. It was found that an overall good prediction was obtained for both K^* and K^{**} in different tunnelling scenarios (i.e. varying C/D_t and I_d). Therefore, Equation 2.16 could be used to predict the settlement profiles above tunnels in sand. Nevertheless, as also highlighted by Franza et al. (2019), this set of equations was derived using centrifuge tests, and thus care should be taken when using these equations in a real tunnelling project.

2.1.5.2 Ground displacement patterns

Using data obtained from geotechnical centrifuge tests of greenfield tunnelling in sands, Marshall et al. (2012), Zhou (2014) and Franza et al. (2019) discussed the effects of tunnel cover depth C/D_t, relative density I_d and tunnel volume loss $V_{l,t}$ on ground displacement patterns.

Figure 2.5 displays normalised horizontal U_x and vertical U_z displacements at $V_{l,t} = 3\%$ for varying C/D_t (left) and I_d (right) from Marshall et al. (2012) and Franza et al. (2019). For the effect of C/D_t in dense soil, the following conclusions are summarised: (i) the increase of the value of C/D_t decreased the size of the zone that exhibits large normalised settlements; (ii) the shallower (low C/D_t value) the tunnel, the narrower the settlement though; this indicates that for a shallow tunnel, large settlements are localised near the tunnel crown, whereas a more spread out displacement pattern is observed for deep tunnels; (iii) with the increase of tunnel

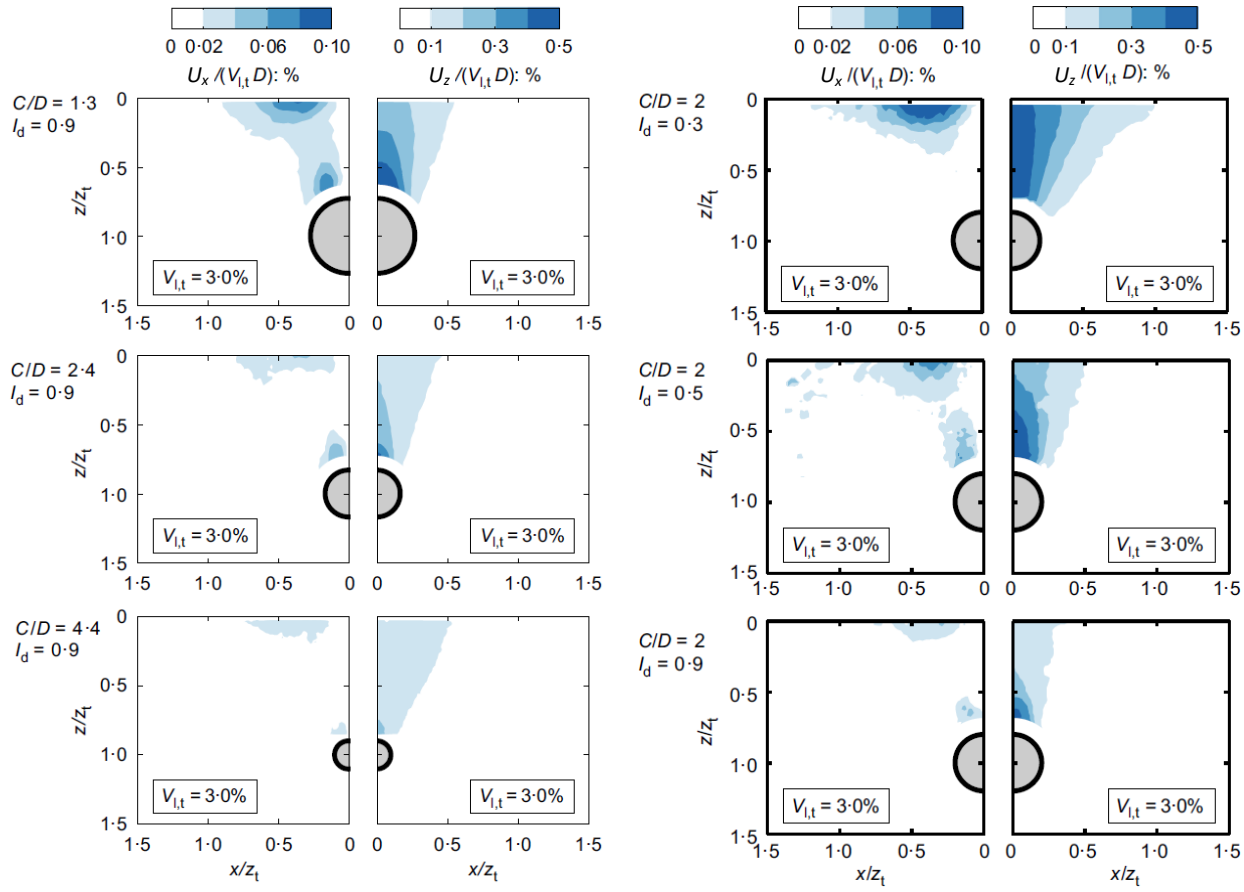


Fig. 2.5. Normalised displacements at $V_{l,t} = 3\%$ for varying C/D_t (left) and I_d (right) (Franza et al., 2019)

volume loss $V_{l,t}$, the deformation pattern becomes narrower.

For the effect of the relative density I_d of sand, data from the right side of Figure 2.5 shows that the denser the soil, the smaller the magnitude of the displacements. Furthermore, the zone having large vertical displacements is localised above the tunnel crown in dense soil, whereas in loose soil, the corresponding zones developed from the tunnel crown toward the surface, and resulted in a wider settlement trough.

To reveal the fundamental mechanism that governs tunnelling-induced displacements, Franza et al. (2019) proposed the use of the soil arching mechanism, aiming to explain the influence of varying tunnel depth, soil density, and volume loss. The arching mechanism is illustrated in Figure 2.6.

In general, in the dense or medium dense sand, a closed arch can generate (Franza et al.,

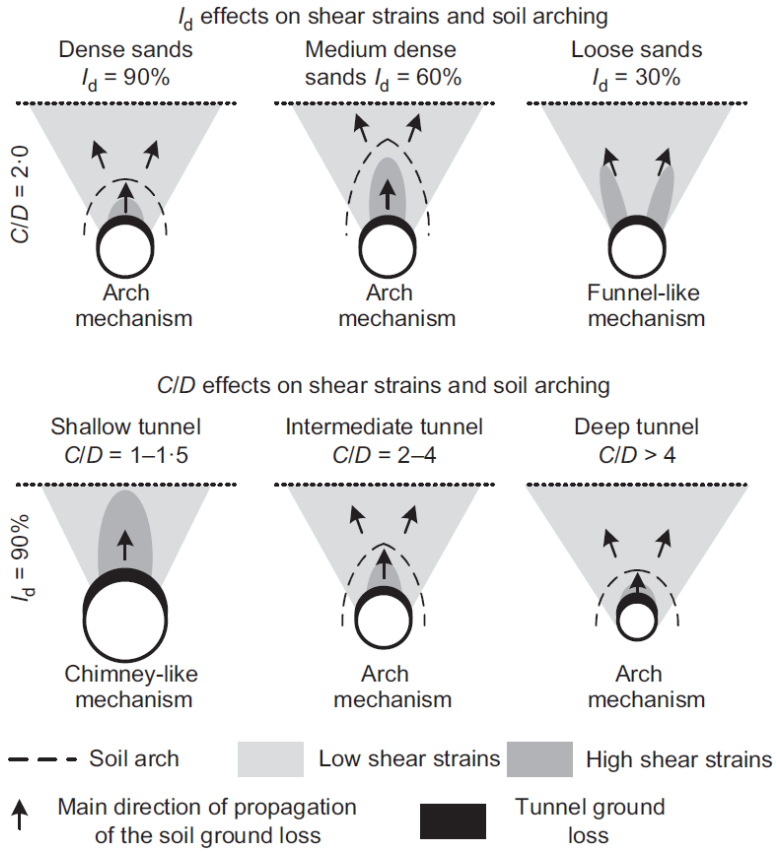


Fig. 2.6. Soil arching mechanism governing the ground displacements (Franza et al., 2019)

2019). Consequently, soil settlements in the region above the forming arch are largely restricted, resulting in a localised large settlement zone between the tunnel crown and the bottom of the arch (see Figure 2.5). Furthermore, the propagation of ground movements above the arch results in a wide displacement pattern. In the loose soil, the arch may not form. Therefore, a large settlement zone develops toward the surface, and thus a narrow settlement trough forms. On the other hand, as displayed in Figure 2.6, the increase of tunnel depth results in a relatively small arch (considering the ratio of the area of the arch to the total area above the tunnel), thus forming a wider settlement trough. Similarly, the increase of tunnel volume loss increases the height of the arch, thereby decreasing the width of settlement trough.

2.1.5.3 Tunnel and soil volume losses

For tunnelling in drained soil (sand or gravels), the volume of the soil may change under shear, resulting in $V_{l,t} \neq V_{l,s}$. Therefore, understanding the volumetric behaviour of the soil is important for engineers to determine the relationship between tunnel $V_{l,t}$ and soil $V_{l,s}$ volume loss.

Based on measured soil displacement data, Marshall et al. (2012) obtained the distribution of shear strain in a centrifuge test ($C/D_t = 2.4$ and $I_d = 90\%$) at $V_{l,t} = 1\%$ and 2.5%, as shown in Figure 2.7. It is shown that high shear strain zones are localised near the tunnel shoulders, and most regions display a low level of shear strain. Using triaxial compression test data from Zhao (2008), Marshall et al. (2012) explained the relationship between engineering volumetric ε_v and shear γ strains of tunnels in sand, as shown in Figure 2.8.

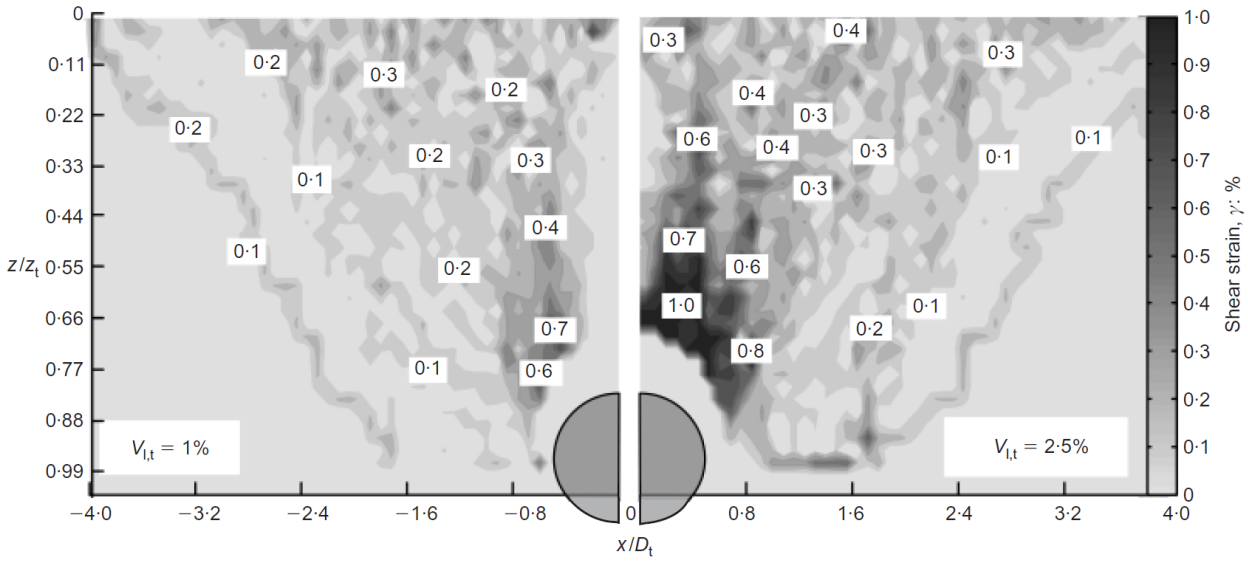


Fig. 2.7. Contours of shear strain from centrifuge tests (Marshall et al., 2012)

Figure 2.8 shows that the dense sand is contractive under small shear strain, whereas dilative behaviour is expected at the high level of shear strain. Consequently, for the shallow and large tunnel, where strains are greater, the overall behaviour of the soil is dilative, resulting in $V_{l,t} > V_{l,s}$. On the other hand, the lower level of shear strains in small and deep tunnel causes overall volumetric contraction (therefore $V_{l,t} < V_{l,s}$). Nevertheless, Marshall et al. (2012) also pointed out that, at a low level of volume loss, $V_{l,s}$ may be greater than $V_{l,t}$ due to the low values of shear strains.

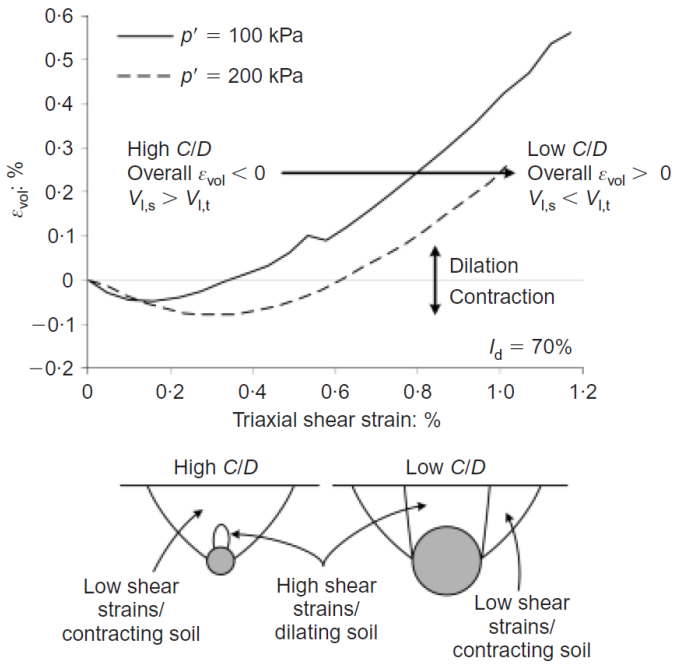


Fig. 2.8. Illustration of soil volumetric behaviour under shear (Marshall et al., 2012)

Data presented in Figure 2.9 (Franza et al., 2019) supports the above conclusions. Figure 2.9 shows that for a given tunnel volume loss $V_{l,t}$, soil volume loss $V_{l,s}$ increased with the increase of C/D_t values due to the lower average values of shear strains for larger C/D_t. As expected, the increase in soil density and tunnel volume loss decreased the ratio of $V_{l,s}$ to $V_{l,t}$.

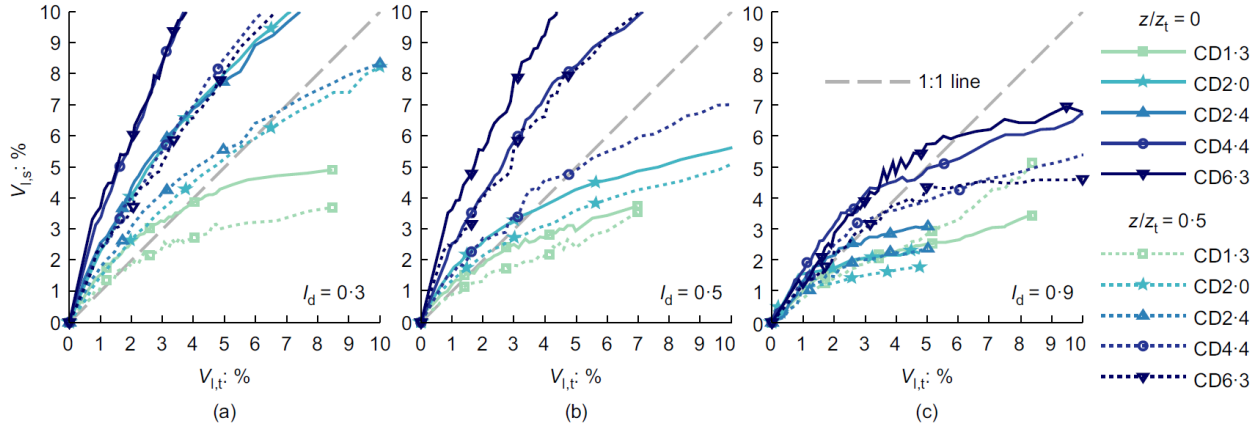


Fig. 2.9. Relationship between soil and tunnel volume losses (Franza et al., 2019)

2.2 The effects of tunnelling on buildings

This section broadly covers a review of existing literature related to the effects of tunnelling on buildings. First, the building damage parameters that are widely used in practice are presented. Then, a staged risk assessment procedure proposed by Mair and Taylor (1997) is introduced. Finally, the evaluation of tunnelling-induced structural damage considering soil-structure interaction is discussed.

2.2.1 Building damage parameters

Building damage is generally caused by the differential foundation movement that results in stress and strain changes, thereby causing structural cracks and damage. The most widely adopted building deformation parameters are those defined by Burland and Wroth (1974) and Burland et al. (1977) using measured displacements at the building foundation level, as shown in Figure 2.10.

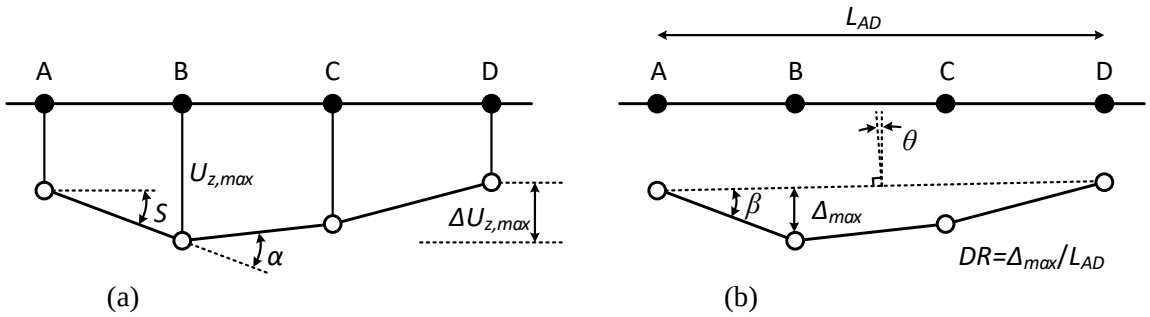


Fig. 2.10. Building deformation parameters defined (after Burland et al. (1977))

- *Settlement*, U_z, is the vertical displacement of the structure, as shown in Figure 2.10(a);
- *Relative/differential settlement*, ΔU_z, gives the differential settlement between two selected points of the structure (Figure 2.10(a));
- *Rotation*, s, describes the change in gradient of a straight line connecting two points on the structure;

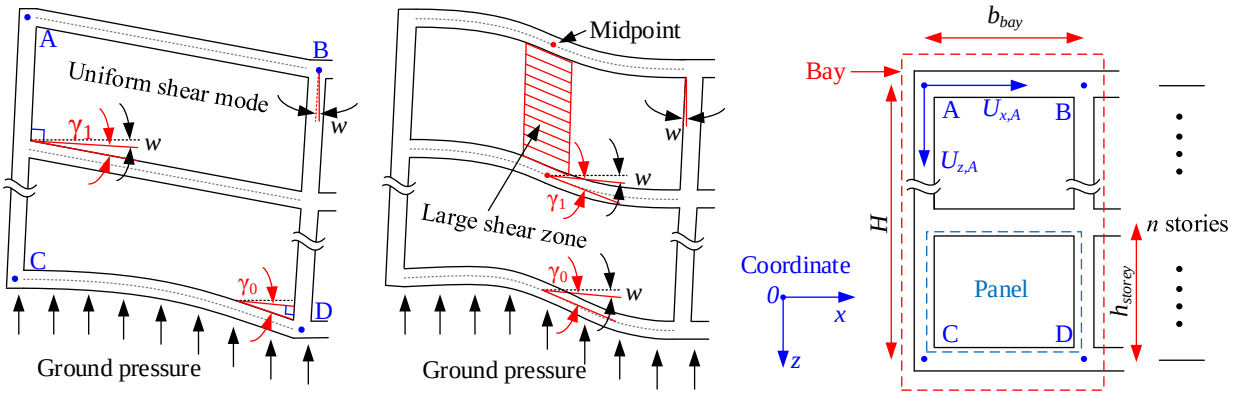
- *Angular strain*, α, shown in Figure 2.10(a), is calculated by $\Delta U_{z,BA}/L_{AB} + \Delta U_{z,BC}/L_{BC}$, with positive value for sagging zone and negative for hogging zone;
- *Relative deflection*, Δ, is given by the maximum settlements relative to a straight line connecting two points on the structure (see Figure 2.10(b))
- *Deflection ratio (DR)*, Δ/L, is the ratio of the relative deflection and the distance of corresponding two points;
- *Tilt*, θ, is defined to describe the rigid body rotation of the structure;
- *Angular distortion*, β, describes the rotation of the line connecting two points of the structure with respect to the tilt, as shown in Figure 2.10(b);
- *Horizontal displacement*, U_x, describes the horizontal movement of the structure; and
- *Horizontal Strain*, ε_h, gives the ratio of the differential horizontal displacements and the horizontal distance between two points on the structure.

Note that deformation parameters illustrated in Figure 2.10 are derived using foundation displacements. Recent studies have linked measured or computed building displacements at varying elevations (considering the building details) to the deformation parameters. In particular, Son and Cording (2005) calculated the angular distortion β using the top and bottom corner displacements of each bay (see Figure 2.11) by subtracting tilt θ from the slope S:

$$\beta = S - \theta = \frac{\Delta U_{tot}}{b_{bay}} - \left(\frac{w_2}{2} + \frac{w_1}{2}\right) \tag{2.17}$$

where $\Delta U_{tot} = U_{z,D} - U_{z,C}$ is the total differential settlement; $w_1 = \left(U_{x,C} - U_{x,A}\right)/H$ and $w_2 = \left(U_{x,D} - U_{x,B}\right)/H$ are left and right edge tilt, respectively; for $U_{i,j}$, $i = x;z$ is the displacement direction; $j = A;B;C;D$ is the location of the panel corner; and b_{bay} and H are, respectively, the bay width and building total height.

Alternatively, Cook (1994) proposed an approach to isolate tilt (ΔU_{tilt}), bending (ΔU_{bend}), and shear (ΔU_{shear}) displacements from the total differential settlement ΔU_{tot}. Based on this



(a) Hinged end beam (b) Fixed end beam (c) Parameter definition

Fig. 2.11. (a) and (b) bay distortion modes; (c) parameter definition

approach, Ritter et al. (2020) derived the shear distortion γ in Equation (2.18) using top and bottom corner displacements of the bay of interest (see Figure 2.11). Interestingly, shear distortion γ of the structure is equal to the angular distortion β estimated by Son and Cording (2005):

$$\begin{aligned}\gamma &= \frac{\Delta U_{shear}}{b_{bay}} = \frac{\Delta U_{tot}}{b_{bay}} - \frac{\Delta U_{tilt}}{b_{bay}} - \frac{\Delta U_{bend}}{b_{bay}} \\ &= \frac{\Delta U_{tot}}{b_{bay}} - w_1 - \frac{w_2 - w_1}{2} = \frac{\Delta U_{tot}}{b_{bay}} - \left(\frac{w_2}{2} + \frac{w_1}{2}\right)\end{aligned} \tag{2.18}$$

Finally, several studies have distinguished between the shear deformations within a bay (averaged along the full-height of the building, as in Son and Cording (2005) and Cook (1994)), and the panel distortions (Boone, 1996; Elkayam and Klar, 2019). For example, for evaluating the distortions of panels, Elkayam and Klar (2019) estimated axial and diagonal strains using the displacements at the four corners of a panel:

$$\begin{aligned}\delta_z &= U_{z,A} + \left(U_{z,B} - U_{z,A}\right)\frac{x}{b_{bay}} + \left(U_{z,D} - U_{z,A}\right)\frac{x}{h_{storey}} \\ &\quad + \left(U_{z,A} - U_{z,B} + U_{z,C} - U_{z,D}\right)\frac{xz}{b_{bay}h_{storey}} \\ \delta_x &= U_{x,A} + \left(U_{x,B} - U_{x,A}\right)\frac{x}{b_{bay}} + \left(U_{x,D} - U_{x,A}\right)\frac{x}{h_{storey}} \\ &\quad + \left(U_{x,A} - U_{x,B} + U_{x,C} - U_{x,D}\right)\frac{xz}{b_{bay}h_{storey}}\end{aligned} \tag{2.19}$$

where δ_x and δ_z are the in-plane displacements of any point within a panel, and $U_{x,i}$ and $U_{z,i}$ are the displacements at the four corners (i = A, B, C and D) of a panel, as shown in Figure 2.12.

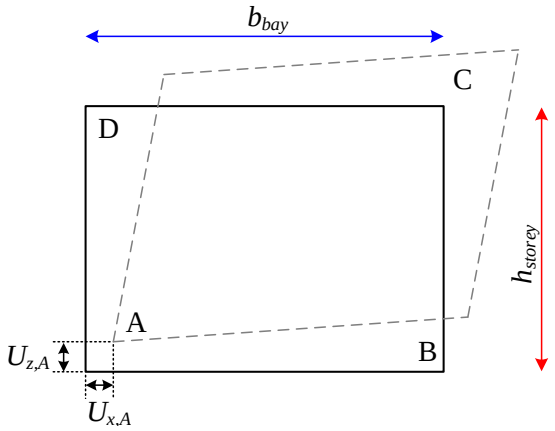


Fig. 2.12. Wall deformation by applying displacement at frame corners (after Elkayam and Klar (2019))

Then, the horizontal ε_{xx}, vertical ε_{zz}, and diagonal ε_{xz} strains can be evaluated using the derived displacement field:

$$\begin{aligned}
\varepsilon_{zz} &= \frac{\partial \delta_z}{\partial z} = \frac{\left(U_{z,D} - U_{z,A}\right)}{h_{storey}} + \left(U_{z,A} - U_{z,B} + U_{z,C} - U_{z,D}\right) \frac{x}{b_{bay} h_{storey}} \\
\varepsilon_{xx} &= \frac{\partial \delta_x}{\partial x} = \frac{\left(U_{x,B} - U_{x,A}\right)}{b_{bay}} + \left(U_{x,A} - U_{x,B} + U_{x,C} - U_{x,D}\right) \frac{z}{b_{bay} h_{storey}} \\
\varepsilon_{xz} = \frac{\partial \delta_x}{2\partial z} + \frac{\partial \delta_z}{2\partial x} &= \frac{\left(U_{z,B} - U_{z,A}\right)}{2b_{bay}} + \left(U_{z,A} - U_{z,B} + U_{z,C} - U_{z,D}\right) \frac{z}{2b_{bay} h_{storey}} \\
&+ \frac{\left(U_{x,D} - U_{x,A}\right)}{2h_{storey}} + \left(U_{x,A} - U_{x,B} + U_{x,C} - U_{x,D}\right) \frac{x}{2b_{bay} h_{storey}}
\end{aligned} \tag{2.20}$$

Finally, the maximum strain (principal strain) is given as:

$$\varepsilon_{max} = \frac{\varepsilon_{zz} + \varepsilon_{xx}}{2} + \sqrt{\frac{1}{4}\left(\varepsilon_{zz} - \varepsilon_{xx}\right)^2 + \varepsilon_{xz}^2} \tag{2.21}$$

On the other hand, for framed buildings with infill walls, to account for the beam/slab to column/wall connections, Boone (1996) suggested that the shear strain γ could be estimated directly from the maximum slope of the beam/slab with respect to the bay tilt w (Figure 2.11).

As illustrated in Figure 2.11, beams/slabs within the superstructure may undergo either a uniform shear strain (γ_1 in Figure 2.11(a)) or a varying profile of shear strain along the beam/slab with a maximum around the mid-point (γ_1 in Figure 2.11(b)). Furthermore, because of ground pressures, the beam/slab shear strains at the foundation level (γ_0) can differ from those within the superstructure (γ_1), as shown in Figure 2.11.

It is debatable which parameters should be adopted when assessing the effect of underground excavation on buildings. The following section will briefly describe several widely accepted damage criteria.

2.2.2 Evaluation of building damage

2.2.2.1 Empirical damage criteria

In order to assess the level of damage of a building, several authors (Skempton and MacDonald, 1956; Polshin and Tokar, 1957; Burland and Wroth, 1974) proposed threshold values of different building deformation parameters. In particular, Skempton and MacDonald (1956) adopted the angular distortion to classify the deformation degree of the buildings, the details of which are shown in Table 2.2. Based on a study on a total of 98 buildings, the authors indicated that the angular distortion needs to be lower than 1/300 to prevent cracking in walls and partitions. However, this value should be reduced to 1/1000 for particularly sensitive brick structures. Furthermore, structural damage of facades can occur if the angular distortion exceeds 1/150.

Table 2.2. Damage criterion based on angular distortion (Skempton and MacDonald, 1956)

Damage description	Limiting angular distortion (β)
Cracking in walls and partitions	1/300
Cracking of particularly sensitive brick structures	1/1000
Structural damage of facade	1/150

Alternatively, Polshin and Tokar (1957) linked the building damage criterion to deflection ratio DR. To describe the building deformation more accurately, building dimensions (e.g. the ratios of building length to height, L/H) and ground conditions (sand or soft clay) were taken into account, as shown in Table 2.3. It can be seen that the limiting deflection ratio is larger for

soft clay than sand. Furthermore, limiting DR should be larger for the buildings with higher ratios of length to height. In addition, the threshold of the ground slope for different structures was also considered. Polshin and Tokar (1957) suggested a maximum allowable slope value of 1/500 for steel and concrete frame infilled structures, whereas this value was increased to 1/200 for structures without infill walls. For masonry, the tensile strain should be considered (Polshin and Tokar, 1957). The author stated that a limiting tensile strain value of 0.05% may give rise to the onset of cracking of masonry. Nevertheless, these criteria only considered the effect of building self-weight, which may differ to the scenario in which the buildings are affected by underground excavation (Rankin, 1988) (the latter generally occurs in a short time).

Table 2.3. Damage criterion based on deflection ratio (Polshin and Tokar, 1957)

Building length to height	Ground conditions	Limiting deflection ratio
$L/H \leq 3$	sand	1/3300
$L/H \leq 3$	soft clay	1/2500
$L/H \geq 5$	sand	1/2000
$L/H \geq 5$	soft clay	1/1430

2.2.2.2 Limiting tensile strain method

Despite the empirical damage criteria mentioned above provide a useful framework to evaluate the degree of building damage, only the deformation caused by building self-weight was considered in these methods, as pointed by Burland and Wroth (1974) and Rankin (1988). Tunnelling induced ground movement can occur in a much shorter time. Therefore, these approaches are not sufficient to make a reliable prediction and assessment for the building damage due to underground excavations. Furthermore, structural details, which may affect the building response to tunnelling, also need to be considered in the risk assessment process. Following the work from Polshin and Tokar (1957), who suggested the use of tensile strains when considering the damage of building caused by ground movements, Burland and Wroth (1974) and Burland et al. (1977) assumed that the onset of visible cracking in buildings was associated with a limiting tensile strain. Boscardin and Cording (1989) extent the works of Burland and Wroth (1974) and Burland et al. (1977), and linked the critical tensile strain values to various serviceability/damage

limit states of buildings, as shown in Table 2.4, which was updated by Son and Cording (2005) with a slight increase for the thresholds of the limiting tensile strain in the category of 3 to 4, and 4 to 5.

Table 2.4. Critical tensile strain and categories of damage (Boscardin and Cording, 1989)

Category of damage	Level of damage	Limiting tensile strain (%)
0	Negligible	0-0.05
1	Very slight	0.05-0.075
2	Slight	0.075-0.15
3 to 4	Moderate to severe	0.15-0.3
4 to 5	Severe to very severe	>0.3

By simplifying the building as a simply supported beam with linear, elastic, and weightless properties, Burland et al. (1977) linked the maximum bending strain, $\varepsilon_{b,max}$, and diagonal strain, $\varepsilon_{d,max}$, to deflection ratio, DR, of the building, as shown in Figure 2.13. Using the Timoshenko beam theory (Timoshenko, 1957), the equations can be derived as:

$$DR = \left(\frac{L}{12t_{axis}} + \frac{3IE}{2tLHG}\right)\varepsilon_{b,max} \tag{2.22}$$

$$DR = \left(1 + \frac{HL^2G}{18IE}\right)\varepsilon_{d,max} \tag{2.23}$$

where E is Young's modulus, G is the shear modulus, I is the second moment of area of the equivalent beam and t_{axis} is the location of the neutral axis.

The determination of the location of the neutral axis is important. Burland and Wroth (1974) pointed out that the values of t_{axis} in sagging and hogging zones were different; for sagging deformation mode, $t_{axis} = H/2$, whereas for hogging zone, $t_{axis} = H$. Based on the results obtained from experiments of model brick walls and field observations, it was shown that cracks generated and propagated from the bottom toward the top of the wall in the hogging zone, resulting in the assumption of $t_{axis} = H$ (i.e. at the foundation level). On the other hand, cracks were not monitored in the building portion of the sagging zone due to the high restraining effect of the foundation to the building, and thus the neutral axis can be assumed to be in the centre of the building (i.e. $t_{axis} = H/2$). This assumption was further supported by Mair and Taylor

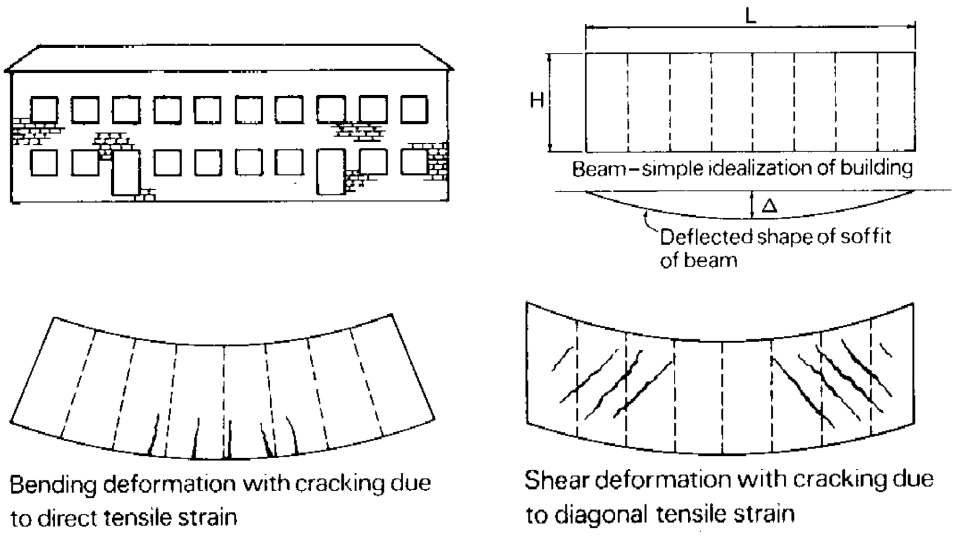


Fig. 2.13. Cracking of a simple beam in bending and in shear (after Burland et al. (1977))

(1997). Figure 2.13 also displayed two possible extreme modes of deformation, pure bending and shearing. Bending deformation with cracking is due to direct tensile strain, so that vertical cracks are generated. Shear deformation with cracking is caused by the diagonal tensile strain, thereby resulting in cracks in the diagonal direction.

The predominant deformation mode depends on the values of E/G and L/H of the building (Burland and Wroth, 1974; Burland et al., 1977). It is suggested that for a short building (small L/H value), diagonal tensile strain plays a more important role than bending strain, whereas bending deformation in a long building (large L/H value) dominates the overall behaviour (Burland and Wroth, 1974). On the other hand, the E/G value is generally assumed to be 2.6 (Poisson's ratio $\nu = 0.3$) (Burland and Wroth, 1974; Melis and Rodriguez Ortiz, 2001) for masonry structures, and 12.5 or even higher for buildings with large openings or framed structures (Burland and Wroth, 1974; Mair et al., 1996; Son and Cording, 2007; Cook, 1994).

Apart from the damage caused by settlement, some researchers (Boscardin and Cording, 1989; Mair et al., 1996; Geddes, 1991) also highlighted the importance of considering the horizontal building strains ε_h induced by the horizontal ground displacements. The horizontal strain of the building is given by $\varepsilon_h = \Delta L/L$, where ΔL is the change of the building length (Son and Cording, 2005). The superposition of bending ε_b and horizontal ε_h strains gives the total

bending strain ε_{bt} (Boscardin and Cording, 1989; Mair et al., 1996; Son and Cording, 2005):

$$\varepsilon_{bt} = \varepsilon_b + \varepsilon_h \tag{2.24}$$

To consider the case of diagonal tension ε_d with horizontal strain, based on the state of strain, the tension strain ε_θ, at any angle θ from the horizontal can be given as (Boscardin and Cording, 1989; Son and Cording, 2005):

$$\varepsilon_\theta = \varepsilon_h \cos^2\theta + 2\varepsilon_{d,max}\cos\theta \sin\theta \tag{2.25}$$

The maximum value of $\varepsilon_{\theta,max}$ (ε_{crit}), is given by (Boscardin and Cording, 1989; Son and Cording, 2005):

$$\begin{aligned}\varepsilon_{crit} = \varepsilon_{\theta,max} &= \varepsilon_h \cos^2\theta_{max} + 2\varepsilon_{d,max}\cos\theta_{max}\sin\theta_{max} \\ &= \varepsilon_h \cos^2\theta_{max} + \beta\cos\theta_{max}\sin\theta_{max}\end{aligned} \tag{2.26}$$

where θ is determined by $\tan(2\theta_{max}) = \beta/\varepsilon_h$ (Son and Cording, 2005). For instance, if $\theta_{max} = 0$, $\varepsilon_{crit} = \varepsilon_h$, so that vertical cracks form; in the scenario of $\theta_{max} = 45°$ (i.e. $\varepsilon_h = 0$), $\varepsilon_{crit} = \beta/2$, and thus cracks develop following 45° planes. As shown in Figure 2.14, Son and Cording (2005) updated the critical tensile strain values from Boscardin and Cording (1989) corresponding to various degrees of damage and compared a vast data set from field observations, physical model tests and numerical studies.

Alternatively, the maximum tensile strain ε_{dt} (total tensile strain due to diagonal and horizontal distortion) can be assessed using Mohr's circle of strain:

$$\varepsilon_{dt} = \frac{\varepsilon_h(1-\nu)}{2} + \sqrt{\frac{1}{4}\varepsilon_h^2(1+\nu)^2 + \varepsilon_d^2} \tag{2.27}$$

Equation 2.27 can be written as different forms depending on stress conditions; for example, $\varepsilon_{dt} = \frac{\varepsilon_h}{2} + \sqrt{\frac{1}{4}\varepsilon_h^2 + \varepsilon_d^2}$ for plane strain conditions, whereas $\varepsilon_{dt} = 0.35\varepsilon_h + \sqrt{(0.65\varepsilon_h)^2 + \varepsilon_d^2}$ for plane stress conditions by assuming the Poisson's ratio $\nu = 0.3$ (Mair et al., 1996). The max-

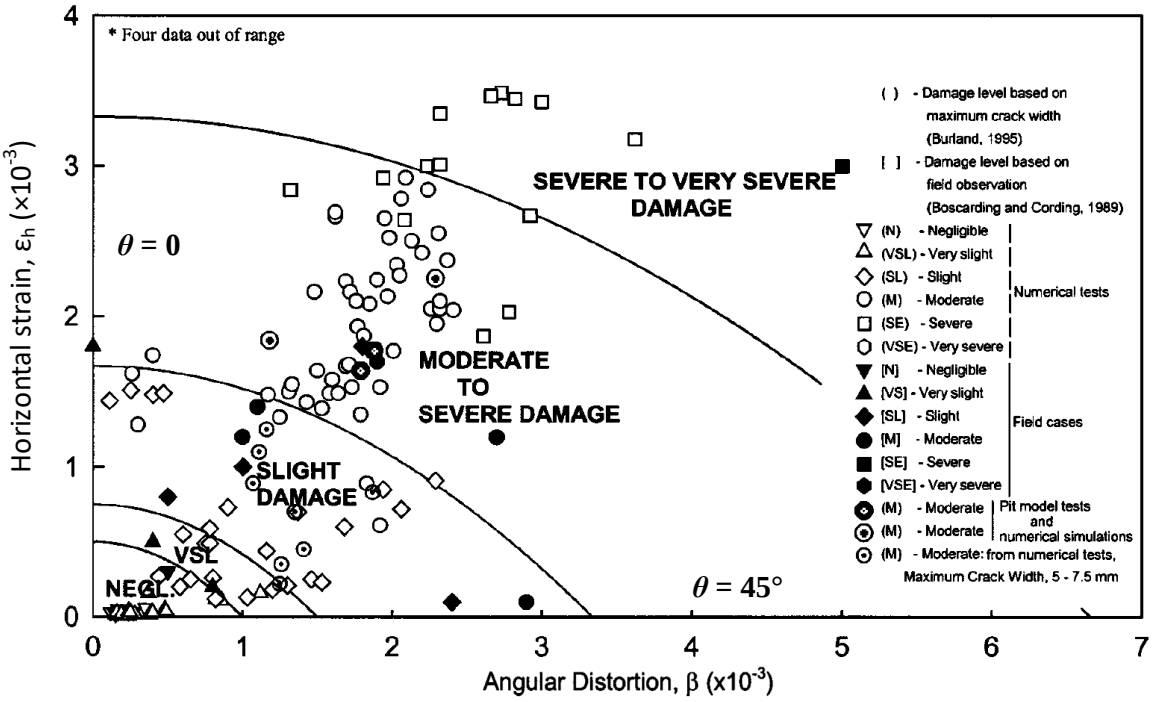


Fig. 2.14. Damage levels of buildings from field observations, physical and numerical model tests (after Son and Cording (2005))

imum tensile strain in a given portion of the building, ε_{max}, is the greater value between the total bending strain ε_{bt} and the total angular/shear strain ε_{dt} (or $\varepsilon_{\theta,max}$ (Equation 2.26) from Boscardin and Cording (1989) and Son and Cording (2005)).

Recently, Franza et al. (2020a) and Ritter et al. (2020) proposed the direct strain-based approach to infer the deformation parameters (average curvature, horizontal and shear strain) of the bay from displacements of its four corner points. The method is based on the works of Cook (1994) (for the calculation of curvature $\chi = \frac{w_2}{2} - \frac{w_1}{2}$) and Son and Cording (2005) (shear strain $\gamma = \beta = S - w$ if shear deformation is dominant, see Equations 2.17 and 2.18). This approach could overcome some limitations relating to the use of Equations 2.22 and 2.23 (where only foundation displacements are measured).

Finally, the approaches for estimating average bay (Son and Cording, 2005; Cook, 1994) and local panel (Boone, 1996; Elkayam and Klar, 2019) shear deformations are also comparable in terms of tensile strain ε_{max} and, thus, categories of damage in Table 2.4. For the considered framed buildings on raft foundations, the high axial stiffness of horizontal elements (slabs)

results in $\varepsilon_h \approx 0$. Consequently, Equation 2.27 simplifies to $\varepsilon_{max} = \varepsilon_d = \gamma/2$ (same as the extreme case in Equation 2.26), which can be computed using (i) β from Son and Cording (2005), considering that $\beta \approx \gamma$, (ii) γ from Cook (1994) and Elkayam and Klar (2019), or (iii) γ_0 or γ_1 from Boone (1996).

2.2.2.3 Staged risk assessment for buildings

Following the concept of Rankin (1988), a three-stage building risk assessment was proposed by Mair et al. (1996), as shown in Figure 2.15. Three steps are described as follows.

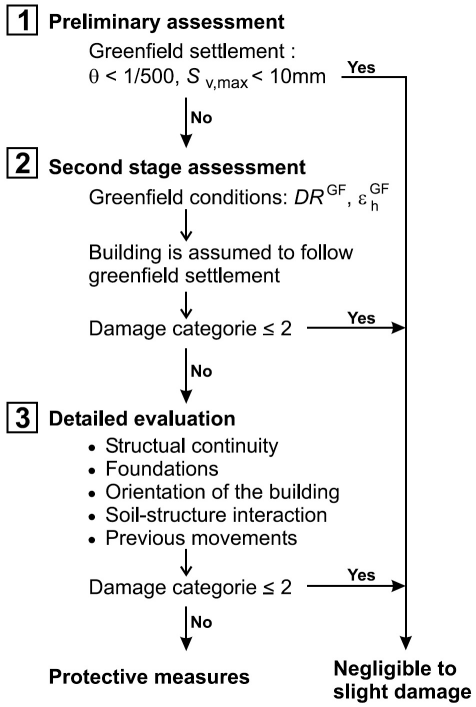


Fig. 2.15. Damage assessment framework according to Mair et al. (1996) after (Franzius, 2003)

Stage one: In this preliminary assessment, the Gaussian assumption is adopted to predict the greenfield settlement profile and the deformation of the building is assessed based on two thresholds: maximum rotation (1/500) and settlement (10 mm). Buildings suffering larger deformation than these thresholds are considered to be at risk and thus will be evaluated in the next stage. It should be noted that tunnel-soil-structure interaction is not considered in this step of the assessment procedure. Therefore, this step is usually conservative.

Stage two: For buildings that are assessed as at risk in the first stage, the tensile strains induced within the buildings are calculated using Equations 2.25 and 2.27 by imposing the greenfield ground settlement predicted by the Gaussian curve on the fully flexible, elastic beam structure. Subsequently, the damage assessment is performed based on the calculated maximum tensile strain ε_{max} and the corresponding damage category can be obtained from Table 2.4. However, given the fact that the structure is assumed to conform to the greenfield displacement (in reality, the structure stiffness and self-weight can reduce the induced building deformation), this stage is also relatively conservative (Mair et al., 1996).

Stage three: In this stage, the effect of tunnel construction method and soil-structure interaction (presented in Section 2.2.3) are considered in the damage assessment for the buildings that are classified in category 3 (moderate) or higher of expected damage. The three-dimensional aspects of the tunnel and the building are also fully considered. Since the soil-structure interaction is considered in this stage, this evaluation generally leads to damage categories below those in the second stage assessment.

2.2.3 Soil-structure interaction

The assessment of the tunnelling effects on buildings and nearby structures is becoming increasingly important. To achieve a better prediction of building damage caused by tunnel construction, it is important to consider the role of tunnel-soil-structure interaction in the risk assessment.

2.2.3.1 Modification factor approach and relative stiffness

Potts and Addenbrooke (1997) carried out a parametric study to investigate the influence of an existing structure on the ground movement due to tunnel construction. In their study, the building modification factor approach was proposed to link the maximum building deflection ratio and horizontal strains caused by tunnelling to the greenfield displacements and strains, as shown in Figure 2.16. For deflection ratios, the modification factors are defined separately for hogging ($M^{DR,hog}$) and sagging ($M^{DR,sag}$) regions (defined by the greenfield settlement trough profile), expressed as (Potts and Addenbrooke, 1997):

$$M^{DR,sag} = \frac{DR_{sag,bldg}}{DR_{sag,gf}} \qquad M^{DR,hog} = \frac{DR_{hog,bldg}}{DR_{hog,gf}} \tag{2.28}$$

where $DR_{sag,bldg}$ and $DR_{hog,bldg}$ are building deflection ratios in sagging and hogging zones, respectively; and $DR_{sag,gf}$ and $DR_{hog,gf}$ are the deflection ratios of the greenfield settlement trough in sagging and hogging zones, as shown in Figure 2.16.

For horizontal strains, the modification factors of maximum tensile/compressive horizontal strains, $M^{\varepsilon h,t}$ and $M^{\varepsilon h,c}$ are defined by (Potts and Addenbrooke, 1997):

$$M^{\varepsilon h,t} = \frac{\varepsilon_{h,t,bldg}}{\varepsilon_{h,t,gf}} \qquad M^{\varepsilon h,c} = \frac{\varepsilon_{h,c,bldg}}{\varepsilon_{h,c,gf}} \tag{2.29}$$

where $\varepsilon_{h,t,bldg}$ and $\varepsilon_{h,c,bldg}$ are the maximum building tensile and compressive strains, respectively; $\varepsilon_{h,t,gf}$ and $\varepsilon_{h,c,gf}$ are, respectively, the maximum greenfield tensile and compressive strains.

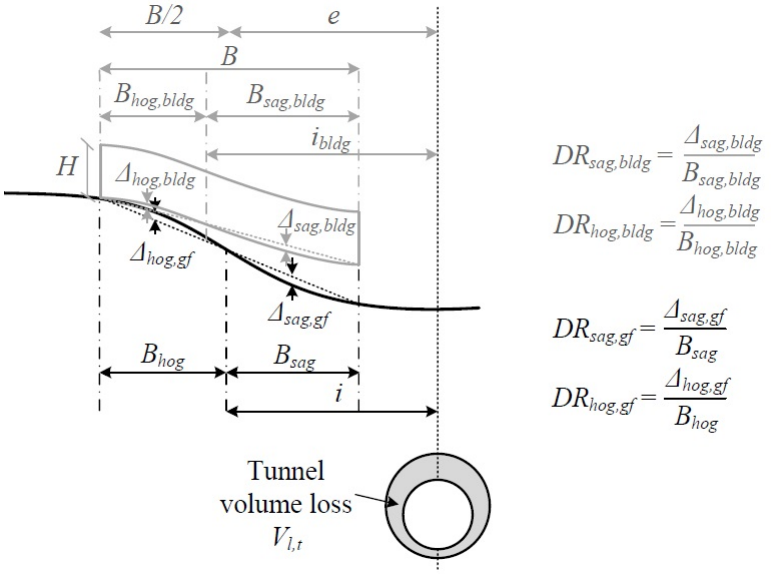


Fig. 2.16. Definition of parameters in modification factor approach (after Franza (2016))

Potts and Addenbrooke (1997) suggested that the building deflection ratio due to ground movement depends on the relative soil-building bending stiffness, ρ^*, whereas the horizontal tensile or compressive strains are mainly dependent on the relative soil-building axial stiffness, α^*. Their definitions can be expressed as:

$$\rho^* = \frac{EI}{E_s(B/2)^4} \qquad \alpha^* = \frac{EA}{E_s(B/2)} \tag{2.30}$$

where E, A, I are the Young's modulus, area of cross section and second moment of area of the building, respectively, and E_s is the representative soil stiffness. Potts and Addenbrooke (1997) also suggested the soil stiffness can be represented by the secant stiffness at 0.01% axial strain of the soil in the triaxial test for a soil sample at a depth of $z_t/2$, where z_t is tunnel axis depth.

Moving from Potts and Addenbrooke (1997), Franzius (2003); Franzius et al. (2004) also carried out parametric studies to expand the existing works by considering more variables including building weight, transverse width B, tunnel cover depth and the effect of longitudinal settlement due to tunnel excavation. It should be noted that for plane strain condition, α^* is dimensionless while ρ^* has a dimension of m^{-1}. Therefore, Franzius et al. (2006) modified Equation 2.30 to a dimensionless form considering the three dimensional condition, given as:

$$\rho^*_{mod} = \frac{EI}{E_s z_t B^2 L} \qquad \alpha^*_{mod} = \frac{EA}{E_s B L} \tag{2.31}$$

where L is the length of the building along the longitudinal direction of the tunnel.

Based on the relative stiffness and modification factor approaches, a design curve approach was proposed by Potts and Addenbrooke (1997). Considering building deformation modes (sagging or hogging for deflection ratio DR, and tension or compression for horizontal strains ε_h) and building eccentricity e/B, where e is the horizontal distance between tunnel centreline and the centre of the building, Franzius et al. (2006) suggested design curves to estimate the building deformation by accounting for the soil-structure interaction, as shown in Figure 2.17. With these design curves, the building deformation (deflection ratios or horizontal strains) can be estimated using Equations 2.28 and 2.29 once the relative stiffness is determined.

Recently, by summarising the findings from centrifuge tests (Farrell, 2010), field monitoring (Goh and Mair, 2011) and numerical analysis (Potts and Addenbrooke, 1997; Franzius et al., 2006), a new form of relative bending stiffness equation was proposed by Farrell (2010); Goh and Mair (2011) to reduce the scatter of the previous equations:

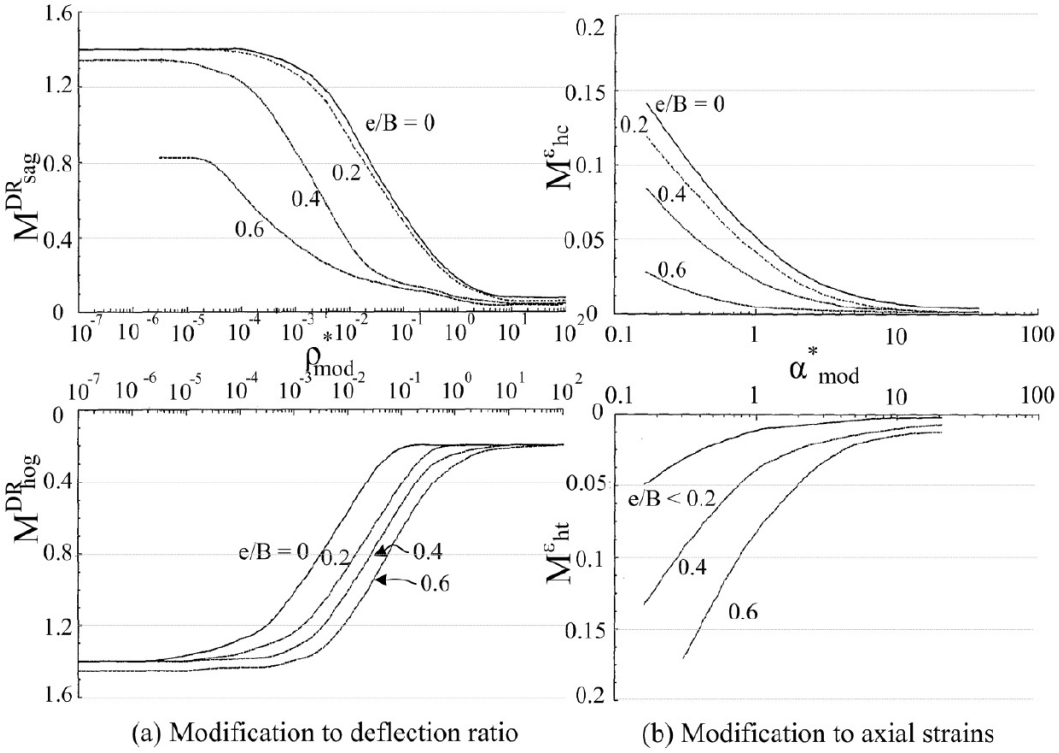


Fig. 2.17. Modified design curves proposed by Franzius et al. (2006) (after Farrell (2010))

$$\rho_{sag} = \frac{EI}{E_s B_{sag}^3 L} = \frac{EI^*}{E_s B_{sag}^3} \qquad \rho_{hog} = \frac{EI}{E_s B_{hog}^3 L} = \frac{EI^*}{E_s B_{hog}^3} \tag{2.32}$$

where EI^* is the bending stiffness of the building per metre (along tunnel axis direction), and B_{sag}, B_{hog} are the lengths of the building in sagging and hogging zones. It is found that tunnel z_t is not accounted for in Equation 2.32, as z_t is indirectly considered in the estimation of $B_{sag/hog}$ and E_s (Farrell, 2010).

New design envelopes of DR were proposed by Mair (2013), as illustrated in Figure 2.18. When plotting the data collected from centrifuge tests, numerical analysis, and case studies, against the relative soil-structure bending stiffness (computed by Equation 2.32), it was found that most of the data points fell into the proposed narrow envelopes, demonstrating the reliability of the framework (see Figure 2.18).

To better represent the stiffness effects, Pickhaver et al. (2010) and Finno et al. (2005) suggested that buildings could be modelled with equivalent Timoshenko and laminated beams

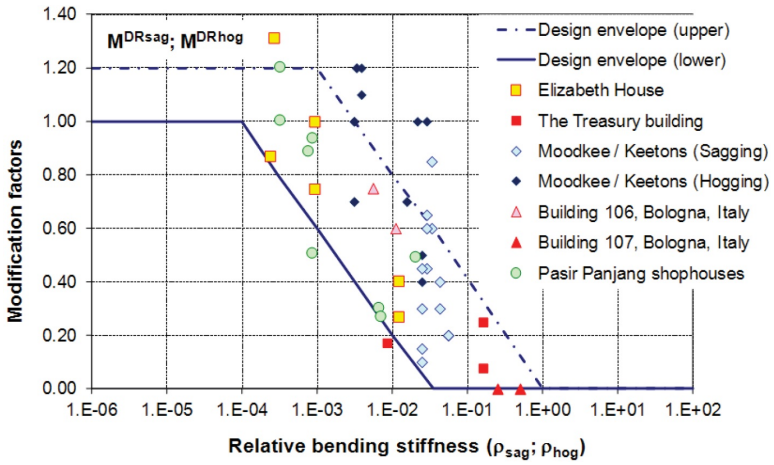


Fig. 2.18. Modification factors of DRs of the buildings in the field monitoring (Mair, 2013)

with both cross-sectional bending stiffness EI and shear stiffness GA_s, whereas Losacco et al. (2016) used anisotropic equivalent solids. To isolate the contributions of shear and bending stiffness, Franza et al. (2020a) modified the relative stiffness parameter η from Timoshenko beam theory as:

$$\eta_{sag/hog} = \frac{\rho_{sag/hog}}{1 + aF_{sag/hog}} = \frac{EI^*}{E_s B^3_{sag/hog,gf}(1 + aF_{sag/hog})} \qquad F_{sag/hog} = \frac{EI}{B^2_{sag/hog,gf} GA_s} \tag{2.33}$$

where $aF_{sag/hog} = \delta_{shear}/\delta_{bending}$ is the ratio between shear (δ_{shear}) and bending ($\delta_{bending}$) deflections, $F_{sag/hog}$ is a dimensionless factor, and $a = 12$ was estimated from a simply supported beam condition. In general, $F_{sag/hog} < 1/25$ results in bending-dominated behaviour, whereas $F_{sag/hog} > 1$ indicates shear-dominated behaviour.

For framed structures, Goh and Mair (2014) considered the maximum tensile ($\varepsilon_{h,t,bldg}$) and compressive ($\varepsilon_{h,c,bldg}$) horizontal strains among all bays at the foundation level, differing from the average horizontal strains within the sagging/hogging zones (Mair et al., 1996). Once the maximum strain is defined, the modification factors for the maximum horizontal strains ($M^{\varepsilon h}$) are defined as follows:

$$M^{\varepsilon h,t/c} = \frac{\varepsilon_{h,t/c,bldg}}{\varepsilon_{h,t/c,GF}} \tag{2.34}$$

where $\varepsilon_{h,t/c,GF}$ is the maximum average compressive or tensile horizontal strains in the portion of the greenfield settlement trough corresponding to the bay width b_{bay}.

Son and Cording (2005) suggested the use of the normalised angular distortion, which is defined by the ratio of angular distortion β of a building to the change in greenfield ground slope ΔGS, and linked $\beta/\Delta GS$ to the newly proposed relative soil-structure shear stiffness ρ_s, given as:

$$\rho_s = \frac{E_s B}{G_{build} H b} \tag{2.35}$$

where G_{build} is the elastic shear modulus of a building; H is the height of a building; and b is the building wall thickness. The increase of the relative soil-structure stiffness (building stiffness decreased) results in a greater building angular distortion, i.e. building distortion would conform more closely to the ground movement.

Son and Cording (2005) summarised the results obtained from a series of field site observations, physical model studies and numerical model tests, and plotted the normalised angular distortion $\beta/\Delta GS$ against the relative soil-structure shear stiffness $E_s B/G_{build} H b$, as shown in Figure 2.19. In general, the value of normalised angular distortion increases with the increase of the relative soil-structure shear stiffness. If no cracks or minor cracks generate, the slope of $\beta/\Delta GS$ - $E_s B/G_{build} H b$ curve is small. However, if extensive cracks occur, building shear stiffness G_{build} significantly decreases, resulting in a greater normalised angular distortion.

2.2.3.2 Estimation of building stiffness

As mentioned in Section 2.2.3, the relative soil-structure stiffness determines the distortion of the building caused by tunnelling. Therefore, a reliable prediction of the building stiffness is vital when using the modification factor approach to estimate the resulting building deformation. Potts and Addenbrooke (1997) adopted the parallel axis theory (Equation 2.36) to calculate the overall bending stiffness of the structure, whereas Lambe (1973) suggested using the algebraic

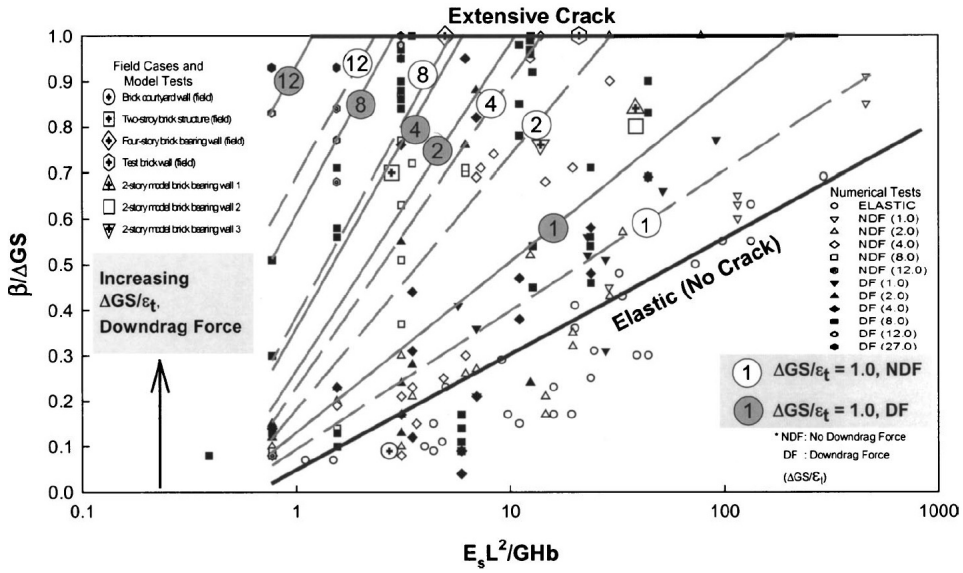


Fig. 2.19. Relationship between normalised angular distortion and relative soil-structure shear stiffness (Son and Cording, 2005)

sum of the independent EI values (Equation 2.37) for each storey:

$$EI = E \sum_{i=1}^{n+1} \left(I_{slab,i} + A_{slab,i} d_i^2 \right) \tag{2.36}$$

$$EI = E \sum_{i=1}^{n+1} \left(I_{slab,i} \right) \tag{2.37}$$

where i is the number of floor slabs, $I_{slab,i}$ is the second moment of area of each slab, $A_{slab,i}$ is the cross-sectional area of each slab, n is the number of storeys, d_i is the vertical distance between the structure's neutral axis and the slab's neutral axis.

However, it is noted that the use of the parallel axis theory and the algebraic sum methods provide, respectively, an overestimation and underestimation of the stiffness of a real building. For framed structures, Meyerhof (1953) and Goh and Mair (2014) assessed the stiffening contribution of the columns on the overall bending stiffness of a framed building, and proposed a factor C to define this effect:

$$C = \left[1 + \left(\frac{B_{sag/hog}}{b_{bay}} \right)^2 \left(\frac{K_{LC} + K_{UC}}{K_{LC} + K_{UC} + K_b} \right) \right] \tag{2.38}$$

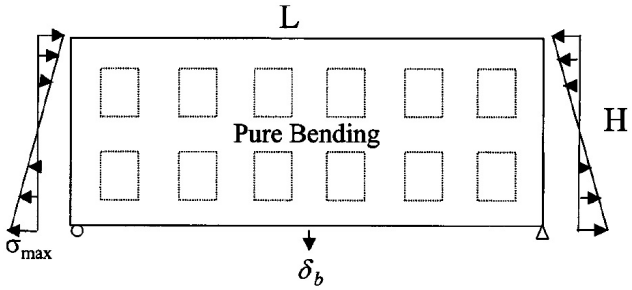
where $K_{LC} = (EI/h_{storey})_{LC}$ is the average stiffness of the lower column, $K_{UC} = (EI/h_{storey})_{UC}$

is the average stiffness of the upper column, and $K_b = (EI/b_{bay})_b$ is the average stiffness of the beam line.

Therefore, the total bending stiffness of the framed building can be expressed as (Goh and Mair, 2014):

$$EI_{frame} = \sum (EI * C)_{ithfloor} \tag{2.39}$$

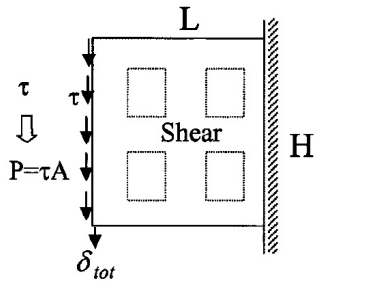
It is suggested that the column stiffening factor provides a better estimation of the building stiffness than the parallel axis theory and the algebraic sum methods (Goh and Mair, 2014). A similar approach was also proposed by Haji et al. (2018), in which the total stiffness of a structure is assessed. However, Franza and Dejong (2018) pointed out that in these methods the shear and bending stiffness are not distinguished, despite that several studies have highlighted the role of shear flexibility in the soil-structure interaction (Son and Cording, 2005; Finno et al., 2005; Franza et al., 2020a). Consequently, Son and Cording (2005) suggested performing pure bending and shear tests to obtain the resulting deflection of the structure when subjected to known bending moment M or shear force τA from numerical tests (see the equations for calculating the bending and shear stiffness for no window openings in Figure 2.20).



Bending for no window openings

	Theory	Numerical
δ_b	0.6858 mm	0.6959 mm
E	13.8 GPa	13.6 GPa

L = 18300 mm, H = 6172 mm, and σ_{max} = 689kPa



Shear for no window openings

	Theory	Numerical
δ_{tot}	2.0980 mm	2.0904 mm
G	5.74 GPa	5.78GPa

L = 18300 mm, H = 6172 mm, and τ = 689 kPa

Fig. 2.20. Estimation of bending and shear stiffness (Son and Cording, 2005)

For framed buildings with infill shear walls, Finno et al. (2005) used a laminate beam to represent a multi-storey building and estimated building shear stiffness by assuming that the load-bearing or infill walls offer shear resistance (the floors provide resistance to bending distortion). The laminate beam model is illustrated in Figure 2.21, comprising layers of plates (modelling the building floors) separated by layers of core material (representing the load-bearing or shear walls).

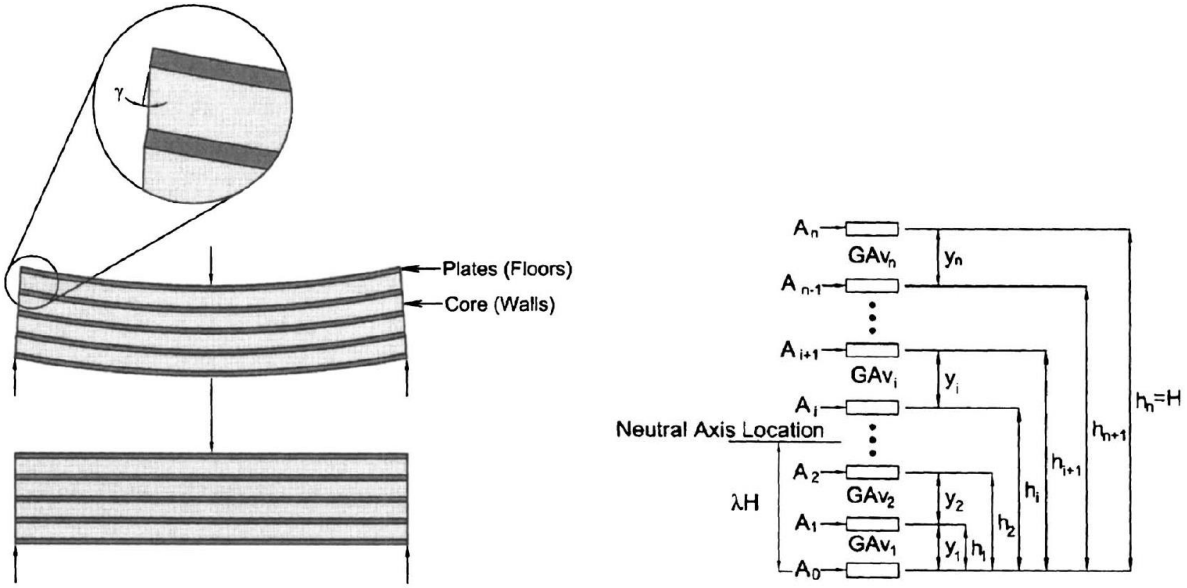


Fig. 2.21. Laminate beam model for the representation of a building (Finno et al., 2005)

According to Finno et al. (2005), the total shear stiffness of each floor $GA_{v,i}$ is given by the sum of the column ($GA_{v,column}$) and wall ($GA_{v,wall}$) stiffness:

$$GA_{v,i} = \sum \left(GA_{v,column} + GA_{v,wall} \left(1 - a_{ratio}\right) \right) \tag{2.40}$$

where a_{ratio} is the percentage opening in a wall.

To determine the column stiffness $GA_{v,column}$, a set of equations was derived (Finno et al., 2005):

$$I = \sum_{i=0}^{n} A_i \left(h_i - \lambda H\right) \qquad \lambda H = \frac{\sum_{i=0}^{n} A_i h_i}{\sum_{i=0}^{n} A_i}$$
$$GA_{v,column} = \frac{12 E_c I_c}{y_i^2} \qquad \frac{V_i}{V} = \frac{y_i}{I} \sum_{j=i}^{n} A_j \left(\lambda H - h_j\right) \tag{2.41}$$

where H is the storey height; λH is the distance between the neutral axis location and the bottom of the beam; A_i is the area of the floor slab cross-section; h_i is the distance from the floor to the bottom of the laminate beam; I is the moment of inertia of the beam; V_i and V are, respectively, the shear force in a storey and the total shear in the beam; $E_c I_c$ is the bending stiffness of the column; and y_i is the storey height.

Finally, the equivalent shear stiffness GA_v of the laminate beam is given by (Finno et al., 2005):

$$GA_v = \frac{1}{\sum_{i=1}^{n} \frac{y_i}{H} \frac{V_i}{V} \frac{1}{GA_{v,i}}} \tag{2.42}$$

As noted by Finno et al. (2005), Equation 2.42 may overestimate the real shear stiffness of the building because the rotation of the ends of the columns was neglected. Therefore, the approach proposed by Finno et al. (2005) is more appropriate for the estimation of the stiffness of a building with stiff floors (no rotation occurs at the end of the columns).

To evaluate the frame footing stiffness against horizontal differential displacements between footings, Goh and Mair (2014) considered a simple pin-supported portal frame with a single bay (Figure 2.22), and determined the reaction force F to a unit differential footing displacement Δ_h. The frame footing stiffness factor is approximated as:

$$\alpha_f = \frac{F}{\Delta_h} = \frac{3 K_b K_c}{h_{storey}^2 \left(2K_b + 3K_c\right)} \tag{2.43}$$

where $K_b = \left(EI/b_{bay}\right)_b$ and $K_c = \left(EI/h_{storey}\right)_c$ are the average stiffness (per metre run) of the beam and footing column, respectively. Note that the frame stiffness factor has dimensions of N/m per metre run.

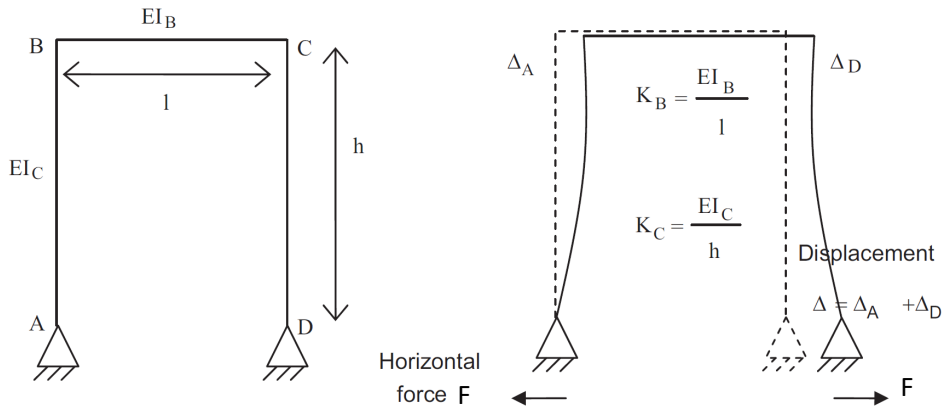


Fig. 2.22. Schematic of the simple portal frame (Goh and Mair, 2014)

2.2.3.3 Tunnel-building interaction: centrifuge modelling

Farrell (2010) carried out a series of centrifuge tests on the 8 m diameter beam centrifuge at the University of Cambridge. In his study, the buildings were modelled as aluminium, masonry and micro concrete plates subjected to ground movements due to tunnelling in fine dry silica sand (known as Leighton Buzzard Fraction E). Farrell (2010) considered four aluminium models (1.6 mm, 5 mm, 10 mm and 20 mm, labelled as STR-1, STR-2, STR-3 and STR-4 respectively), one micro-concrete model and three masonry models in the tests. An example of the aluminium plate building model (STR-2) is shown in Figure 2.23.

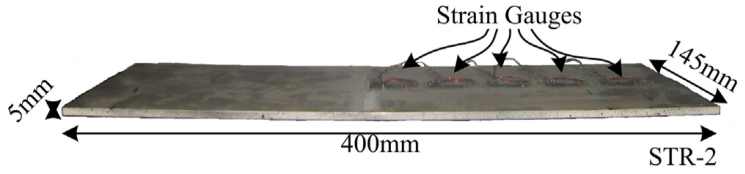


Fig. 2.23. Model aluminium beam building (STR-2) (Farrell, 2010)

The centrifuge testing results demonstrated that, compared with the greenfield scenario, buildings can significantly alter the greenfield ground deformation, in both vertical and horizontal directions. Figure 2.24 shows the results of the settlement profiles for structures STR-1 to STR-4 at a tunnel volume loss of 2%, along with the greenfield settlement trough for reference. It is shown that the response of the building highly depends on its stiffness; the stiffer the structure, the more rigid the response to tunnelling. STR-1 had the most flexible response to

tunnelling (largest deflection ratio), whereas structure STR-4 exhibited the most rigid response, with its edges settling more than the greenfield trough.

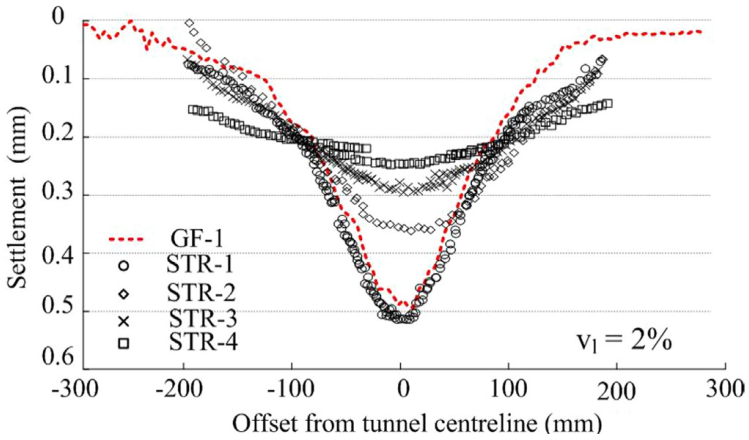


Fig. 2.24. Settlement profile for structures STR-1 to STR-4 (Farrell et al., 2014)

The result obtained from the centrifuge test of masonry models also suggested the importance of considering the non-linear behaviour of building material. It was shown that cracks can be seen to pass straight through both the mortar and the bricks of the structure at high volume loss, and cracks were observed in both hogging and sagging zones, as shown in Figure 2.25. It is generally believed that building damage in the hogging deformation mode of deformation is the primary concern for engineers when doing the risk assessment for an urban tunnelling project. The centrifuge testing result of Farrell et al. (2014), however, indicates that tunnelling induced building damage in the sagging region should also be of concern.

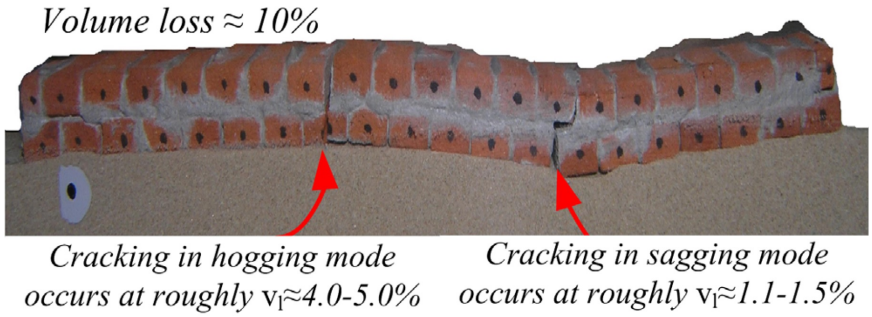


Fig. 2.25. Observed cracking of building (Farrell et al., 2014)

Moving from the equivalent plate approach (Farrell, 2010; Farrell et al., 2014), Ritter (2018); Ritter et al. (2020) presented the results of a series of centrifuge tests in which surface structures

with layouts and facade opening were subjected to tunnel construction in sand. The author adopted the powder-based 3D printing technology to manufacture the building models founded on strip footings, as shown in Figure 2.26. The authors stated that this 3D printing material had Young's modulus and a brittle response similar to historic masonry.

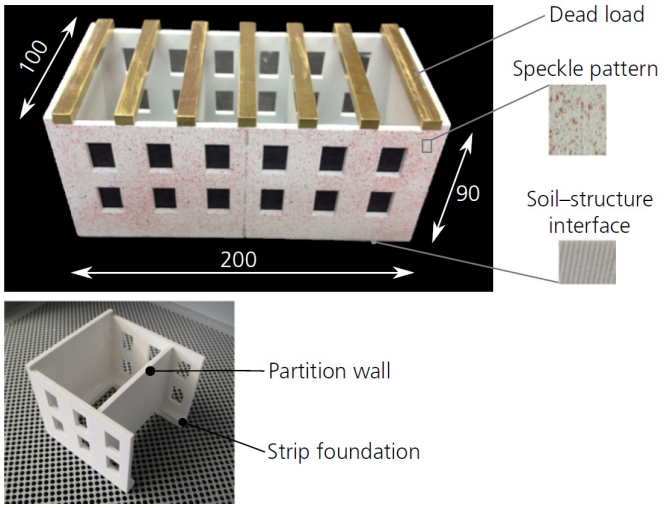


Fig. 2.26. Three-dimensional printed building model (Ritter, 2018)

For the effect of the presence of a surface building on tunnelling induced ground deformation, Ritter et al. (2018) obtained similar results as those from Farrell et al. (2014); for instance, the buildings could widen the vertical soil settlement trough compared with the greenfield case, and the horizontal ground displacement beneath the surface buildings was restrained by the roughness and pressure from the foundation. These results are also similar to those obtained from numerical analyses (Franzius et al., 2004, 2006).

Importantly, to distinguish between shear and bending distortion from the total deformation of the building, Ritter et al. (2020) adopted the framework proposed by Cook (1994), and examined the influences of building transverse width B and facade opening. Results of the building bending and shear displacements in a bay of the same position (see Figure 2.27(a)-(b)) are presented in Figure 2.27(c).

Figure 2.27(c) shows that the increase of building transverse width increased the bending deformation, but affected marginally the shear distortion. For the long building, the increase of the facade opening area tended to increase building distortion. The authors also concluded that

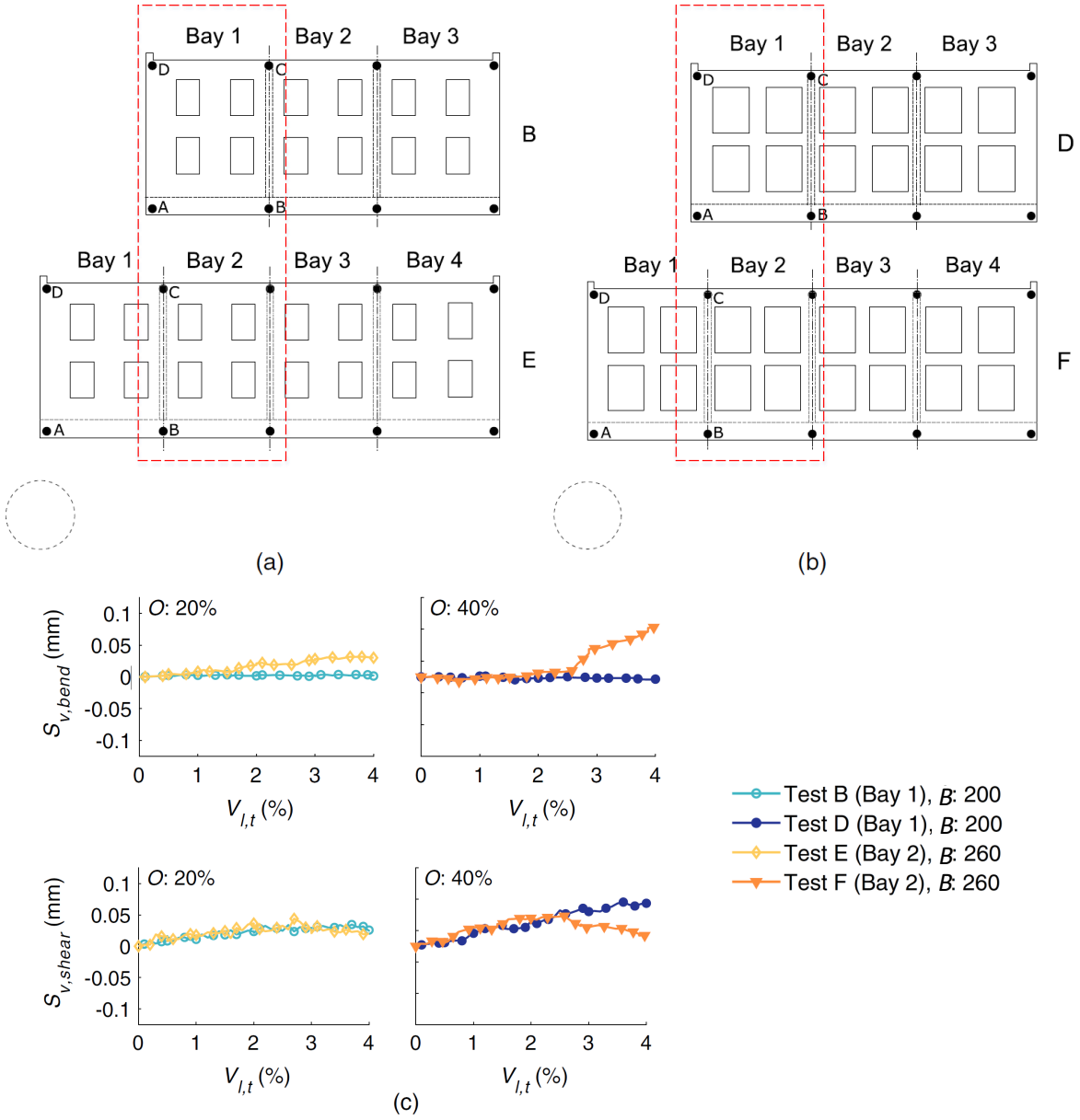


Fig. 2.27. Centrifuge results: the effects of building width and opening ((a) 20% opening; (b) 40% opening; and (c) centrifuge results) (Ritter et al., 2020)

structures located in both hogging and sagging regions of the tunnelling-induced settlement trough were more vulnerable than those of identical length that spanned entirely within the sagging or hogging zone (Ritter et al., 2020), indicating that the increase of building width increases the potential of damage.

A recent centrifuge study (Franza and Marshall, 2018) also adopted the equivalent beam

approach when considering the global tunnel-pile-building interaction problem. In their experiments, the stiffness and weight effects of piled structures were assessed independently using aluminium plates with varying stiffness (Figure 2.28(a)) and weight (Figure 2.28(b)).

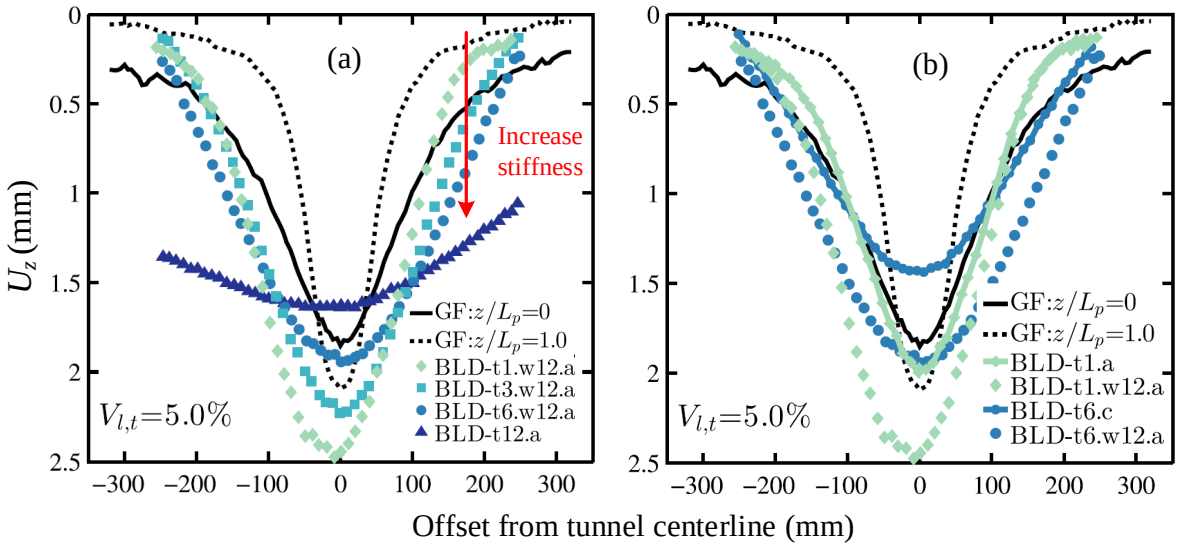


Fig. 2.28. Experimental results of piled structures (after Franza and Marshall (2018))

Based on collected data, the authors stated that the piled foundation causes a greater potential for damage of flexible structures with respect to shallow foundations (Farrell et al., 2014). As shown in Figure 2.28(a), the flexible structures displayed larger deflection ratios than the greenfield value. In general, Figure 2.28(a) shows that the increase of building stiffness decreases the structure deformation, whereas Figure 2.28(b) illustrates that the heavier the structure, the larger the deflection ratio (consistent with Franzius et al. (2004); Farrell et al. (2014)). Finally, these results also suggested that only assuming the tunnel-pile interaction (i.e., only consider the structure weight and neglect its stiffness and load redistribution) in preliminary risk assessment procedures for piled buildings can lead to an overestimation of the structural distortion (Franza and Marshall, 2018). Franza and Marshall (2019a) further explored the global tunnel-pile-building interaction using a real-time hybrid testing technique, in which foundation-superstructure interaction was modelled numerically, whereas the centrifuge model was adopted to reproduce the tunnel-foundation interaction. The results highlight that pile settlements and failure mechanisms highly depend on the structural load distribution (related to weight and stiffness) that occurs between piles.

2.2.3.4 Tunnelling effects on framed structures

Moving from the equivalent plate/solid approach, recent numerical studies (Goh and Mair, 2014; Fu et al., 2018; Boldini et al., 2018) have also realised the importance of considering the realistic framed structure characteristics in tunnel-building interaction problems. In particular, Goh and Mair (2014) quantified the influence of the frame action on the overall bending stiffness through a frame column stiffening factor C (Meyerhof, 1953), which is given by Equation 2.38.

Goh and Mair (2014) examined the effectiveness of the proposed column stiffening factor through a series of finite element model tests. The authors investigated the response of the framed structures resting on either continuous or individual footings with varying configuration (therefore different stiffness) to the braced excavation in soft clay. Results of the deflection ratio modification factors M^{DR} in sagging or hogging zones were plotted against the building stiffness estimated using either the parallel axis theory (Equation 2.36) or the algebraic sum of the floor stiffness (Equation 2.37), and were contrasted against the data obtained from the simple beam models (deformed purely in bending), as shown in Figure 2.29. It is shown that the algebraic sum approach underestimated the frame bending stiffness (for the same M^{DR} values, lower stiffness was obtained), whereas the parallel axis theory highly overestimated the bending stiffness (much greater stiffness for the identical M^{DR}) of the framed structures. Interestingly, when plotting deflection ratio modification factors M^{DR} against the bending stiffness assessed by the column stiffening factor approach, the data points agreed well with the equivalent beam model data.

For the horizontal displacements of the individual footings, Goh and Mair (2014) derived Equation 2.43 to assess the frame stiffness against horizontal differential displacements between footings. The authors computed the horizontal strain modification factors (Equation 2.34) from the frames with individual footings and linked these results against the proposed frame stiffness factor, as shown in Figure 2.30. Based on the results, Goh and Mair (2014) suggested an upper envelope, from which the maximum horizontal strains of the frames with individual footings can be reasonably estimated. However, as noted by the authors (Goh and Mair, 2014), the horizontal strain modification factors are rather scattered for an identical frame, indicating that

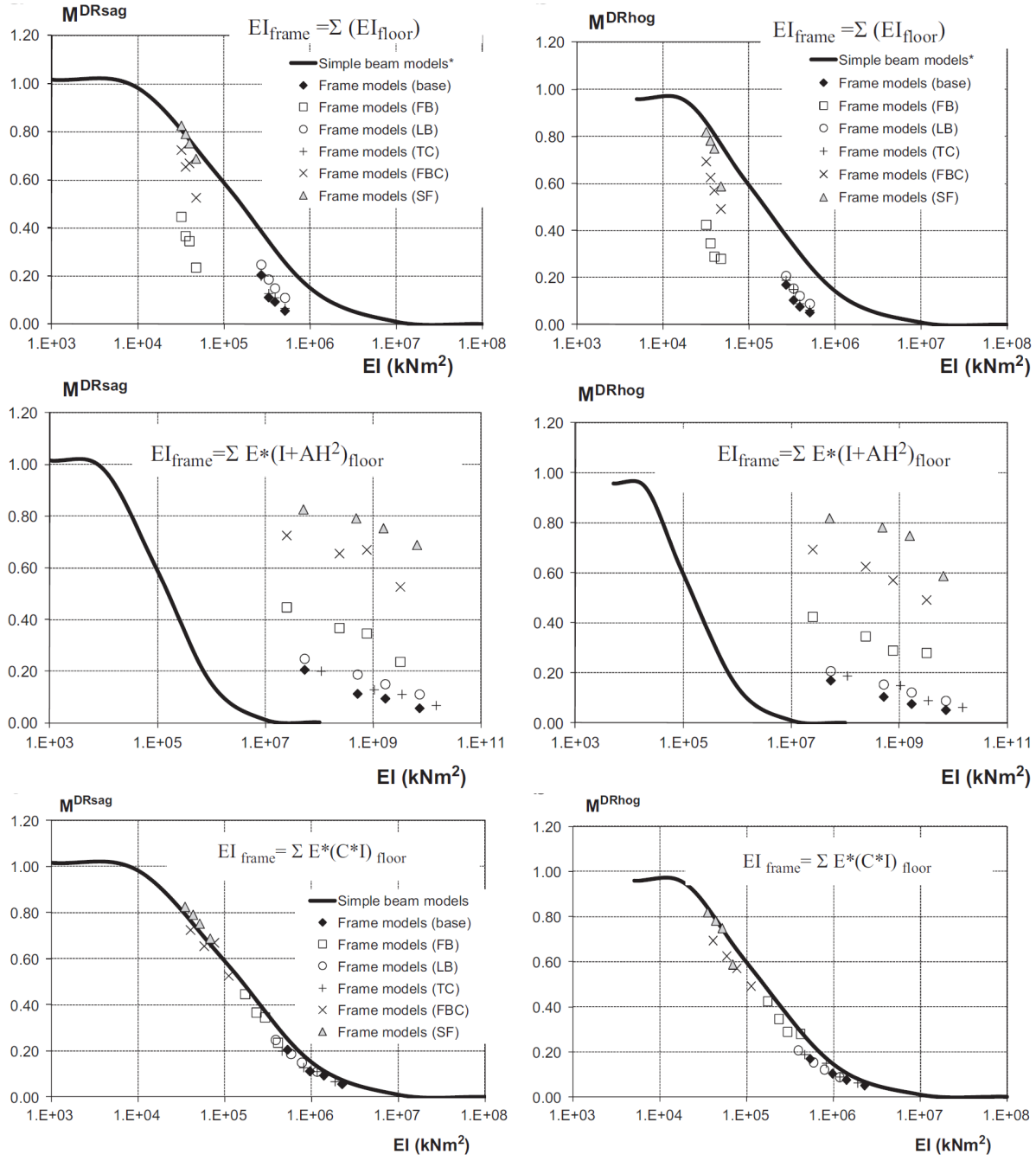


Fig. 2.29. Deflection ratio modification factors against bending stiffness calculated using different approaches (Goh and Mair, 2014)

there may be other influencing factors that affect the horizontal displacements.

To account for the influence of the frame-wall interaction, Fu et al. (2018) carried out a comprehensive parametric study on the response of the framed buildings with individual footings

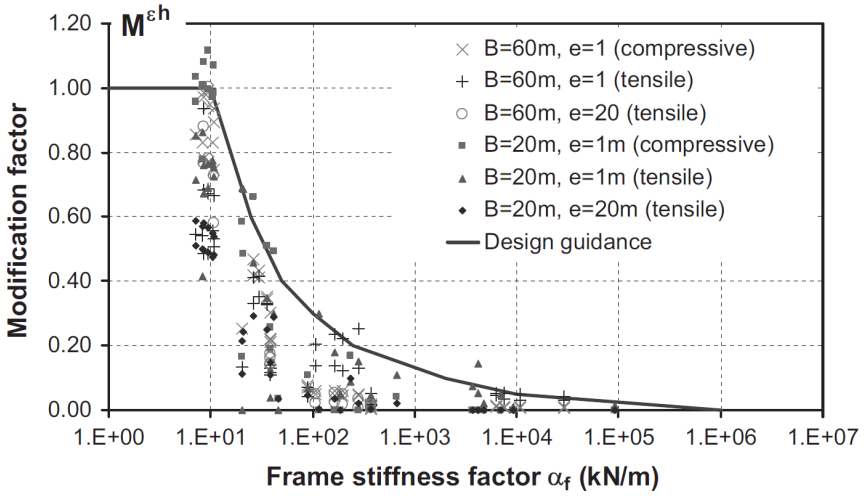


Fig. 2.30. Horizontal strain modification factors against frame stiffness factors (Goh and Mair, 2014)

subjected to tunnelling induced displacements. The analysis considered the frame-wall interaction by varying the ground stiffness and infill wall configuration. The authors emphasised the role of the infill walls in reducing the structural distortion due to tunnel construction, which can not be considered for an equivalent plate approach. Interestingly, the horizontal response of the individual footings to tunnelling presented in Fu et al. (2018) is complex, with the moving direction either the same as or opposite to the greenfield horizontal displacements. The authors stated that the horizontal displacements of the footings primarily depend on the soil-foundation interface friction. However, the role of the structural deformation on the footing horizontal displacements has not been revealed.

Franza and DeJong (2019) revealed the complex rotation-translation displacements of the footings in a framed building when subjected to tunnelling-induced ground movements. The coupling effects of both vertical and horizontal degrees of freedom (DOFs) of the frame are illustrated in Figure 2.31. If releasing the DOFs in the horizontal direction, the deflection of the superstructure causes the footing head rotation and the horizontal displacements of the footing bases (Figure 2.31(a)). On the other hand, ground horizontal movements result in the horizontal displacements of the footing bases while the deflection of the superstructure is negligible due to high axial stiffness, as shown in Figure 2.31(b). Consequently, the final horizontal displacements of the footings depend on the coupling effects of the two mechanisms described

above.

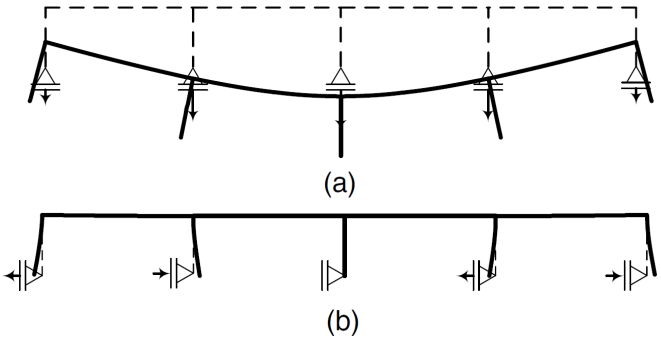


Fig. 2.31. Deformed shapes of a frame to (a) vertical and (b) horizontal displacements (Franza and DeJong, 2019)

A recent parametric study of the response of reinforced concrete framed structures to tunnelling was presented in Boldini et al. (2018) using the finite element method and found that framed structures always display hogging zones at the ends of the foundation due to the non-uniform contract pressure at the soil-foundation interface. Son (2015) considered the distortion and cracking of two different framed structures subjected to tunnelling in sandy ground, in which tunnelling-related parameters and ground condition were varied. The author stated that for an identical magnitude of soil volume loss, the buildings on dense soil deformed more severely than the structure resting on loose soil, indicating that the movements of loose soil are affected/modified more by a building.

2.3 Summary and research gap

Prediction of structural distortion due to tunnel construction is vital for risk assessment and mitigation. In practice, a three-stage procedure proposed by Mair et al. (1996) is generally adopted. In the first stage, greenfield displacements are predicted using one of the available empirical or semi-empirical approaches (Peck, 1969; Mair et al., 1993; Loganathan and Poulos, 1998; Marshall et al., 2012; Franza et al., 2019; Franza and Marshall, 2019b); two thresholds are considered, ground settlement (10 mm) and slope (1/500); if the buildings undergo larger deformation than the thresholds, greenfield displacements are imposed to the simplified beam

structures. Maximum tensile strains induced within the buildings are calculated using Equations 2.25 or 2.27, and corresponding damage category (Boscardin and Cording, 1989; Son and Cording, 2005) can be assessed from Table 2.4. If the predicted damage category exceeds the allowable value, soil-structure interaction should be considered. This can be done using either the modification factor approach or numerical analysis considering the full soil and structure details.

When considering the soil-structure interaction problem due to tunnelling, while several studies have indicated the importance of considering realistic (framed) building characteristics (Boone, 1996; Boldini et al., 2018; Fu et al., 2018; Franza and DeJong, 2019; Son, 2015), equivalent beam or plate models are still frequently adopted (Franzius et al., 2006; Pickhaver et al., 2010; Maleki et al., 2011; Namazi and Mohamad, 2013; Farrell et al., 2014; Bilotta et al., 2017; Franza and Marshall, 2018). This simplification involves uncertainties that have not yet been sufficiently investigated. For instance, when estimating the total stiffness of a framed structure, most researchers have adopted a pure bending stiffness (Franzius et al., 2006; Goh and Mair, 2014; Haji et al., 2018) despite the evidence that shear flexibility can have an important role (Potts and Addenbrooke, 1997; Finno et al., 2005). Also, Franza et al. (2020a) highlighted that bending and shear deformation modes of equivalent solids have not always been well distinguished because of the focus on the structure settlement profile. Finally, the local deformations of infill walls in frames is potentially not well described by equivalent beams or plates. Therefore, despite recent numerical studies dealing with the response of a framed structure to tunnelling (Goh and Mair, 2014; Son, 2015; Boldini et al., 2018; Fu et al., 2018), there is still a lack of experimental evidence to substantiate many of the findings reported by the above numerical analyses.

Chapter 3

Methodology and experimental equipment

In this chapter, the geotechnical centrifuge technique and its associated limitations are briefly presented. Then, the experimental package, building models, centrifuge testing plan, model preparation and testing procedure are illustrated.

3.1 Geotechnical centrifuge technique

This section broadly presents the background of centrifuge technology used in geotechnical engineering, including the centrifuge principles and scaling factors. The limitations of geotechnical centrifuge testing as it relates to this research are also briefly discussed.

3.1.1 Centrifuge principles and scaling factors

Geotechnical engineers frequently encounter the task of understanding the complex soil behaviour and soil-structure interaction problems caused by various forms of construction activities. However, this is not easy to achieve because construction materials such as soil, and excavation-induced soil-structure interaction problems often exhibit complex non-linear behaviour. It has been confirmed that soil behaviour highly depends on its current stress state and stress history. Therefore, one prerequisite for reproducing the complex soil behaviour and soil-structure interaction phenomena is to make sure that the simulated stress condition of the soil, either in physical or numerical models, is comparable with that in engineering sites.

To consider the variables that affect problems in geotechnical engineering, one straightforward way is therefore to monitor the soil behaviour and structure response during construction activities. Nevertheless, related problems often arise in field site monitoring. First, the geological conditions of real construction sites are generally complex so that it is not easy to isolate the effect of an individual parameter of interest. Furthermore, available projects are rather limited and cost associated with field site monitoring is quite high (Marshall, 2009). The use of scaled-down models in a normal laboratory environment (one gravity level) to investigate geotechnical problems is feasible but not ideal because the stress level within the scaled-down model is much lower than that in the prototype. Using a geotechnical centrifuge, the gravity of a model scaled down by a factor N can be accelerated by N times so that the same stress level within the small model as that in the prototype can be achieved. Therefore, the geotechnical centrifuge is a powerful tool that can provide a controlled research environment to replicate the real soil stress (therefore its behaviour) and soil-structure interaction behaviour using a scaled-down model.

In the application of centrifuge testing, understanding of scaling laws is important for the

transformation of model data to the values in the simulated prototype scenario. Taylor (1995a) summarises the centrifuge scaling laws of the typical parameters, as shown in Table 3.1.

Table 3.1. Centrifuge scaling laws (after Taylor (1995a))

Parameter	Metric unit	Model scale	Prototype scale
Gravity	m/s^2	N	1
Length	m	1	N
Area	m^2	1	N^2
Volume	m^3	1	N^3
Force	$N = kgm/s^2$	1	N^2
Density	kg/m^3	1	1
Stress	$Pa = N/m^2 = kg/(ms^2)$	1	1
Strain	-	1	1
Axial Stiffness (EA)	N	1	N^2
Bending stiffness (EI)	Nm^2	1	N^4

For the scale-down model by a factor of N, its gravity level needs to be accelerated by a factor of N to represent the prototype scenario. This factor of N can be linked to the rotational velocity ω of the centrifuge once the effective centrifuge radius R_e is determined:

$$N = \frac{\omega^2 R_e}{g} \tag{3.1}$$

Nevertheless, the size of the centrifuge model is generally non-negligible with respect to the dimension of the centrifuge itself. Consequently, the accelerated gravity of an arbitrary position within the model is not always identical because the distance between an arbitrary point of the model to the centre of rotation is not always constant. Therefore, an effective centrifuge radius R_e was suggested by Taylor (1995a):

$$R_e = R_t + \frac{h_m}{3} \tag{3.2}$$

where R_t is the distance between the top of the model and rotation axis, and h_m is the total height of the model. It can be seen that the effective radius defined by Taylor (1995a) equals the distance between centrifuge centre of rotation and two-thirds the height of the model.

3.1.2 Limitations in centrifuge modelling

Despite the advantages of geotechnical centrifuge testing described in Section 3.1.1, limitations still exist when modelling the prototype using a small centrifuge model. Apart from the variation of the stress levels at different depths of the model mentioned above, two aspects should be particularly noticed for this project:

- **Boundary effect**. The boundary effect could affect the accuracy of measured PIV (particle image velocimetry data acquisition technique, refer to Section 3.4.1) data due to the surface friction force of the acrylic front wall of the model container (refer to Section 3.2), which might affect the movements of the soil;
- **Particle size effect**. The effect of the ratio between modelled structures (for instance, model tunnel and footing foundation) to the particle size of sand (normally refer to average grain size diameter D_{50} value) would affect soil-structure behaviour.

Regarding the first point, Marshall et al. (2009) assessed the boundary effect using a discrete element modelling study and compared the results obtained from the centrifuge tests. The author demonstrated that the friction on the acrylic front wall doesn't have a significant effect on the soil settlement. Data measured from GeoPIV (White et al., 2003) (refer to Section 3.4.1) can reach more than 85% of the results measured by linear variable differential transformers (LVDTs) installed in the middle of the model, and the important features of the data, for example, the shape of the settlement trough, can be well captured. This demonstrated that taking measurements of soil displacements at a transparent wall of a plane-strain tunnelling model provided measurements that represented the plane-strain values sufficiently well to be used. On the other hand, when modelling the response of a surface structure to underground construction, the measured foundation settlements might not be identical to the vertical displacements of the soil directly beneath the foundation (Farrell, 2010; Ritter et al., 2018). This inconsistency occurs because the front of the frames is not immediately against the inner face of the acrylic wall. This aspect will be explained in detail in Section 4.2 using collected centrifuge data.

In terms of the size effect, it is arguably accepted that the size of the sand used in a centrifuge model should not be scaled down according to the scaling laws. This is due to the fact that the

behaviour of the soil highly depends on its particle size. The works from Kutter et al. (1994) is of importance because it dealt with cavities in sands using centrifuge models. The authors presented the relationship between normalised crater volume (the volume of the crater created V_{cr} normalised against the volume of the cavity V_{ci}) and normalised cavity diameter (D_{ci}/D_{50}), as shown in Figure 3.1. It is shown that an increasing trend of the normalised crater volume within the normalised cavity diameter between 30 and 1000 is observed, with an asymptotic value of 1 if the normalised cavity diameter is greater. However, Marshall (2009) suggested that V_{cr}/V_{ci} line should be asymptotic to approximately 0.8 for dilative dense sand. Therefore, the scale effects can be negligible if the normalised cavity diameter is larger than 500 for collapse condition, and a lower value may be acceptable for the pre-collapse condition. In this study, the ratio of the tunnel diameter D_t = 90 mm to D_{50} = 0.122 mm of the sand is 90/0.122 = 738, thus the scale effect is not considered.

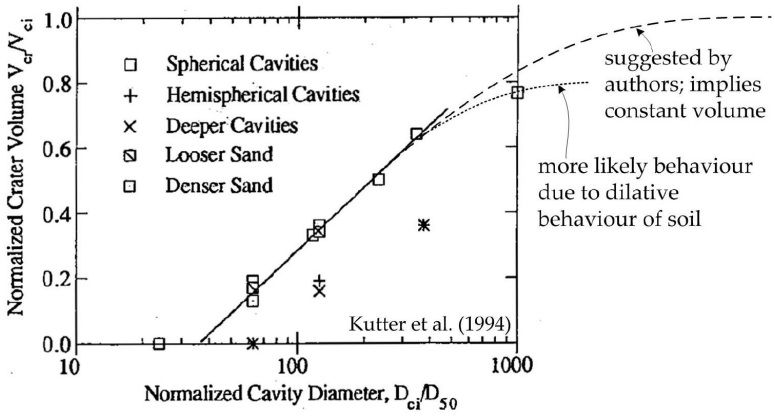


Fig. 3.1. Normalised crater volume against normalised cavity diameter (after Kutter et al. (1994); Marshall (2009))

On the other hand, to provide reliable simulation on the soil-structure interaction problems, the ratio of the size of the structure to the particle size of the soil should be greater than a certain value. Fuglsang (1988) suggested that this value should be larger than 30. For this study, the minimum size of the structural elements is the separate footings, which are 12 mm wide. Therefore, this ratio is 12/0.122 = 98, which is sufficiently greater than the suggested limit.

3.2 Experimental package

This section covers the description of experiment equipment, data acquisition method, and centrifuge testing plans in this study. The geotechnical centrifuge at the University of Nottingham Centre for Geomechanics is also briefly described in this section.

3.2.1 Geotechnical centrifuge at the University of Nottingham

This project adopted the geotechnical centrifuge at the University of Nottingham Centre for Geomechanics as the main tool to investigate the effects of tunnel construction on framed buildings with various foundation configurations. The diameter of the beam of the centrifuge is 4 m, with one swinging cradle and one counterweight at each end of the beam, as shown in Figure 3.2. The capacity of the centrifuge is 50 G-Tonne, with the maximum acceleration gravity level of 150 g (for the maximum payload of 333 kg) and a maximum payload of 500 kg (for the maximum gravity level of 100 g). Ellis et al. (2006) presented a comprehensive description of this centrifuge.

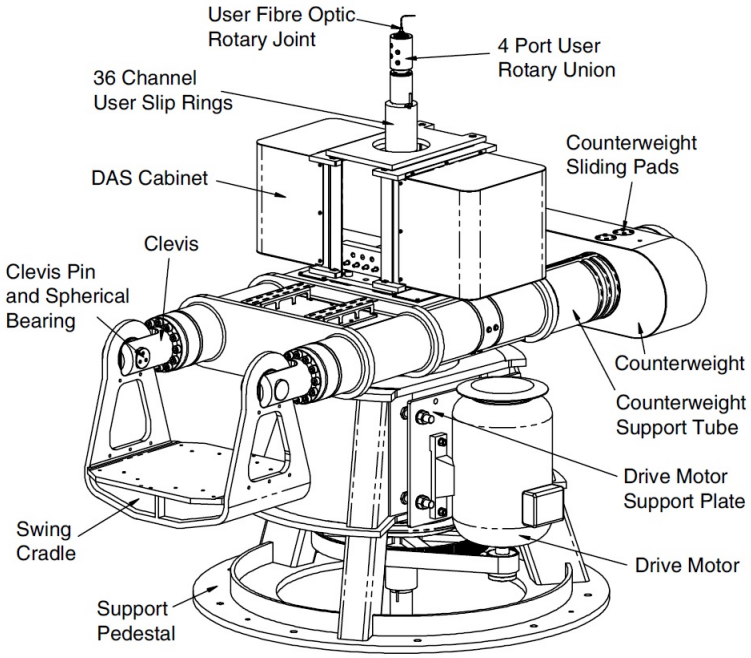


Fig. 3.2. Geotechnical centrifuge at the University of Nottingham Centre for Geomechanics (Ellis et al., 2006)

3.2.2 Strongbox

The strongbox was designed and manufactured to contain soil, the model tunnel and any structures that need to be tested (Zhou, 2014). The components of the strongbox include a steel U-shaped section component, a 95 mm thick acrylic front wall, a front frame, and an aluminium back wall, as shown in Figure 3.3. Long bolts are used to assemble these components together. The strongbox is placed on a 5 cm thick base plate, along with the components of volume loss control system, and other components such as the light-emitting diodes (LEDs) strips for lighting. U-channels were machined on both the front and back sides of the U-shaped section. This allows the rubber cords to be placed in between the front or back wall and U-shaped section (see details in Figure 3.3(b)). The dimension of the inner cross-section of the strongbox is 640 × 260 mm, and the maximum allowable height of the soil model can be up to approximately 500 mm.

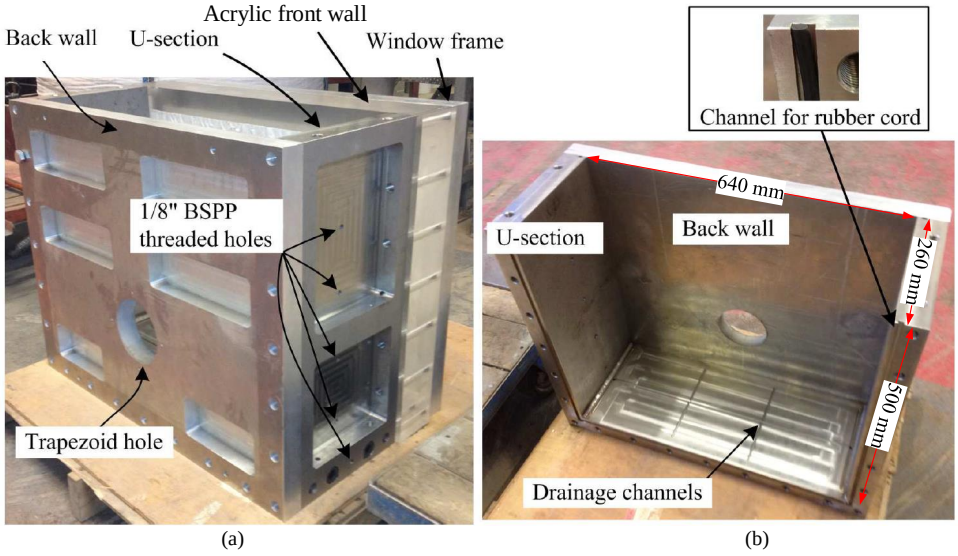


Fig. 3.3. Components of the strongbox (after Zhou (2014))

3.2.3 Model tunnel and volume control system

The model tunnel used in this study was developed by Zhou (2014), which consists of a 68 mm diameter aluminium hollow cylinder, two O-rings, 1 mm thick latex membrane and two end plates, as shown in Figure 3.4. The latex membrane is sealed at the two ends of the tunnel with

the help of O-rings (Figure 3.4(f)) and grease. The O-rings are placed between the annular gap and enlarged end of the model tunnel (see Figure 3.4(f)). The front end of the model tunnel is placed in the recess of the inner surface of the acrylic wall (Figure 3.4(c)), whereas the back end is sealed into the annular gap of the back aluminium wall (Figure 3.4(d)). The model tunnel is filled with water, giving a designed diameter of the tunnel of 90 mm, as shown in Figure 3.4(h). In addition, the cross-section of the model tunnel (Figure 3.4(h)) shows that the inner cylinder was designed to be placed at the downward eccentric point. This is because previous studies have confirmed that for the shallow tunnel, the majority of the volume loss occurs close to the tunnel crown (Loganathan and Poulos, 1998; Marshall, 2009; Zhou, 2014).

In this study, tunnel volume loss during the tunnel construction process is simulated by extracting water from the model tunnel. This volume loss control system was developed by Zhou (2014). To achieve more accurate control of the simulated volume loss, Franza (2016) modified the system by replacing the previous actuator with a stronger one. The volume loss control system consists of a water-filled hydraulic cylinder (SMC CP96SDB50-30C), an L03 MecVel ball screw actuator, an linear variable differential transformer (LVDT), a solenoid valve, a Pore Pressure Transducer (PPT) and a constant-head standpipe. The hydraulic cylinder, PPT, standpipe and solenoid valve are connected with the model tunnel using the pipeline system, as shown in Figure 3.5. The actuator is used to move the hydraulic cylinder for water extraction.

The working principle of the volume loss control system and the function of each component are briefly described as following using Figure 3.6. Before centrifuge spin up (at 1 g), the solenoid valve is closed to prevent the possible volume loss caused by the elasticity of the latex membrane. The solenoid valve is opened at 5 g. This allows the model tunnel to be connected with the constant head standpipe. The function of the standpipe is to provide a constant water pressure equal to the estimated vertical overburden pressure at the tunnel axis level, to compensate for any volume change caused by the compression of air within the volume loss control system (despite great care taken during model preparation to remove air) during centrifuge spinning. The constant water pressure is achieved by providing continuous water supply to the standpipe with a certain height (calculated based on the overburden pressure at the depth of the tunnel axis) of overflow hole. When the targeted g-level is reached, the solenoid

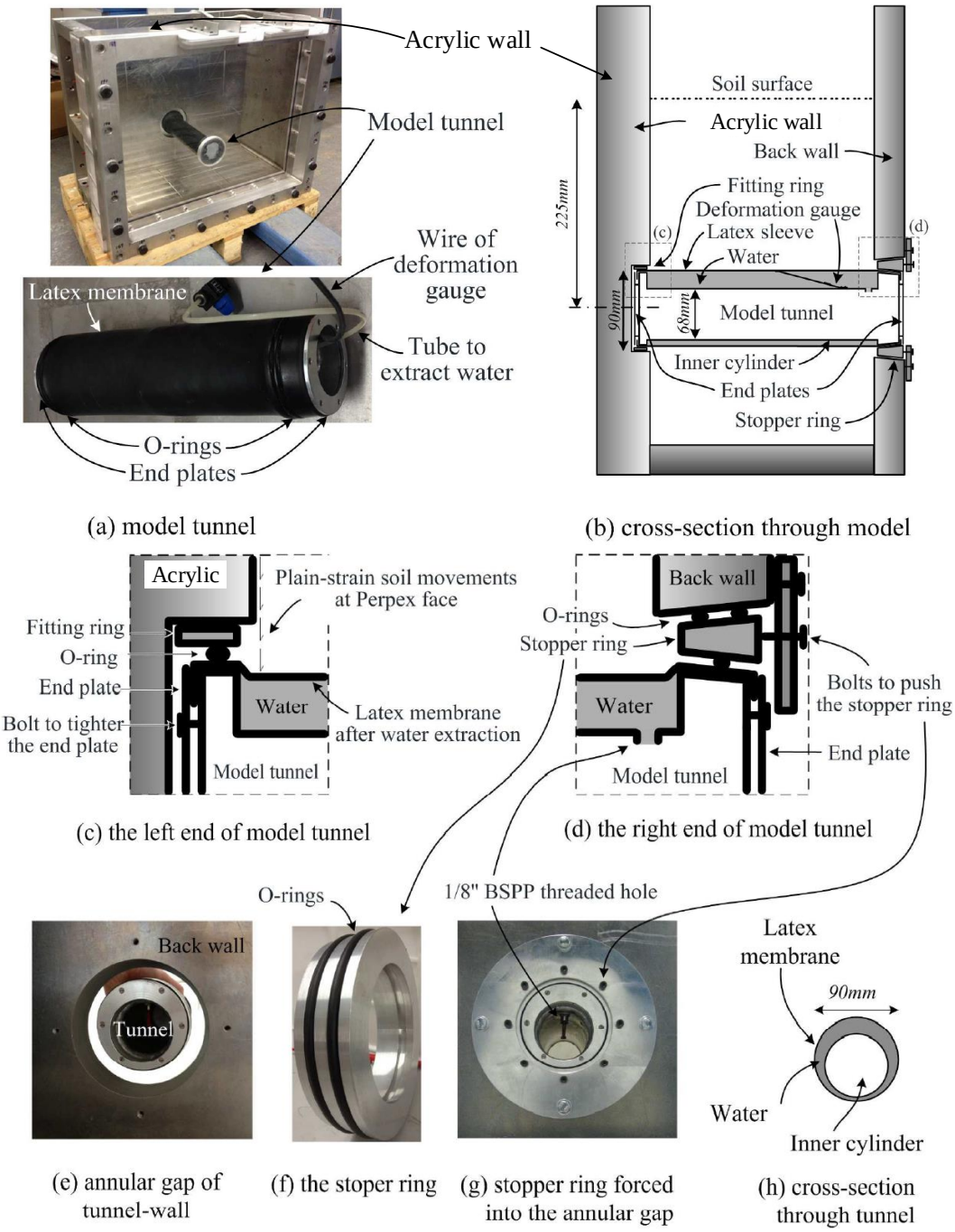


Fig. 3.4. Components of model tunnel and its installation (Zhou, 2014)

valve is closed again (the model tunnel is connected exclusively to the hydraulic cylinder) and the actuator is activated to drive the hydraulic cylinder to extract water from the model tunnel to simulate volume loss during the tunnel construction process. The moving distance (measured

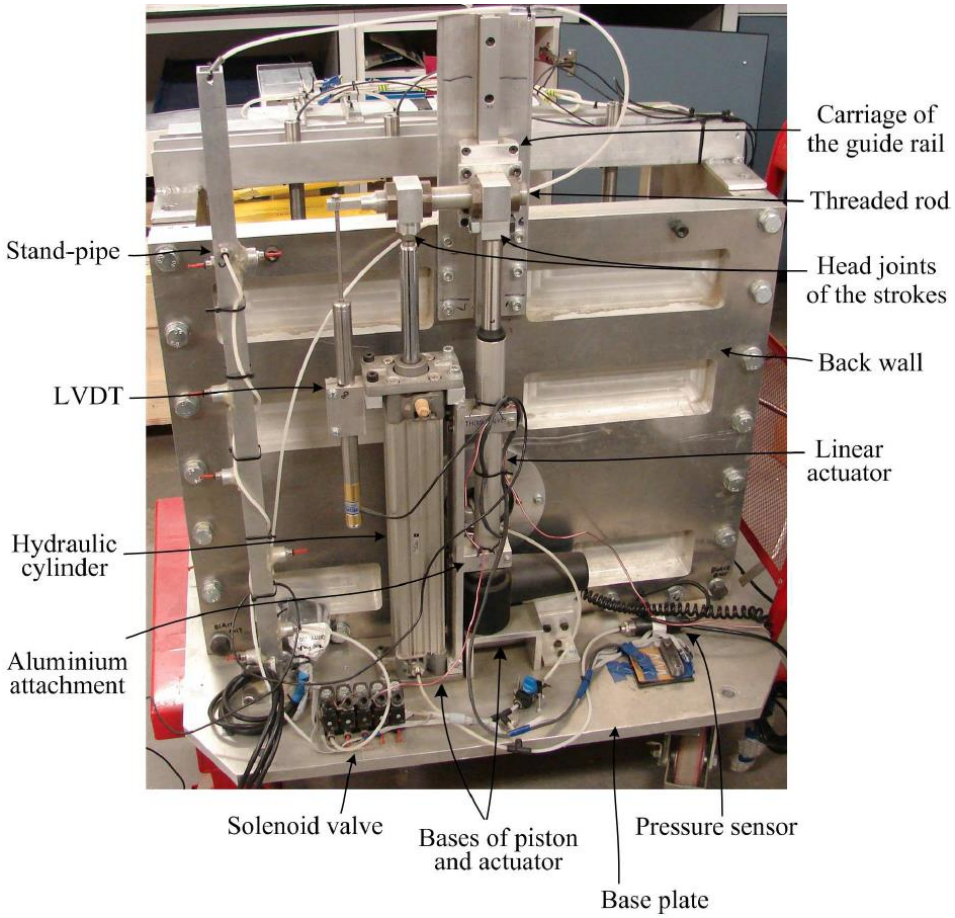


Fig. 3.5. Tunnel volume loss control system components (Zhou, 2014)

by an LVDT) of the hydraulic cylinder was calibrated to relate the volume of the extracted water, which is directly converted to the simulated tunnel volume loss. The moving speed of the actuator can be set very low and be well controlled using a compiled LabView program so that a precise volume loss can be achieved. Finally, a PPT is connected with the model tunnel so that the change of the tunnel pressure can be monitored throughout the tests.

3.2.4 Soil

This project aims to investigate the response of framed buildings with either rafts or separate footings to tunnel construction in sandy ground. Therefore, a fine-grained silica sand known as Leighton Buzzard Fraction E silica sand was used in this research (characterised by Zhao (2008); Lanzano et al. (2016)). The grading of Fraction E sand ranges from 90μm to 150μm

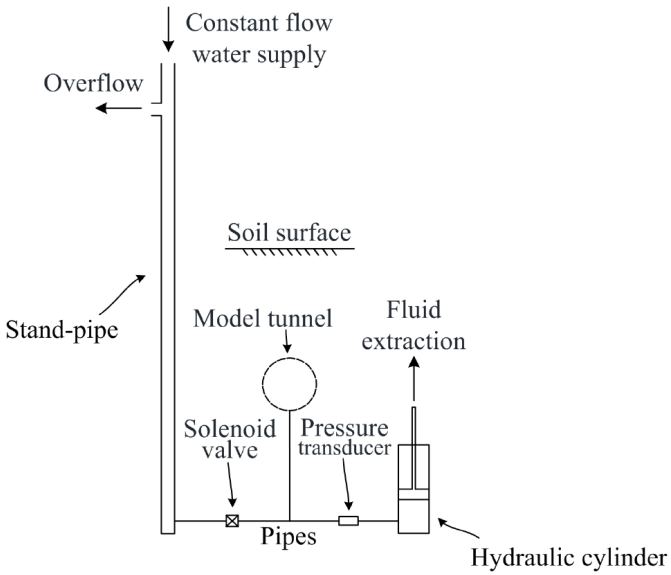


Fig. 3.6. Sketch of the tunnel volume loss control system (Zhou, 2014)

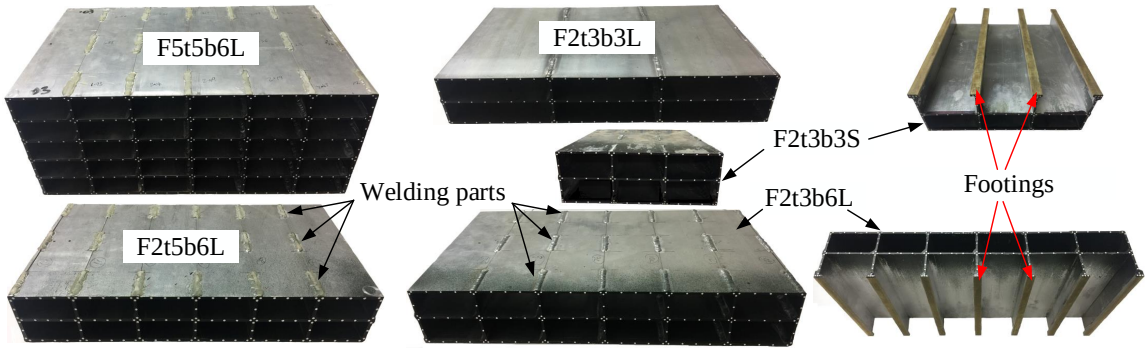
with a D_{50} grain size of 122μm. The specific gravity (G_s), minimum (e_{min}) and maximum (e_{max}) void ratios of the sand are 2.67, 0.64 and 0.97, respectively. In this study, two values of the relative density of sand are considered: 30% (loose sand) and 90% (dense soil), which correspond to the unit weight of sand of 1399 kg/m^3 and 1603 kg/m^3, respectively. The properties of Leighton Buzzard Fraction E silica sand are summarised in Table 3.2.

Table 3.2. The properties of Leighton Buzzard Fraction E silica sand

Fraction E property	value
Min. grain size (mm)	0.09
D_{50} grain size (mm)	0.122
Max. grain size (mm)	0.15
Min. voids ratio e_{min} (-)	0.64
Max. voids ratio e_{max} (-)	0.97
Specific gravity G_s (-)	2.67
critical state friction angle (°)	32
Unit weight for I_d = 30% (kg/m^3)	1399
Unit weight for I_d = 90% (kg/m^3)	1603

3.3 Framed building models

In this study, five framed building models on raft foundations and two models with separate footings were manufactured by machining and welding aluminium plates and angles, as shown in Figure 3.7. In addition, a framed building model with separate footings was also designed and manufactured by bolting plates, T-bars and square bars (discussed later). Considering that the Young's modulus of aluminium and concrete have a similar order of magnitude and that the Young's modulus is not affected by the centrifuge scaling laws (Taylor, 1995b), the prototype cross-sectional stiffness of the model slabs and walls replicates reinforced concrete structures in the elastic range of behaviour.



(a) Raft foundation (b) Separate footings

Fig. 3.7. Framed building models: (a) raft foundation; (b) separate footings

For the frames with raft foundations, the welding process can be summarised as follows (referring to Figure 3.8): 1) with the foundation plate and the right-side wall being placed perpendicular to each other, their junction was welded together to obtain an L-shaped section (see Figure 3.8(a)); 2) the first angle was welded to the L-shaped section and foundation plate (see Figure 3.8(b)); 3) the second angle was then welded to the first angle and the foundation plate; 4) the rest of the angles were welded in a similar sequence (see Figure 3.8(d)). The walls/slabs were connected by welding 60% of the length along the longitudinal direction (Xu et al., 2019) (see the top of the frame model in Figure 3.7(a)). The proportion of 60% was chosen based on a finite element modelling study which showed that the frame with 60% of the length welded can achieve approximately 90% of the stiffness of the model with the full length welded (see Appendix A1). On the other hand, a fully welded building model has a significantly

greater level of distortion (particularly for the raft foundation) than the frame with 60% of the length welded, which is not ideal for this study (resulting in non-uniform pressure distribution at the soil-foundation interface when the framed building is placed on the soil surface).

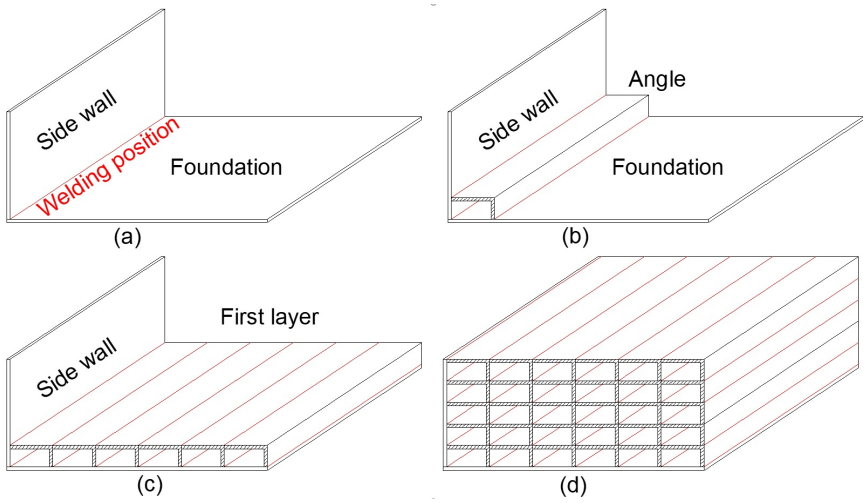


Fig. 3.8. Illustration of the welding process of the framed building on raft foundation (F5t5b6L)

To create the frames with separate footings, two frames (F2t3b6L and F2t3b3S, see Figure 3.7) with raft foundations were modified by cutting out sections of the foundation plate between columns and adding material (epoxy adhesive) to the external footings to achieve the designed footing width (12 mm), as shown in Figure 3.9. The adopted Araldite epoxy adhesive has an excellent bonding effect with the aluminium plate, and its Young's modulus can reach up to 9.8 GPa, which is sufficiently stiff (compare against the relatively low soil stiffness) for the simulation of soil-foundation interaction problem.

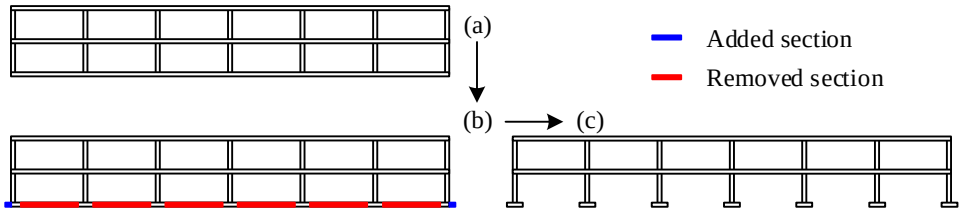
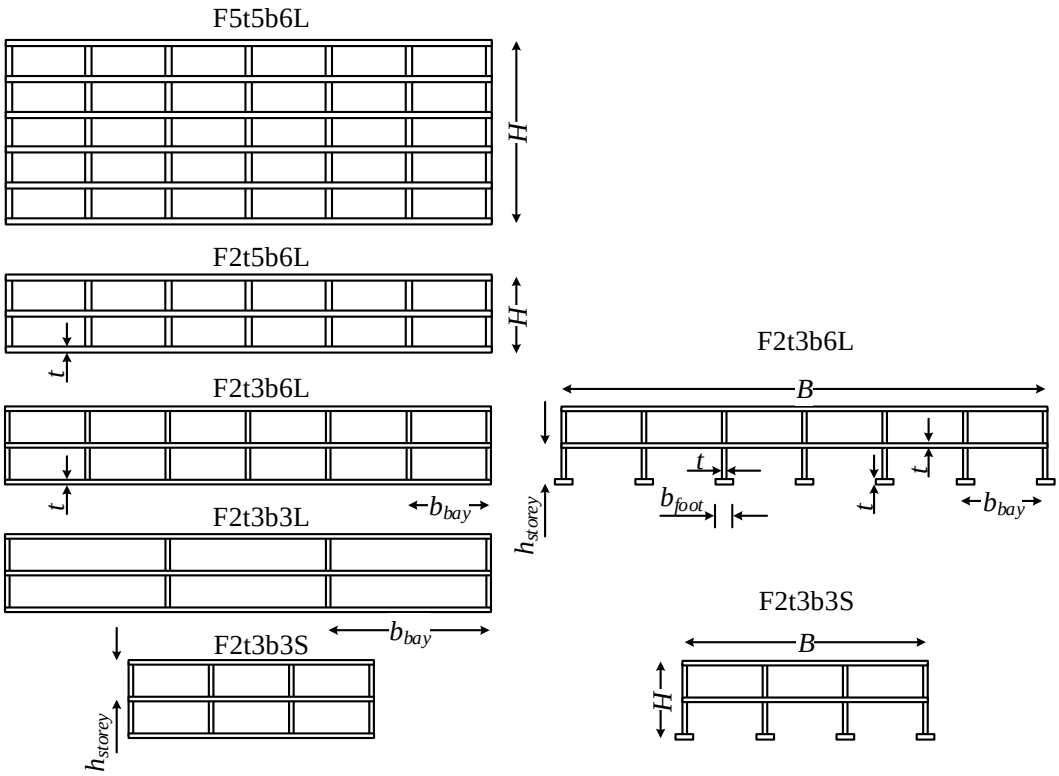


Fig. 3.9. Manufacture process of the separate footings (F2t3b6L)

Figure 3.10 and Table 3.3 show the geometric parameters (in model scale and prototype (68 g, refer to Section 3.6.2)) of the welded frame models. The model frames are labelled based on their structural characteristics as either FxtybzS or FxtybzL: x indicates the number

of storeys, y the thickness in millimetre of the structural elements (model scale), z the number of bays, and the suffix L and S are used for transversely long and short structures, respectively. As can be seen in Figure 3.7, frames F5t5b6L, F2t5b6L and F2t3b3L are only rested on raft foundations, whereas frames F2t3b6L and F2t3b3S have both rafts and separate footings foundations.



(a) Raft foundation (left column) (b) Separate footings (right column)

Fig. 3.10. Illustration of the configuration of the framed building models

To achieve the plane-strain condition, the model structures extended the full width of the centrifuge strongbox in the direction of the tunnel axis, with continuous vertical walls and horizontal slabs (for both foundations and floors). The building models are 258 mm long in the tunnel longitudinal direction, leaving a 1mm gap at the front/back walls of the 260 mm wide centrifuge strongbox (the possible effect of this on the accuracy of measured displacement data will be discussed in Section 4.2). The thicknesses (t) of the building elements (foundation, elevated slabs, and walls) for a given building model are the same.

As can be gleaned from Table 3.3, the number of storeys, the thickness (t) of building

elements, the building transverse width (B), the number of bays along the transverse width, and the width (b_{bay}) of the bays varies between building models to isolate the influence of individual structural characteristics on the interaction problem. The height per storey (h_{storey}) is 38.1 mm for all building models, hence the building height H varies according to the number of storeys. A thin layer of sand was bonded to the underside of the building foundations to replicate a rough soil-foundation interface. The GeoPIV digital image analysis technique (White et al., 2003; Stanier et al., 2016) was used to measure soil and structure displacements (the details related to this will be presented in Section 3.4). To enhance the performance of the image analysis of the model frames, the front faces of the models were painted matt black and small circular insets were machined within a grid on each face, which were subsequently painted white (see the building models in Figure 3.7).

Table 3.3. Framed building configurations

Label	No. of storeys	No. of bays	Model scale (dimension in mm)				Prototype (dimension in m)			
			t	H	B	b_{bay}	t	H	B	b_{bay}
F5t5b6L$^{\#}$	5	6	4.8	195.3	462.0	76.2	0.32	13.3	31.4	5.2
F2t5b6L$^{\#}$	2	6	4.8	81.0	462.0	76.2	0.32	5.5	31.4	5.2
F2t3b6L*	2	6	3.2	79.4	460.4	76.2	0.22	5.4	31.3	5.2
F2t3b6LN†	2	6	3.2	79.4	460.4	76.2	0.22	5.4	31.3	5.2
F2t3b3L$^{\#}$	2	3	3.2	79.4	460.4	152.4	0.22	5.4	31.3	10.4
F2t3b3S*	2	3	3.2	79.4	231.8	76.2	0.22	5.4	15.8	5.2

Note: for all frames, h_{storey} = 38.1 mm at model scale and 2.6 m at prototype, respectively;
footing width b_{foot} = 12 mm at model scale and 0.82 m at prototype, respectively.
* has both raft and separate footing foundations; † has only separate footings; $^{\#}$ has only rafts

As mentioned earlier, the frames on raft foundations were made by welding aluminium angles and plates, whereas the frames with separate footings were manufactured by cutting out sections of the raft foundation plate between columns and adding material to the external footings. However, this process resulted in an asymmetric connection for the footing columns with the slabs (refer to the results of the loading tests in Section 3.7.2). To overcome this issue, a new framed building model (F2t3b6LN) was designed and manufactured, as shown in Figure 3.11. This model frame consists of 2 long plates, 7 T-bars, 7 short plates, 42 square bars all assembled by nuts and bolts. Square bars were located at the wall/slab nodes to achieve a nodal fixed-fixed connection, as shown in Figure 3.11(a) and (d). In addition, shallow slots

were machined in the slabs where walls/columns were placed, as shown in Figure 3.11(a). This ensured the alignment of the vertical walls with the slabs during assembly of the frame.

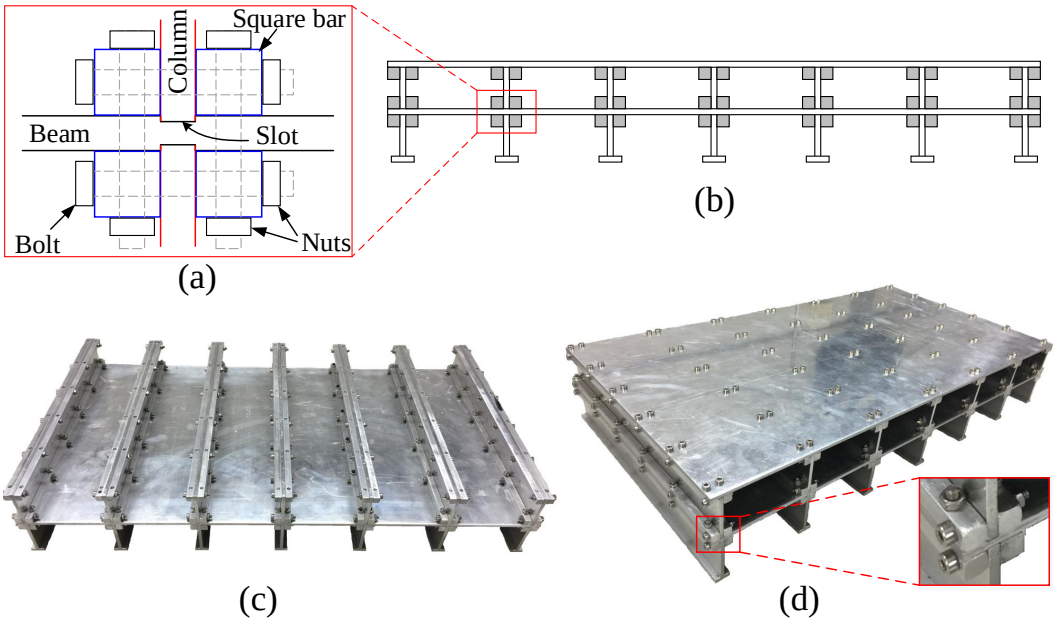


Fig. 3.11. Illustration of the new frame (F2t3b6LN) with separate footings: (a) illustration of node connection; (b) sketch of the frame; (c) top removed; (d) node connection detail

This new frame has the same configuration as that of frame F2t3b6L with separate footings. As with the other frames, a thin layer of sand was bonded to the underside of the building foundations to replicate a rough soil-foundation interface. The front faces of the models were also painted matt black and small circular insets were machined within a grid on each face, which were subsequently painted white.

Finally, the stiffness of these framed building model was evaluated by performing a series of loading tests, as presented in Section 3.7.

3.4 Data acquisition methods

3.4.1 Particle image velocimetry (PIV) technique

To measure the displacements of both the soil (surface and subsurface) and the structures during tests, the particle image velocimetry (PIV) technique based on close-range photogrammetry

was used in this study. This technique was first developed and adopted in the field of fluid mechanics experiments by Adrian (1991). Later on, White et al. (2003) introduced this technique to the field of geotechnical engineering, also known as GeoPIV technique. Recently, some improvements were also made by Stanier et al. (2016), for instance, the ability of accounting for rotation of soil patches.

The principle of GeoPIV is to track the pixel movement through a series of images taken during the experiments, and then to convert the image-space coordinate of the targeted points into an object-space coordinate. In order to do this, a number of reference points (termed as control markers) with known object-space coordinates are required in the calibration process. The control markers were painted on the inner surface of the acrylic front wall. Their object-space coordinates were calibrated using a photogrammetric Mylar sheet (containing black dots with known coordinates) before the formal centrifuge tests. The calibration process in this study is the same as that described by Marshall (2009); Zhou (2014). To improve the texture of the soil, a thin layer of dyed sand was sprinkled on the inner surface of the acrylic front wall before sand pouring (described in Section 3.6).

In this study, two Dalsa Genie Nano-M4020 monochrome cameras, with 12.4-megapixel sensors and 8 mm Tamron lens, were used in the experiments, as shown in Figure 3.12(b). The cameras were installed and fixed in front of the model using a frame, as shown in Figure 3.12(c). Importantly, to combine the images taken by different cameras into a full experimental image, an overlap between the fields of view is necessary (see Figure 3.12(a)). Furthermore, single wavelength (amber) light-emitting diodes (LEDs) were adopted for the lighting of the model to avoid issues related to chromatic aberration, which has been observed to cause a rainbow effect around the outer areas of images due to refraction of light within the acrylic wall of the strongbox (having a negative impact on the image analysis). The details related to this are described as follows.

The chromatic aberration is caused due to the difference of refractive indexes between colours with different wavelengths. In general, the white colour LEDs, which are frequently adopted in the geotechnical centrifuge testing, are created by a mixture of various types of colours. Therefore, the resulting images suffer from an effect similar to radial blur and the

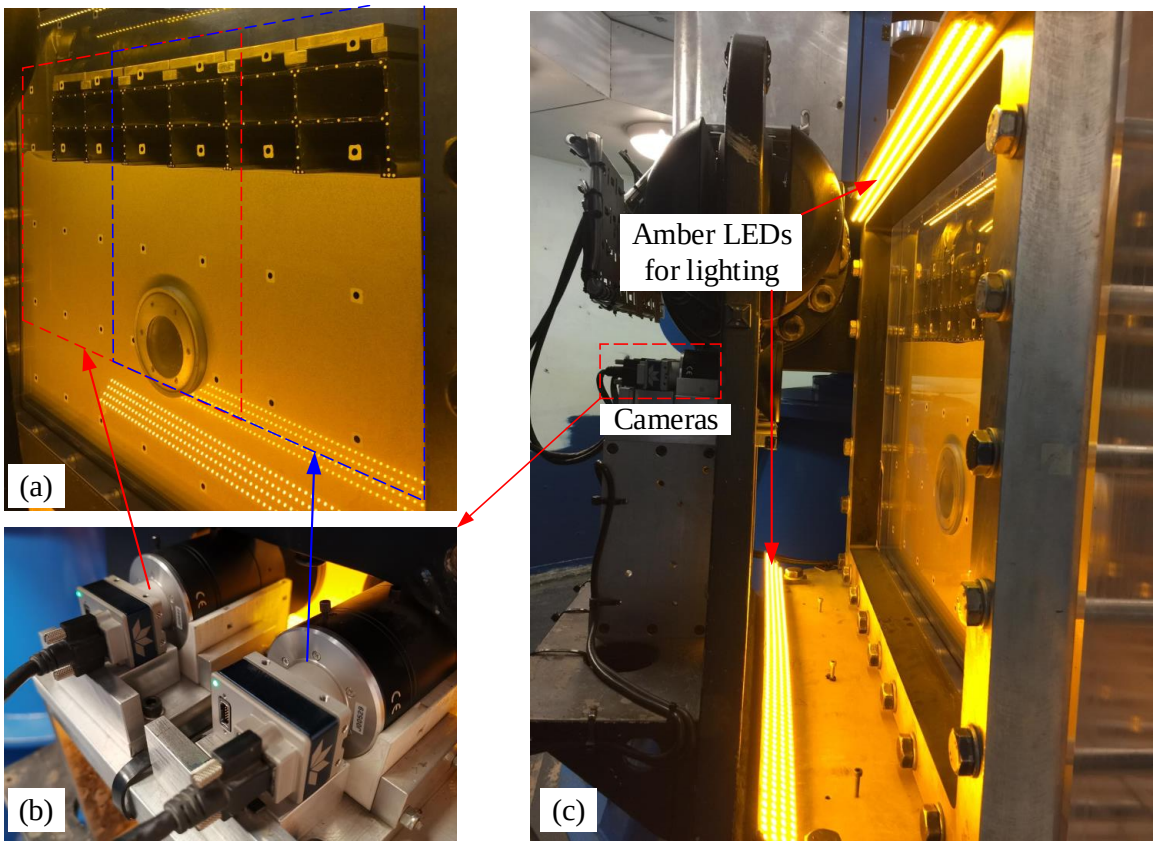


Fig. 3.12. Illustration of the image-based deformation measurement equipment: (a) camera field of view; (b) setup of the cameras; (c) relative camera-model position

sharpness and quality of the soil texture are reduced. Moreover, control markers (especially in the corners) show the same effect and the accuracy of the detection of their centroid is diminished. An example of such an effect is shown in Figure 3.13, in which the same corner region of an image is compared between lighting with white LEDs (Figure 3.13(a)) and monochromatic LEDs (Figure 3.13(b)); the image in Figure 3.13(a) is visually more blurry than that in Figure 3.13(b).

To improve the image quality, it is therefore beneficial to use lighting that outputs a sharp spectral response, such as monochromatic LEDs, to decrease chromatic aberration. Consequently, monochromatic amber LEDs were adopted for this research (see Figure 3.12(c)). To obtain a uniform lighting environment, two LED strips were installed, respectively, on the top and the bottom of the model.

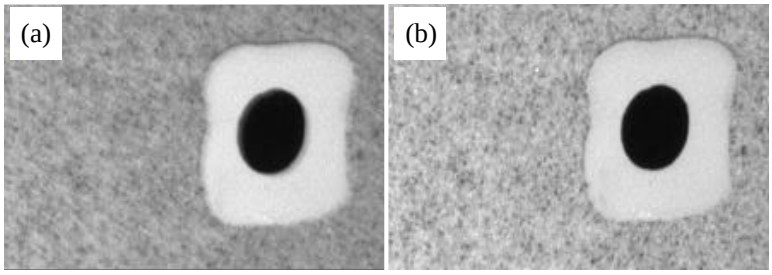


Fig. 3.13. Example of the same picture (at the corner) taken with (a) white LEDs, and (b) monochromatic amber LEDs

3.4.2 Other instruments

As discussed earlier, a Linear Variable Differential Transformer (LVDT) was used to measure the moving distance of the hydraulic cylinder within the volume loss control system (refers to Section 3.2.3). The working voltage of the LVDT is 12V, with ±5V DC output and ±50mm stroke. A Pore Pressure Transducer (PPT) was also used to monitor the change of the model tunnel pressure. A UNIK 5000 PPT, produced by General Electric, with a maximum capacity of 1000 kPa with ±0.1mV output, was used. Apart from the instruments mentioned above, two load cells were also used in the foundation loading tests presented in Section 5.2, along with two LVDTs (±15 mm stroke). The in-line load cell, produced by Richmond Industries, has a 5 kN capacity with a nominal sensitivity of 2.0mV/V. All instruments were calibrated to obtain the factors to convert the voltage data to the required engineering unites (force, pressure and displacement) before use. A LabVIEW user interface provided a useful and reliable approach to control and monitor the installed instruments during centrifuge tests. The module used for each instrument and the specifications of all the equipment are summarised in Appendix A2.

3.5 Experimental testing plan

A total of 41 centrifuge tests including 4 greenfield (GF) tests and 37 framed buildings tests were performed, as summarised in Table 3.4. Figure 3.14 shows the definition of the tunnelling-related parameters. In general, for a given welded frame model, the relative density of the sand I_d, the eccentricity e of the building with respect to the tunnel, and the building self-weight

(SW: standard self-weight; 2SW: doubled self-weight) were varied in the experiments. Frame F2t5b6L was also tested with a higher cover depth C of the tunnel. For frame F2t3b6LN, the relative density of the sand I_d, the buried depth d_f of the footings, and the cover depth C of the tunnel were varied. The standard self-weight SW is due to the weight of the aluminium used for the model frames and was calculated for in-flight conditions considering the variation of gravity level along the vertical axis of the frames. The doubled self-weight 2SW was achieved by adding simply supported (at wall locations) weights to the top of the frame; with this system, the additional weight did not increase the frame stiffness (see Figure 3.14).

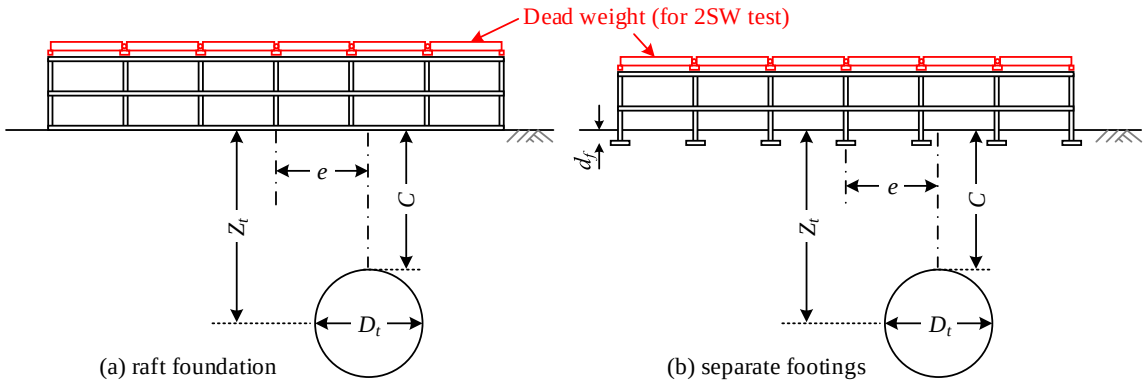


Fig. 3.14. Experimental layout and parameter definition

Specifically, for each of the long welded frames on rafts (label ending in "L"), a total of 4 tests were performed with identical cover depth (C = 117 mm): 2 tests involving a central tunnel (e/B = 0) in loose and dense sands (I_d = 30 and 90%) for a standard weight SW of the building, 1 test with a central tunnel (e/B = 0) in dense sand (I_d = 90%) and the 2SW frame, and 1 test for an eccentric tunnel case (e/B = 0.2) in loose sand (I_d = 30%) and SW frame. In addition, one more test was also performed for SW frame F2t5b6L on the raft with a central position (e/B = 0) and a greater tunnel cover depth (C= 180 mm) in loose sand (I_d = 30%). For the short building models (F2t3b3S) on rafts, 6 tests were performed (all with tunnel cover depth C= 117 mm); for the loose sand I_d = 30%, normalised eccentricity e/B of 0 and 0.5 was tested for the standard building weight SW only, whereas for the dense sand I_d = 90%, both normalised eccentricity (e/B = 0; 0.5) and building weight (SW and 2SW) were varied.

For frames F2t3b6L and F2t3b3S with separate footings, 4 and 6 tests were performed, respectively, with identical parameters/variables as those for the tests with raft foundations (see

Table 3.4. Centrifuge testing plan (dimension in model scale)

No.	Test item	Foundation	I_d (%)	e/B	D_t (mm)	C (mm)	C/D_t	d_f (mm)	Weight
1	Greenfield	-	30	-	90	117	1.3	-	-
2	Greenfield	-	30	-	90	117	2.0	-	-
3	Greenfield	-	90	-	90	180	1.3	-	-
4	Greenfield	-	90	-	90	180	2.0	-	-
5	F5t5b6L	Raft	30	0	90	117	1.3	0	SW
6	F5t5b6L	Raft	30	0.2	90	117	1.3	0	SW
7	F5t5b6L	Raft	90	0	90	117	1.3	0	SW
8	F5t5b6L	Raft	90	0	90	117	1.3	0	2SW
9	F2t5b6L	Raft	30	0	90	117	1.3	0	SW
10	F2t5b6L	Raft	30	0.2	90	117	1.3	0	SW
11	F2t5b6L	Raft	30	0	90	180	2.0	0	SW
12	F2t5b6L	Raft	90	0	90	117	1.3	0	SW
13	F2t5b6L	Raft	90	0	90	117	1.3	0	2SW
14	F2t3b6L	Raft	30	0	90	117	1.3	0	SW
15	F2t3b6L	Raft	30	0.2	90	117	1.3	0	SW
16	F2t3b6L	Raft	90	0	90	117	1.3	0	SW
17	F2t3b6L	Raft	90	0	90	117	1.3	0	2SW
18	F2t3b6L	Footings	30	0	90	117	1.3	0	SW
19	F2t3b6L	Footings	30	0.2	90	117	1.3	0	SW
20	F2t3b6L	Footings	90	0	90	117	1.3	0	SW
21	F2t3b6L	Footings	90	0	90	117	1.3	0	2SW
22	F2t3b6LN	Footings	30	0	90	117	1.3	0	2SW
23	F2t3b6LN	Footings	90	0	90	117	1.3	0	2SW
24	F2t3b6LN	Footings	90	0	90	117	1.3	10	2SW
25	F2t3b6LN	Footings	90	0	90	180	2.0	10	2SW
26	F2t3b3L	Raft	30	0	90	117	1.3	0	SW
27	F2t3b3L	Raft	30	0.2	90	117	1.3	0	SW
28	F2t3b3L	Raft	90	0	90	117	1.3	0	SW
29	F2t3b3L	Raft	90	0	90	117	1.3	0	2SW
30	F2t3b3S	Raft	30	0	90	117	1.3	0	SW
31	F2t3b3S	Raft	30	0.5	90	117	1.3	0	SW
32	F2t3b3S	Raft	90	0	90	117	1.3	0	SW
33	F2t3b3S	Raft	90	0	90	117	1.3	0	2SW
34	F2t3b3S	Raft	90	0.5	90	117	1.3	0	SW
35	F2t3b3S	Raft	90	0.5	90	117	1.3	0	2SW
36	F2t3b3S	Footings	30	0	90	117	1.3	0	SW
37	F2t3b3S	Footings	30	0.5	90	117	1.3	0	SW
38	F2t3b3S	Footings	90	0	90	117	1.3	0	SW
39	F2t3b3S	Footings	90	0	90	117	1.3	0	2SW
40	F2t3b3S	Footings	90	0.5	90	117	1.3	0	SW
41	F2t3b3S	Footings	90	0.5	90	117	1.3	0	2SW

For FxtybzS or FxtybzL, x indicates the number of storeys, y the thickness in mm of the structural elements, z the number of bays, and the suffix L and S are used for transversely long and short structures, respectively. F2t3b6LN is the transversely long structures assembled by nuts and bolts.

Table 3.4). On the other hand, for frame F2t3b6LN, a total of 4 tests were performed, all with central ($e/B = 0$) tunnel and 2SW frame: 2 tests involving the footings on the surface ($d_f = 0$) in loose and dense sands ($I_d = 30$ and 90%) with a tunnel cover depth $C = 117$ mm, 2 tests involving the footings with a buried depth $d_f = 10$ mm in dense sands ($I_d = 90\%$) and a tunnel with either $C = 117$ mm or 180 mm.

3.6 Experimental setup and testing procedure

3.6.1 Model preparation

The soil samples were prepared at 1 g. The preparation of dense ($I_d = 90\%$) and loose ($I_d = 30\%$) sand models was carried out differently. The dense sand sample was prepared using the sand pluviation method (consistent with Jacobsz (2002); Vorster et al. (2005); Marshall et al. (2012); Farrell et al. (2014); Franza et al. (2019)) before moving the package onto the centrifuge cradle. The sand was pluviated using a hopper hung to a certain height (calibrated to achieve the desired density), and the hopper was manually moved horizontally during the sand pouring process. To achieve a consistent density of the soil around the tunnel, the strongbox was placed on its acrylic front wall (face down). This allows the dense sand to be poured into the container in-line with the model tunnel. For greenfield tests and the tests involving the foundations on the surface ($d_f = 0$), a wooden plate was used for the temporary top of the sample, whereas a different procedure was carried out for the tests with buried footings (described in detail below). Note that when the model tunnel was placed vertically, the stiffness of the membrane cannot maintain the shape of the tunnel (bulge at the bottom) due to the pressure of the water within the membrane. To overcome this issue, a paper sleeve was used during sand pouring (see Figure 3.15), and the sleeve was gradually pulled up as the level of the soil increased. After pouring of the dense soil sample, the back wall was installed back and the strongbox was turn up to its upward position. Then, the building model was carefully placed on the soil surface.

The preparation of loose sand models was carried out using a scoop with the experimental package on the centrifuge cradle after the previous sample was excavated down to tunnel axis depth (consistent with Franza and Marshall (2018), who showed good repeatability of results),

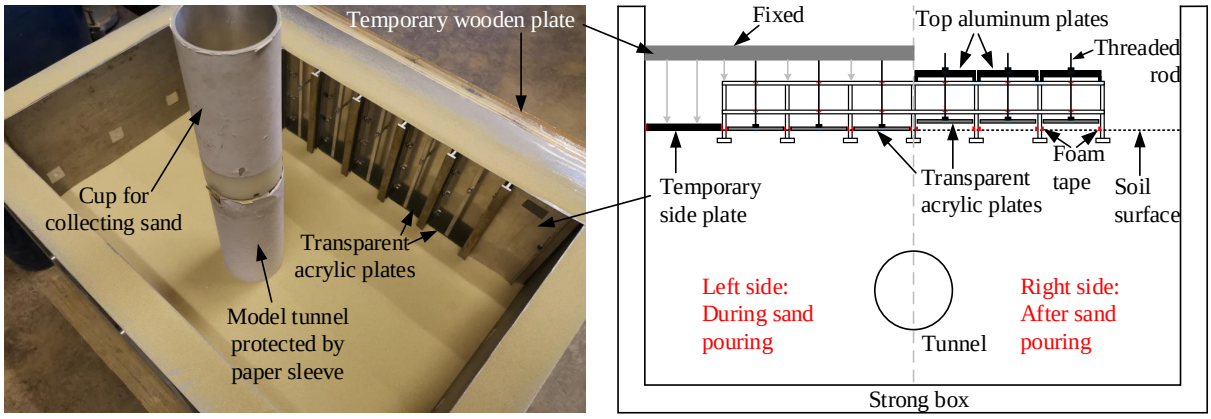


Fig. 3.15. Illustration of the sand pouring for buried separate footings

achieving a relative density of I_d = 30±5%. This relatively quick preparation method for loose soil does imply a greater level of uncertainty relating to soil homogeneity (compared to sand pluviation approach), however, the loose soil test results are mainly used to establish the contrasting effect of loose versus dense soil, hence this issue is not considered to be significant. After pouring of the loose sample, the surface was levelled to ensure uniform contact at the soil-foundation interface when the building model was placed on the surface.

For the tests involving buried footings, a different preparation procedure was design to achieve uniform ground conditions around the footings. As shown in Figure 3.15(a), the building model was placed inside the strongbox prior to sample preparation, and sand was poured in-line with the longitudinal direction of both footings and the tunnel. To achieve this, a set of equipment, including transparent acrylic plates, threaded rods and aluminium plates, was developed. To set the ground level above the footings, two temporary aluminium plates were used at each side of the building model, whereas acrylic plates were placed inside each panel of the first storey. A temporary wooden plate was also fixed to the strongbox for providing lateral restriction to the temporary side plates and the building model, as shown in Figure 3.15. For each acrylic plate, the lateral restriction was applied by two threaded rods drilled through the building floors; the threaded rods were supported by the temporary wooden plate. For sealing, thin foam tape sections were attached to the gap between the temporary plates and strongbox/footings. Importantly, after sand pouring, the strongbox was turned to its upward position (the back wall was installed). Thus, there is no access to remove the acrylic plates inside the first storey be-

cause of the plane-strain condition. To avoid the possible interaction between acrylic plates and the soil surface during tests, the plates were pulled up through the threaded rods, and hung onto the top aluminium plates, whose two sides were simply supported by a row of bolts (see Figures 3.15(b) and 3.16). Furthermore, a 2 mm gap was formed between the acrylic plates and the sides of the footings (foam tape sections were left on the footings), so that the acrylic plates would not affect the horizontal displacements of the footings. Therefore, using this system, the stiffening effect of the acrylic plates is eliminated and, during the tests, they only contributed as additional weight to the buildings.

3.6.2 Testing procedure

After the preparation of the sample, the package was mounted onto the centrifuge cradle, along with the setup of the cameras and the components of tunnel volume loss control system. Figures 3.12 and 3.16 show, respectively, the setup of the cameras and a centrifuge model with buried footings.

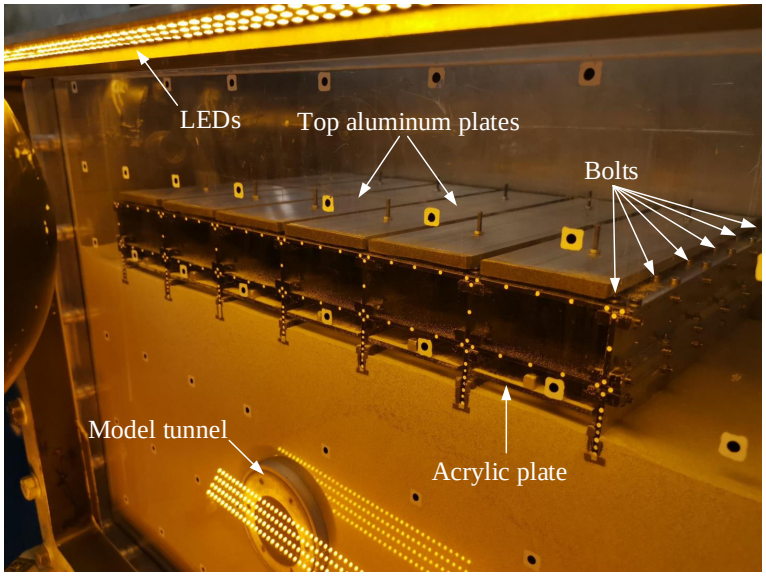


Fig. 3.16. Set up of the centrifuge model with buried footings

To compare experimental results against similar centrifuge tests using equivalent plate model structures (same type of sand and modelling procedure), the prototype scenario considered by Farrell (2010) was replicated. The diameter of the model tunnel and the gravity level used by

Farrell (2010) were D_t = 82 mm and 75 g. In this study, the diameter of the model tunnel is D_t = 90 mm. Therefore, to match the prototype scenario, the tests presented in this study were carried out at 75×82/90=68 g. Also note that, for the tests with different cover depths of the tunnel, different speeds of the centrifuge were adopted. For the tests with C = 117 mm, a speed of 191 rpm was adopted, whereas for the tests with C = 180 mm, 194 rpm was used (refer to Equations 3.1 and 3.2).

The testing procedure is summarised as follows. After the instruments were connected to the data acquisition system, the model was gradually spun to 68 g (at 5 g the solenoid valve was opened and the model tunnel was connected to the standpipe), and two stabilisation cycles were performed (going from 68 g to 15 g and back to 68 g); the stabilisation cycles are done to help achieve consistency between tests by reducing localised high-stress zones ('hung-up' particles), thereby achieving more uniformly stressed soil profiles. During the centrifuge spin-up, the stress imbalance between the pressures within the model tunnel and the surrounding soil, as well as the increase of the self-weight of the soil and the building, inevitably result in some non-uniformity of stress profiles around the tunnel and an increase of the soil density, however, the effects of these issues have been shown to be minimal (Zhou, 2014; Ritter et al., 2018). This issue is further evaluated in detail in Section 4.2. After stabilisation cycles, the solenoid valve was closed. Tunnel volume loss $V_{l,t}$ was then simulated by extracting water from the model tunnel in increments (0.1% to $V_{l,t}$ = 3%, 0.2% to $V_{l,t}$ = 5% and 0.5% to $V_{l,t}$ = 10%) up to a maximum $V_{l,t}$ of 10%. At each $V_{l,t}$ increment, digital images were taken, including both the soil and, when applicable, the model frame structure. The tunnel volume loss simulation process was terminated and the centrifuge was spun down. The data (including image and instruments) acquisition process was stopped.

3.7 Evaluation of building stiffness

3.7.1 Shear and bending stiffness

The relative soil-structure stiffness plays an important role in tunnel-structure interaction problems (refer to Section 2.2.3). Therefore, it is necessary to evaluate the real stiffness of the framed

building models in order to analyse their response to tunnelling. To evaluate the total stiffness of the long frame models while distinguishing between bending and shear contributions, multiple load-deflection ($P-\delta$) tests were performed at 1 g with varying constraint conditions, following the approach of Son and Cording (2007). The frame stiffness was evaluated at 1 g considering that the model building response (i.e. its stiffness) is not dependent on the centrifuge g-level given the assumption that building elements and node connections remain within the linear elastic range, which was confirmed by checking that 1 g loading test results agreed for tests done both before and after centrifuge tests.

In this research, simply supported 3-point and 4-point loading tests were carried out with varying spacings between the supports (see Figure 3.18(a)-(b)). The Zwick/Roell static materials testing system (Zwick/Roell 1484, 200 kN loading capacity, with both compression or pulling working modes) was used to load the framed building models. The frame was supported by two rollers at the designed supported points and was loaded by one or two rollers (for 3- or 4-point tests) at the column positions of the frame, as shown in Figure 3.17. A cantilever loading test was also carried out on model building F2t3b6L (raft) with one fixed-end and the free-end subjected to a concentrated load (see Figure 3.18(c)). Digital image analysis was used to measure the vertical and horizontal displacements of all wall-slab corners.

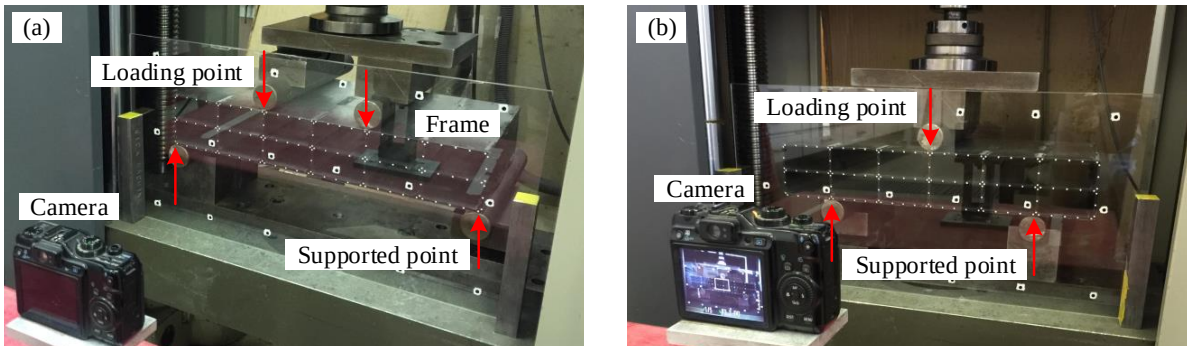
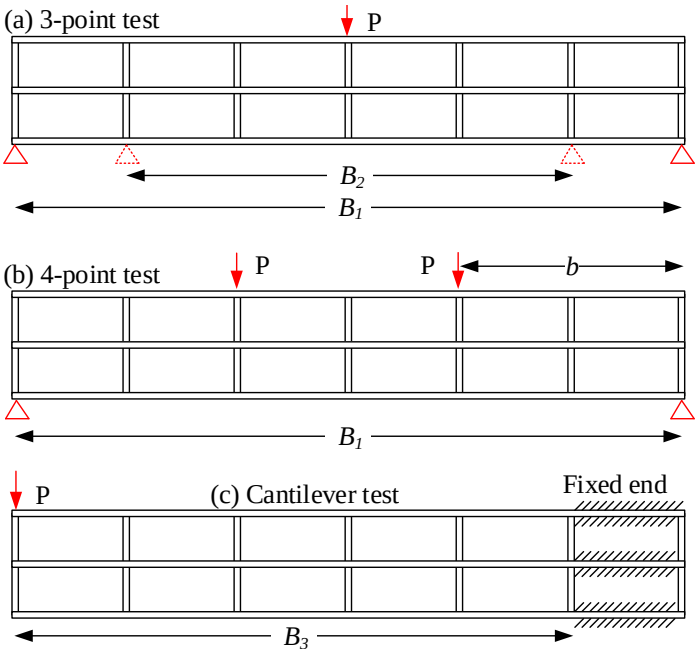


Fig. 3.17. Setup of the loading tests: (a) four-point test; (b) three-point test

The values of experimental bending (EI^*_{exp}) and shear ($GA^*_{s,exp}$) stiffness of the framed building models were inferred from the load-deflection tests using Timoshenko beam theory (see formulas in Figure 3.18). Results are summarised in Table 3.5, in which tests 1 and 2 refer to 3-point loading tests with a free span length of B_1 and B_2, respectively, test 3 is a 4-point



Timoshenko Beam Theory

(a) 3-point loading test:

$$\delta_{total} = \delta_{shear} + \delta_{bending} = \frac{PB}{4GA_s} + \frac{PB^3}{48EI}$$

$$\frac{\delta_{shear}}{\delta_{bending}} = \frac{12EI}{B^2GA_s} = 12F$$

(b) 4-point loading test:

$$\delta_{total} = \delta_{shear} + \delta_{bending} = \frac{Pb}{GA_s} + \frac{Pl(3B^2 - 4b^2)}{24EI}$$

$$\frac{\delta_{shear}}{\delta_{bending}} = \frac{24EI}{(3B^2 - 4b^2)GA_s} = \frac{24B^2}{(3B^2 - 4b^2)}F$$

(c) Cantilever beam test:

$$\delta_{total} = \delta_{shear} + \delta_{bending} = \frac{PB}{GA_s} + \frac{PB^3}{3EI}$$

$$\frac{\delta_{shear}}{\delta_{bending}} = \frac{3EI}{B^2GA_s} = 3F$$

Fig. 3.18. Configuration of experimental tests to evaluate building stiffness

loading test with a free span length of B_1, and test 4 is the cantilever test with a free deflection length of B_3. As shown in Table 3.5, for frame F2t3b6L on the raft, four tests were performed; tests 1 to 3 were done for frames F2t5b6L and F5t5b6L; tests 1 to 2 were carried out for frames F2t3b6L (footings) and F2t3b6LN; whereas only test 3 was performed for F2t3b3L because, for this frame, there is no central column.

The values of experimental bending and shear stiffness (EI^*_{exp} and $GA^*_{s,exp}$) were evaluated for the long frames F2t3b6L, F2t3b6LN, F2t5b6L and F5t5b6L by combining results from two of the load-deflection tests (i.e. two unknowns in two equations). Interestingly, the average experimental building bending stiffness, $EI^*_{exp,avg}$, was found to be about one-third of the theoretical bending stiffness $EI^*_{parallel}$ obtained using parallel axis theory (Equation 2.36) for all the welded frames (i.e. except for F2t3b6LN). This is certainly related to the manufacturing approach of the framed buildings (i.e. 60% welding with angles and plates). On the other hand, the value of $EI^*_{exp,avg}$ was found to be much greater than the theoretical bending stiffness EI^*_{sum} obtained using the algebraic sum method (Equation 2.37) for all the frames, indicating that the use of Equation 2.37 may significantly underestimate the real bending stiffness of the building. Only a 4-point load-deflection test was performed for the long frame F2t3b3L. Therefore, to

Table 3.5. Experimental results of bending and shear stiffness (per running meter) of building models (at model scale)

Frame	Tests (†)	EI^*_{exp} (Nm)	$EI^*_{exp,avg}$ (Nm)	$EI^*_{parallel}$ (Nm)	EI^*_{sum} (Nm)	$GA^*_{s,exp}$ (N/m)	$GA^*_{s,exp,avg}$ (N/m)	$\delta_{shear}/\delta_{bending}$
F2t3b6L (raft)	1 & 2	1.8E+05	1.9E+05	6.6E+05	5.7E+02	6.2E+05	6.2E+05	18.0
	1 & 3	2.1E+05				6.2E+05		
	1 & 4	2.0E+05				6.2E+05		
	2 & 3	2.1E+05				6.2E+05		
	2 & 4	2.0E+05				6.2E+05		
	3 & 4	1.8E+05				6.2E+05		
F2t3b6L (footings)	1 & 2	5.4E+04	-	1.6E+05	3.8E+02	3.6E+05	-	8.6
F2t3b6LN	1 & 2	3.4E+04	-	1.6E+05	3.8E+02	6.6E+05	-	3.3
F2t5b6L	1 & 2	2.9E+05	2.8E+05	9.7E+05	1.9E+03	1.9E+06	1.9E+06	8.2
	1 & 3	2.9E+05				1.9E+06		
	2 & 3	2.4E+05				1.9E+06		
F5t5b6L	1 & 2	3.1E+06	3.1E+06	8.5E+06	3.8E+03	3.9E+06	3.9E+06	44.5
	1 & 3	3.1E+06				3.9E+06		
	2 & 3	3.1E+06				3.9E+06		
F2t3b3L	3	1.9E+05	-	6.6E+05	5.7E+02	2.1E+05	-	51.7

(†) #1: 3-point bending with B_1; #2: 3-point bending with B_2; #3: 4-point bending with B_1; #4: cantilever.

calculate the shear stiffness of this frame from the single test, it was assumed that EI^*_{exp} of F2t3b3L was equal to the average EI^*_{exp} of F2t3b6L, which is reasonable given the identical element thickness and transverse width. No load-deflection tests were performed for the short frame F2t3b3S; it was assumed that the values of EI^*_{exp} and $GA^*_{s,exp}$ for the short frame matched those of the long frame F2t3b6L because of the identical element thickness and bay width.

Furthermore, Table 3.5 also reports the value of $\delta_{shear}/\delta_{bending}$ in the 3- or 4-point tests with a free span length of B_1. Interestingly, shear deflection dominates the total deformation for all the welded frames (except for F2t3b6LN), with a shear deflection ranging between about 8 and 50 times the bending deflection. This is also confirmed by the measured deformed shape of frame F2t3b6L in Figure 3.19. The axial strains within the top and bottom slabs were minimal (indicating minimal global bending deformation of the structure), whereas differential settlements between adjacent bays occurred due to the shear deformation of panels. Also, note that the ratio of δ_{shear} to $\delta_{bending}$ for F2t3b6LN is significantly smaller than the welded frame F2t3b6L with separate footings. This is due to the presence of the square bars at beam-column corners, which increases the rigidity of shearing (compared with the welded frame F2t3b6L). It is also reasonable to infer that for the frame with raft foundation assembled by nuts and bolts

(as with F2t3b6LN), the ratio of shear to bending deflection should also be smaller than the welded frame due to the presence of the square bars.

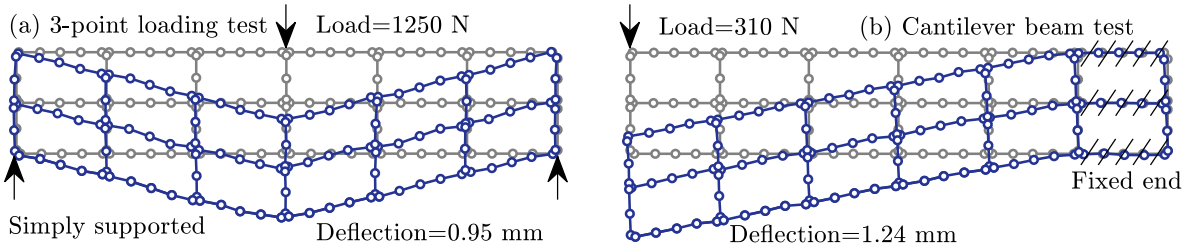


Fig. 3.19. Deformed shape of F2t3b6L on the raft in the load-deflection tests (scale factor: 50)

Finally, as displayed by Figure 3.19(a), the deflection in a shear-dominated building is the result of the changing of the sign of the shear deformations, rather than the absolute value of shear distortions. Figure 3.19(b) also illustrates that (neglecting the presence of the fixed bay), an approximately straight settlement profile (associated with $DR \approx 0$ and a given total tilt w') may be associated with large shear deformations if local tilt w is prevented (e.g. $\beta = S$ when $w = 0$, refer to Section 2.2.1 for the parameter definition). On the other hand, for a frame that is able to undergo tilt w, a straight settlement profile can indicate rigid body motion with no deformations (e.g. $\beta = 0$ when $S = w$).

3.7.2 Issue related to welding

Figure 3.20 shows the deformed shapes of frames F2t3b6L and F2t3b6LN with separate footings. The results of the loading tests highlighted an issue related to the manufacturing (welding) process of the model frame buildings, which in particular affected the separate footing model frames. The effect of this issue on the frames with raft foundations is considered negligible because the deformed shape of the frame on raft foundation in Figure 3.19(a) shows a symmetric response to vertical loading. To facilitate the description, the numbering of the panel/bay or footings is shown in Figure 3.22.

In Figure 3.20(a), the central footing (i.e. Foot-4 in Figure 3.22) of the welded frame F2t3b6L is shown to rotate in an anticlockwise direction, whereas ideally no rotation should occur for this footing in the case of a perfectly symmetric scenario; for example, consider the de-

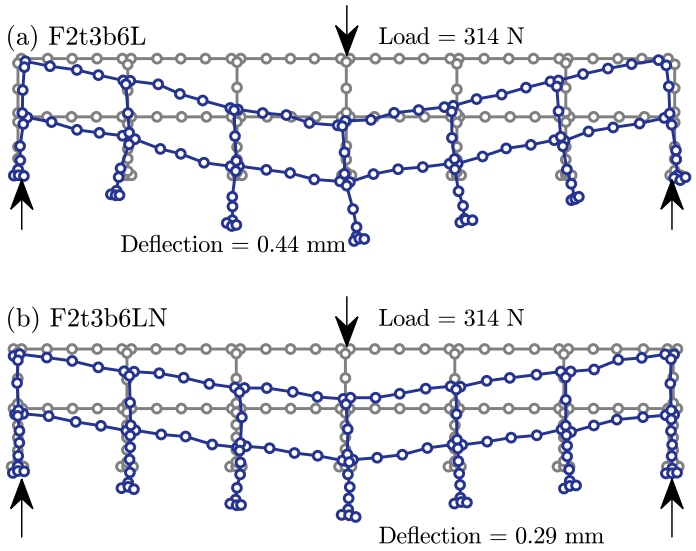


Fig. 3.20. Deformed shapes of the frames with separate footings in the loading tests (scale factor=100)

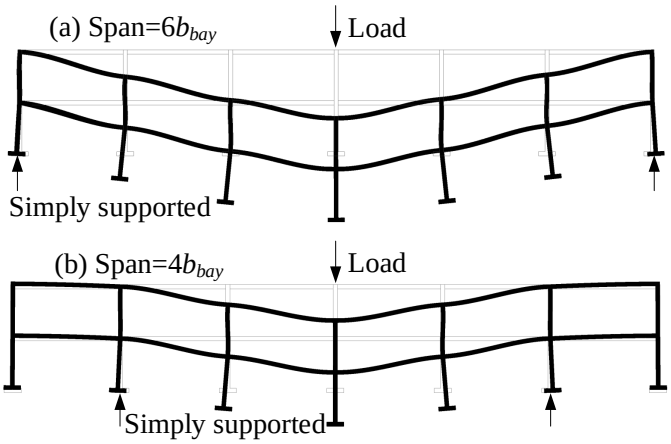


Fig. 3.21. Deformed shapes of the frames with rigid connections from finite element modelling

formed shape obtained from a finite element simulation of the frame loading in Figure 3.21 (the simulation was done in Autodesk Inventor by loading (standard 3- and 4-point) a rigidly connected frame model with the same dimension and configuration as the welded frame F2t3b6L). This experimental rotation occurred because the footing column is rigidly connected with the right-side beam/slab of the 1st storey (i.e. Panel-4 in Figure 3.22; this component is a single aluminium angle), whereas the column is welded to the left-side beam/slab of Bay-3. This result indicates that the welding of the connections between slabs and walls did not achieve a perfect

fixed-fixed condition (only the top of the slab-column connection is welded) and, consequently, the ground-floor columns did not respond entirely as they should for fixed-fixed connections. This issue mainly affected the horizontal displacements of the separate footings. As a result of this issue, the focus of analyses for the welded frame with separate footings is on settlements of the foundations and distortions of the panels. Finally, note that the left (Foot-1 to 3) and right (Foot-5 to 7) three footings moved outwards under loading due to the node rotation caused by the shear deformation; this behaviour is as expected (also observed in the finite element modelling in Figure 3.21), however each of these footings would also be affected by the issue discussed above.

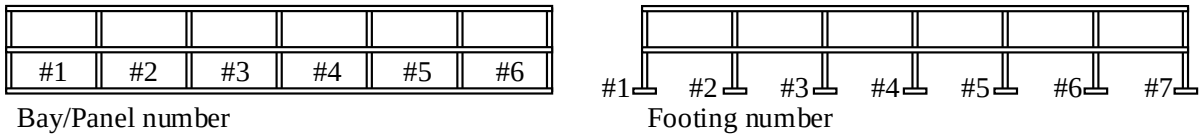


Fig. 3.22. Definition of bay, panel and footing number

The deformed shape of frame F2t3b6LN in Figure 3.20(b) shows a symmetric response of the frame to vertical loading. The result is similar to the finite element simulation result in Figure 3.21. Therefore, the horizontal displacements of the footings in the tests with frame F2t3b6LN are considered to be reliable and thus are selected for analysis.

3.7.3 Equivalent bending stiffness

To compare the results of the frames on raft foundations against the centrifuge data for plates from Farrell (2010); Farrell et al. (2014) (labelled as 'STR'), "pure" equivalent bending stiffness, $EI^*_{EB,eq}$, of building models were computed assuming rigid behaviour in shear (i.e. GA_s is infinite and pure bending deformations occur, as for an Euler-Bernoulli beam). The thicknesses of the corresponding equivalent plates t_{eq} and $\log_{10}\left(EI^*_{EB,eq}\right)$ are reported in Table 3.6 in prototype scale; the latter is provided because tunnel-structure interaction varies with relative stiffness parameters according to a semi-log scale (Potts and Addenbrooke, 1997; Mair, 2013).

From Table 3.6, it can be seen that the stiff frame F5t5b6L and the equivalent plate STR4 have nearly identical values of $EI^*_{EB,eq}$; however, the average pressure beneath model F5t5b6L

Table 3.6. Equivalent EI of structures on rafts and pressure beneath the foundations (prototype scale)

Structure	$EI^*_{EB,eq}$ (GNm)	t_{eq} (m)	$\log_{10}\left(EI^*_{EB,eq}\right)$ (Nm)	$EI^*_{exp,avg}$ (GNm)	$GA^*_{s,exp,avg}$ (MNm)	Pressure (kPa) SW / 2SW
F2t3b3L	1.48	0.63	9.17	-	14	19.4 / 38.8
F2t3b6L	3.24	0.82	9.51	60	42	22.8 / 45.6
F2t5b6L	9.31	1.17	9.97	88	130	34.8 / 69.6
F5t5b6L	21.11	1.54	10.32	970	270	73.5 / 147
STR2	0.32	0.38	8.50	-	-	9.9 /
STR3	2.46	0.75	9.40	-	-	19.8 /
STR4	19.69	1.50	10.30	-	-	39.7 /

Note: Pressure for SW and 2SW of F2t3b3S are 23.9 and 47.8 kPa, respectively

is almost twice that of STR4. Frame F2t3b6L has slightly larger values of $EI^*_{EB,eq}$ and pressure than plate STR3. The rather flexible plate STR2 is less stiff than the frame F2t3b3L. Finally, note that the variation of $\log_{10}\left(EI^*_{EB,eq}\right)$ values for all frames is rather limited. The context of these results will be clearer in later chapters (Chapters 4, 5) of the thesis where results from tunnel-building interaction tests are compared.

3.8 Summary

This chapter described the design and development of the experimental equipment and building models used for the centrifuge tests of this research. Firstly, the main components of the experimental package, developed by Zhou (2014) for performing greenfield tunnelling tests, were described in Section 3.2. The design and manufacturing process of the framed building models were detailed in Section 3.3. This was followed by the description of the data acquisition methods adopted in this research (Section 3.4). Then, the centrifuge testing plan and procedures were described in, respectively, Sections 3.5 and 3.6. Finally, building stiffness was evaluated by performing a series of loading tests at 1 g (Section 3.7).

Chapter 4

Response of buildings on raft foundations

Tunnels are often constructed beneath congested urban areas to satisfy needs for new infrastructure. Associated with these underground construction activities is the requirement to evaluate the potential for damage to existing buildings that are subjected to tunnelling-induced ground deformations.

The response of buildings to tunnelling has been investigated extensively. While several studies have indicated the importance of considering realistic (framed) building characteristics (Boone, 1996; Boldini et al., 2018; Fu et al., 2018; Franza and DeJong, 2019; Son, 2015), equivalent beam or plate models are still generally adopted (Franzius et al., 2006; Pickhaver et al., 2010; Maleki et al., 2011; Namazi and Mohamad, 2013; Farrell et al., 2014; Bilotta et al., 2017; Franza and Marshall, 2018). This simplification involves uncertainties that have not yet been sufficiently investigated for framed buildings. When estimating the total structure stiffness, most researchers have adopted a pure bending stiffness (Franzius et al., 2006; Goh and Mair, 2014; Haji et al., 2018) despite the evidence that shear flexibility can have an important role (Potts and Addenbrooke, 1997; Finno et al., 2005). Also, Franza et al. (2020a) highlighted that bending and shear deformation modes of equivalent solids have not always been well distinguished because of the focus on the structure settlement profile. Finally, the local deformations of infill walls in frames is potentially not well described by equivalent beams or plates (Goh and Mair, 2014; Boldini et al., 2018).

The aim of this chapter is to investigate, through reduced-scale centrifuge tests, how a

framed building on a raft foundation responds to tunnelling-induced ground movements in terms of foundation and superstructure displacements. The chapter includes results from 24 plane-strain geotechnical centrifuge tests designed to model tunnelling-induced ground displacements in dry sand and its effect on multi-storey framed buildings with different characteristics and locations. Soil and building displacements were measured and, subsequently, used to relate bay and panel distortions to greenfield settlements. The response to tunnelling of framed buildings on raft foundations are also compared against the results obtained from the scenario in which equivalent plates were used. Limitations associated with the simplification of frames as equivalent isotropic plates are illustrated.

4.1 Considered tests

Five framed building models on raft foundations, including four long buildings (F5t5b6L, F2t5b6L, F2t3b6L and F2t3b3L) and one short building (F2t3b3S), are considered in this chapter (refer to Section 3.3 for details of the models). In particular, the model frames are labelled based on their structural characteristics as either FxtybzS or FxtybzL: x indicates the number of storeys, y the thickness in mm of the structural elements, z the number of bays, and the suffix L and S are used for transversely long and short structures, respectively. This chapter presents results from 24 centrifuge tests including 2 greenfield (GF) tests and 22 framed buildings (on raft foundations) tests, as shown in Figure 4.1. For a given frame model, the relative density of the sand (I_d), the eccentricity (e) of the building with respect to the tunnel, and the building self-weight (SW: standard self-weight; 2SW: doubled self-weight) were varied in the experiments (see detail in Figure 4.1). For each of the long frames (label ending in "L"), a total of 4 tests were included, whereas, for short frame F2t3b3S, 6 tests were presented. All tests have the same tunnel cover depth C = 117 mm (8.0 m at prototype).

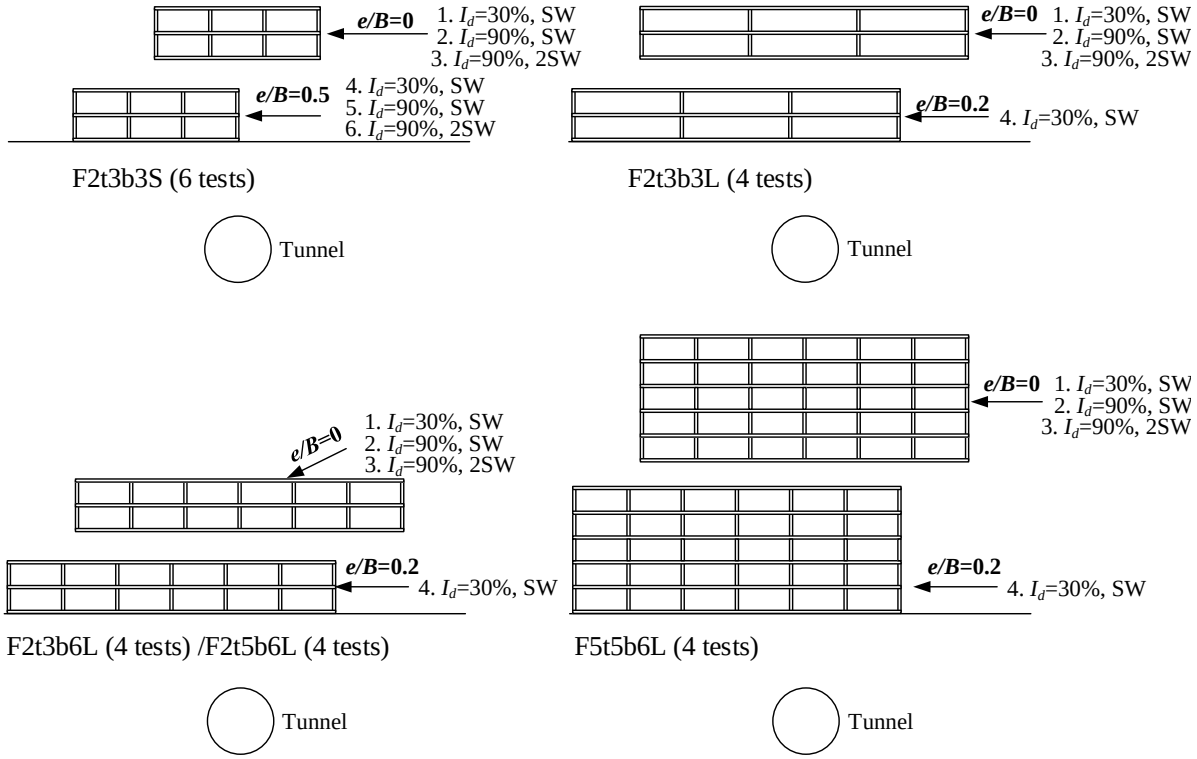


Fig. 4.1. Considered tests with framed building models on raft foundations

Apart from the soil density, building eccentricity and weight, the effects of the number of storeys (n), thickness of building elements (t), building transverse length (B) and bay width (b_{bay}) are also investigated.

4.2 Model spin-up

4.2.1 Effect of the building presence on soil movements

As illustrated in Chapter 3, model preparation was done at 1 g. Then, the centrifuge was spun up to the targeted gravity level (68 g). During spin-up, the self-weight of the soil and the building model (in tunnel-building interaction tests) would inevitably compact the soil, thereby changing the soil uniformity.

Figure 4.2 presents contours of horizontal (U_x) and vertical (U_z) displacements (normalised by the tunnel diameter D_t) of the soil after centrifuge spin-up (including stabilisation cycles) in selected tests, all in dense soil. In this thesis, positive horizontal and vertical displacements are oriented, respectively, towards the right and downwards (refer to Figure 2.11), unless otherwise indicated. In general, Figure 4.2(a) shows that a greater greenfield soil settlement is observed for the soil in a shallower region due to the accumulation of the settlement of the soil. Furthermore, settlement of the surface soil in the centre of the strongbox (above the tunnel) is larger than that at the side regions. Interestingly, soil directly above the tunnel crown has a smaller settlement than the soil in other regions with an identical depth. This is because the difference in the density between soil and the fluid in the model tunnel results in the buoyancy of the model tunnel. To mitigate this effect, a heavier liquid may be used in future tests, for instance, Sodium PolyTungstate. However, in order to compare the results against the data from Farrell et al. (2014), who used water for the model tunnel, this research adopted the same type of liquid (i.e. water). In the horizontal direction, tunnel ovalisation was observed due to the greater horizontal stress of the fluid within the model tunnel compared to the soil lateral stress. These results are consistent with previous research (Zhou, 2014; Ritter, 2018; Song and Marshall, 2020).

Next, the impact of the presence of the building is assessed. In general, Figure 4.2(b)-(c) shows that the effect of the building presence on soil settlements is not significant. An eccentric

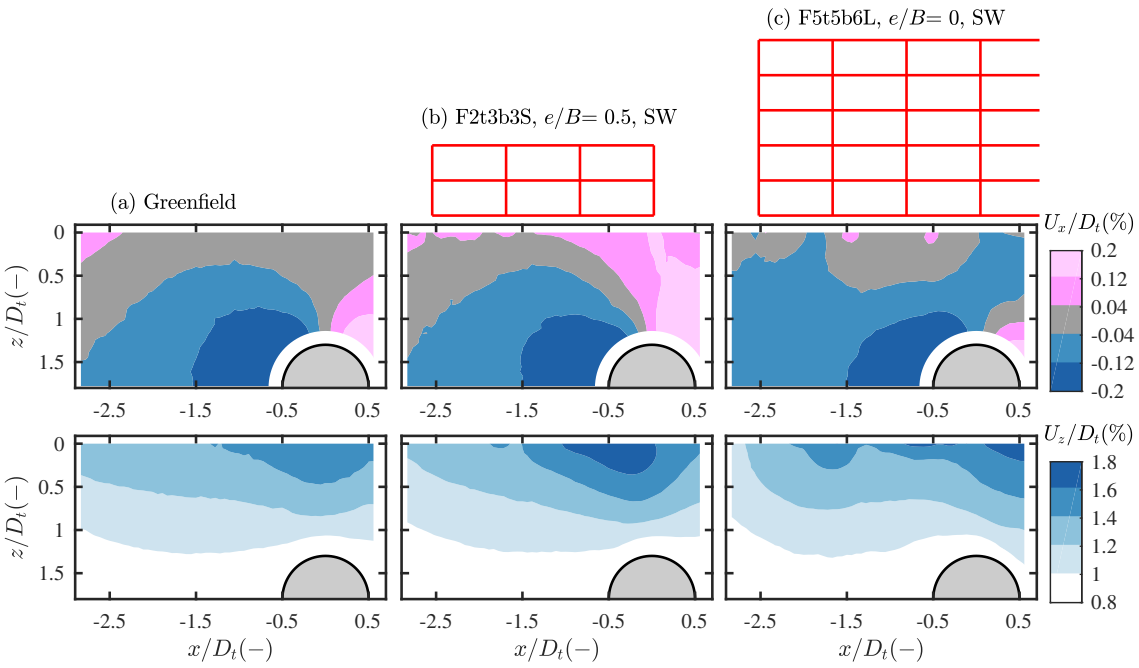


Fig. 4.2. Horizontal U_x and vertical U_z displacements of the dense (I_d = 90%) soil in selected tests after centrifuge spin-up (data outside the contour thresholds were set equal to the closest limit value)

building (F2t3b3S with $e/B = 0.5$) mainly increased the settlement of the soil directly above the tunnel, whereas a central heavy building (F5t5b6L with $e/B = 0$) slightly increased the overall magnitude of the settlement. In the horizontal direction, Figure 4.2(b) shows that an eccentric structure also dragged the soil toward the right due to the freedom of tilt (the settlement of the soil in the centre is the greatest). Consequently, the soil directly beneath the building right side moved toward the right due to the impact of the eccentric structure F2t3b3S.

For both greenfield scenario and the tests involving the buildings in dense soil (I_d = 90%), the soil densification effect resulted in an average increase of soil density $\Delta I_d \approx$ 1.0-1.5% (calculated based on the average settlement of the surface soil). For loose soil tests, an average increase of soil density $\Delta I_d \approx$ 1.5-2.0% was estimated. Overall, during centrifuge spin-up, the effects of tunnel buoyancy and ovalisation, as well as the sand densification phenomenon on the interpretation of the results are judged acceptable considering that all the models would suffer similar effects.

4.2.2 Response of the foundations

During centrifuge spin-up, the deflection of the building foundation can be induced by the differential soil settlements and the redistribution of building self-weight. Figure 4.3 presents the surface soil and the foundation settlements in selected tests.

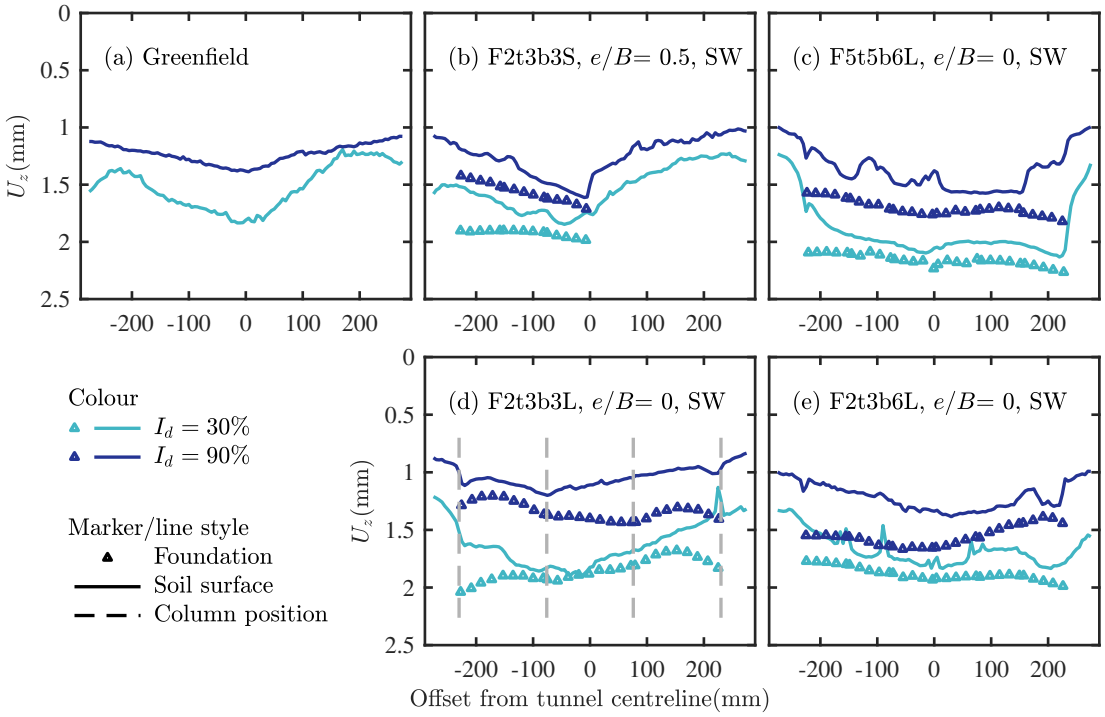


Fig. 4.3. Settlements of the rafts and surface soil in selected tests during centrifuge spin-up from 1 to 68 g

First, some comments on the measurement error are presented. Figure 4.3(b)-(e) shows that the building foundations settled more than the underlying soil, which is not possible for a perfect plane-strain condition. This issue was also observed in previous similar experiments (Farrell, 2010; Ritter, 2018), and can be explained in detail using Figure 4.4.

One possible reason for this discrepancy is due to the adopted image-based displacement measurement technique. The displacements of the foundation were measured by tracking the movements of the white dots painted on the front surface of the foundation, whereas soil displacement was obtained by tracking a certain size of the soil patches (around 4 × 4 mm was adopted). Therefore, the measurements for the soil and foundation are not at the same level

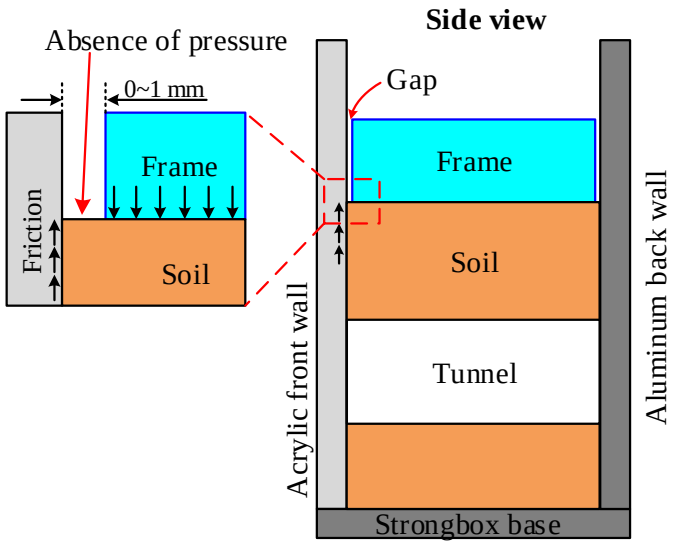


Fig. 4.4. Illustration of the boundary effect

(i.e. not perfectly at the soil-structure interface). If the soil patches near the surface level were compressed, the measured vertical displacements of their centroids would underestimate the settlements of the soil at the surface. On the other hand, to fit the strongbox, the longitudinal length of the framed building model is slightly smaller than the strongbox dimension. As shown in Figure 4.4, a small gap exists between the front face of the frame and the inner surface of the acrylic wall. Therefore, the soil directly against the acrylic wall near the surface was not subjected to the pressure from the foundation. Furthermore, the sand also experienced boundary effects described in Section 3.1.2 (i.e. the reduction effect of friction between the sand and acrylic wall on the soil displacements). Consequently, it is not surprising that the measured soil vertical displacements are smaller than the foundation settlements in Figure 4.4 and other figures presented in the thesis. However, it is reasonable to assume that the real settlement of the soil is equal to the foundation settlement where the measured soil vertical displacements are smaller than the foundation settlement.

Surface soil and foundation settlements in Figure 4.3 are now discussed. As expected, the settlements of the surface and the foundations in loose soil tests are greater than in dense soil cases. Moreover, the average settlements of the foundations are, respectively, around 1.5 and 2.0 mm in dense and loose soil tests, regardless of the building weight and configuration. This means that the presence of the building has a minor effect on the ground settlement. Finally, also

note that hogging zones are observed in the two ends of the settlement profiles of the long frames (F2t3b3L, F2t3b6L and F5t5b6L), particularly for frame F2t3b3L in Figure 4.3(d), which has a wider bay (column positions shown in the figure). This is due to the re-balancing of the pressure beneath the raft foundation during centrifuge spin-up. Superstructure weight increased with g-level. To satisfy the stress equilibrium, the support pressure from the ground also increased, thereby causing the deflection of the foundation, as shown in Figure 4.5. However, based on the consistent frame loading test results pre- and post- centrifuge testing (not reported in this thesis), these deflections were all elastic and would not affect results. In reality, the deflection of the foundation also exists due to the self-weight of the superstructure. Nevertheless, to isolate the effect of tunnelling process on the structural distortion and ground movements, the final state of the model after reaching the targeted g-level is taken as the reference (i.e. initial condition).

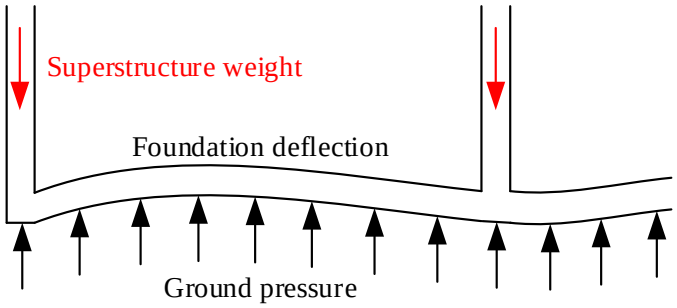


Fig. 4.5. Illustration of the foundation deflection during centrifuge spin-up

4.3 Tunnel pressure

The ground reaction curves, which describe the change of tunnel pressure at tunnel axis level against tunnel volume loss in selected tests, are presented in Figure 4.6. Data from the dense soil tests are summarised in Figure 4.6(a) and results from loose soil tests are displayed in (b).

Figure 4.6 shows that there is a steep drop of tunnel pressure over a range of low tunnel volume loss (< 1%) for all tunnelling cases. This is due to soil strength mobilisation combined with soil arching that occurs for shallow tunnelling in sand (Iglesia et al., 2014; Franza et al., 2019). Furthermore, the decreasing rate in dense soil tests is notably greater than in loose soil cases. This is because the higher the density, the greater the peak friction angle, and thus the

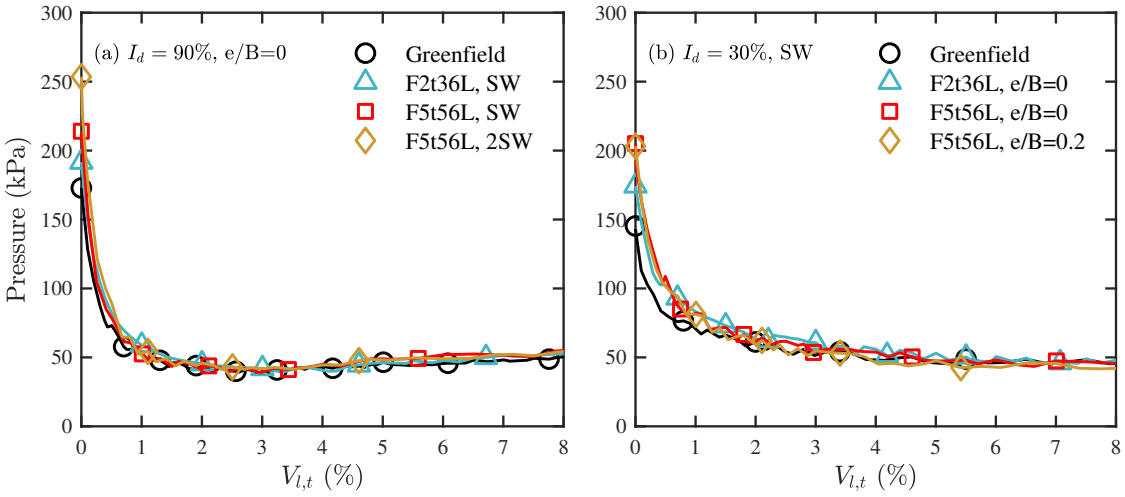


Fig. 4.6. Tunnel pressure at axis level against tunnel volume loss in selected tests

smaller the arch initially formed (Iglesia et al., 2014; Franza et al., 2019). For dense soil, the pressure reached the lowest point at $V_{l,t}$ = 3-4%, and increased steadily over higher values of $V_{l,t}$. However, the trend of the ground reaction curves in loose soil tests is continuously decreasing throughout the investigated tunnel volume loss, despite the decreasing rate decreased with the tunnel volume loss. Interestingly, for both density tests, the presence of the building model primarily affected the initial pressure (depending on the structural weight) and had a minor effect on the ground reaction.

4.4 Frame foundation displacements

4.4.1 Comparison against equivalent plates

In Section 3.7, the stiffness of the framed buildings was experimentally assessed, with the results summarised in Table 3.5. To compare these frame results against the centrifuge data for plates from Farrell (2010); Farrell et al. (2014) (labelled as 'STR'), "pure" equivalent bending stiffness, $EI^*_{EB,eq}$, of building models and the thicknesses of the corresponding equivalent plates t_{eq} are reported in Table 3.6 in prototype scale. To facilitate the comparison, results of the thicknesses of the corresponding equivalent plates are also illustrated in Figure 4.7. Based on Figure 4.7, data from frames F5t5b6L, F2t3b6L are compared against the results of plates

STR4 and STR3, because they have similar equivalent bending stiffness $EI^*_{EB,eq}$. Note that the most flexible frame F2t3b3L is still stiffer than plate STR2.

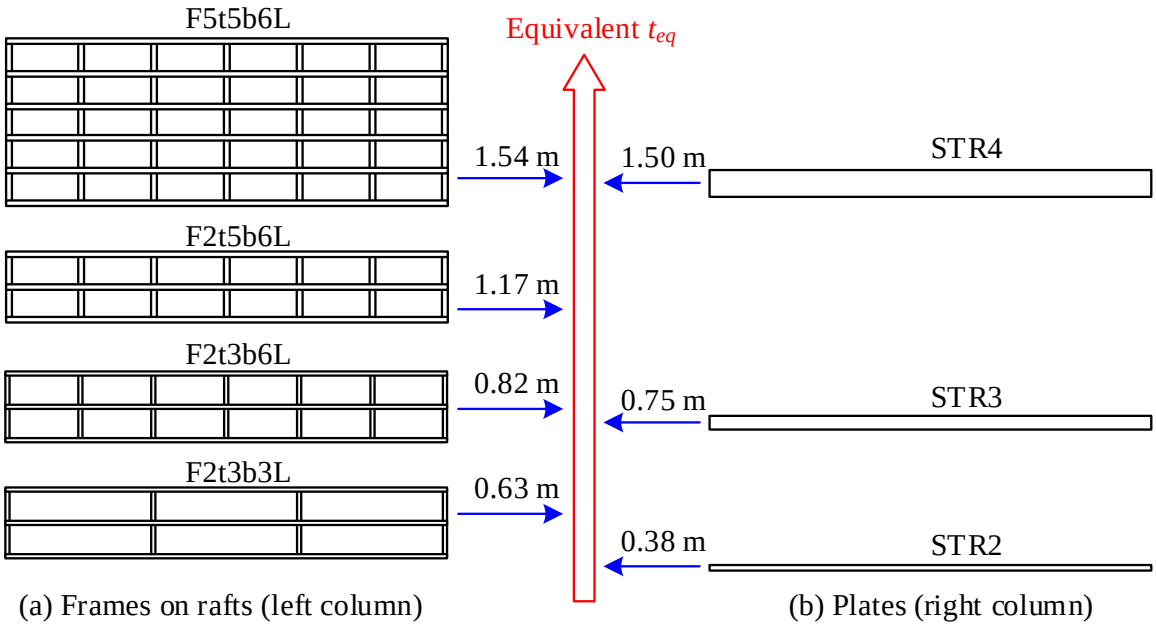


Fig. 4.7. Comparison of t_{eq} (prototype scale) between framed buildings on raft foundations and plates from Farrell (2010)

The settlements, U_z, and the horizontal displacements, U_x, of the foundations of the model framed buildings and equivalent plates at a tunnel volume loss $V_{l,t}$ = 1% are presented in Figure 4.8 along with the greenfield displacements at the surface. The greenfield (GF) settlements between the two data sets (GF-Xu is the new data in Figure 4.8(a); GF-Farrell in Figure 4.8(b) is from Farrell (2010)) are sufficiently consistent to allow comparison of the tunnel-structure interaction outcomes. It was found that (not reported in this thesis), after about $V_{l,t}$ = 3%, differences between the greenfield data became greater (related to the size of the centrifuge, see Appendix A3), hence comparisons are not made outside of this range of $V_{l,t}$.

In terms of minimum and maximum structure settlements, frames and plates follow the same principle: 1) the lower the total stiffness (depending on t_{eq}) of the structure, the greater the maximum settlement; and 2) the stiffer the structure, the greater the minimum settlement. However, the self-weight (discussed later) also has a role. Both the frames and plates responded rigidly to tunnelling in the horizontal direction, resulting in very small differential horizontal displacements in the frame foundation slabs and plates, as shown in Figure 4.8(c)-(d).

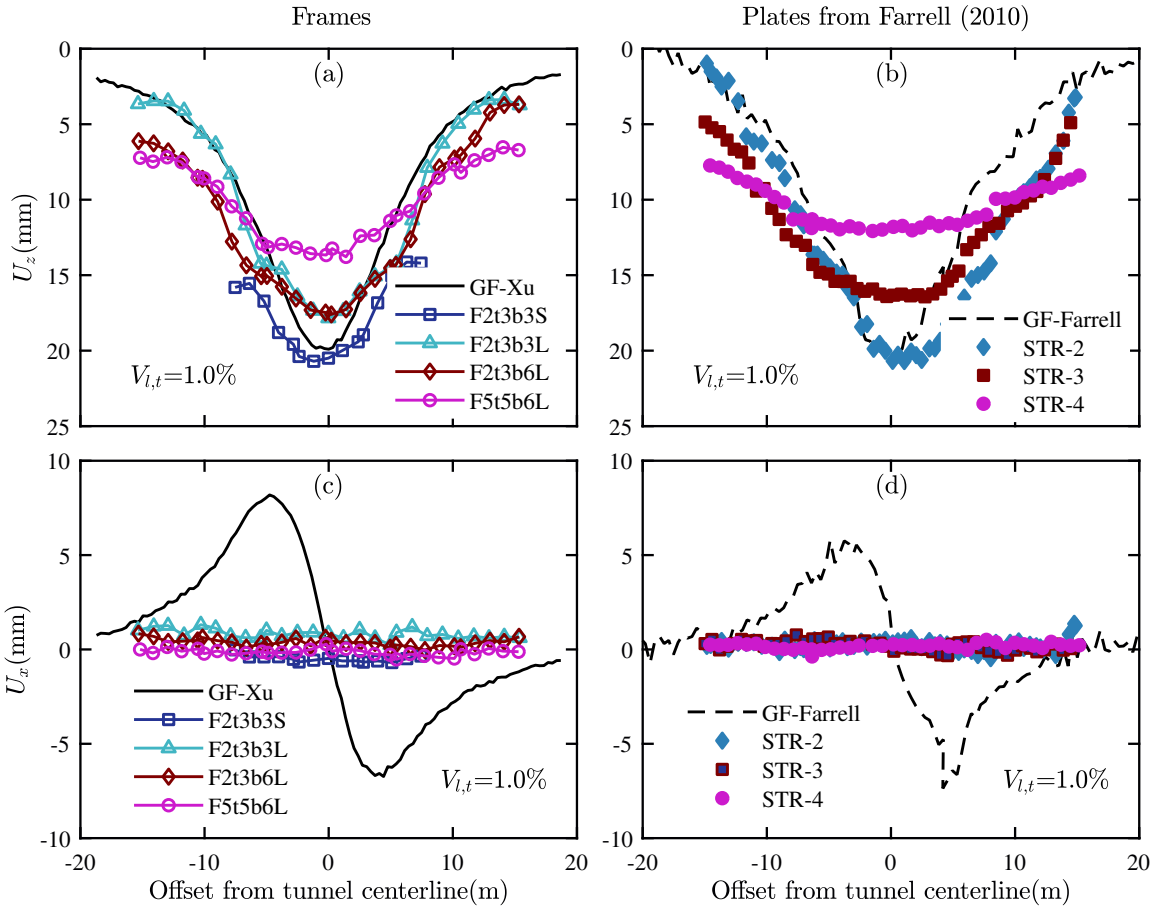


Fig. 4.8. Displacements of model frame foundations and equivalent plates for $e/B = 0$ and $V_{l,t} = 1\%$

Figure 4.8 indicates that all frames have both sagging and hogging regions, whereas the plates mostly undergo a sagging deformation mode, regardless of their stiffness and transverse width. On the other hand, for the structures with similar equivalent bending stiffness, $EI^*_{EB,eq}$ (refer to Table 3.6 and Figure 4.7), framed buildings tend to have a more flexible response to tunnelling than equivalent plates (compare frame F5t5b6L against plate STR-4, and frame F2t3b6L against plate STR-3). This point can also be demonstrated by comparing frame F2t3b3L and plate STR-2 (the former is stiffer than the latter), in which the frame not only has a large deflection ratio in the sagging zone, but also displays significant hogging zones. This mechanism is likely due to the role of the shear flexibility being negligible ($1/GA_s \approx 0$) for the equivalent isotropic plates. Similar phenomena for frames have also been observed in numeri-

cal studies (e.g. Boldini et al. (2018)), whereas Franza et al. (2020c) discussed how equivalent Euler-Bernoulli beams and structures that are rigid in shear tend to undergo singular sagging or hogging settlement profiles for central and eccentric tunnels, respectively.

These observations indicate that, although frames F5t5b6L and F2t3b6L have similar values of $EI_{EB,eq}$ as plates STR-4 and STR-3, respectively, the structural characteristics (i.e. those producing a shear-dominated or a bending-dominated deformation behaviour) have a significant effect on the resulting soil-structure interactions. The presented data therefore confirm that the tunnelling-induced settlement profile depends on the structure configuration; furthermore, the use of equivalent pure bending $EI_{EB,eq}$ representations of building behaviour may lead to significant errors for some tunnel-building interaction cases.

4.4.2 Effect of building weight

To evaluate the impact of structure weight, the vertical (U_z) and horizontal (U_x) displacements of the foundations of the model framed buildings and soil beneath the foundations are presented in Figure 4.9 at $V_{l,t} = 2\%$ for a selection of centrifuge tests, together with greenfield test results. Results are compared using tunnel volume loss $V_{l,t}$ rather than soil volume loss $V_{l,s}$ (calculated as the integration of surface settlements) because $V_{l,t}$ is a more generally used parameter that relates to the performance of tunnelling operations. In Figure 4.9, markers are used for foundation displacements, and lines are used for surface soil displacements in greenfield and framed building tests. The data can be used to distinguish a gap forming between the soil and foundation in some tests; to better illustrate this feature, the maximum gap height is plotted against tunnel volume loss $V_{l,t}$ in Figure 4.10. In some cases, the data indicate that the foundations settled slightly more than the soil beneath them at the edges of the building models. This inconsistency was also observed in Farrell (2010) and Ritter et al. (2018)), and has been explained in Section 4.1 (because the front of the frames was not immediately against the inner face of the acrylic wall). As a result, a negative gap height in Figure 4.10 relates to measurement errors.

First, settlement profiles in Figure 4.9 are considered. The dense sand data (dark colour) in Figure 4.9 can be used to demonstrate the effect of building weight: an increase of weight increases the distortions of centrally located structures (see Figure 4.9(a), (c)-(f)), and decreases

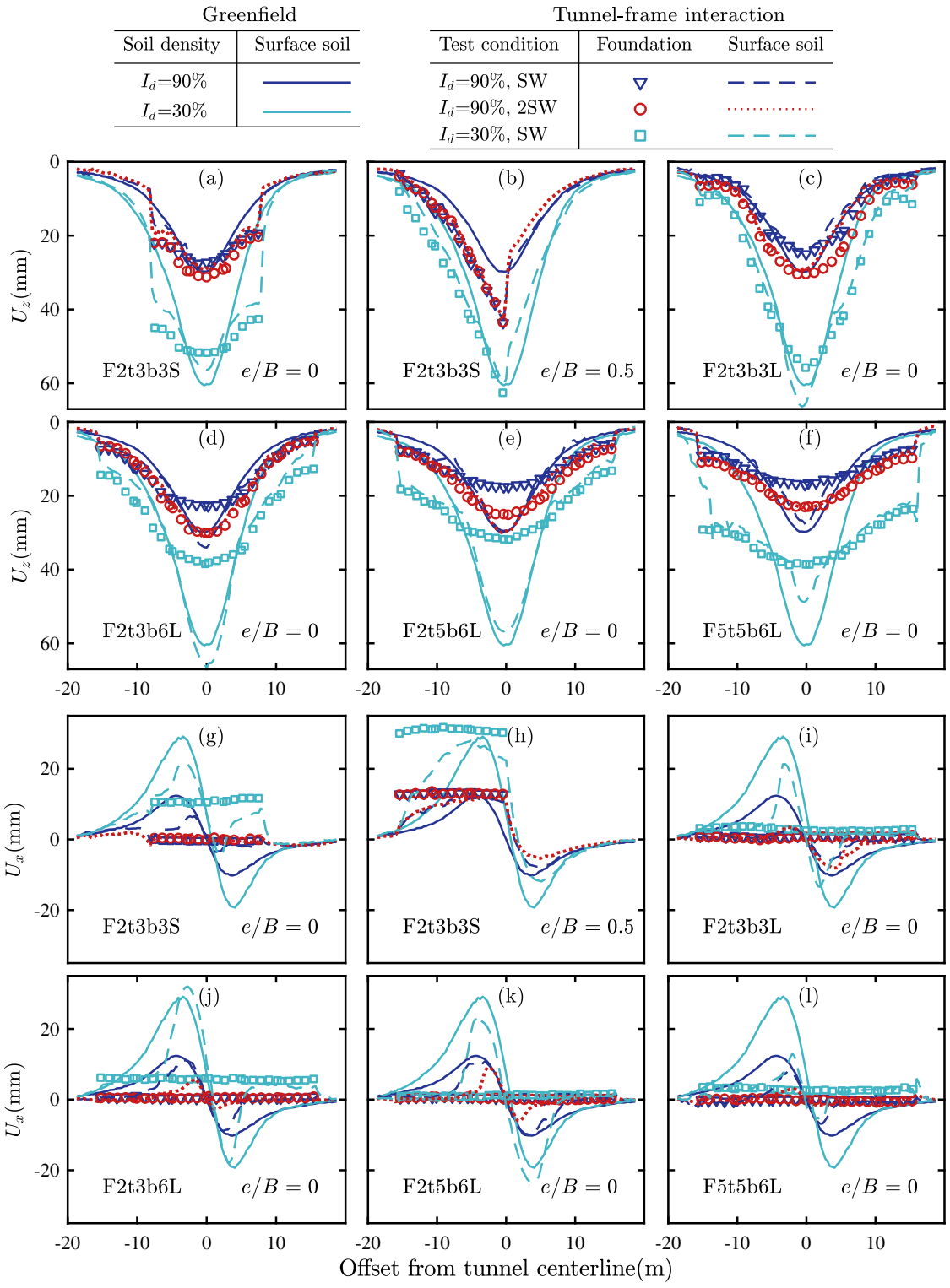


Fig. 4.9. Displacement of model frame foundations and underlying soil at $V_{l,t}$ =2 %

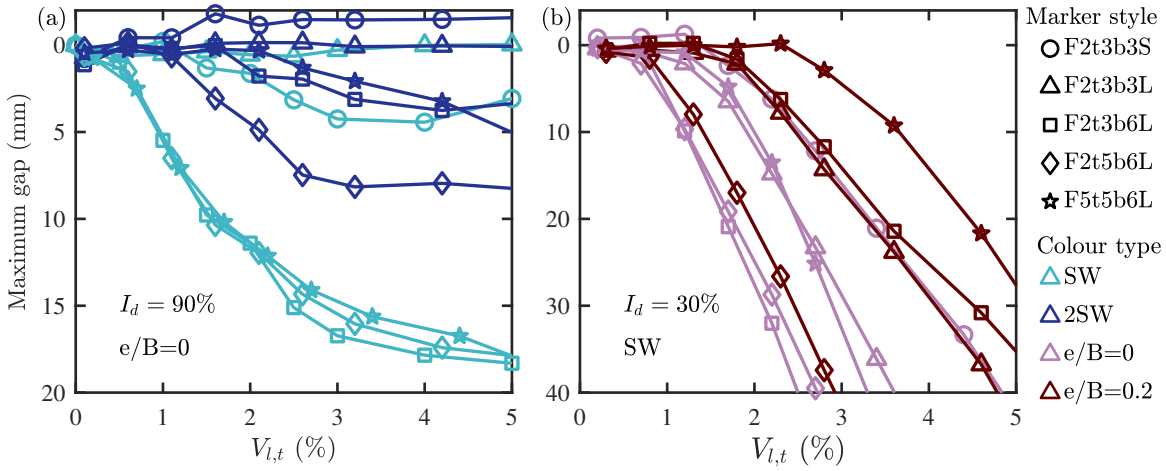


Fig. 4.10. Maximum gap height against tunnel volume loss

the size of the gap formed between the soil and foundation, whereas the effect of weight on settlement at the edges of the buildings is minor. Note that, at $V_{l,t} = 2\%$, a gap was not observed beneath the centrally located structures with double weight 2SW, except for frame F2t5b6L, whereas only frame F2t3b3L did not show a gap for standard weight SW. Importantly, for the short frame F2t3b3S, the influence of building weight was lower for the eccentric case $e/B = 0.5$ than for the central case $e/B = 0$.

An interesting comparison can also be made between tests with frame F2t5b6L with 2SW and frame F5t5b6L with SW because they have a similar pressure acting beneath the foundations, but different stiffness (compare dark circles in Figure 4.9(e) with dark triangles in Figure 4.9(f)). As expected, a larger deflection ratio and smaller gap (quantified in Figure 4.10(a)) are observed in the former test since the frame has a smaller stiffness.

In Figure 4.9(g)-(l), all frames with $e/B = 0$ experienced negligible horizontal displacements (except for the short frame in Figure 4.9(g) on loose soil) and the restriction provided by the foundation roughness and building weight acted to reduce horizontal soil displacements. When the building weight was doubled (i.e. 2SW compared to SW), the restraint provided by the foundations to the underlying soil was increased and horizontal soil displacements decreased. In the tests where nearly no gap was observed, surface horizontal soil displacements were found to be very small or negligible (e.g. test 2SW in Figure 4.9(j)-(l)).

4.4.3 Effect of soil relative density

First, the effect of soil relative density is discussed using the data in Figure 4.9 for a constant tunnel volume loss $V_{l,t} = 2\%$. Because of the different volumetric response of the dense and loose sands to tunnelling induced soil shear strains, the greenfield surface settlements in the loose sand are much higher than in the dense sand (also refer to the tunnel versus soil volume loss data in Figure 4.13). This caused the frames to experience larger average and differential settlements in the loose sand tests compared to the dense sand. Relative density also affected the size of gap that formed at the soil-foundation interface; for example see Figure 4.10 for $V_{l,t} = 2\%$, where larger gaps formed for $I_d = 30\%$ because of the higher levels of ground movement near the surface.

To evaluate the soil-structure interaction for settlement troughs of equal volume, results are also compared for a given soil volume loss $V_{l,s} = 1.6\%$ at the surface. First, trough characteristics of the greenfield settlements for $I_d = 30$ and 90% are listed in Table 4.1, which were obtained by fitting modified Gaussian curves (Vorster et al., 2005) to the settlement data. The settlement trough for loose soil is slightly wider (a larger i and K) than in dense sand, although the maximum settlement values are close. The wider greenfield settlement curve for $I_d = 30\%$ should result in lower differential settlements and distortion levels of a building than the dense soil $I_d = 90\%$. The settlements of central building foundations ($e/B = 0$) with standard weight (SW) are presented in Figure 4.11 for $V_{l,s} = 1.6\%$ (calculated using soil settlements beneath the building foundations). Except for the most flexible frame F2t3b3L, a greater maximum settlement is observed for the building foundations in loose soil. Differential settlements along corresponding building foundations are qualitatively similar for the given magnitude of soil volume losses; a more direct assessment of building deformations is given later (Section 4.7.1) by considering angular distortions of the buildings.

Table 4.1. Greenfield settlement trough characteristics (prototype scale)

I_d (%)	$V_{l,t}$ (%)	$V_{l,s}$ (%)	$U_{z,max}$ (mm)	i (m)	K
30	1	1.6	31.68	3.79	0.344
90	2.5	1.6	32.78	3.32	0.302

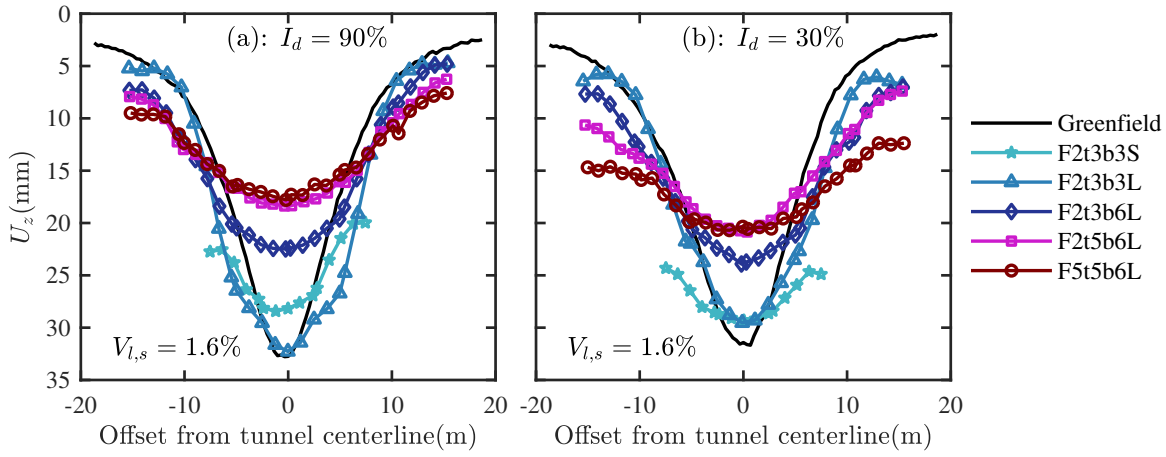


Fig. 4.11. Displacements of selected model foundations ($e/B = 0$, SW) at identical $V_{l,s} = 1.6\%$: (a) $I_d = 90\%$ and (b) $I_d = 30\%$

4.4.4 Effect of relative tunnel-building location

The data in Figure 4.9(a) and (b), and loose soil data in Figure 4.9(c)-(f) and Figure 4.12 can be used to study the effect of relative tunnel-building location. Results indicate that the eccentric short frames in Figure 4.9(b) have a smaller relative deflection Δ than the central frames in Figure 4.9(a) because of building tilt w for the eccentric cases. This effect of e/B on relative deflections was not as significant for the long frames (compare Figure 4.12 against Figure 4.9(c)-(f)), partly because the maximum eccentricity e/B achievable in the centrifuge tests for the long frames was 0.2, compared to 0.5 for the short frames. However, Figure 4.12(a)-(b) shows a greater embedment of the building right corner into the soil surface than the cases of central structures; this was induced by a rigid body rotation (tilt) of the building model towards the tunnel, which was prevented in the $e/B = 0$ tests.

At the soil-structure interface, the increase of building eccentricity e/B reduced the size of the gap formed beneath the foundation (see also Figure 4.10(b)), in agreement with the trends highlighted by Franza and DeJong (2019). The short frames with normalised eccentricity $e/B = 0.5$ show horizontal movements that are approximately equal to the maximum greenfield horizontal displacement (see Figure 4.9(h)), whereas for the eccentric long frames with $e/B = 0.2$ (see Figure 4.12), horizontal movements of the foundations were minimal (similar to the results in Figure 4.9). The horizontal displacements of the soil beneath the short frame

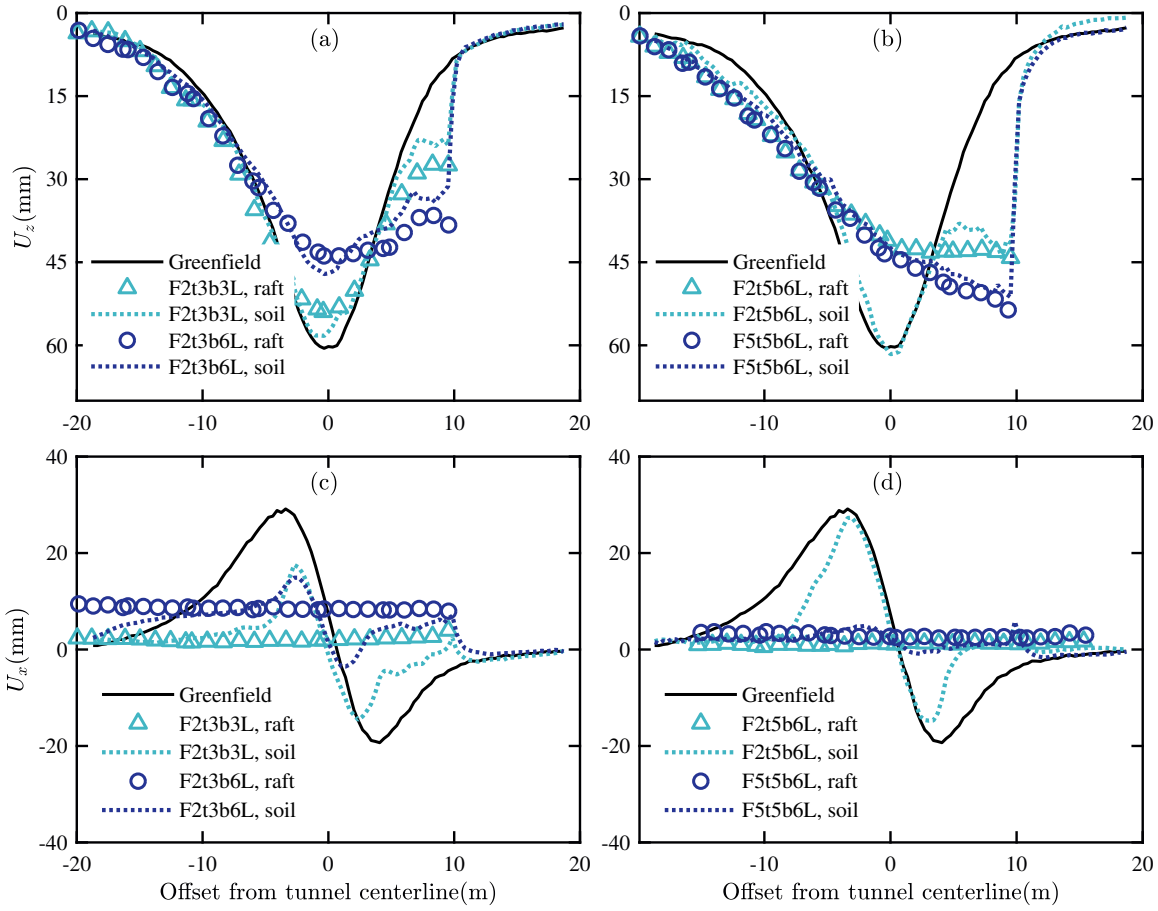


Fig. 4.12. Displacement of model frame foundations and underlying soil at $V_{l,t}$ = 2% with e/B = 0.2 in loose soil

with e/B = 0.5 are generally greater than greenfield ground displacements; this is due to the compliance of the soil-foundation interface (see Figure 4.9(h)). The horizontal displacements of the soil beneath the long frames with e/B = 0.2 also decreased compared with the central frame tests (due to the decrease of the size of the gap at the soil-foundation interface). Interestingly, for eccentric long frame tests (see Figure 4.12(c)-(d)), the horizontal displacements of soil beneath frame F2t5b6L are the greatest because of the large gap that formed beneath the foundation (see also Figure 4.10(b)).

4.5 Soil volume losses

4.5.1 Soil volume losses against tunnel volume losses

Under drained soil conditions, because of their contractive/dilative response to shearing, the relationship between soil volume loss $V_{l,s}$ (given by the integration of the soil settlements at a given depth) and tunnel volume loss $V_{l,t}$ (the ground loss at the tunnel boundary) is not 1:1 (as would be the case in undrained soils). It could be argued that the variation of soil volume loss $V_{l,s}$ at the surface (given by the integration of the surface settlements) with building self-weight may impact the structure distortion. Engineers tasked with designing excavations need to predict/assume reasonable values of soil volume losses given an expected level of tunnel volume loss for the applied tunnelling operations (Franza et al., 2019).

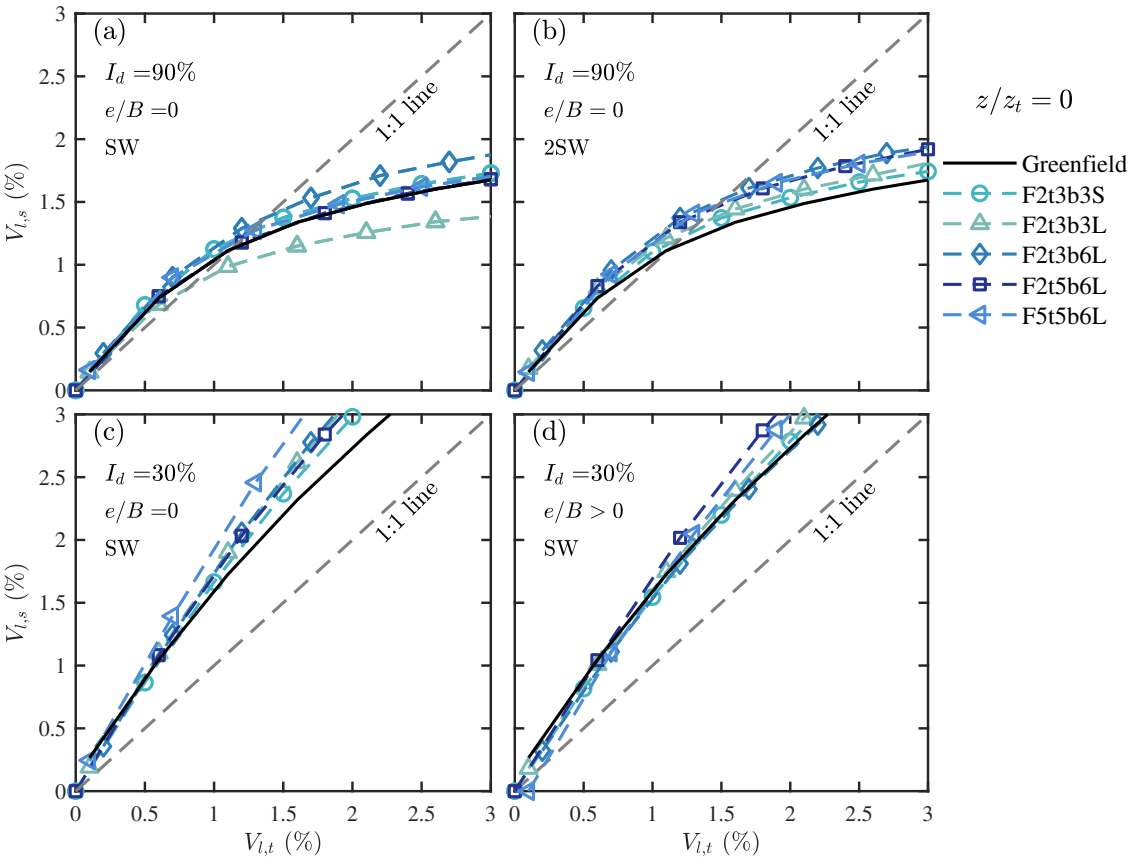


Fig. 4.13. Variation of surface ($z/z_t = 0$) soil volume loss with tunnel volume loss

To investigate this aspect, soil volume losses $V_{l,s}$ at the surface against tunnel volume loss

$V_{l,t}$ is shown in Figure 4.13. Interestingly, there is only a minor increase in the value of $V_{l,s}$ when the self-weight of the frame is doubled for central tunnels in dense sand, while an increase of normalised eccentricity e/B for loose sand slightly reduced $V_{l,s}$. Soil relative density I_d clearly dominated the $V_{l,s}-V_{l,t}$ relationship for all considered structures, which impacted the overall structure settlement level. Similar to greenfield tunnelling data (Marshall et al., 2012; Franza et al., 2019), in the tunnel-structure interaction tests, the loose soil exhibits a contractive response, whereas the dense soil transitions from contractive at lower values of $V_{l,t} < 1\%$ towards dilative at higher tunnel volume losses.

Figure 4.14 also shows the relationship between soil volume losses $V_{l,s}$ at the depth of $z/z_t = 0.5$ and tunnel volume loss $V_{l,t}$. Clearly, soil volume losses $V_{l,s}$ at the depth of $z/z_t = 0.5$ are lower than at the surface $z/z_t = 0$ for all tests. This indicates that the behaviour of the soil between $(z/z_t = 0-0.5)$ is overall contractive in both the loose and dense soil tests. Furthermore, soil volume losses $V_{l,s}$ at the depth of $z/z_t = 0.5$ are never greater than tunnel volume losses $V_{l,t}$ in the dense tests, whereas $V_{l,s} - V_{l,t}$ relationships of the loose soil tests are rather close to the 1:1 line. Finally, it is found that the effects of building self-weight and normalised eccentricity on $V_{l,s} - V_{l,t}$ relationships at the depth of $z/z_t = 0.5$ are identical with those in the $z/z_t = 0$ scenario (Figure 4.13).

4.5.2 Soil volume loss with varying depths

To better quantify the impact of the structure on the ground volumetric behaviour, subsurface values of soil volume loss $V_{l,s}$ at tunnel volume loss $V_{l,t} = 1$ and 2% are shown in Figures 4.15 and 4.16, respectively.

First, the relative dilatancy index approach (Bolton, 1986) was used to consider the effect of the building (on average) on the relative dilatancy of the soil. A relative dilatancy index I_R is defined as:

$$I_R = I_d \times I_c - 1 \tag{4.1}$$

where I_d is the relative density; $I_c = \ln\frac{p_c}{p'}$ is the relative grain strength; p_c is a parameter relating

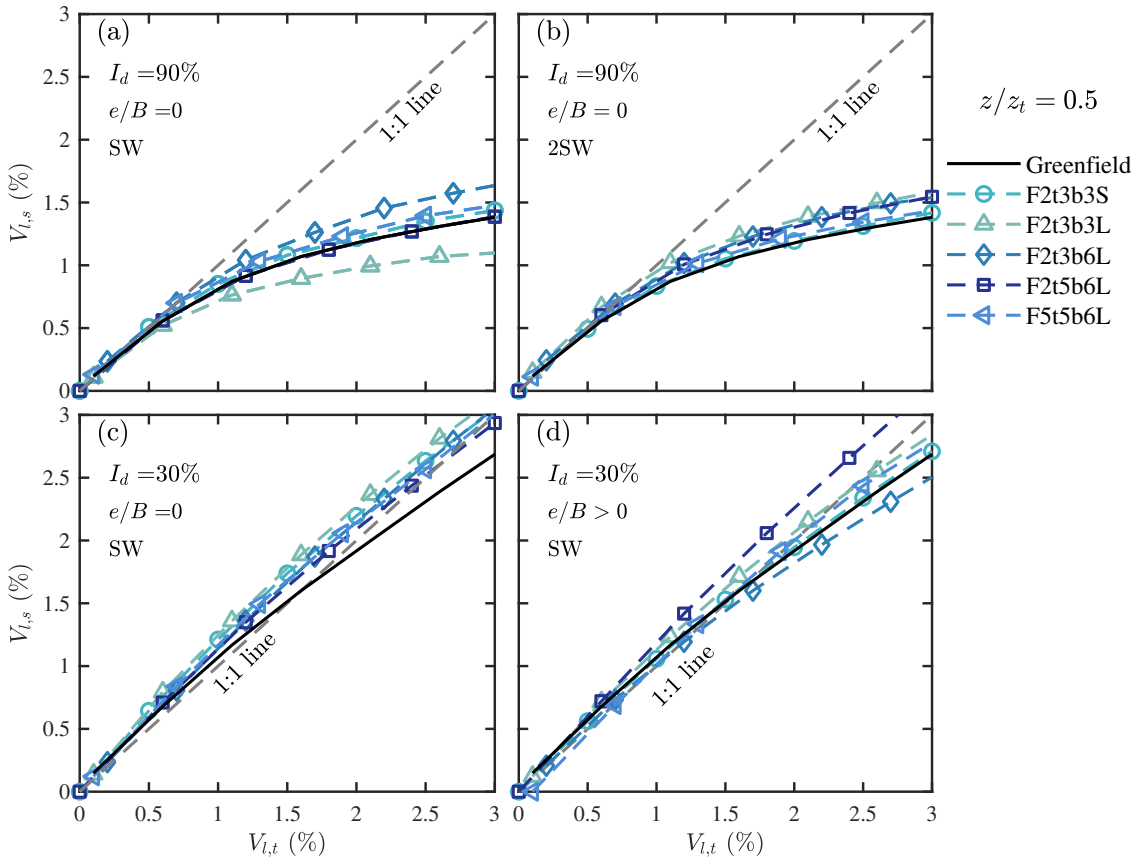


Fig. 4.14. Variation of subsurface ($z/z_t = 0.5$) soil volume loss with tunnel volume loss

to the crushing strength of the grain (20000 kPa for medium quartz sand) and p' is the mean effective stress at failure. A larger value of I_R indicates a greater tendency to dilate of the soil, whereas values of I_R less than zero indicate conditions which are initially contractile but which tend ultimately to a critical state with $I_R = 0$ (Bolton, 1986). However, at low shear strains, both loose and dense sands are contractive (also refer to Figure 2.8 (Marshall et al., 2012; Zhao, 2008)).

Using Equation 4.1, the values of the relative dilatancy of the soil (both I_d = 30 and 90%) at z/z_t = 0.5 and 0.72 (tunnel crown) considering the additional surcharge of the building (refer to Table 3.6) were calculated (Figure 4.17). Results show that the dense soil (I_d = 90%) shows a larger tendency to dilate, whereas the loose soil (I_d = 30%) displays a much lower dilative tendency. The surcharge of the building non-linearly reduces the tendency to dilate of the soil for both I_d = 30 and 90% soil.

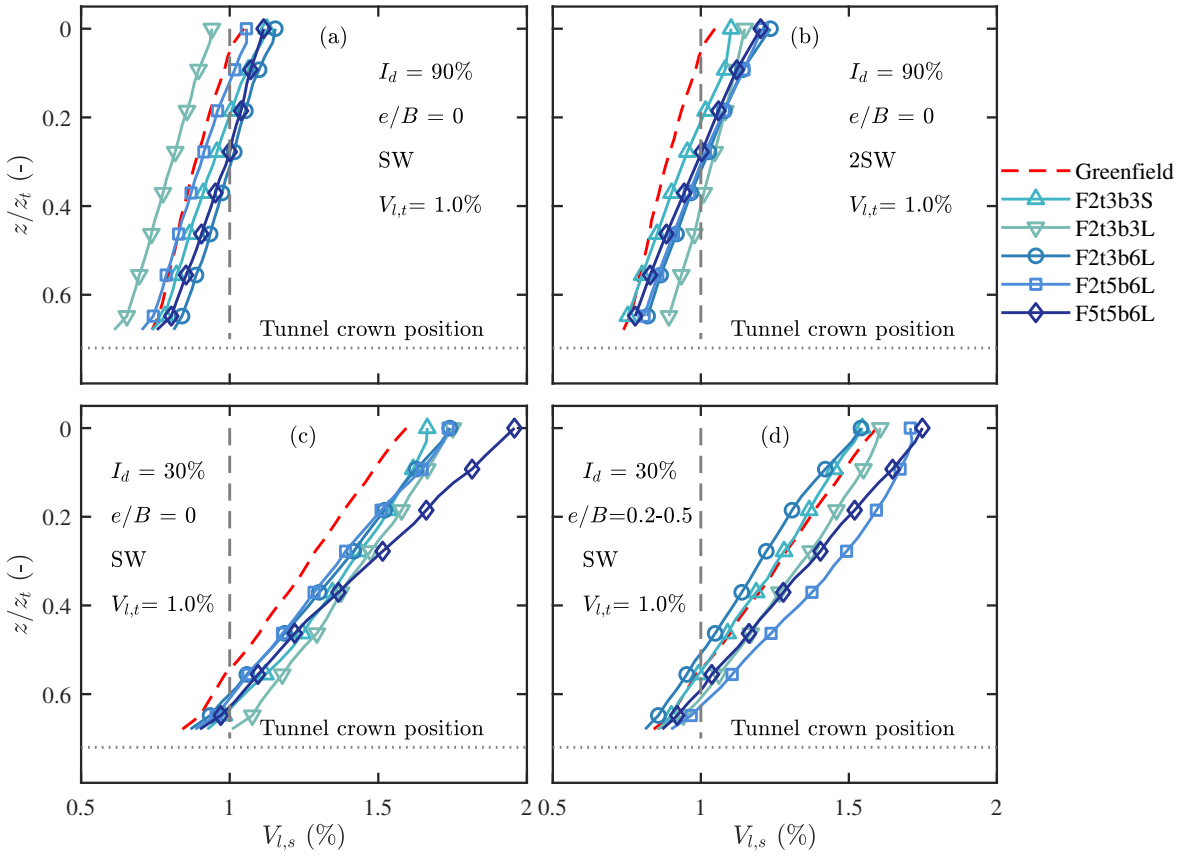


Fig. 4.15. Soil volume loss with varying depths at $V_{l,t}$ = 1%

Figures 4.15 and 4.16 show that, the interaction curves of the tunnel-frame interaction tests, with respect to the greenfield data, show an overall shift towards greater soil volume loss $V_{l,s}$ values for most tests. This shift, due to soil contractive strains (associated with the impact of the buildings on soil dilation, as discussed above), tends to be greater in loose soil tests (Figure 4.15(c)-(d) and Figure 4.16(c)-(d)). This nearly uniform shift indicates that most of the change in the soil volumetric response (between greenfield and interaction tests) happened at $z/z_t \geq 0.7$, i.e. close to the tunnel. Interestingly, the shift of the interaction curves is relatively constant with depth for most tests, except for the heavier structures (for instance, frames F2t5b6L and F5t5b6L in Figure 4.15(b)-(d) and Figure 4.16(b)-(d)). This indicates that a light structure has a minor effect on the ground volumetric behaviour (refer to Figure 4.17), whereas a heavy building may significantly affect the ground movements caused by tunnelling, particularly in the loose soil. This aspect will be clearer in the following section (Section 4.6). Also,

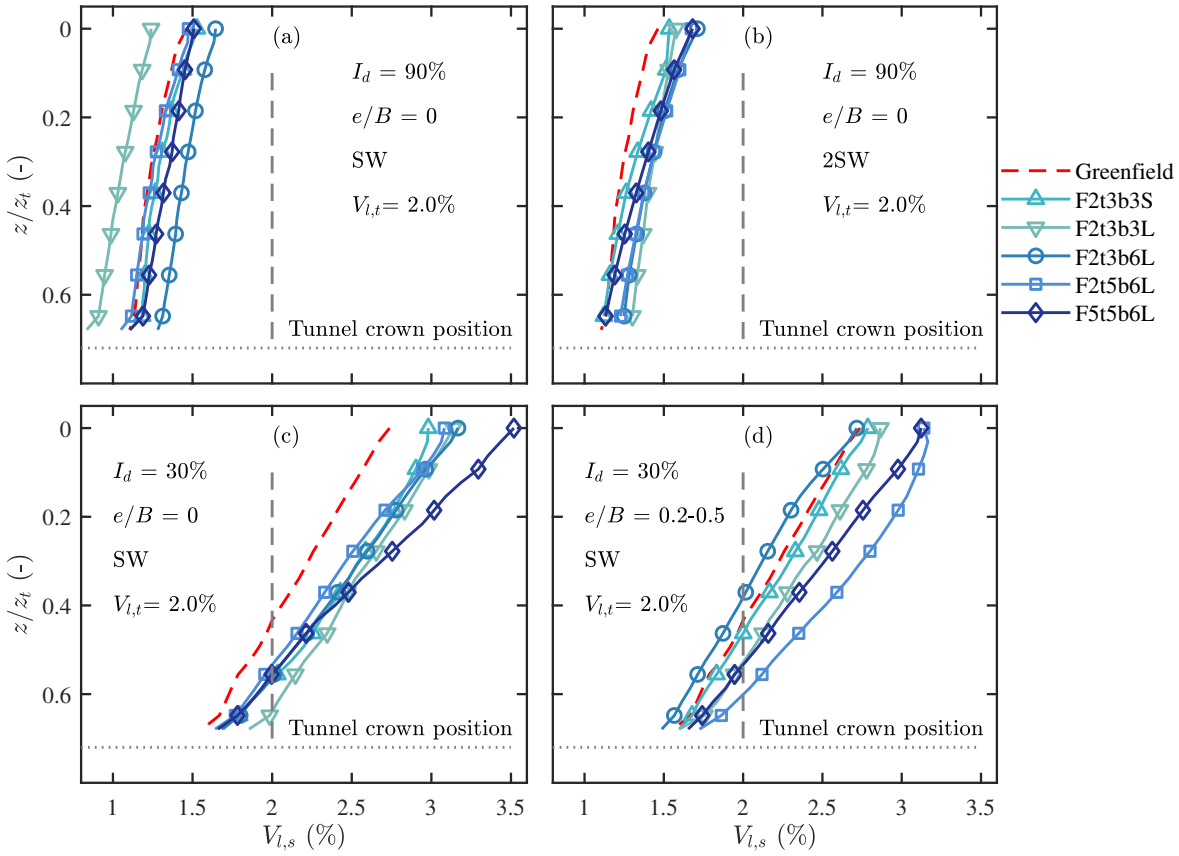


Fig. 4.16. Soil volume loss with varying depths at $V_{l,t}$ = 2%

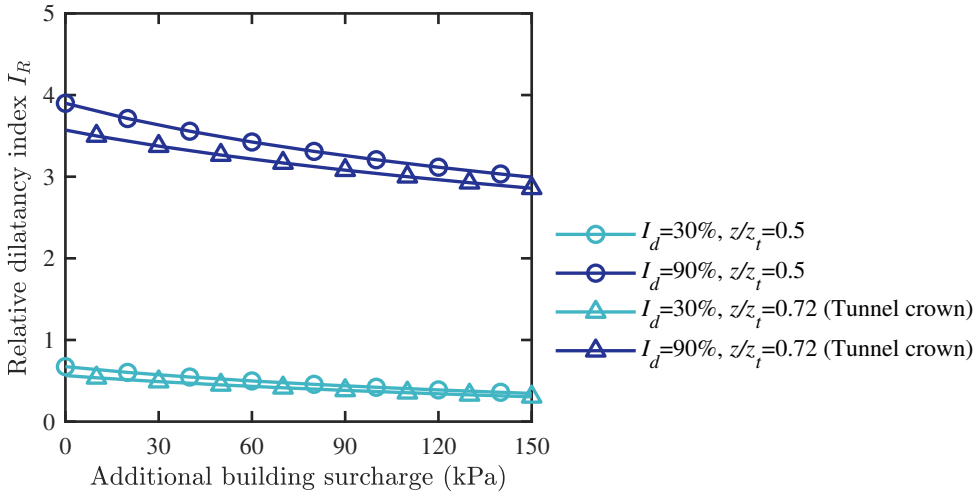


Fig. 4.17. Variation of relative dilatancy index against the pressure change

note that the behaviour of the soil between the surface and the tunnel crown ($z/z_t = 0 - 0.7$) is overall contractive in both the loose and dense soils, with $V_{l,s}$ at $z/z_t = 0$ greater than $V_{l,s}$ at $z/z_t = 0.7$. Differently, the slopes of the curves in the dense soil tests are greater than those in the loose soil tests, indicating a higher level of contraction for the loose soil. Interestingly, $V_{l,s}$ at $z/z_t = 0.7$ is always smaller than $V_{l,t}$ in both Figures 4.15 and 4.16, hence the dilative response of sand happened close to the tunnel for both the dense and loose soil tests (soil shear strains near the tunnel are very high (see Section 4.6), resulting in the dilative response of both dense and loose soil, see Figure 4.17). However, note that the quick preparation of the loose soil (only the soil above the tunnel axis level was re-prepared) sample may have had an influence on the soil volumetric response to tunnelling, possibly overestimating the dilation of the loose soil. Finally, at $V_{l,t} = 1\%$, Figure 4.15 shows that $V_{l,s}$ at $z/z_t = 0$ is greater than $V_{l,t}$ for nearly all tests, whereas at $V_{l,t} = 2\%$ (Figure 4.16), $V_{l,s}$ of dense soil at $z/z_t = 0$ is never greater than $V_{l,t}$.

4.6 Ground deformation affected by building

Tunnelling-induced ground deformation can be affected by the foundation roughness and pressure of the surface structures. Engineers may be tasked with the prediction of tunnelling-induced ground displacements in the scenario where structures rest on the surface.

4.6.1 Greenfield tunnelling

Figure 4.18 shows the greenfield ground movements (horizontal U_x and vertical U_z), and strains (engineering shear γ_s and volumetric ϵ_v) contours. In particular, Figure 4.18(a) and (b) displays the data at $V_{l,t} = 2.0\%$ of the greenfield tunnelling in dense ($I_d = 90\%$) and loose ($I_d = 30\%$) soil, respectively; whereas Figure 4.18(c) presents the results of the greenfield tunnelling in loose sand at $V_{l,t} = 1.0\%$, resulting in a similar $V_{l,s}$ value (1.5-1.6%) with tunnelling in dense sand at $V_{l,t} = 2.0\%$ (Figure 4.18(a)). In Figure 4.18, positive horizontal and vertical displacements are oriented towards the right and downwards, respectively, while positive volumetric strains are contractive. Data outside the contour thresholds were set equal to the closest limit

value.

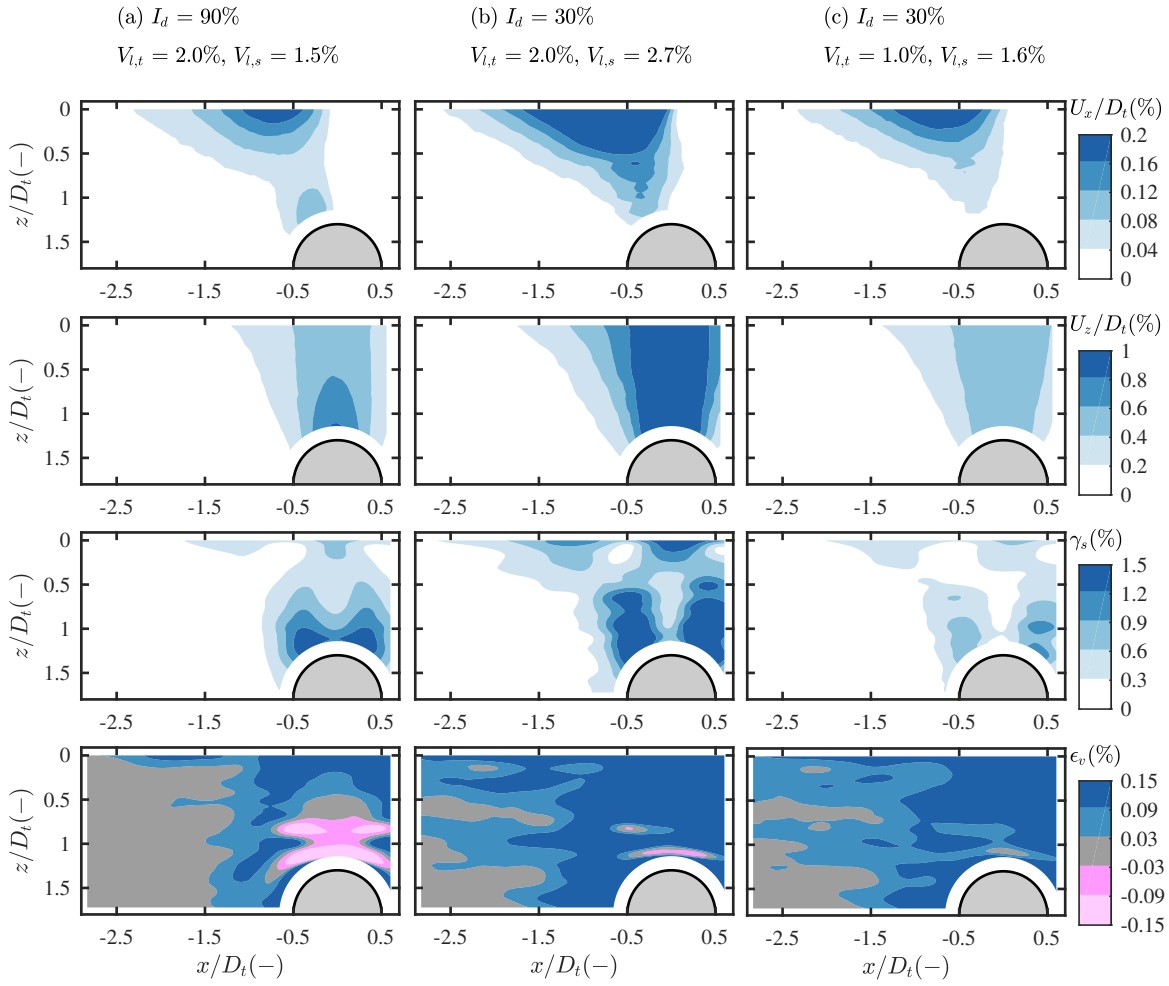


Fig. 4.18. Soil movements normalised by the tunnel diameter, engineering shear and volumetric strains ($\epsilon_v < 0$ indicates dilation) in greenfield tests (data outside the contour thresholds were set equal to the closest limit value)

From Figure 4.18(a), the greenfield ground settlement in dense soil shows a chimney-like pattern due to the low C/D_t value (Marshall et al., 2012; Franza et al., 2019) with clear evidence of an arch forming, and large shear strains are observed at the tunnel shoulders. Soil directly above the tunnel crown experienced high levels of dilation, whereas the soil experienced intermediate levels of contraction within bands spanning from the tunnel springline to the surface. As discussed by Marshall et al. (2012), the zones of dilation and contraction correspond approximately to the areas of high and low shear strains, respectively. A zone of large contraction is noted centrally above the tunnel and near the surface; this zone is likely caused by

the compressive action of the near-surface horizontal displacements on either side of the tunnel.

Next, data of greenfield tunnelling in loose soil shown in Figure 4.18(b) is considered. The response of the loose soil (I_d = 30%) is dominated by soil contraction (refer also to Figure 4.13). Consequently, for the identical tunnel volume loss ($V_{l,t}$ = 2.0%), the normalised horizontal and vertical displacements, as well as the shear strain, were significantly increased compared to the I_d = 90% test in Figure 4.18(a). However, when comparing the ground movements for surface settlement troughs of equal volume (Figure 4.18(a) and (c), with $V_{l,s}$ = 1.5-1.6%), normalised horizontal displacements U_x near the surface in (c) are slightly greater than in (a), whereas the U_x near the tunnel shoulders in (c) are smaller than in (a). Furthermore, despite a wider ground settlement field formed in the loose soil (Figure 4.18(c)), a localised large vertical displacement zone (0.8-1.0% D_t) is observed above the tunnel crown in the dense soil test (Figure 4.18(a)), whereas the settlement field in the loose sand is more uniform (0.4-0.6% D_t from tunnel crown toward the surface). Consequently, the level of the engineering shear strain in the loose soil is much lower than in the dense sand (at tunnel shoulder positions, the value of shear strain for the loose soil was 0.6-0.9%, whereas for the dense soil, the value increased to 1.2-1.5%)).

4.6.2 Effect of building weight

To investigate the impact of the surface building and the role of building self-weight on tunnelling induced ground movements, soil displacements (horizontal U_x and vertical U_z), and strains (engineering shear γ_s and volumetric ϵ_v) contours of central frames F2t3b3L, F2t5b6L and F5t5b6L with varying building weight (standard weight SW and double weight 2SW) in dense soil (I_d = 90%) are presented in Figures 4.19, 4.20 and 4.21, respectively.

The effects, relative to the greenfield case, of the presence of surface structures on tunnelling-induced ground horizontal movement, is considered. For all presented tests in Figures 4.19, 4.20 and 4.21, the horizontal displacements of the soil near the surface were largely restricted by the foundation roughness and building pressure towards the external part of the building (compare Figures 4.19, 4.20 and 4.21 against Figure 4.18(a)). However, the degree of the influence clearly depends on the building weight and structural configuration. For the most flexible two-storey frame F2t3b3L (no gap was formed, refer to Figure 4.10), horizontal displacements U_x of the

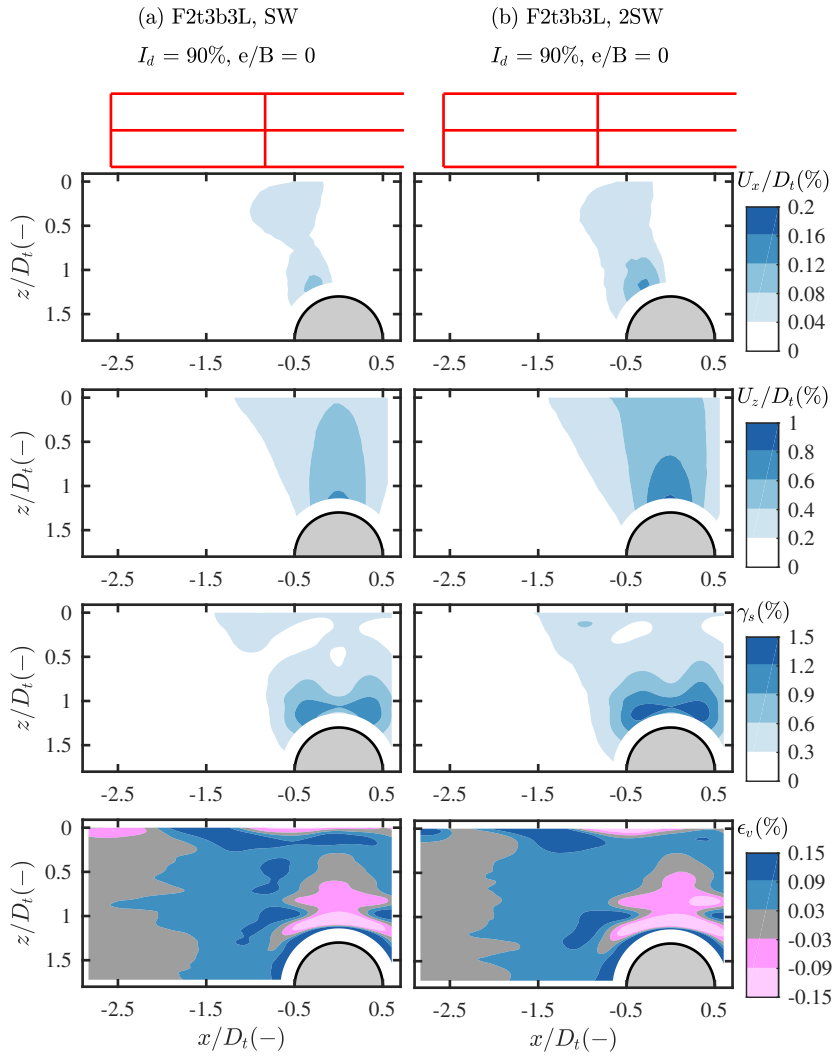


Fig. 4.19. Soil movements normalised by the tunnel diameter, engineering shear and volumetric strains ($\epsilon_v < 0$ indicates dilation) at $V_{l,t}$ = 2% for frame F2t3b3L (data outside the contour thresholds were set equal to the closest limit value)

soil near the surface were nearly completely restricted for both SW and 2SW tests. This is due to the high axial stiffness and roughness of the foundation, as well as the pressure from the building. On the other hand, the horizontal restriction of the rigid two-storey frame F2t5b6L to the soil was not as significant as frame F2t3b3L (compare Figure 4.20 and 4.19), despite the former having a greater average pressure beneath the foundation (refer to Table 3.6). This is due to the gap formation beneath the foundation of frame F2t5b6L (refer to Figure 4.10). As expected, when the weight of frame F2t5b6L increased (compare Figure 4.20(a) and (b)), the

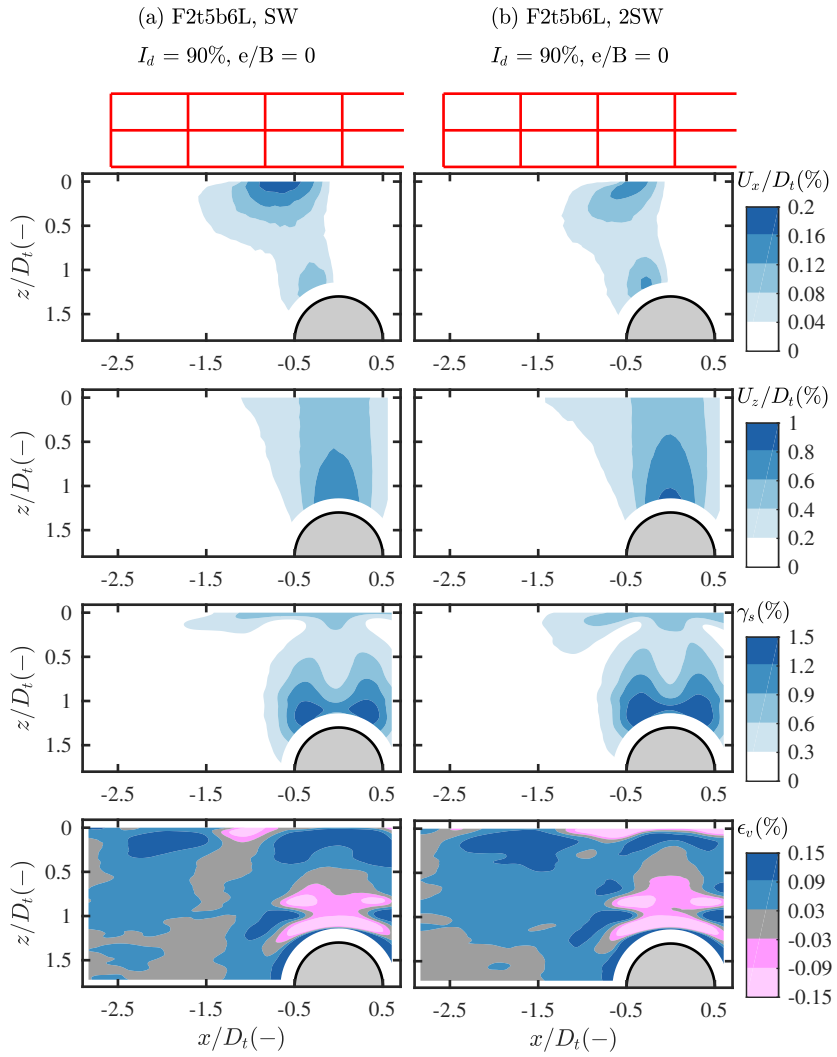


Fig. 4.20. Soil movements normalised by the tunnel diameter, engineering shear and volumetric strains ($\epsilon_v < 0$ indicates dilation) at $V_{l,t}$ = 2% for frame F2t5b6L (data outside the contour thresholds were set equal to the closest limit value)

horizontal restriction of the foundation to the soil also increased; this is due to the increase of the pressure beneath the foundation, as well as the decrease of the gap at the soil-foundation interface (refer to Figure 4.10). A similar phenomenon is also observed for frame F5t5b6L (Figure 4.21).

In the vertical direction, the effects of the presence of the structures with varying configuration and weight on tunnelling-induced ground settlements are also different. For frame F2t3b3L with standard self-weight SW in Figure 4.19(a), the average ground settlement was lower than

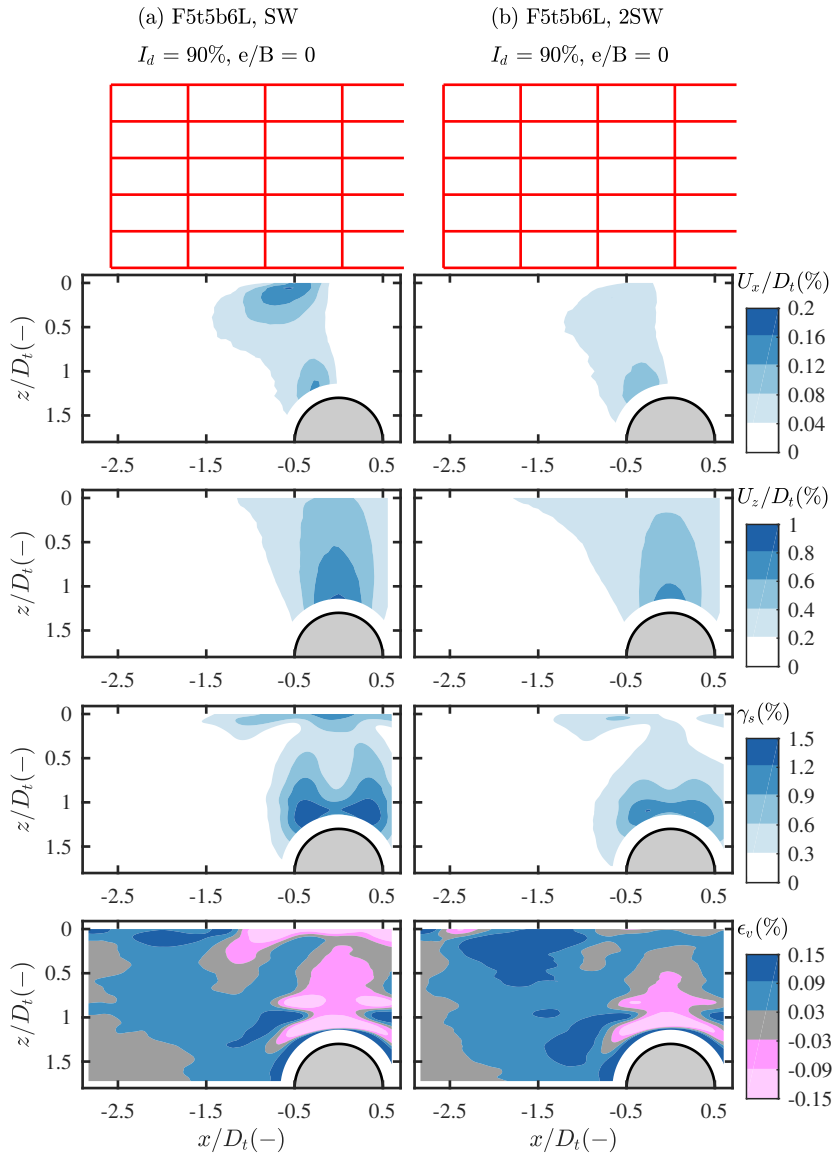


Fig. 4.21. Soil movements normalised by the tunnel diameter, engineering shear and volumetric strains ($\epsilon_v < 0$ indicates dilation) at $V_{l,t}$ = 2% for frame F5t5b6L (data outside the contour thresholds were set equal to the closest limit value)

the greenfield result (Figure 4.18(a)). When the building weight doubled (Figure 4.19(b)), the average ground settlement also increased, and the ground settlement field was wider than those in the SW test (Figure 4.19(a)) and the greenfield scenario (Figure 4.18(a)). The role of building weight in affecting the tunnelling-induced settlement for frame F2t5b6L (see Figure 4.20(a) and (b)) follows a similar principle with that of frame F2t3b3L. Interestingly, for the relatively heavy building F5t5b6L (Figure 4.21), the increase of the building self-weight (from standard

weight SW to doubled weight 2SW) decreased the magnitude of the ground settlement field. Furthermore, because of the high pressure beneath the foundation, the settlement field was also much wider than the greenfield scenario (Figure 4.18(a)) and the SW test (Figure 4.21(a)).

Finally, the influence, relative to the greenfield case, of the presence of framed buildings with raft foundations on tunnelling-induced ground strains is considered. Figures 4.19, 4.20 and 4.21 show that the restriction of the horizontal soil movements resulted in a thin shear band at the soil-foundation interface with a decreased maximum contraction level and some areas of dilation now present. Interestingly, for frame F2t3b3L with a wider bay, the dilation zones near the surface tended to occur at the column positions (see Figure 4.19); for frames F2t5b6L and F5t5b6L, the dilation zones were observed near the locations where gaps first formed (refer to Figure 4.9(e)-(f)). Therefore, in the test of frame F5t5b6L with doubled weight 2SW, no gap formed at the soil-foundation interface, and thus only a small dilation zone was observed at the building edge (see Figure 4.21(b)). The effects, relative to the greenfield case, of the buildings on tunnelling-induced subsurface soil shear and volumetric behaviours are minor, and are related to the magnitude of the ground displacements; the greater the vertical displacement, the higher the soil shear and volumetric strains.

4.6.3 Effect of soil density

Figure 4.22 shows the soil movements normalised by the tunnel diameter, as well as engineering shear and volumetric strains of the soil with different density in the tests with central frame F2t3b3S and standard weight SW.

For the same tunnel volume loss $V_{l,t}$ = 2.0%, due to the fact that the response of the loose soil (I_d = 30%) in Figure 4.22(b) is dominated by contraction (refer also to Figure 5.9), the horizontal and vertical displacements, as well as the shear strain, were significantly increased compared to the I_d = 90% test (compare Figure 4.22(a) and (b)). Soil dilation zones were observed at the soil-structure interface for both tests (Figure 4.22(a) and (b)). Consistent with the greenfield case, for similar soil volume loss $V_{l,s}$ = 1.5-1.6% (compare Figure 4.22(a) and (c)), the horizontal displacements of the soil near the surface in loose soil were slightly greater than in dense soil; the loose soil settlement field, although having a smaller maximum settlement

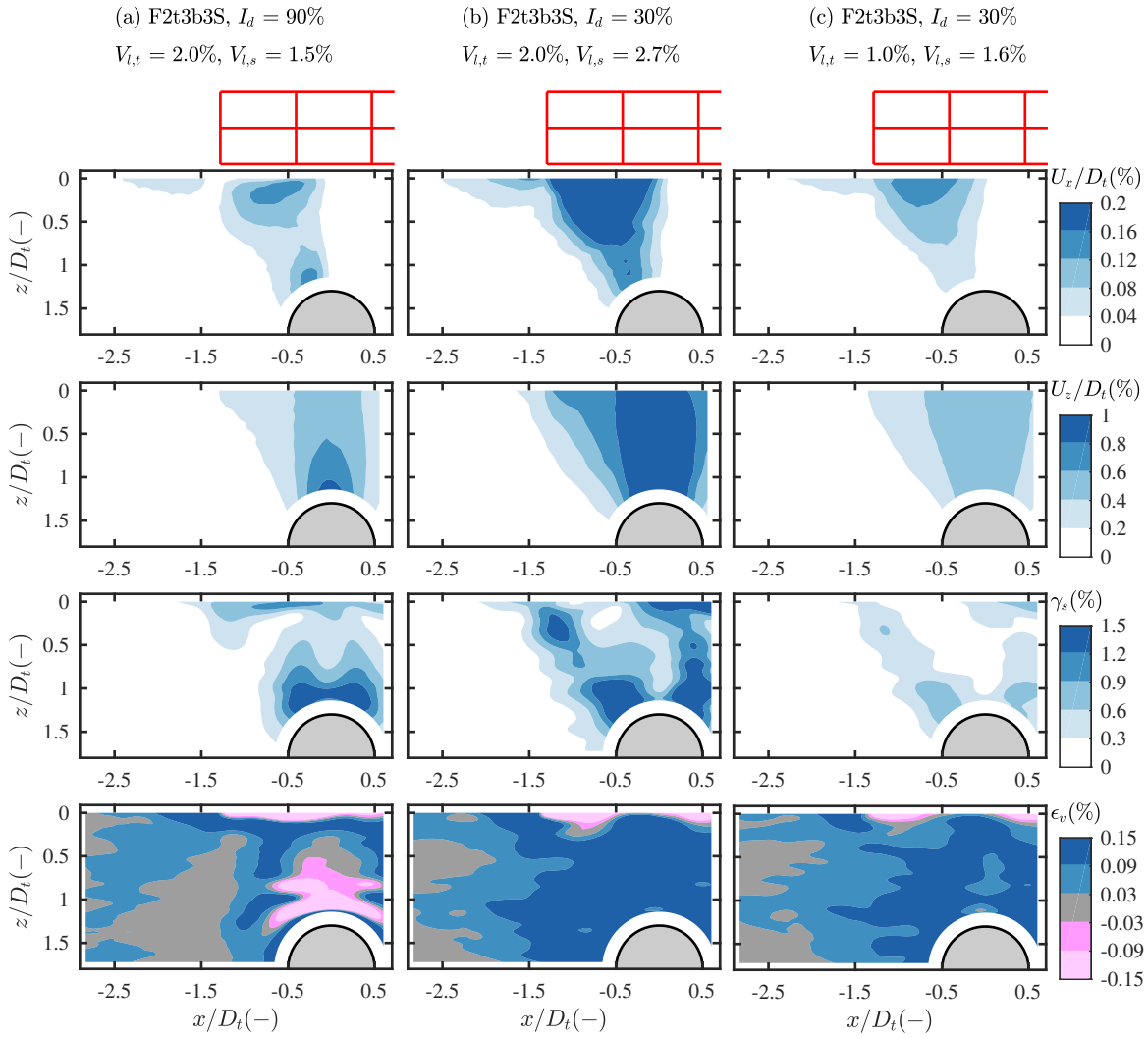


Fig. 4.22. Soil movements normalised by the tunnel diameter, engineering shear and volumetric strains ($\epsilon_v < 0$ indicates dilation) in central short frame F2t3b3S (SW) tests: effect of soil density (data outside the contour thresholds were set equal to the closest limit value)

value, was wider than that of dense soil; the level of the shear strains in the loose soil were much lower than in the dense sand (similar to the greenfield scenario presented in Figure 4.18, at tunnel shoulder positions, the value of shear strain for the loose soil was 0.6-0.9%, whereas for the dense soil, the value increased to 1.2-1.5%).

4.6.4 Effect of building width and eccentricity

In tunnel-structure interaction problems, the building width and location also play an important role (Ritter, 2018). To assess the impacts of building width and eccentricity on tunnelling induced ground movements, Figure 4.23 presents the selected centrifuge tests involving the buildings varying transverse width and eccentricity, all with dense soil (I_d = 90%) and doubled weight 2SW.

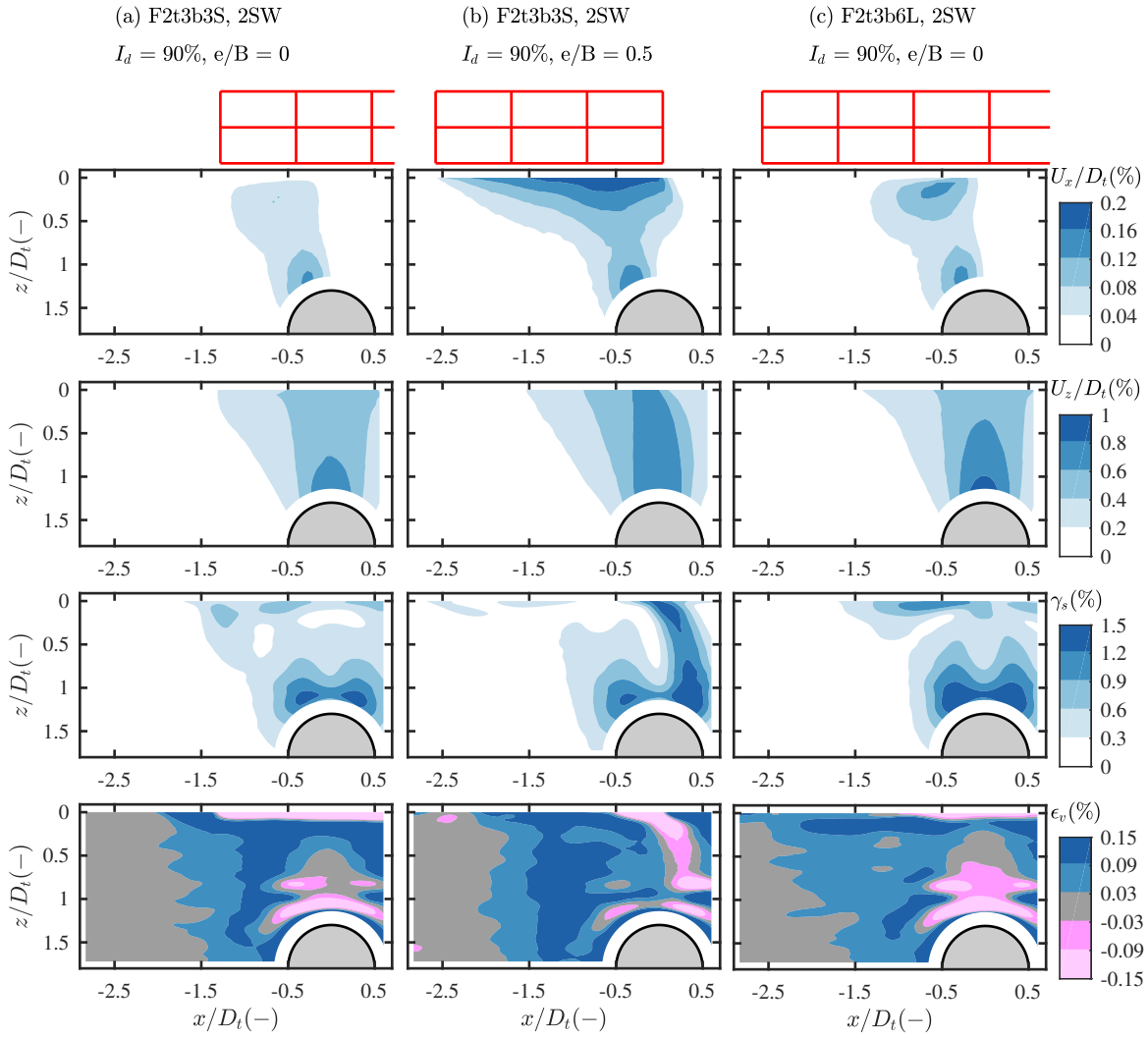


Fig. 4.23. Soil movements normalised by the tunnel diameter, engineering shear and volumetric strains ($\epsilon_v < 0$ indicates dilation) at $V_{l,t}$ = 2%: effect of building width and eccentricity (data outside the contour thresholds were set equal to the closest limit value)

First, the influence of building transverse width is considered using data in Figure 4.23(a)

and (c). For central structures, the short building (F2t3b3S) tended to have a greater impact on the tunnelling-induced ground displacements than the long structure (F2t3b6L); the horizontal and vertical displacements in Figure 4.23(a) (short structure) were smaller than those in Figure 4.23(c) (long building). Furthermore, the shear band at the soil-structure interface of the short frame F2t3b3S was thicker than that of the long structure F2t3b6L (possibly due to the greater average settlement of the short frame F2t3b3S than the long frame F2t3b6L, refer to Figure 4.9(a) and (d)); however, the overall shear strain level in the short structure test (Figure 4.23(a)) was lower than in the long building test (Figure 4.23(c)). Interestingly, the zone having the dilative response of the soil above the tunnel crown in (a) also decreased compared with that in (c). This is because the short building imposed its weight in a more localised region above the tunnel crown than the long building. Therefore, the vertical stresses in the soil above the tunnel for the short building are higher, making the soil less likely to dilate (refer to Figure 4.17). On the other hand, the weight of the long building would likely be transferred to the sides of the tunnel within "columns" of highly stressed soil, with the central region above the tunnel being relatively unloaded (because of the gap formation) and therefore more likely to dilate than the short frame case.

Next, the impact of building eccentricity is assessed using data in Figure 4.23(a)-(b). For the short structure in the dense soil, Figure 4.23(b) shows that, because of the freedom to shift, the eccentric ($e/B = 0.5$) short frame, which can also be seen as half of the long frame in Figure 4.23(c), considerably increased the horizontal displacement of the soil near the surface compared with the central ($e/B = 0$) short frame in Figure 4.23(a) and the long frame in Figure 4.23(c). At the same time, the action of the right edge of the short frame with $e/B = 0.5$ resulted in the soil chimney reaching the surface (i.e. larger soil settlements directly above the tunnel up to the surface), and the formation of large shear and dilative strain bands between the building right edge and the right shoulder area of the tunnel (consistent with Ritter et al. (2017)). On the other hand, the level of shear strain at the soil-foundation interface in (b) decreased compared with the central short and long frames in (a) and (c).

Finally, the impact of the presence of the heavy building F5t5b6L with varying eccentricity values on the tunnelling-induced ground movements of loose soil is discussed (Figure 4.24). In

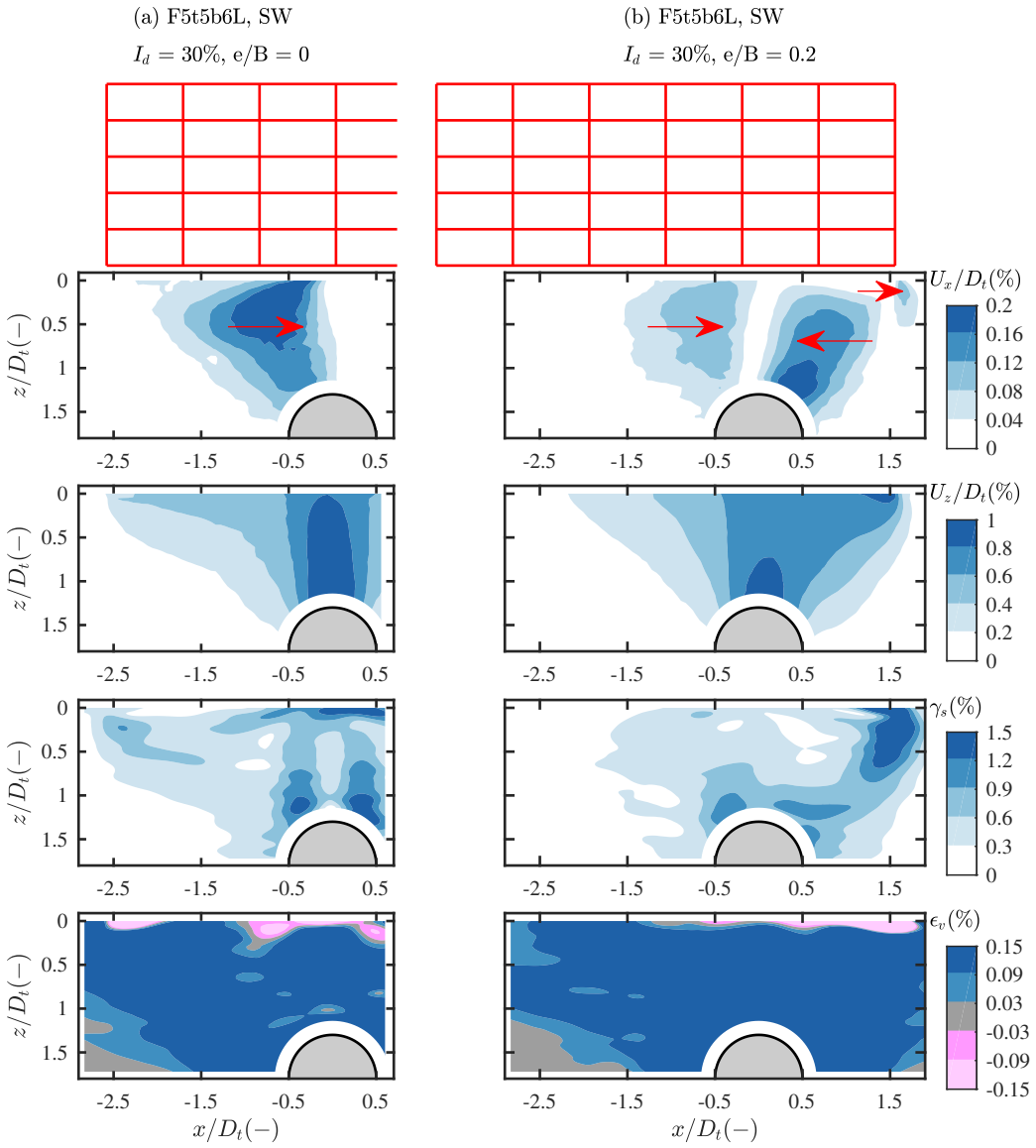


Fig. 4.24. Soil movements normalised by the tunnel diameter, engineering shear and volumetric strains ($\epsilon_v < 0$ indicates dilation) at $V_{l,t}$ = 2%: F5t5b6L in the loose soil (the direction of the horizontal displacement is denoted by the arrows; data outside the contour thresholds were set equal to the closest limit value)

Figure 4.24, the direction of the horizontal displacement is denoted by the arrows.

For the central frame F5t5b6L in (a), similar with the previous discussion, the horizontal displacements of the soil near the surface were restricted by the foundation roughness and building pressure towards the external part of the building. It is worth noting that the ground vertical displacement field was considerably widened by the foundation pressure of frame F5t5b6L, com-

pared with the greenfield tunnelling in Figure 4.18(b). Consequently, a large shear zone was developed beneath the building corner, but the overall magnitude of the shear strain decreased. For the eccentric frame F5t5b6L in (b), the restriction of the building to the soil horizontal displacements was much greater than in (a), particularly for the left half side of the soil. The chimney-like settlement pattern was considerably modified by the building action, with a large vertical displacement zone developing toward the building right corner. As a consequence, the zone having the largest shear strain level transmitted from the tunnel shoulders to the zone directly beneath the building right corner.

4.7 Structural distortion

4.7.1 Deformation parameters and modification factor approach

Deflection ratios, DR, of the framed buildings in selected tests are presented in Figure 4.25(a) and (b) according to normalised eccentricity for tunnel volume loss up to 3%. A complete set of results of building deformation parameters (DR, M^{DR} and β) are reported in Figure 4.28. To compute the deflection ratios of the buildings, both the length of sagging and hogging zones as well as the relative deflections were determined from the frame settlement profiles (considering points at raft-column intersections and the centre of rafts between two columns). On the other hand, greenfield values of DR and lengths of sagging/hogging zones were interpolated using modified Gaussian curves (Vorster et al., 2005).

Results of DR in Figure 4.25 show that long frames underwent both sagging and hogging deformations, whereas short frames mostly displayed either a sagging or hogging deformation mode when $e/B = 0$ or 0.5, respectively. For the centrally located long frames, sagging DR values tend to be larger in magnitude than hogging values. For all tests with long framed buildings, a stiffer frame tends to reduce DR in both sagging and hogging (see Figure 4.28). Results in Figure 4.25 also show that the increase of building weight (compare solid and hollow markers) tends to increase DR values, especially in sagging. In addition, the decrease of soil relative density (from 90% to 30%; compare results in dark and light colours) increases DR values for a given $V_{l,t}$; this effect is significant for the very flexible frame F2t3b3L (displayed

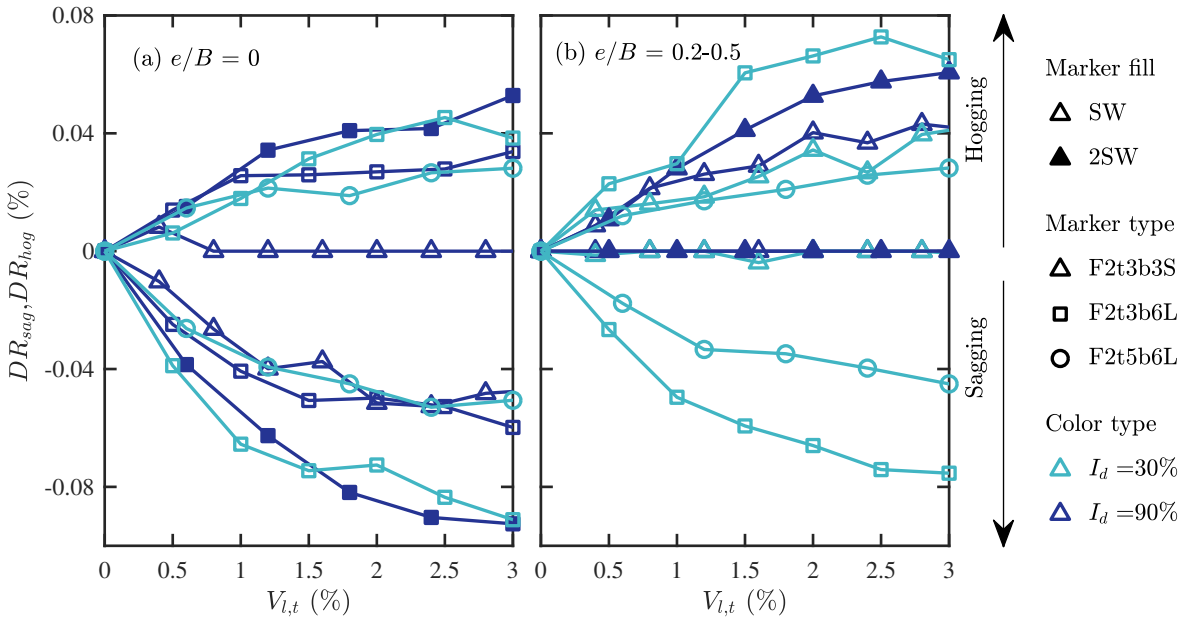


Fig. 4.25. Building deflection ratios against tunnel volume loss in selected tests

in Figure 4.28(b)-(c)) because the frame tends to conform to the greenfield tunnelling-induced ground movements. Finally, results in Figure 4.25(a)-(b) indicate that the increase of building eccentricity has a reducing effect on DR values for most frames (also see Figure 4.28).

Deflection ratio modification factors, M^{DR}, of the framed buildings in selected tests are presented in Figure 4.26 according to normalised eccentricity for tunnel volume loss up to 3%. Results of the deflection ratio modification factors M^{DR} in Figure 4.26 show that most M^{DR} trends are characterised by a steady decrease with $V_{l,t}$ over the investigated range, and a greater rate of decrease is obtained for the loose soil (also see Figure 4.28). The decrease of M^{DR} with $V_{l,t}$ is due to both soil stiffness degradation that occurs with tunnel volume loss (Farrell et al., 2014) and, when present, gap formation (quantified in Figure 4.10) (Deck and Singh, 2012; Franza and DeJong, 2019). Furthermore, increased building stiffness tends to decrease M^{DR}. In the sagging deformation mode, the increase of soil relative density (from 30% to 90%), building weight, and normalised eccentricity tend to increase, increase, and decrease, respectively, the $M^{DR,sag}$ values for a given $V_{l,t}$. The values of $M^{DR,hog}$ tend to be larger than $M^{DR,sag}$ for all tests (see Figure 4.28) due to 1) the effect of gap formation in the sagging zone, and 2) embedment at the building corners in the hogging zones. Generally, $M^{DR,hog}$ values in

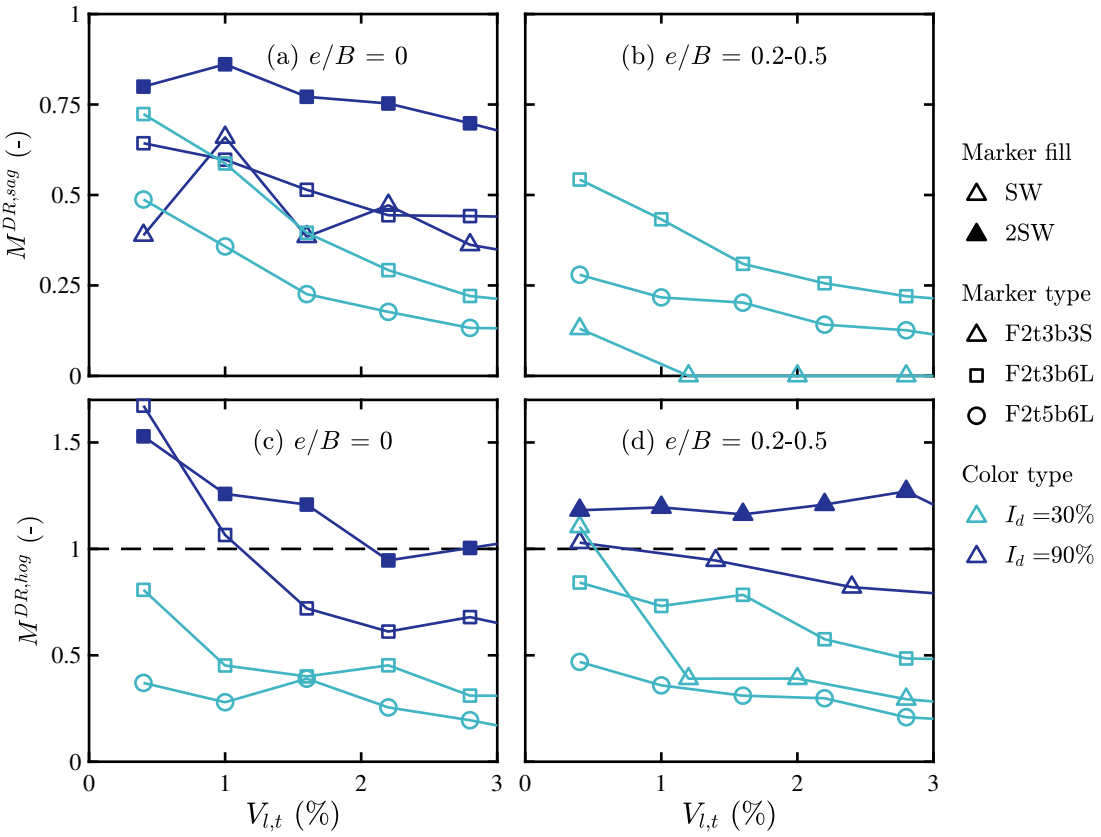


Fig. 4.26. Building modification factors of deflection ratios against tunnel volume loss in selected tests

the dense soil tests tend to be larger than in the loose soil tests. Interestingly, the increase of frame eccentricity tends to increase $M^{DR,hog}$, likely because a larger portion of the building was subjected to the hogging deformation mode in these cases.

The maximum values of the building angular distortion, β, within bays in selected tests are reported against $V_{l,t}$ in Figure 4.27(b), along with the maximum magnitude of the building deflection ratios in sagging, $DR_{sag,bld}$, in Figure 4.27(a). It is found that the effects of building weight, soil relative density, and building eccentricity on β mostly agree (qualitatively) with the trends relating to DR (see figures 4.28 and 4.25).

Despite this agreement, building angular distortion is not only related to building stiffness, but also to the structural configuration. On one hand, for the long frames F2t3b6L, F2t5b6L, and F5t5b6L with the same bay and building widths, the increase of building stiffness (due to

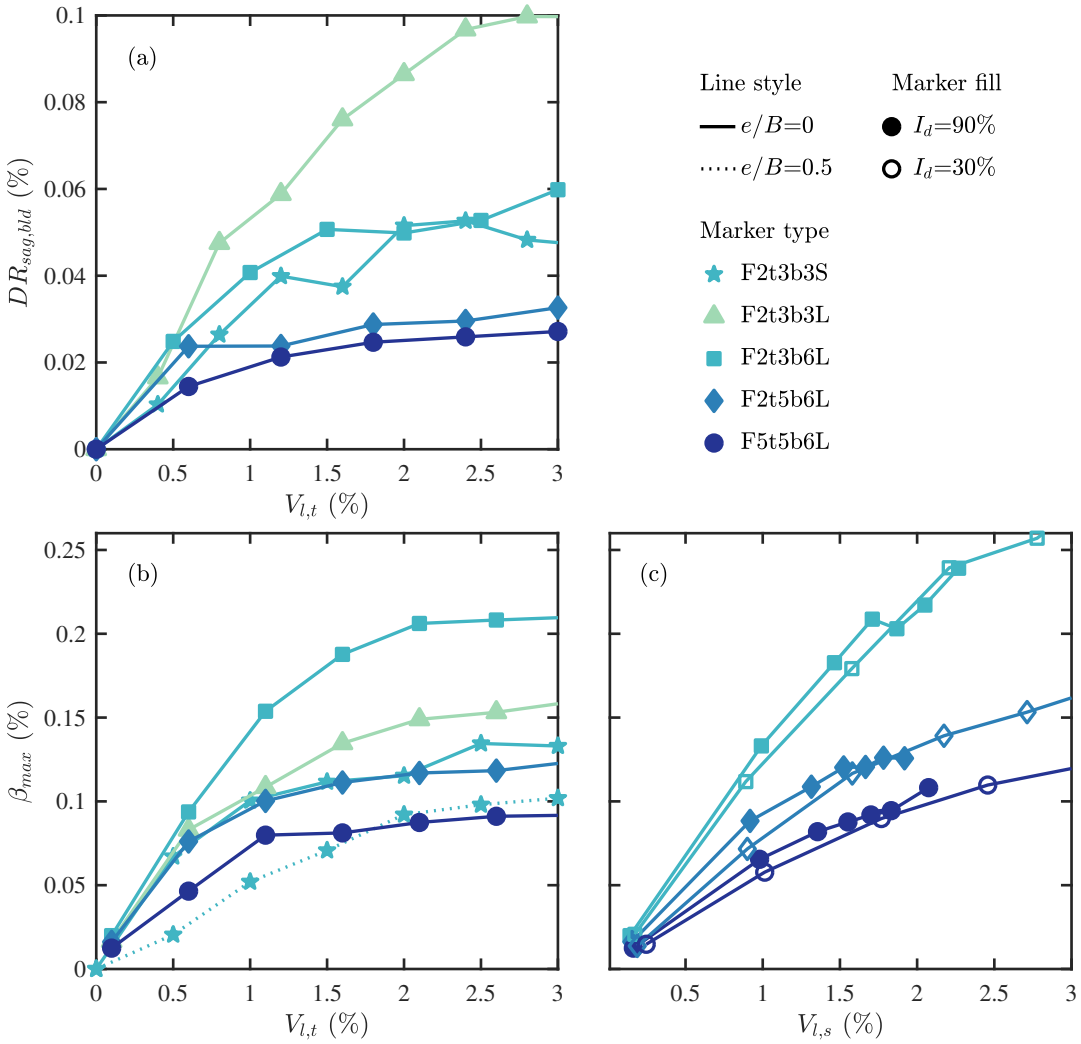


Fig. 4.27. Building deflection ratios and angular distortions against tunnel/soil volume loss in selected tests (SW)

thicker elements or additional stories) decreased the angular distortion (see Figure 4.27(b)). On the other hand, shorter bay length is observed to increase bay distortions; in Figure 4.27(b), the most flexible frame F2t3b3L (with a long bay length; consider stiffness values in Table 3.6) has β values lower than F2t3b6L (with similar characteristics but shorter bays), although F2t3b3L did undergo the largest DR values. Furthermore, Figure 4.27(a) also displays that the short frame F2t3b3S and the long frame F2t3b6L have similar sagging deflection ratios, however the angular distortion for the shorter frame is much smaller. These results indicate that the deflection ratios are not always as efficient as angular/shear distortions for quantifying framed

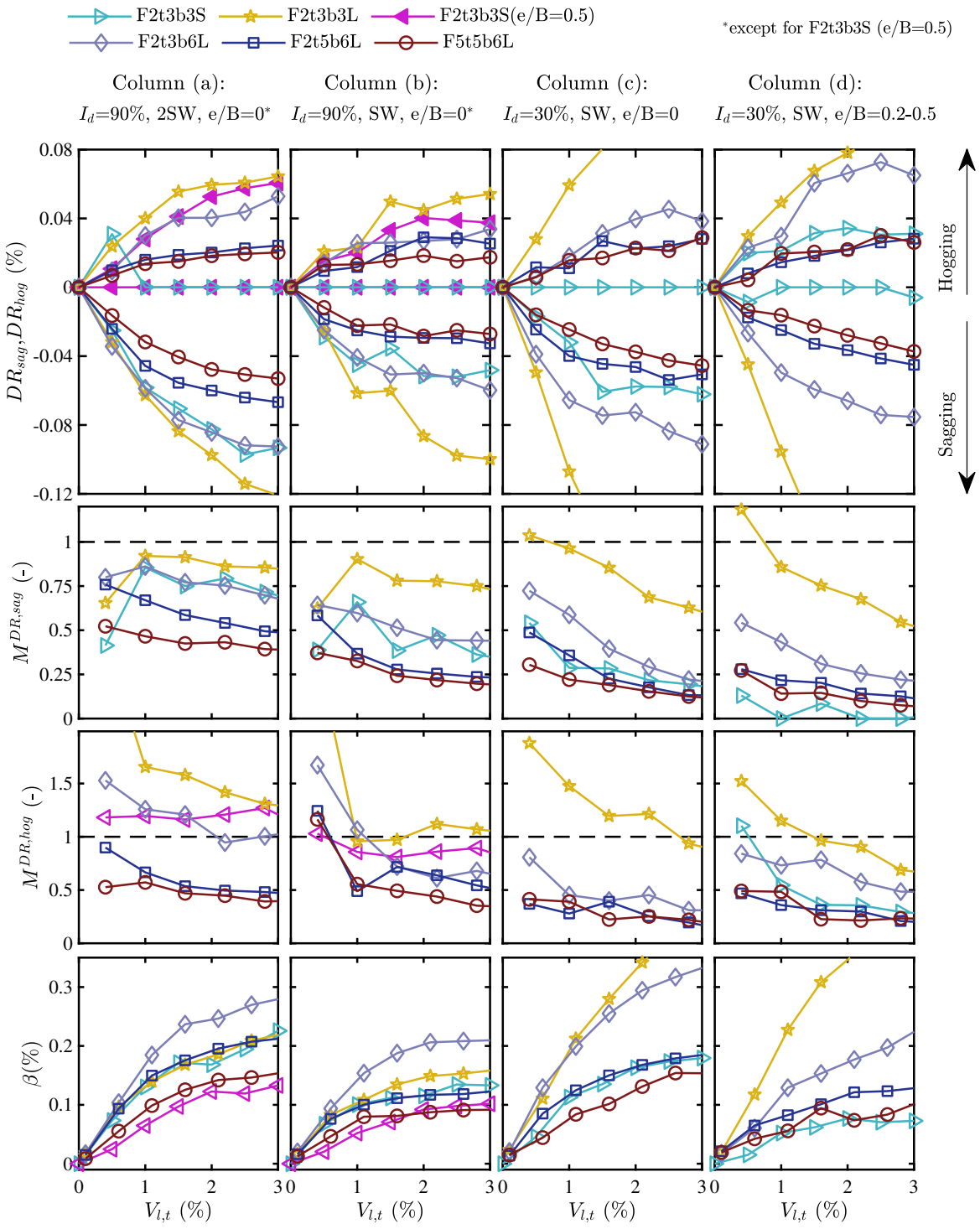


Fig. 4.28. Building distortion parameters (DR, M^{DR}, β) against tunnel volume loss

building distortions. To summarise, a more flexible structure, although generally having a larger deflection ratio, may not exhibit a greater distortion level if its stiffness is decreased through the increase of bay width. This highlights the importance of considering the realistic framed building details in the risk assessment of a real tunnelling project. This aspect will be clearer when the frame deformed shapes are presented (see Section 4.7.2).

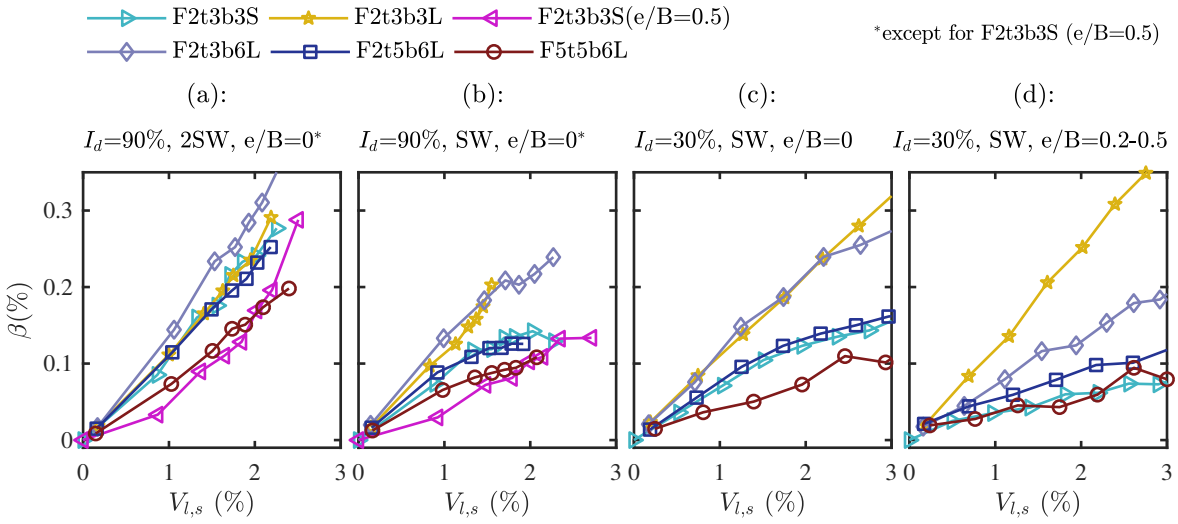


Fig. 4.29. Building angular distortion against soil volume loss

It is also of interest to analyse building angular distortion β for a given soil volume loss $V_{l,s}$. In Figure 4.27(c), the maximum β for tests with $e/B = 0$ and SW (see Figure 4.11) are plotted against $V_{l,s}$ (full data set is in Figure 4.29). Interestingly, for a given $V_{l,s}$, Figure 4.27(c) shows that there is little difference in building deformation of long frames for loose and dense sand, with a slightly larger deformation for dense sand cases. However, deformation for separate footings is much greater in dense sand than in loose sand (discussed in Chapter 5).

Finally, the role of structure tilt on the frame deformations is discussed. The short frame F2t3b3S with $e/B = 0.5$ can be regarded as half of the long frame F2t3b6L with $e/B = 0$. Interestingly, the eccentric short frame F2t3b3S has a much smaller angular distortion than the central long frame F2t3b6L in Figure 4.27(b), despite the fact that they have similar values of DR_{hog} and $M^{DR,hog}$ (see Figure 4.25 and Figure 4.26(c)-(d)). As will be displayed later by plotting the frame deformed shapes, this behaviour is due to the fact that the eccentric (short) frame can tilt to accommodate ground settlements, whereas tilt is prevented by the symmetry

condition for the central structure. These outcomes confirm that DR alone does not always provide an accurate description of distortion for a shear-dominated building.

4.7.2 Level of damage based on strain theory

Figure 4.30 shows frame deformed shapes and ground movements for 14 of the centrifuge tests at $V_{l,t}$=2%; for F5t5b6L only the results of the first and second storeys are presented because the cameras cannot capture the rest of the floors. However, note that shear distortion, which is the result of the differential settlements between columns, dominates the behaviour of the framed buildings; therefore, the deformation levels of the upper storeys are considered to be identical to the second storey distortion level, given the fact that the differential settlements in different levels of storeys should be very similar due to the high axial stiffness of the columns.

To quantify the deformation levels of bays and panels across the frames, indicators (markers) are used which are associated with a range of shear strains γ and a category of damage; the category was computed using a Mohr's circle of strain under plane-strain conditions (i.e. $\epsilon_{max} = \epsilon_{xz}$ for framed buildings on raft foundations). In Figure 4.30, the left and right columns relate to dense and loose sands, respectively. Indicators plotted within bays are indicative of γ values (calculated based on the displacements at the corners of bays), whereas indicators of γ_0 and γ_1 (computed from slab slopes) are placed along the foundations or floor slabs. A colour scheme was adopted to denote low (category of 0-1); medium (category 2), and high (category 3+) levels of deformation (see Table 2.4). For reference, the values of γ presented in Figure 4.30 are also listed in Table 4.2.

First, the deformed shapes of the short frame F2t3b3S tests are considered to evaluate the effects of normalized eccentricity e/B and soil relative density I_d. Figure 4.30(a) and (b) show the results for frame F2t3b3S with $e/B = 0.5$. Although the frame tested in loose sand was subjected to larger settlements and global tilt, the same level of deformation is observed for both soil densities: low levels in all bays and medium levels at the foundation level (due to the ground pressure). When the same short frame was centrally located with $e/B = 0$ (Figure 4.30(c) and (d)), the external bays underwent larger distortions (medium level for all slabs according to Boone (1996)) than for the eccentric configuration $e/B = 0.5$ in Figure 4.30(a) and (b). For

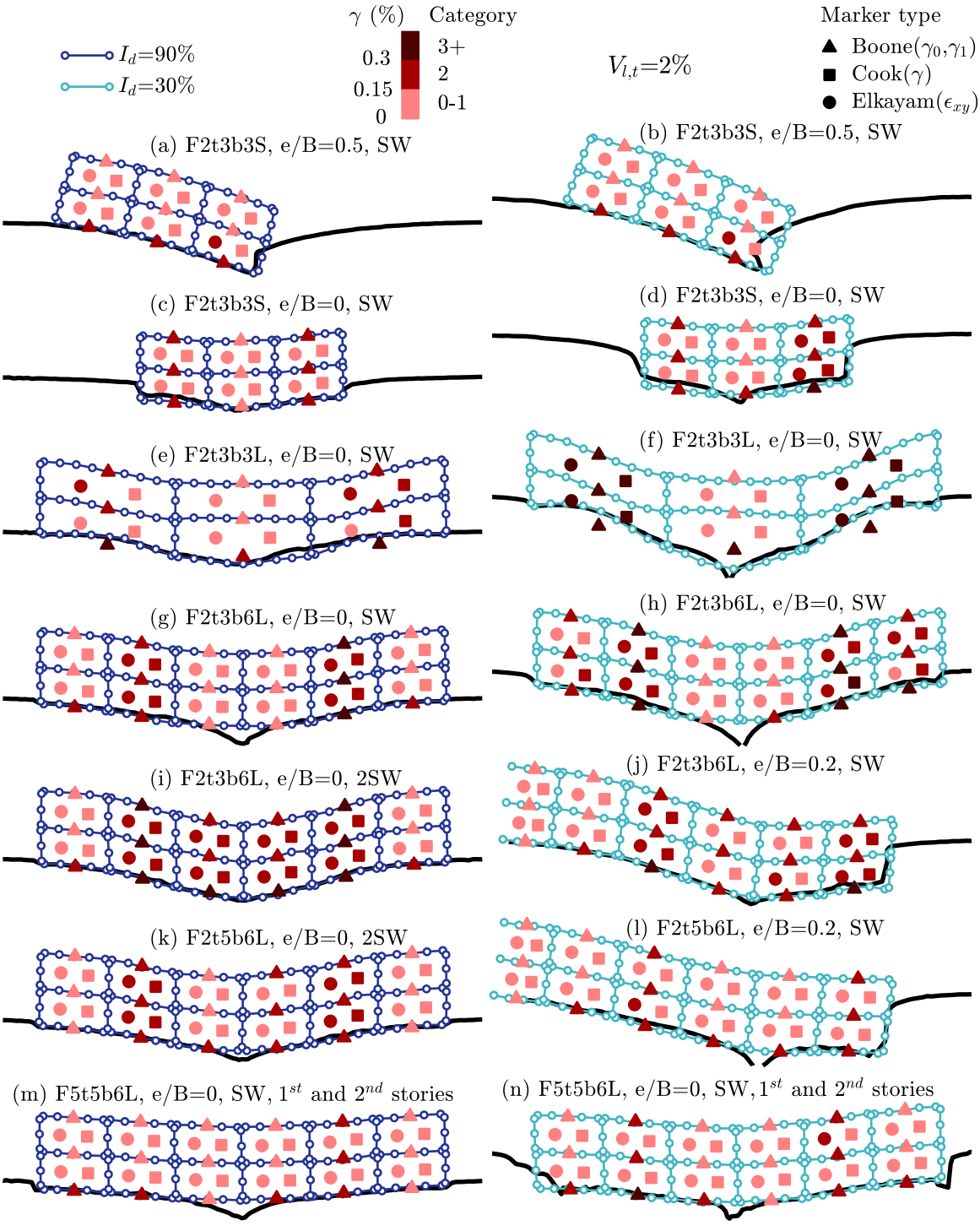


Fig. 4.30. Post-tunnelling frame deformed shapes and level of damage (scale factor: 100); left column is dense sand tests, right column is loose sand tests

$e/B = 0$, the looser soil led to slightly increased values of γ related to panel deformations.

Table 4.2. Maximum building angular distortion ($\gamma = \beta$) at $V_{l,t}$=2%

Test label	Bay-1 (%)	Bay-2 (%)	Bay-3 (%)	Bay-4 (%)	Bay-5 (%)	Bay-6 (%)	Soil relative density
F2t3b3S_eB0.5_SW	0.06	0.02	0.09	-	-	-	
F2t3b3S_eB0_SW	0.10	0.02	0.12	-	-	-	
F2t3b3L_eB0_SW	0.14	0.00	0.15	-	-	-	
F2t3b6L_eB0_SW	0.08	0.15	0.03	0.06	0.20	0.10	$I_d = 90\%$
F2t3b6L_eB0_2SW	0.08	0.23	0.15	0.16	0.25	0.09	
F2t5b6L_eB0_2SW	0.09	0.17	0.08	0.11	0.19	0.08	
F5t5b6L_eB0_SW	0.05	0.07	0.05	0.01	0.09	0.05	
F2t3b3S_eB0.5_SW	0.07	0.02	0.08	-	-	-	
F2t3b3S_eB0_SW	0.11	0.03	0.16	-	-	-	
F2t3b3L_eB0_SW	0.30	0.03	0.33	-	-	-	
F2t3b6L_eB0_SW	0.13	0.24	0.09	0.08	0.28	0.15	$I_d = 30\%$
F2t3b6L_eB0.2_SW	0.04	0.02	0.16	0.12	0.14	0.19	
F2t5b6L_eB0.2_SW	0.00	0.07	0.11	0.03	0.09	0.11	
F5t5b6L_eB0_SW	0.07	0.12	0.07	0.06	0.13	0.06	

The impact of the transverse width B is now considered. First, the short structure F2t3b3S can be seen as a portion (sub-structure) of the long frame F2t3b6L. Comparing Figure 4.30(c) to (g) and Figure 4.30(d) to (h) shows that increasing building transverse width (from spanning only the sagging zone to spanning both sagging and hogging zones) significantly increases the maximum angular distortion; from low to medium levels based on Cook (1994) and Elkayam and Klar (2019), and from medium to high levels according to Boone (1996). Second, the short frame F2t3b3S in Figure 4.30(a)-(b) can be regarded as the left half of the long frame F2t3b6L in Figure 4.30(g)-(h). Results show that the short frame F2t3b3S with $e/B = 0.5$ underwent significantly lower levels of distortion (low level for most panels) than the long frame F2t3b6L with $e/B = 0$ due to the effect of tilt for the eccentric configuration. These experimental results clearly display that the decrease of the transverse width B has a positive effect on reducing framed building distortions (for both central and eccentric tunnelling scenarios).

The effect of the width of the bay can be illustrated by comparing Figure 4.30(e)-(h). The results show that the external bays of the frame F2t3b3L (with larger bay width) experienced high levels of distortion in Figure 4.30(f) based on all approaches; this frame conformed closely to the ground movements. Frame distortion in Figure 4.30(e) tends to be similar to that in

Figure 4.30(g), possibly due to the effect of averaging the β values.

Interestingly, the decrease of soil relative density from $I_d = 90\%$ to 30% tends to increase the building distortion at a given $V_{l,t}$ because of higher values of $V_{l,s}$ (caused by greater levels of soil contraction for $I_d = 30\%$, refer to Figure 4.13), despite the increase of relative structure-soil stiffness. This can be seen in Figure 4.30(c-d), (e-f), (g-h), and (m-n); the stiffer the structure, the less the impact.

It is of interest to evaluate the efficiency of DR in identifying the structures with the largest distortions. Figure 4.30(g), (h), (i), and (k) show that the maximum shear distortion of the central long frames was generally observed at the second and fifth bays (near where the maximum slope of the ground settlement trough occurs), whereas for the third and fourth bays, which were subjected to the largest relative deflections associated with DR, building distortions are relatively small. The underlying cause of these limitations related to the deflection ratio, as also pointed out by Finno et al. (2005), can be mechanically interpreted as follows. The experimental load-deflection tests illustrated that the structure deformations (i.e. their response to loadings) were shear-dominated (refer to Section 3.7). For Timoshenko beam theory, while bending-dominated structure settlement profiles naturally display a relative deflection, in a shear-dominated structure the relative deflection (of sagging/hogging portions) is due to the change in the value of internal shear forces (e.g. change in sign of the shear due to a concentrated force). Because diagonal strains $\epsilon_{xz} = \gamma/2$ are proportional to the absolute value of the shear forces rather than the changes in forces, DR is not as efficient as $\gamma \approx \beta$ to evaluate distortions of framed buildings.

Figure 4.30(g) and (i) show that the increase of building weight significantly increased the angular distortion for the third and fourth bays of the frame: from low to medium levels based on Cook (1994) and Elkayam and Klar (2019), and to a high level according to Boone (1996). At the same time, angular distortion is also observed to increase in the second and fifth bays according to Boone (1996); from medium to high. Furthermore, high levels of damage are observed for most parts of the foundation slab due to the redistribution of pressure along the soil-foundation interface.

Consistent with the short frame F2t3b3S, Figure 4.30(h) and (j) illustrate that the increase

of building eccentricity decreased maximum shear distortions: from high to medium levels of damage for elevated slabs. The increase of the thickness t of building elements, which increased both stiffness and weight, resulted in the decrease of the structure distortions despite the increment in pressure beneath the building, as shown by comparing Figure 4.30(k) against (i), as well as (j) against (l).

Finally, to isolate the effects of building stiffness from changes in pressure, experimental results in Figure 4.30(k) and (m) can be compared since these two frames result in similar magnitudes of pressure beneath the building (refer to Table 3.6). As expected, results show that, for the given pressure, the increase of stiffness significantly reduced building distortions; from medium to low levels of damage for the second and fourth bays.

4.7.3 Modification factor against relative soil-building stiffness

4.7.3.1 Estimation of soil stiffness

In this study, the representative soil stiffness E_s was estimated using the approach adopted by Farrell (2010), which consists of two steps: 1) a representative soil shear strain (considering stiffness degradation due to tunnel volume loss) is assessed at a mid-point ($z = z_t/2$) between the surface and the tunnel axis for each tunnel-building interaction test; 2) soil stiffness E_s is estimated using triaxial test provided by Zhao (2008) (for the same sand used in these tests). The detailed process is illustrated below.

In the first step, the average shear strain γ_{avg} at the depth of $z = z_t/2$ within the tunnelling influence zone (settlement trough extension ±2.5i) was computed for each centrifuge test as the representative shear strain value, given as:

$$\gamma_{avg} = \frac{1}{5i}\int_{-2.5i}^{+2.5i} \gamma_s dx \tag{4.2}$$

Second, in order to estimate the soil stiffness degradation from experimental average shear strain γ_{avg}, it is important to understand the relationship between shear strain and soil stiffness. Zhao (2008) performed triaxial tests using the same sand (Fraction E), and obtained the required relationships, as shown in Figure 4.31(a)-(b). However, the sample tested by Zhao (2008) is at

a relative density of 70% and a confining pressure of 100 kPa, which differ from the soil density and confining pressure in the greenfield and tunnel-frame interaction tests in this study. Therefore, to consider these differences (soil state and confining pressure), the framework presented by Lehane and Cosgrove (2000) is used.

$$\begin{aligned} E_v^{'} &= \frac{E_0}{1+\left(\frac{\epsilon-\epsilon_{el}}{\epsilon_r-\epsilon_{el}}\right)^n} && \text{for } \epsilon \geq \epsilon_{\text{el}} \\ E_v^{'} &= A_E F(e)\left(\frac{\sigma_v^{'}}{p_{atm}}\right)^{0.5} = E_{v0} && \text{for } \epsilon \leq \epsilon_{\text{el}} \end{aligned} \tag{4.3}$$

where E_{v0} is the maximum stiffness at low axial strain, $E_v^{'}$ is secant axial stiffness, ϵ is axial strain, ϵ_{el} is the strain when the soil stiffness-strain becomes non-linear, ϵ_r is the reference strain equalling to the value of ϵ when $E_v^{'} = 0.5E_{v0}$, n and A_E are constant values depending on the material property, $\sigma_v^{'}$ is the vertical effective stress, p_{atm} is atmospheric pressure (100 kPa), $F(e) = (2.17-e)^2/(1+e)$ (Hardin and Richart, 1963), and e is the void ratio.

The data from Zhao (2008) was used to determine the values of unknowns ($F(e)$, n and A_E) using known values ($\epsilon_{el} = 1\times10^{-5}$, $\epsilon_r = 4\times10^{-4}$, $E_{v0} = 220$ MPa, $E_v^{'} = 100$ kPa, and $e = 0.73$). Figure 4.31(a) and (b) shows, respectively, the fitted lines for $E_{v,sec}$ and G_{sec} of triaxial data ($I_d = 70\%$ and $E_v^{'} = 100$ kPa). In particular, the fitted line for $E_{v,sec}-\epsilon_v$ was obtained using Equation 4.3, whereas the equation from Franza (2016) was used to find the fitted line for $G_{sec}-\gamma$. Next, the value of E_{v0} for a given centrifuge test was computed by Equation 4.3 using corresponding $F(e)$ (depending on I_d) and $\sigma_v^{'}$ (considering the pressure from the structures in the tunnel-building interaction tests). Therefore, new relationships of $E_{v,sec}-\epsilon_v$ and $G_{sec}-\gamma$ were obtained (see Figure 4.31(a) and (b) for greenfield tunnelling in loose and dense sand results). Finally, the representative soil stiffness E_s (i.e. $E_{v,sec}$) can be estimated from the average shear strain γ (obtained by Equation 4.2) assuming $E_{v,sec} = G_{sec}\times2(1+\nu)$.

Using this approach, for greenfield tunnelling tests, at $V_{l,t} = 1-2\%$, $E_s = 68-45$ MPa for $I_d = 90\%$ and $E_s = 34-21$ MPa for $I_d = 30\%$ (see Figure 4.31(d)). For the extreme cases with the heaviest frame F5t5b6L, again at $V_{l,t} = 1-2\%$, $E_s = 93-60$ MPa for $I_d = 90\%$, and

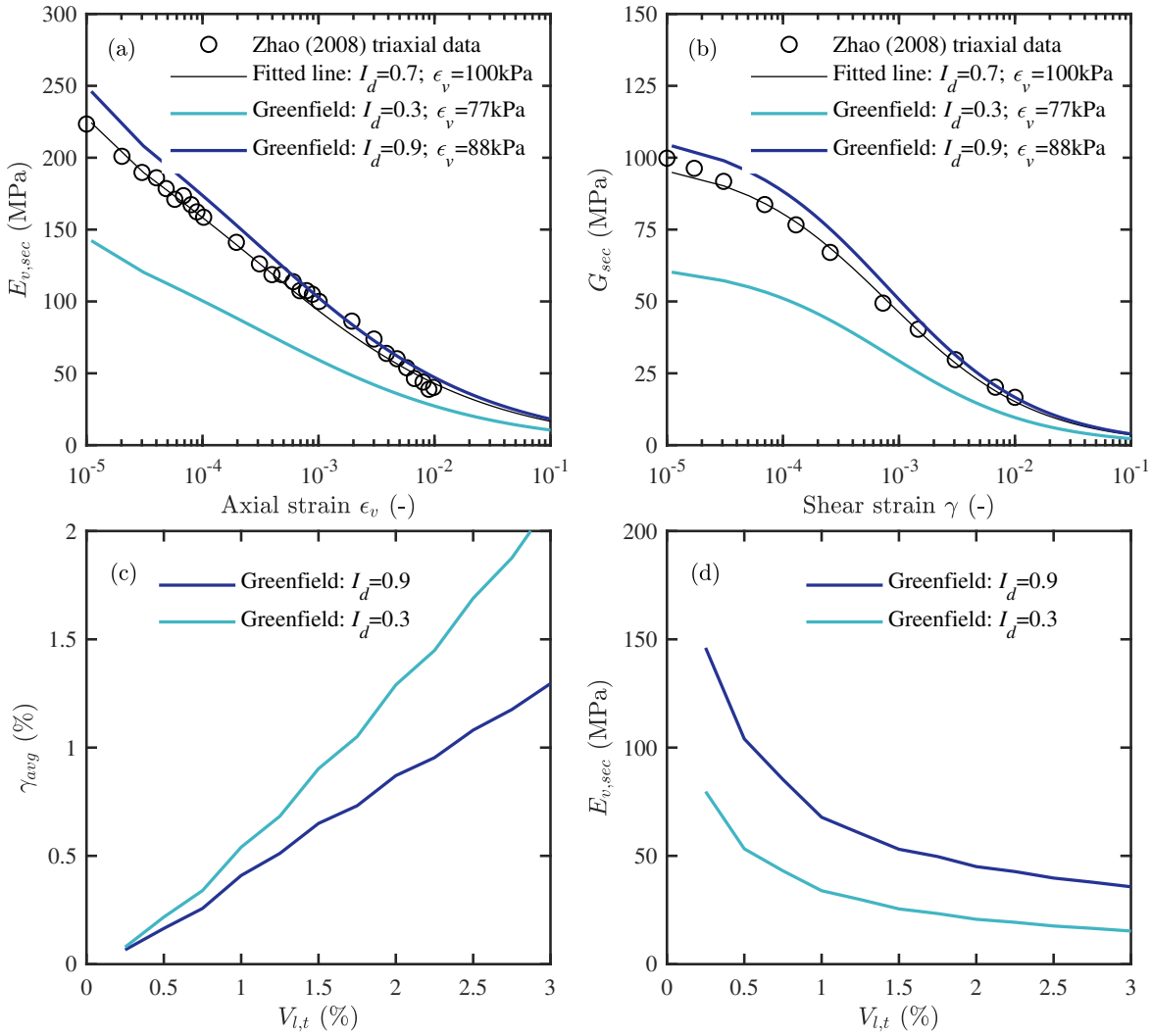


Fig. 4.31. (a) Vertical and (b) shear stiffness degradation with strains, (c) average shear strain and (d) soil stiffness with volume loss

$E_s = 65 - 37$ MPa for $I_d = 30\%$.

4.7.3.2 Modification factor of deflection ratio

Although deflection ratios DR may not be fully representative when estimating the shear deformations of long frames, they are still valuable for evaluating the efficiency of design charts and interaction models in predicting the effects of soil-structure interaction.

Figure 4.32 displays the modification factors $M^{DR,sag}$ and $M^{DR,hog}$ at $V_{l,t} = 1\%$ and 2%

against relative bending stiffness, $\rho_{sag/hog}$ (Mair, 2013) and $\eta_{sag/hog}$ (Franza et al., 2020a), which were estimated using Equations 2.32 and 2.33 with EI_{exp} and $GA_{s,exp}$ as well as the values of $B_{sag/hog,gf}$ (i.e. based on greenfield displacements). Data from all 22 tunnel-framed building interaction centrifuge tests presented in this chapter are reported in Figure 4.32. Upper and lower envelopes suggested by Mair (2013) and Franza et al. (2020a) are also included in Figure 4.32(a) and (b), respectively. In Figure 4.32(b), the envelopes for plane-strain conditions were selected.

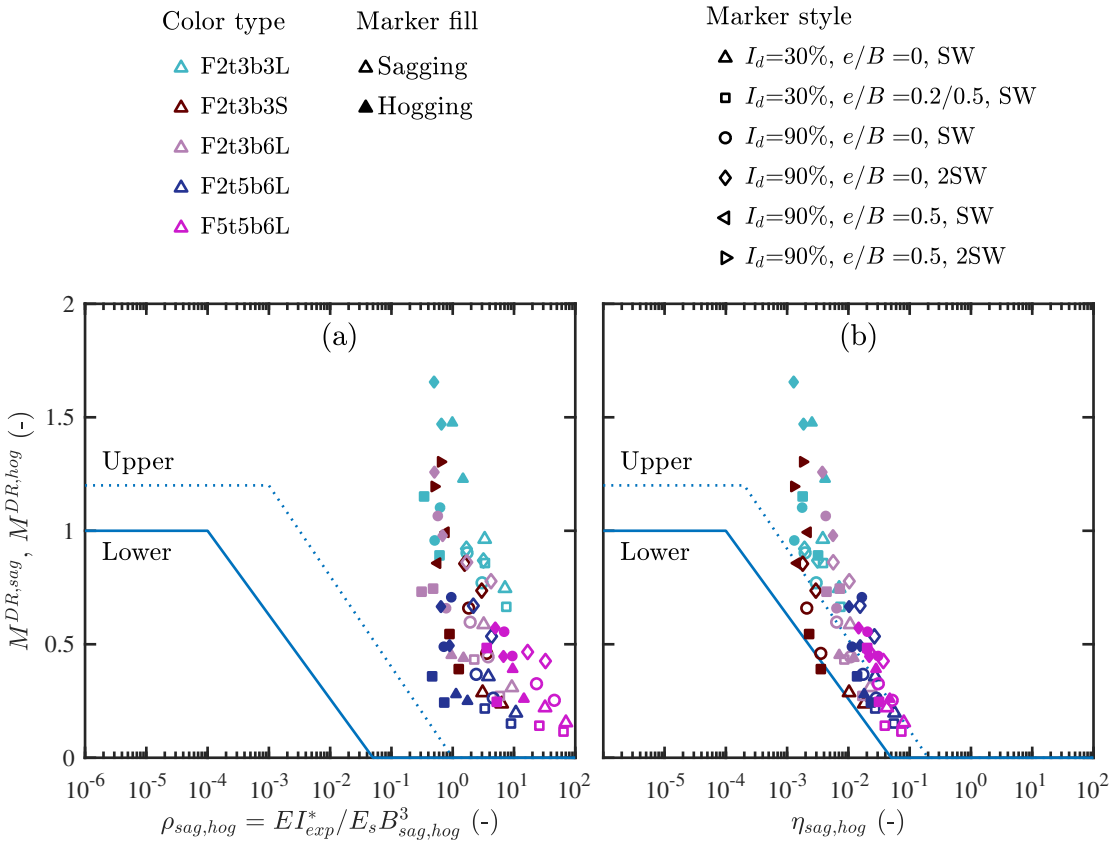


Fig. 4.32. Modification factors of DR against relative stiffness ($V_{l,t}$ = 1 and 2%): (a) $\rho_{sag/hog}$ (Mair, 2013), and (b) $\eta_{sag/hog}$ (Franza et al., 2020a)

The results in Figure 4.32(a) show that all the framed building data points are outside the envelopes when $\rho_{sag/hog}$ is estimated from the actual structure bending stiffness EI^*_{exp}, which for the considered frames is about a third of the bending stiffness suggested by Franzius et al. (2006) obtained when using the parallel axis theory (Equation 2.36). The structure stiffness

relative to the soil was overestimated, and thus values of M^{DR} are significantly underestimated. This is because this method neglects the impact of the global shear flexibility of the frame, which dominates the interaction problem for framed structures (with no bearing infill walls).

Figure 4.32(b) shows that $\eta_{sag/hog}$ provides a better description of the relative structure-soil stiffness for framed buildings, supporting the robustness of the analytical interaction solutions of Franza et al. (2020a). However, it is important to note that $\eta_{sag/hog} = \rho_{sag/hog}$ is obtained from Equation (2.32) by assuming $EI^* = EI^*_{EB,eq} = Et^3_{eq}/12$. This confirms the reliability of the framework provided by Mair (2013) relating the equivalent (pure) bending stiffness $EI_{EB,eq}$ to the deflection ratio modification factor through $\rho_{sag/hog}$. Therefore, when estimating building stiffness, it is important to distinguish if the equivalent bending stiffness $EI_{EB,eq}$ is already decreased (to account for the shear flexibility) from the actual value of EI; for instance, $EI_{EB,eq}$ is obtained by using the column stiffness factor with the algebraic sum proposed by Goh and Mair (2014) rather than EI.

Regarding trends shown in Figure 4.32, the values of $M^{DR,hog}$ (solid markers) tend to be larger than $M^{DR,sag}$ (hollow markers) for all frames. The largest measured values of $M^{DR,sag}$ are approximately 1.0, whereas the more flexible frames give $M^{DR,hog}$ values greater than unity. This is possibly due to the effects of gap formation in the sagging zone (at $V_{l,t} = 2\%$) and frame embedment at its edges (with the formation or increase of a hogging settlement profile in the outer regions of the building).

4.7.3.3 Modification factor of angular distortion

To link angular distortion with relative soil-building stiffness, a logic similar to Son and Cording (2005) is followed by developing a modification factor chart to estimate β from the slope of the greenfield surface settlement profile and a relative stiffness parameter that relates to the structure shear stiffness. First, for each bay of a given frame, the building angular distortion β (estimated using Equation 2.17) and average greenfield ground slope ($\overline{GS} = \Delta U_{z,gf,max}/b_{bay}$, where $\Delta U_{z,gf,max}$ is the differential settlement of the portion of greenfield surface settlement trough corresponding to b_{bay}) are calculated. Then, the maximum experimental angular distortion among all bays β_{max} is normalised by the maximum greenfield slope corresponding to the

building ($\overline{GS}_{max}$) to obtain a modification factor of angular distortion, M^{β}:

$$M^{\beta} = \frac{\beta_{max}}{\overline{GS}_{max}} \tag{4.4}$$

For instance, $M^{\beta} = 1$ for a fully flexible structure deforming purely in shear according to the greenfield settlement trough with local tilt $\omega = 0$. The modification factor of angular distortion is then related to the relative soil-building shear stiffness, estimated as

$$\kappa = \frac{E_s B}{GA_s^*} = \frac{E_s BL}{GA_s} \tag{4.5}$$

where GA_s^* is the building shear stiffness per meter run (i.e. GA_s normalised by the building length L in the longitudinal direction of the tunnel).

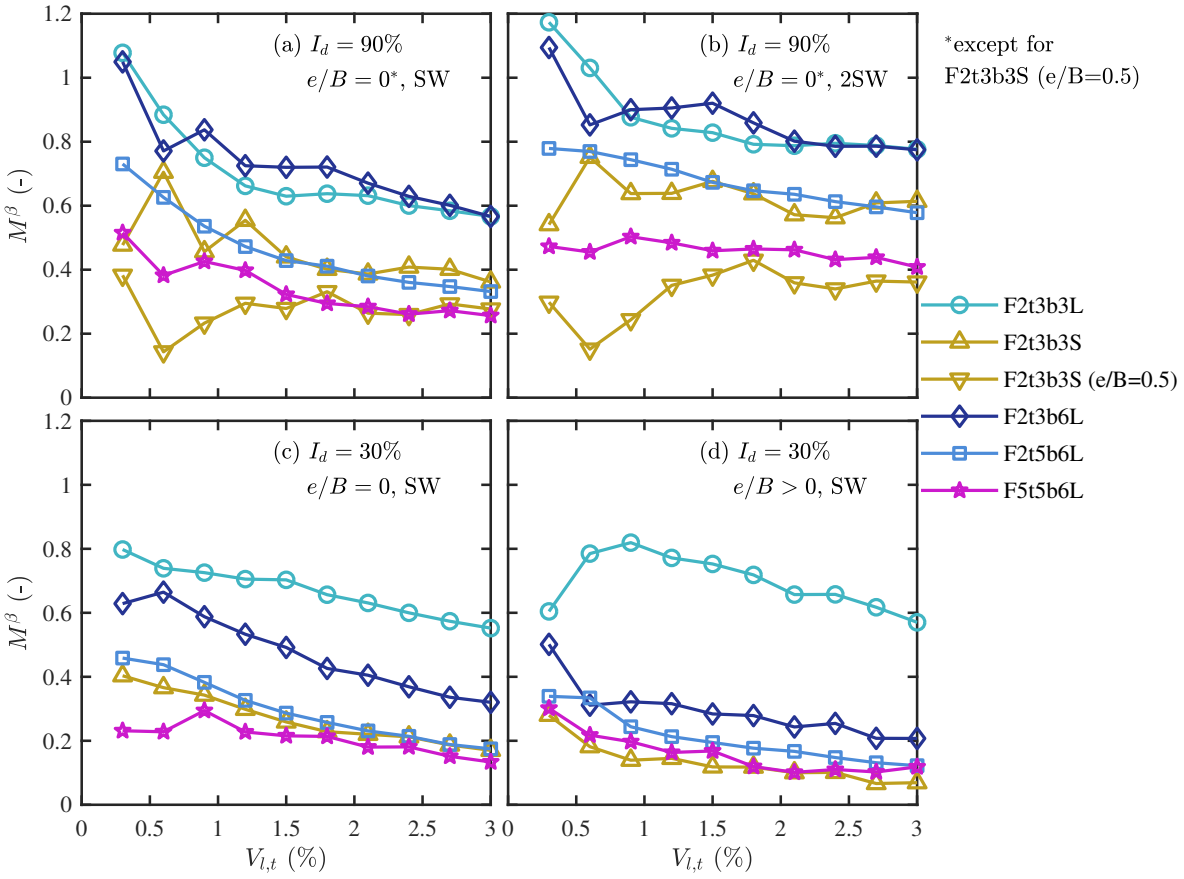


Fig. 4.33. Modification factors of β against tunnel volume loss $V_{l,t}$

First, the variation of the modification factor of angular distortion M^{β} with tunnel volume loss $V_{l,t}$ is discussed. Results in Figure 4.33 show that most M^{β} trends are characterised by a steady decrease with $V_{l,t}$ over the investigated range, and a greater rate of decrease is obtained for the loose soil tests. This is consistent with the trends of the modification factor of deflection ratio (see Figure 4.28). The decrease of the modification factor of angular distortion M^{β} with tunnel volume loss $V_{l,t}$ is due to both soil stiffness degradation that occurs with tunnelling process and, when present, gap formation (see Figure 4.10). Moreover, the increase of structural stiffness, soil density (from 30% to 90%), building weight, and normalised eccentricity tends to decrease, increase, increase, and decrease, respectively, the M^{β} values for a given $V_{l,t}$, while the decrease of building transverse width significantly decrease the M^{β} value (compare long frame F2t3b6L and short frame F2t3b3S). Data of frames F2t3b3L and F2t3b6L in Figure 4.33(a) and (b) highlight again the importance of considering the structural configuration; M^{β} values of two frames are similar, despite frame F2t3b3L being more flexible than frame F2t3b6L. Interestingly, the curves of the eccentric short frame F2t3b3S in the dense soil (Figure 4.33(a) and (b)) show significant fluctuation, possibly due to the localised soil failure and slippage at the soil-structure interface (because of the freedom of tilt and rotation).

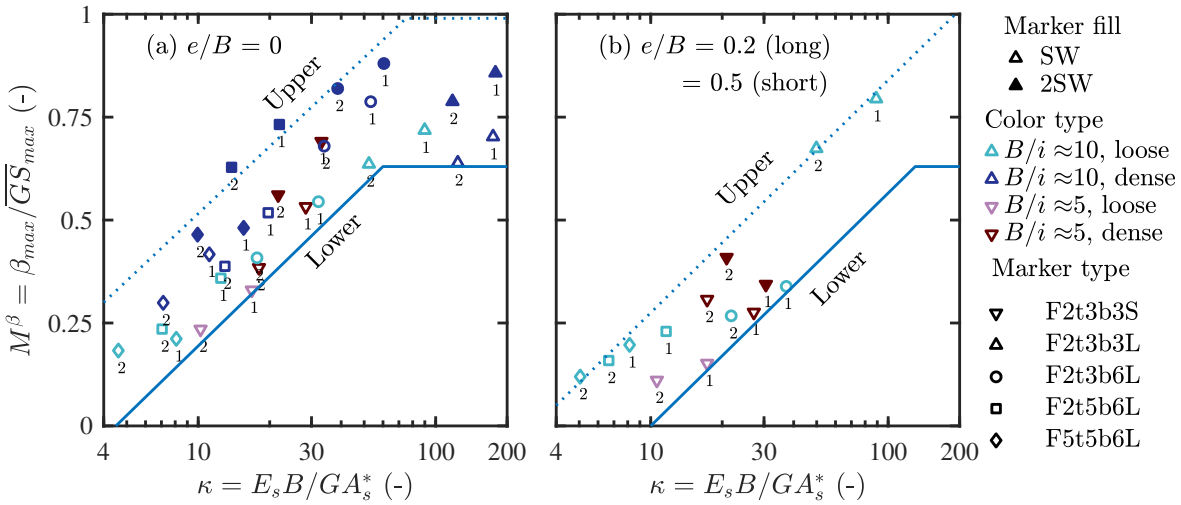


Fig. 4.34. Modification factors of β against relative soil-building shear stiffness (numbers beneath markers indicate $V_{l,t}$)

Figure 4.34 presents the relationship between M^{β} and κ (in log scale) at $V_{l,t} = 1$ and 2%

(numbers beneath markers indicate $V_{l,t}$). To highlight the effects of soil density and building transverse width, a colour scheme was adopted to distinguish between soil density and the value of the ratio B/i, where i is the distance to the inflection point of the greenfield settlement trough. Data from central ($e/B = 0$) and eccentric ($e/B > 0$) structures are plotted in Figures 4.34(a) and (b), respectively. Several trends can be gleaned from Figure 4.34: M^{β} tends to increase linearly (in semi-log scale) with an increase of relative soil-building shear stiffness (which agrees with Son and Cording (2005)); a decrease in building width ratio B/i decreases M^{β}; and an increase of building eccentricity e/B reduces M^{β} (because of the building tilt, which is in agreement with Figure 4.30). Finally, an increase of building weight also results in a higher M^{β} (compare hollow to solid markers), partially because of greater ground deformations transmitted to the heavier buildings in cases where gap formation was less significant.

Based on the distribution of the data points, upper and lower empirical envelopes for the modification factors of building angular distortions are also suggested in Figure 4.34. For the central structures ($e/B = 0$), the upper envelope can be expressed as:

$$\begin{aligned} M^{\beta} &= 0 && \text{for } \kappa < 1.2 \\ M^{\beta} &= 0.56\log\kappa - 0.0436 && \text{for } 1.2 \le \kappa \le 75 \\ M^{\beta} &= 1 && \text{for } \kappa > 75 \end{aligned} \tag{4.6}$$

and the lower envelope can be expressed as:

$$\begin{aligned} M^{\beta} &= 0 && \text{for } \kappa < 4.5 \\ M^{\beta} &= 0.56\log\kappa - 0.366 && \text{for } 4.5 \le \kappa \le 60 \\ M^{\beta} &= 0.63 && \text{for } \kappa > 60 \end{aligned} \tag{4.7}$$

For the eccentric scenarios ($e/B > 0$), the upper envelope can be expressed as:

$$\begin{aligned} M^{\beta} &= 0 && \text{for } \kappa < 3.3 \\ M^{\beta} &= 0.56\log\kappa - 0.2886 && \text{for } 3.3 \le \kappa \le 200 \\ M^{\beta} &= 1 && \text{for } \kappa > 200 \end{aligned} \tag{4.8}$$

and the lower envelope can be expressed as:

$$\begin{aligned} M^{\beta} &= 0 && \text{for } \kappa < 10 \\ M^{\beta} &= 0.56\log\kappa - 0.5569 && \text{for } 10 \leq \kappa \leq 132 \\ M^{\beta} &= 0.63 && \text{for } \kappa > 132 \end{aligned} \tag{4.9}$$

Because of the limited number of considered cases in this study (for instance, the scenarios with stiffer structures, or long frames with a greater eccentricity (>0.2) could be tested), and given that the envelopes are based solely on experimental results, care should be taken when the suggested empirical envelopes are referenced for real tunnelling projects. Despite these limitations, the proposed empirical envelopes do provide a useful framework for the preliminary assessment of building damage caused by tunnel construction.

4.8 Summary

A comprehensive study on the response of framed buildings on raft foundations to tunnelling was presented in this chapter, including data from a unique set of centrifuge tests. The tunnelling-induced displacements of the framed buildings and the underlying soil were analysed; the tunnelling-induced ground movements affected by the presence of the buildings are presented; the framed structure deformations were studied using deflection ratios, angular distortions, and strain-based damage categories. The following conclusions can be drawn from the work.

- Comparison of settlement profiles demonstrated that the settlements of equivalent isotropic plate models (with a bending dominated deformation mode) do not always adequately match those from framed building models, missing important features mainly with respect to the shape of the foundation settlement.

- Generally, for both loose and dense soil, a greater building weight and larger transverse width increase the tunnelling-induced framed building distortions, whereas a larger building eccentricity (facilitating building tilt) and higher stiffness tend to reduce frame distortions.

- For a given tunnel volume loss (representative of the performance of tunnelling operations), the relative density of dry sands impacted the level of settlement of the ground surface and, consequently, the distortions of the frames. Loose sands have greater potential for building distortions than dense sands at a given tunnel volume loss. On the contrary, for a given soil volume loss at the ground surface, buildings experienced similar levels of settlement and distortion for varying sand densities, with loose sand tests giving slightly smaller distortions.

- Soil relative density I_d dominated the $V_{l,s} - V_{l,t}$ relationship for all presented centrifuge tests, which impacted the overall structure settlement level; therefore, for the loose soil tests, the loose sand exhibits a contractive response, whereas the dense soil transitions from contractive at lower values of $V_{l,t} < 1\%$ towards dilative at higher tunnel volume losses.

- The presence of the framed buildings on raft foundations has a great impact on the tunnelling-induced ground movements. For the central long structures, or the long buildings with limited eccentricity (for instance, $e/B = 0.2$ in this study), the horizontal displacements of the soil near the surface are largely restricted by the foundation roughness and building pressure towards the external part of the building; the smaller the gap formed at the soil-foundation interface, or the heavier the structure, the greater the restriction to the horizontal displacements of the soil. For the short structure, the eccentric ($e/B = 0.5$) building increases the horizontal displacement of the soil near the surface because of the freedom to shift, compared with the central short frame. The influence of the building on the ground settlement field is minor for relative lightly structures, whereas a heavy building tends to widen the soil vertical displacement field, particularly for the loose sand. The restriction of the foundation to the soil horizontal movements generally results in a thin shear band at the soil-foundation interface with a decreased maximum contraction level and some areas of dilation present; the overall level of the shear strains depends on the magnitude of the soil vertical displacements. For a given tunnel volume loss, soil density mainly affects the magnitude of the displacements; due to the fact that the response of the loose soil is dominated by contraction, soil horizontal and vertical displacements, as well as the shear strain, were significantly increased compared with the dense soil test. However, settlements and shear strains of the loose soil are smaller

than those of the dense soil for a given soil volume loss.

- Experimental data of deflection ratio modification factors agreed with existing charts; in particular, experimental results confirmed that the bending and shear stiffness of framed buildings may be directly estimated by modelling load-deflection tests.
- A modification factor was suggested to link framed building angular distortion to relative soil-building shear stiffness, in which interesting linear trends were highlighted (in semi-log scale); upper and lower envelopes for preliminary damage assessment considering building eccentricity were suggested.
- Several key aspects were highlighted from the work which have implications for engineering practice. First, the need to monitor/evaluate framed building displacements at multiple elevations to better estimate deformations and damage was confirmed; foundation level deformations may be greater than within the superstructure. Framed buildings on raft foundations will likely have a shear dominated deformation mode. Framed structures centrally located above a tunnel will have the greatest potential for distortions compared to eccentric cases. When possible, to better estimate the distortions of frames, shear strains should be evaluated using the displacements of the corners of bays/panels rather than using a deflection ratio based evaluation.

In this chapter, the considered scenarios were limited to a tunnel with a constant cover-to-diameter ratio constructed in dry sand beneath an elastic framed building with a raft foundation. Chapter 5 will investigate the effect of foundation type on tunnelling-induced building and ground distortion, whereas Chapter 6 will study the roles of footing embedment and tunnel cover depth on tunnel-foundation interaction.

Chapter 5

Comparison between rafts and separate footings

Chapter 4 provided experimental evidence that framed buildings on raft foundations primarily exhibit shear distortions when subjected to tunnelling-induced displacements and suggested, by contrasting framed building results with equivalent plate test results from Farrell et al. (2014), that the use of equivalent beams/plates with minimal shear flexibility may not be adequate for framed buildings.

With regard to foundation effects, while structural horizontal strains at the ground level are negligible for continuous foundations (Franzius et al., 2006; Dimmock and Mair, 2008), discontinuous foundations can result in large differential horizontal displacements (Laefer et al., 2009; Goh and Mair, 2014; Fu et al., 2018), which have the potential to affect the deformation mechanisms of framed buildings (Franza and DeJong, 2019; Fu et al., 2018). Experimental data related to tunnelling-induced ground displacements and deformations are limited to continuous foundations (i.e. strips and rafts) (Farrell et al., 2014; Ritter et al., 2017), whereas field data are sparse with limited insights into the subsurface soil behaviour (Dimmock and Mair, 2008; Goh and Mair, 2014). Because of the lack of a systematic experimental investigation of the effects of foundation configuration on both structural distortion and soil movements, the research community is limited in their capability to develop and verify reliable numerical and analytical tools.

This chapter investigates the influence of foundation configuration on the tunnel-soil-frame interaction. Two configurations are considered: a 'raft' foundation that is continuous beneath the entire building footprint, and a 'separate footing' foundation (strip footings parallel to the tunnel axis) that is discontinuous in the direction transverse to the tunnel axis (see Figure 5.1). The chapter presents data obtained from plane-strain geotechnical centrifuge tests using dry sand. Greenfield and raft foundation test data from Chapter 4 are used here as a reference for comparison with the separate footing results. A parametric study considering building width, weight, eccentricity (i.e. lateral offset from the location of the tunnel), and soil density is presented. Tunnelling-induced soil movements and deformation fields, framed building displacements, and structure shear distortions (with associated modification factors) are illustrated.

5.1 Considered tests

Data from 22 centrifuge tests are selected and presented in this chapter, as shown in Table 5.1 and Figure 5.1, including 2 greenfield tests and 20 tunnel-frame interaction tests (involving a long frame F2t3b6L and a short frame F2t3b3S, with either a raft or separate footings). For a given frame model, the relative density of the sand (I_d = 30, 90%), the eccentricity (e) of the model building with respect to the tunnel, and the building self-weight (SW: standard self-weight; 2SW: double self-weight) were varied in the experiments. For the long frame (F2t3b6L), a total of 4 tests were performed for each foundation configuration: 2 tests involving a central tunnel in loose and dense soil for a standard weight SW building, 1 test with a central tunnel in dense sand and the 2SW frame, and 1 test for an eccentric tunnel case with $e/B = 0.2$ in loose sand and the SW frame. For the short building model (F2t3b3S), 6 tests were performed for each foundation configuration: for the loose sand, normalised eccentricity e/B of 0 and 0.5 were tested for the standard weight SW case only; for dense sand, both cases of e/B (0 and 0.5) and building weight (SW and 2SW) were tested.

Table 5.1. Considered centrifuge tests in Chapter 5

Total No.	Label	Foundation type	I_d (%)	e/B	Weight (pressure†, kPa)
2	Greenfield	-	30 & 90	-	-
6	Short	Raft	30	0 & 0.5	SW(19.4)
			90	0 & 0.5	SW(19.4) & 2SW(38.8)
6	Short	Separate footings	30	0 & 0.5	SW(94.4)
			90	0 & 0.5	SW(94.4) & 2SW(189)
4	Long	Raft	30	0 & 0.2	SW(22.8)
			90	0	SW(22.8) & 2SW(45.6)
4	Long	Separate footings	30	0 & 0.2	SW(103)
			90	0	SW(103) & 2SW(206)
3	Loading	Separate footings	30 & 90	-	-

† Average value beneath the foundation at 68 g

The average pressure data beneath the foundation at 68 g are also presented in Table 5.1. Clearly, the average pressure beneath the footing is much higher than the pressure beneath the raft foundation. Based on the loading test results that will be presented in Section 5.2, the safety factor with respect to nominal average building pressure can be assessed based on the soil density and the average pressure beneath the foundation.

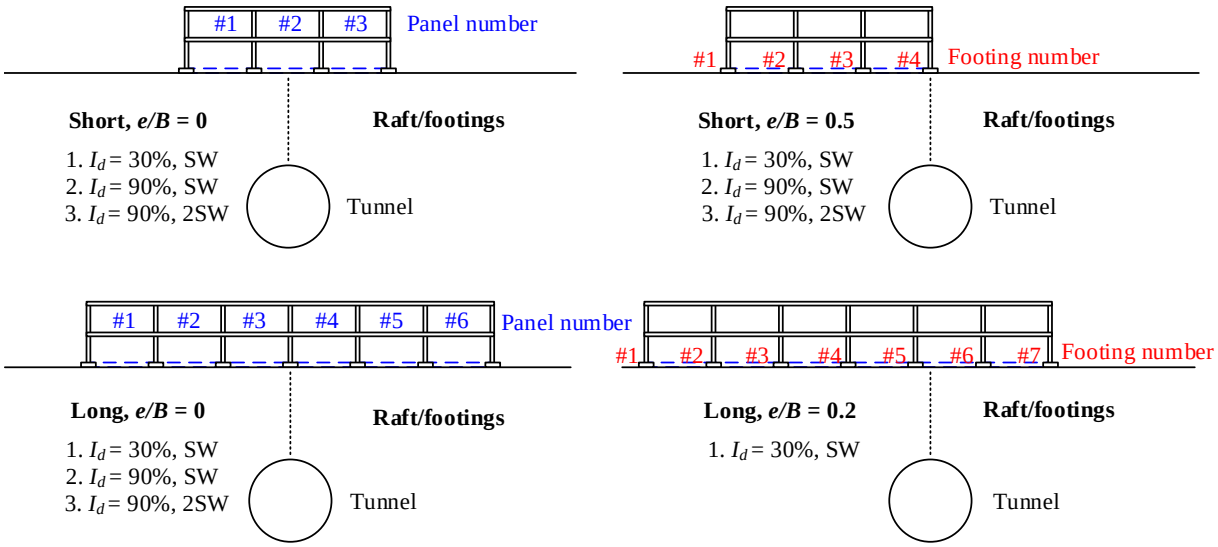


Fig. 5.1. Illustration of the 20 considered tunnel-frame interaction tests

5.2 Evaluation of footing capacity

5.2.1 Experimental setup

Based on the total weight of the building model (considering the variation of the gravity level), and the total area of the footings, the average pressure beneath the footings for SW and 2SW frames are calculated to be around 100 and 200 kPa, respectively (refer to Table 5.1). To evaluate the ultimate capacity of the footings, a series of loading tests were conducted; this information is used in the interpretation of results presented in this chapter and Chapter 6, and may be useful for others conducting the numerical analysis of the problem.

Figure 5.2 shows the setup and layout of the loading tests. The loading system developed by Song (2019) was used, including stepper motors, gearboxes, couplers, loading bars and die springs. The control program compiled under the LabVIEW environment was used to achieve displacement control of the footing model. LVDTs and load cells were used to measured the induced displacements and applied loads of the footing models. To diminish the effect of bending moment on the accuracy of the load cell, a ball-joint mechanism connecting the load cell and the model footing was adopted, as shown in Figure 5.2. The footing models were loaded vertically with the guide of the fixed plates. To reduce the effect of the friction force, low-friction PTFE (polytetrafluoroethylene) sections were bonded to the surfaces of both the footing models and

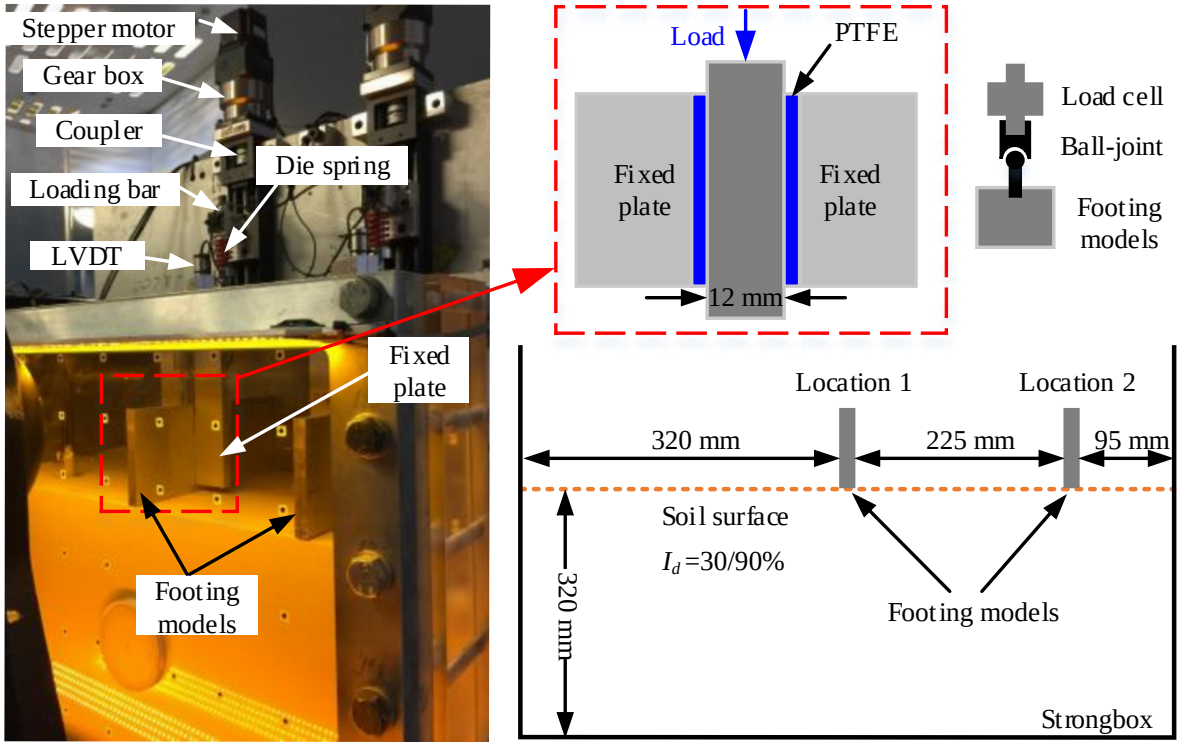


Fig. 5.2. Setup and configuration of the footing loading tests

fixed plates (Figure 5.2).

The loading tests were performed at two locations within the strongbox: position 1 at the centre of the strongbox, and position 2 at 225 mm from the centre and 95 mm away from the sidewall. These locations correspond to the positions of the central and external footings, respectively, of the long frame with $e/B = 0$. Using a load controlled system, two loading conditions were implemented during the spin-up phase of the loading tests to achieve either a footing initially detached from the surface (null initial pressure q_0) or a footing loaded such that the average applied pressure was equivalent to the pressure beneath the model building footings (which varied during centrifuge spin-up). The latter was considered to assess the influence of placing the building model at 1 g on the pressure-settlement relationship. Upon reaching 68 g, a displacement controlled system was activated and the footing in position 1 was jacked at 0.02 mm/s and then unloaded. The footing in position 2 was then tested in the same way.

Table 5.2. Footing loading test results (prototype scale)

No.	Test	I_d (%)	Pos.	q_0 (kPa)	q_p or q_c (kPa)	S_c (mm)	Initial loading stiffness (kPa/mm)	Unloading stiffness (kPa/mm)
(1)	1	30	1	101	460	120	2.7	64.8
(2)			2	0	460	170	2.8	78.3
(3)	2	90	1	202	-	-	15.1	76.0
(4)			2	0	-	-	14.8	100.1
(5)	3	90	1	0	2010	185	14.5	73.9
(6)			2	0	2086	180	16.1	111.2

5.2.2 Loading test results

The results of the separate footing loading tests, conducted in loose and dense sand to assess the pressure-settlement relationship, are shown in Figure 5.3, while Table 5.2 summarises the tested configurations and results. As mentioned earlier, the non-zero initial pressure q_0 in tests 1 and 2 was used to replicate the effect of the stress beneath the SW and 2SW separate footings of the model frames (100 and 200 kPa for SW and 2SW frames, respectively). Due to the limited capacity of the loading actuator used in test 2 for dense sand, the footing was unloaded prior to reaching a peak load (still providing data for initial and unloading stiffness). Table 5.2 also provides a summary of the main features of the pressure-displacement curves: the peak resistance of the footing q_p in the dense sand tests; the stress in the loose sand tests at which a significant change (decrease from around 2.8 to 0.8 kPa/mm) in the tangent stiffness occurred q_c; the settlement S_c corresponding to q_p and q_c; the initial loading stiffness and the unloading stiffness, taken as a tangent to the 'linear' portion of the initial loading and unloading curves (accepting that the curves are not perfectly linear).

The pressure-settlement curves are highly dependent on soil density, whereas the initial pressure q_0 and footing position have minor effects. The soil reaction pressure of the loose sand tests (test 1; positions 1 and 2) continuously increased with footing displacement with a distinct change in a rate at q_c = 460 kPa but with no peak pressure, while the full pressure-settlement curves of the dense sand tests (test 3; positions 1 and 2) present a peak resistance followed by a reduction at higher settlements (consistent with Vesic (1963); Lau and Bolton (2011)).

Interestingly, when the initial pressure is $q_0 = 0$, the settlement S_c for both soil densities is

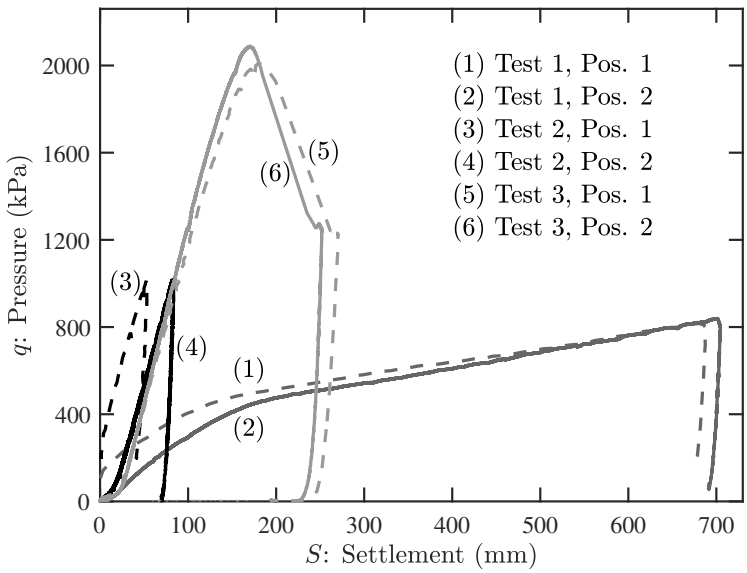


Fig. 5.3. The response of the footing models to vertical loading (dimension in prototype)

within 170-185 mm, corresponding to 21-23% of the transverse width of the footing. In relation to the tunnel-frame interaction test results presented later (where $q_0 \neq 0$), the effect of applying q_0 =101-202 kPa was to decrease the value of S_c to 120-150 mm (estimated for dense soil from test 2, position 1 by projecting the trend to $q_p \approx 2000$ kPa), corresponding to 15-18% of the transverse footing width. Using the values of q_p and q_c for the dense and loose sand cases, respectively, a safety factor with respect to nominal average building pressure (see Table 3.4) can be computed as $SF \approx 20$ and 10 for the frame on dense soil with standard self-weight SW and double self-weight 2SW, respectively, while $SF \approx 4.5$ and 2.3 for the SW and 2SW frames on loose soil, respectively. The SF values of the footings are certainly low for the loose soil scenario, particularly for 2SW frame (only one test in Chapter 6). As mentioned earlier, the results of the loose soil tests are mainly used to establish the contrasting effect of loose versus dense soil, hence, this issue is considered to be minimal.

5.3 Model spin-up

5.3.1 Effect of the building presence on soil movements

Figure 5.4 shows horizontal (U_x) and vertical (U_z) displacement contours (normalised by the tunnel diameter D_t) of the soil during centrifuge spin-up in selected tests, all in dense soil. In Figure 5.4 and this chapter, positive horizontal and vertical displacements are oriented, respectively, towards the right and downwards (refer to Figure 2.11), unless otherwise indicated. Greenfield ground behaviour in Figure 5.4(a) has been discussed in Section 4.2 of Chapter 4, including the buoyancy and ovalisation of the model tunnel, as well as the soil densification phenomenon during centrifuge spin-up.

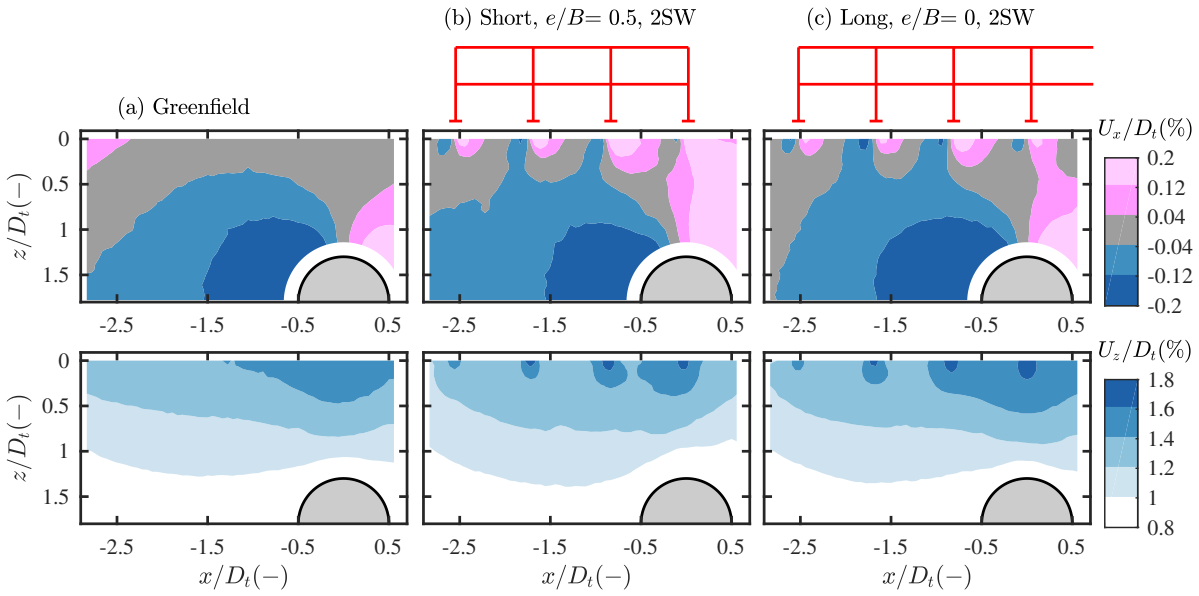


Fig. 5.4. Horizontal and vertical displacements (normalised by the tunnel diameter D_t) of the dense (I_d = 90%, 2SW) soil in selected footing tests during centrifuge spin-up from 1 to 68 g (data outside the contour thresholds were set equal to the closest limit value)

The impact of the footings on ground movements is assessed. Contrasted against the scenarios of raft foundations in Figure 4.2 of Section 4.2, separate footings significantly affected the behaviour of the soil near the surface level. As shown in Figure 5.4(b)-(c), the footings embedded into the soil during centrifuge acceleration. Therefore, soil directly beneath the footings settled more than the surrounding sand, and the soil at the left and right sides of the footings

was driven to move towards left and right, respectively. Same as the raft foundation test, the eccentric (e/B = 0.5) structure F2t3b3S in Figure 5.4(b) pushed the soil in the centre of the strongbox to move toward the right. Nevertheless, Figure 5.4(b)-(c) shows that the impact of the separate footings on the movements of the soil with a greater depth is not significant.

5.3.2 Response of the separate footings

The settlements of the surface soil and the foundations in selected centrifuge tests are presented in Figure 5.5. Results are displayed in model scale.

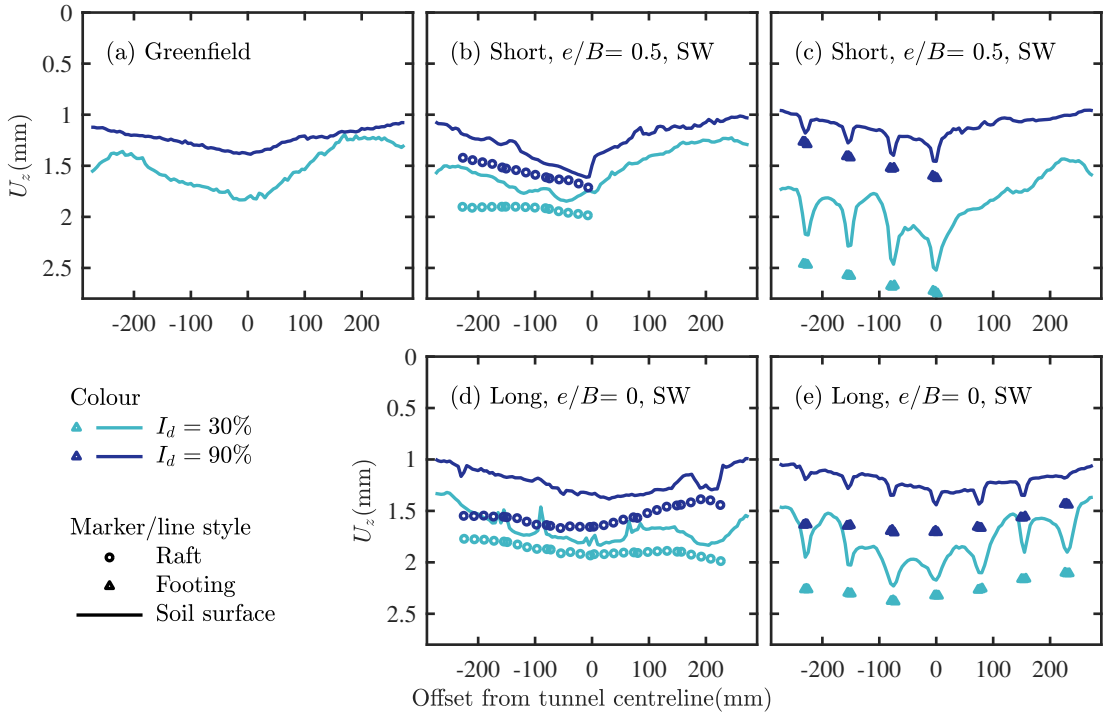


Fig. 5.5. Settlements of the foundations and surface soil in selected tests during spin-up: comparison between rafts and separate footings

Again, Figure 5.5 shows that measured soil settlements directly beneath the foundations were slightly less than those of the foundation in some areas due to image analysis errors associated with the small gap between the model frame building and the acrylic wall (refer to Section 4.2). For both foundation types, the settlements of the surface and the foundations in loose soil tests (light colour) are greater than in dense soil (dark colour) cases. Interestingly,

in the dense soil tests, separate footings and raft foundations have nearly identical settlement values. For the loose soil tests, separate footings have a greater settlement level than raft foundations. For eccentric structure cases (Figure 5.5(b)-(c)), building tilt occurred for both foundation types. However, the deflection ratio of the foundations in all the frame tests are rather limited, and are much smaller than tunnelling induced structural distortions (refer to Section 5.4). This indicates that the framed building models are still within the elastic range (also confirmed by the consistent frame loading test results pre- and post- centrifuge testing). Therefore, consistent with Chapter 4, the final state of the model after reaching the targeted g-level is taken as the reference (i.e. initial condition).

5.4 Foundation and ground displacements

5.4.1 Consideration of the welding issue

Due to uncertainties caused by the model frame manufacturing process mentioned in Section 3.7.2, horizontal displacement data of the footings are not analysed quantitatively. Considering that the effects of the welding on the horizontal response of the footing to tunnelling are similar between tests with the same building, it is reasonable to use the footing horizontal displacements to indicate general trends caused by a change in test parameter (i.e. those in Table 5.1). However, because of the existence of the uncertainties related to welding, care needs to be taken when using the findings related to the horizontal response of the footings to tunnelling.

On the other hand, it is believed that the effects of welding on the settlements of the footings and other building elements are negligible because these settlement data are mainly related to soil-structure interaction in the vertical direction (building load redistribution due to differential ground settlements, which is closely related to the building stiffness (estimated by loading tests)). Therefore, the presented foundation settlements and superstructure shear distortion (determined by the differential settlements between columns) are regarded as sufficiently reliable for the subsequent data interpretation.

5.4.2 Centrifuge results

The prototype scale settlement U_z and horizontal displacements U_x of the foundations (both raft and separate footings) and underlying soil are presented in this section at a tunnel volume loss $V_{l,t}$=2%. Figure 5.6 focuses on the effect of soil relative density whereas Figure 5.7 relates to building self-weight. To facilitate data interpretation, selected central structure tests with $e/B = 0$ are also directly compared in Figure 5.8.

The greenfield settlement troughs, which are also provided in Figures 5.6-5.8, were characterised by fitting modified Gaussian curves (Vorster et al., 2005) to surface settlement data. As shown in Table 5.3, the settlement trough width i is similar for both $V_{l,t} = 1$ and 2%. However, the maximum settlement $U_{z,max}$ in the loose soil is considerably larger than that in the dense soil, due to the ratio of $V_{l,s}/V_{l,t}$ presented in Figure 5.9.

Table 5.3. Greenfield settlement trough characteristics (prototype scale)

I_d (%)	$V_{l,t}$ (%)	$V_{l,s}$ (%)	$U_{z,max}$ (mm)	i (m)	K (-)
30	1	1.6	31.7	3.8	0.34
90	1	1.1	19.9	3.8	0.34
30	2	2.8	60.3	3.4	0.31
90	2	1.5	29.7	3.4	0.31

To facilitate the description of soil-structure interaction, foundation settlements U_z are discussed first. Settlements in Figure 5.6(a)-(d) show that the raft foundation frame has a smaller average settlement than the footings. This occurs because the building with a raft foundation is stiffer (see loading test results in Table 3.5) and has a lower average soil-foundation contact pressure than the building with separate footings (the raft contact area is around 5 times larger than the footings; see pressures in Table 5.1). On one hand, for the eccentric configurations with $e/B = 0.5$ in Figure 5.6(d), all footings and the underlying soil settled more than the soil between the footings, particularly for loose soils. This embedment is probably caused by the coupled vertical-horizontal actions of the footings caused by tunnelling, as reported by Elkayam and Klar (2019). On the other hand, as shown in Figure 5.6(b) for $e/B = 0$, no embedment was measured for the central Foot-4 above the tunnel, which was uplifted by the frame action, while the external footings were embedded by the redistributed building weight (see Figure 5.1 for footing and bay numbering). Thus, the footing embedment is due to both an in-

crease in vertical loads and/or shearing of the underlying soil. Finally, a gap is observed (where soil settlements are greater than foundation settlements) beneath the middle portion of the long raft in Figure 5.6(a), as well as beneath the central footing in Figure 5.6(b) for the loose soil case. In general, centrifuge results in Figure 5.6(a)-(d) confirm the outcomes of Elkayam and Klar (2019) that average footing settlements are greater than average greenfield settlements for semi-flexible buildings.

Regarding horizontal displacements U_x, Figure 5.6(e)-(h) shows that raft foundations were axially rigid and effectively resisted horizontal ground movements, whereas separate footings underwent non-negligible differential horizontal displacements. The soil was restricted horizontally where the foundation moved less than the greenfield, whereas movements increased where the foundation shifted more than the greenfield (the trend being continuous for the raft foundations and discontinuous for the separate footings). It is expected that this horizontal action of the foundation, which introduced further shearing within a narrow zone of the soil beneath the foundation (see surface shear band in Figure 5.13), would degrade the contact shear stiffness of the soil. This aspect could be important for the development of design charts and in evaluating horizontal strain modification factors, similar to Goh and Mair (2014). Finally, the data of U_x and U_z show that soil density affected the magnitude of the displacements, but did not change the soil-foundation interaction mechanism for the identical $V_{l,t}$.

Figures 5.7 and 5.8 show the displacement data of the foundations and underlying soil for the central buildings with standard self-weight SW and double weight 2SW in the dense soil cases. The increase of building weight increased the maximum and differential settlements of the structures on both rafts (accompanied by a decrease of the size of gap in subplots (a) and (c)) and separate footings (associated with an increase of the embedment depth for the footings near the area of maximum soil settlement, for example Foot-3 to 5 in subplot (b) and Foot-2 and 3 in subplot (d)). A heavier building tends to have larger footing differential horizontal displacements (subplots (f) and (h)), especially for the short frame in (h), whereas the horizontal displacements of the raft foundations (subplots (e) and (g)) are negligible. The raft foundation provided a more significant restriction to the underlying soil horizontal displacement for the increased building weight (subplots (e) and (g)), whereas the effect was marginal for the

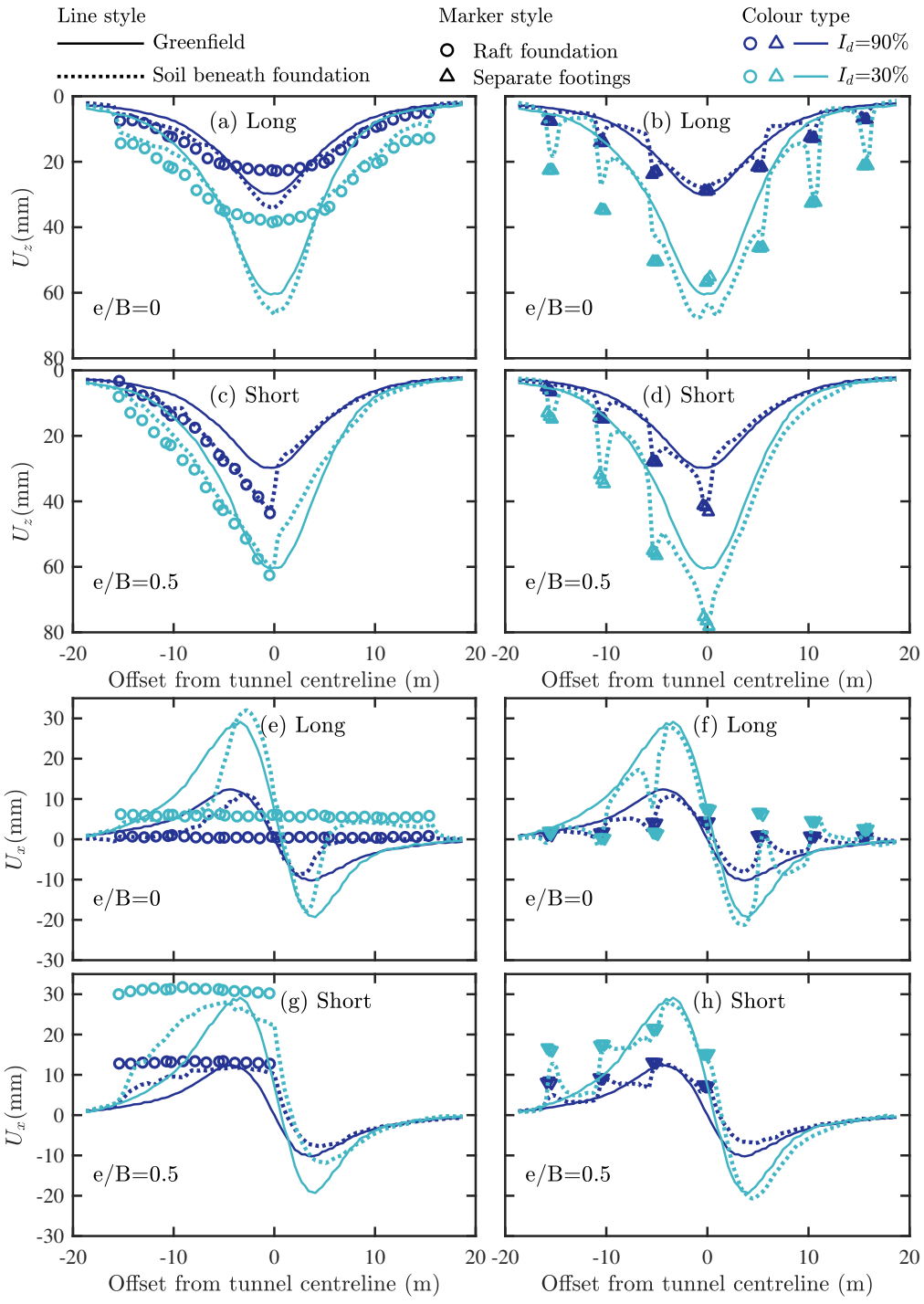


Fig. 5.6. Foundation and underlying soil displacements for loose and dense soil at $V_{l,t}$ = 2% (SW)

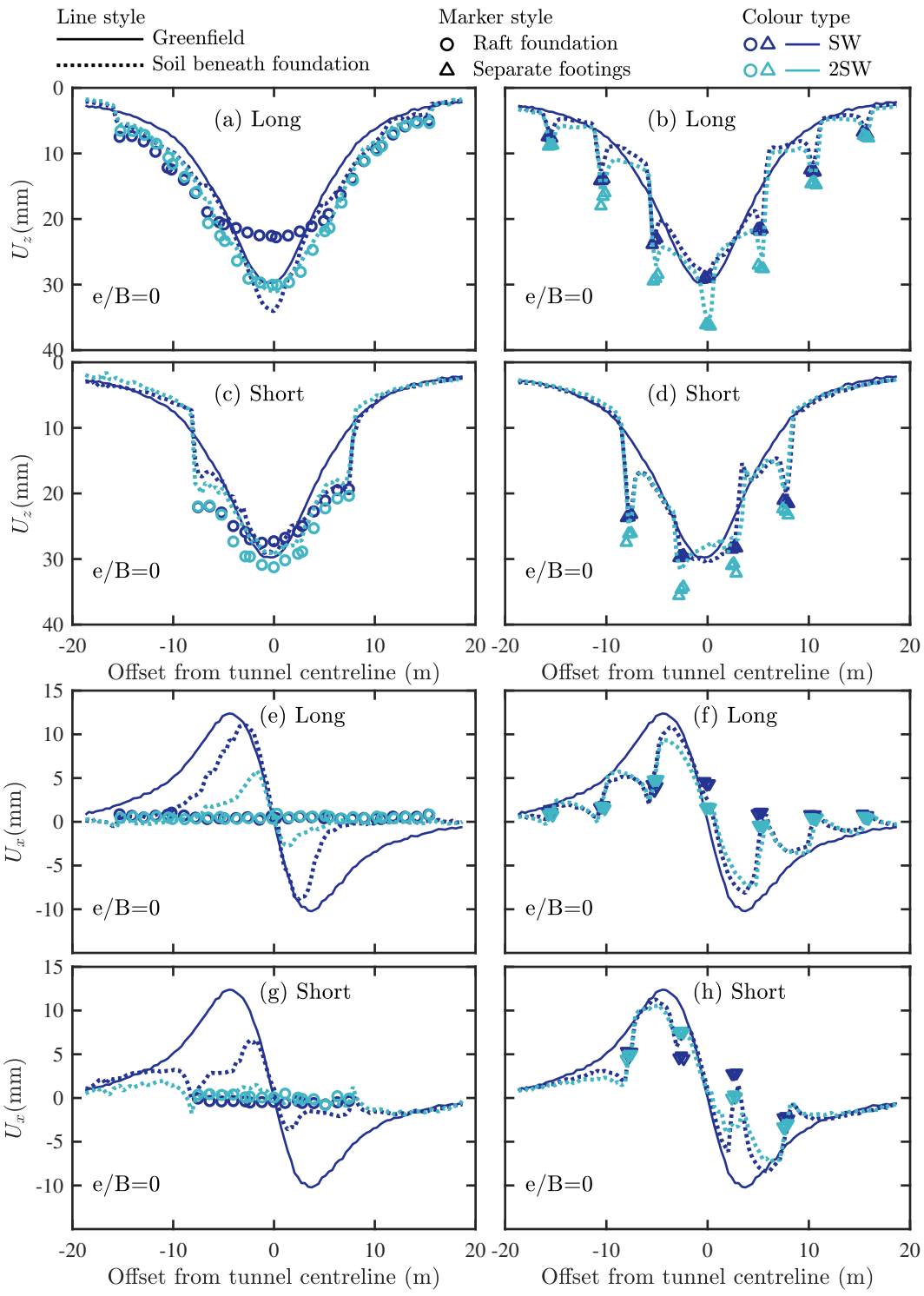


Fig. 5.7. Foundation and underlying soil displacements with different building weights for dense soil at $V_{l,t} = 2\%$ ($I_d = 90\%$)

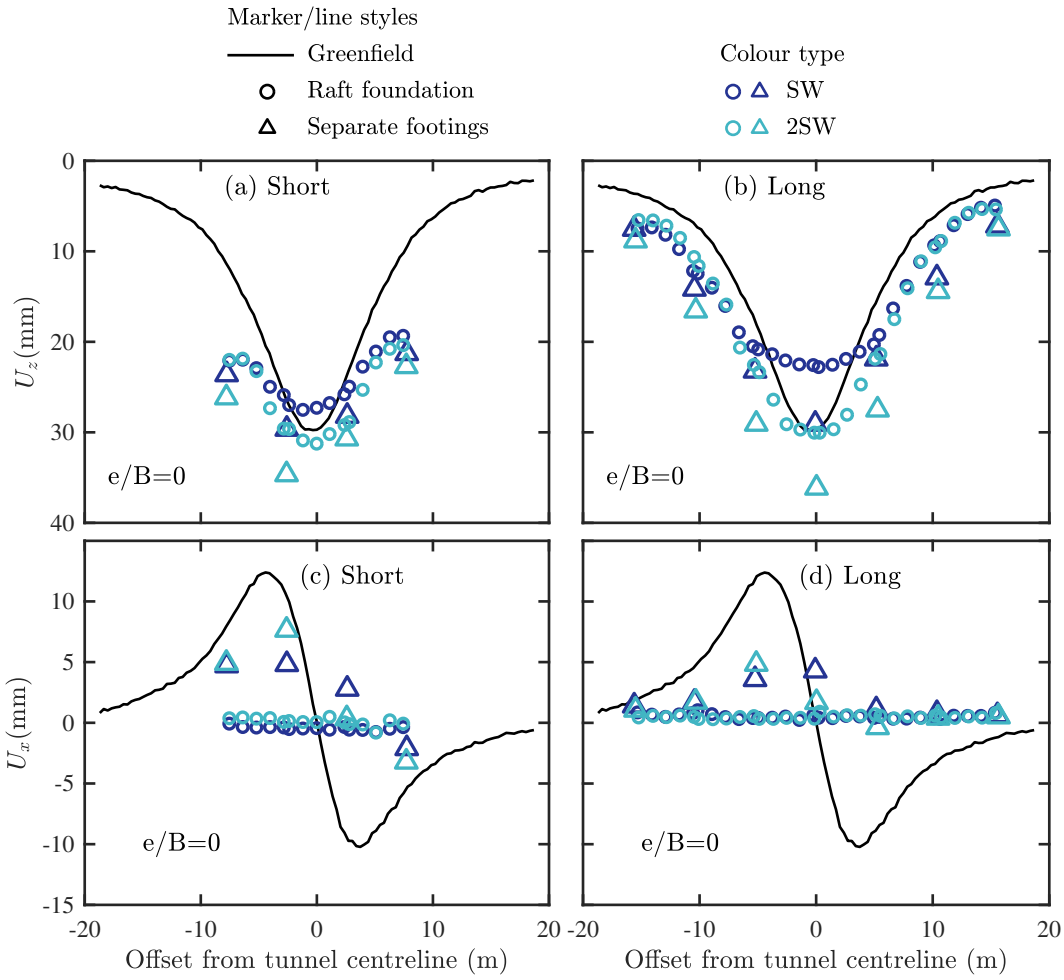


Fig. 5.8. Foundation displacements for central buildings founded on dense soil at $V_{l,t} = 2\%$

separate footing cases (subplots (f) and (h)).

Next, the effect of the building width is considered using data presented in Figure 5.7. The decrease of building width increased the maximum settlement of the central structures with raft foundations (less true for the 2SW cases) and underlying soil (subplots (a) and (c)), whereas the change of building width had less of an effect on the settlement of the central frame with separate footings (subplots (b) and (d)). For the frames with separate footings, no gap formed regardless of frame width. On the other hand, the short frames with raft foundations embedded into the soil at their edges and showed no gap formation, in contrast to the long frames with raft foundations which showed little edge embedment and a considerable gap for the SW case (but not the 2SW case). For horizontal displacements, the shorter frame on the raft foundation had

a more significant effect on restricting the underlying soil (subplots (e) and (g)). This is due to the difference in gap size beneath the foundations for the long and short frame tests, with a wide gap forming beneath the long frame and no gap forming beneath the short frame.

Finally, the effect of the relative tunnel-building location is discussed, referring to both Figures 5.6 and 5.7. For raft foundations, the increase of eccentricity from $e/B = 0$ to 0.5 of the short frame (dark colour in subplots (c) and (g)) decreased the flexural distortion of the building and increased horizontal soil displacements, whereas the central structure restricted them. Similarly, the eccentric short frame on separate footings also displayed lower flexural distortions (subplot (d)). However, the increase of eccentricity of the separate footing buildings changed the deformation mode of the bays at the ground level; for example, differential horizontal displacements of the footings of Bay-2 changed from compression in Figure 5.7(h) for the central frame to tension in Figure 5.6(h) for the eccentric frame.

5.5 Soil volume losses

5.5.1 Soil volume losses against tunnel volume losses

As discussed in Chapter 4, in drained soils, because of their contractive/dilative response to shearing, the relationship between soil volume loss $V_{l,s}$ (given by the integration of the soil settlements at a given depth) and tunnel volume loss $V_{l,t}$ (the ground loss at the tunnel boundary) is not 1:1 (as would be the case in undrained soils), which could also have an impact on the tunnel-framed building interaction behaviour. Engineers tasked with designing excavations need to predict/assume reasonable values of soil volume losses given an expected level of tunnel volume loss $V_{l,t}$ for the applied tunnelling operations (Franza et al., 2020b). For this, the foundation configuration may also play a role. Figures 5.9 and 5.10 present the surface and subsurface soil volume losses against tunnel volume losses.

First, the relationship between surface soil volume loss $V_{l,s}$ and tunnel volume loss $V_{l,t}$ is considered in Figure 5.9. Overall, soil relative density dominates the $V_{l,s} - V_{l,t}$ relationship. Similar to greenfield tunnelling data (Marshall et al., 2012; Franza et al., 2019), in the tunnel-structure interaction tests, the loose soil exhibits a contractive response, whereas the dense

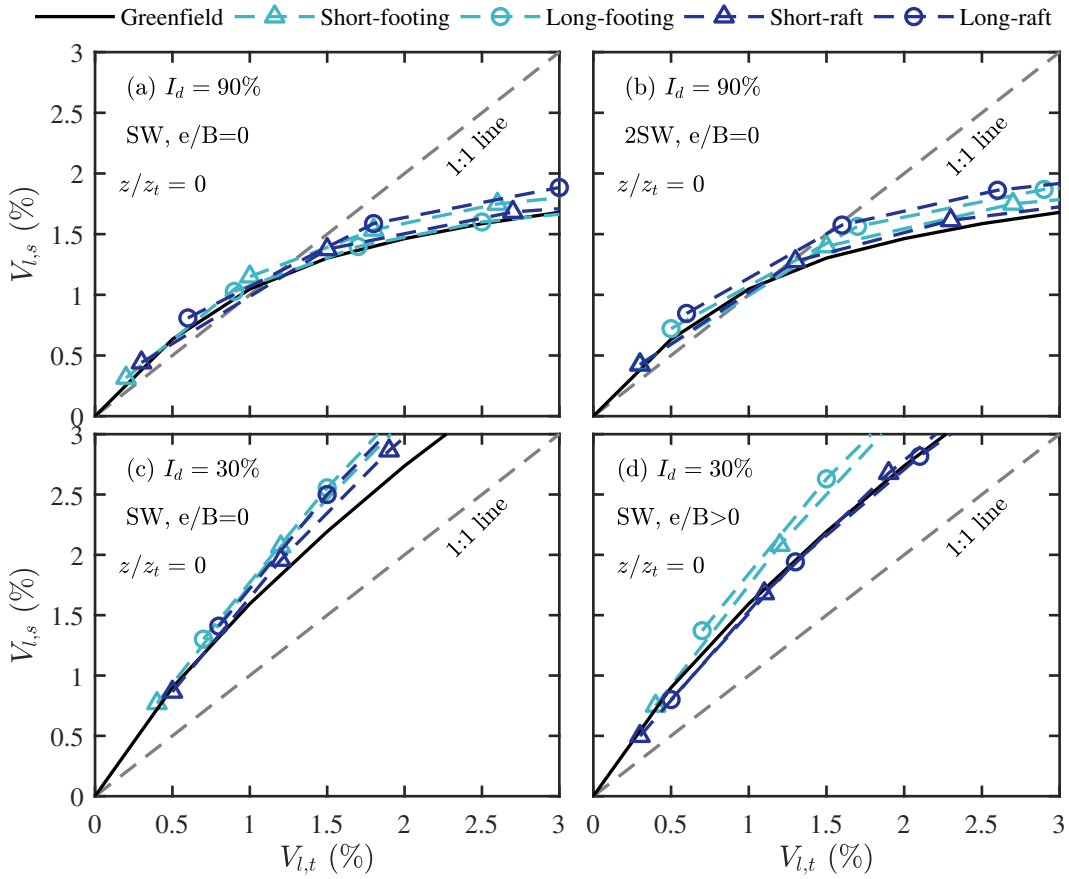


Fig. 5.9. Surface soil volume loss against tunnel volume loss: (a) central structures with self-weight SW in dense soil cases; (b) central structures with double self-weight 2SW in dense soil cases; (c) central structures with self-weight SW in loose soil cases; (d) eccentric structures with self-weight SW in loose soil cases

soil transitions from contractive at lower values of $V_{l,t} < 1\%$ towards dilative at higher tunnel volume losses. Regarding the influence of the building, all tests show relatively small effects at $V_{l,t} < 1\%$, whereas minor increases in $V_{l,s}$ can be seen at $V_{l,t} = 2-3\%$. Among the variation of building characteristics (weight, width, foundation type, e/B), only the building foundation type played a notable role for eccentric structures (see Figure 5.9(d)).

Figure 5.10 shows the relationship between subsurface ($z/z_t = 0.5$) soil volume losses $V_{l,s}$ and tunnel volume loss $V_{l,t}$. Because the foundation configuration has minor effect on the soil volume loss, the conclusions from the tests with raft foundation in Chapter 4 are also applicable for the tests involving separate footings: subsurface soil volume losses $V_{l,s}$ at the depth of

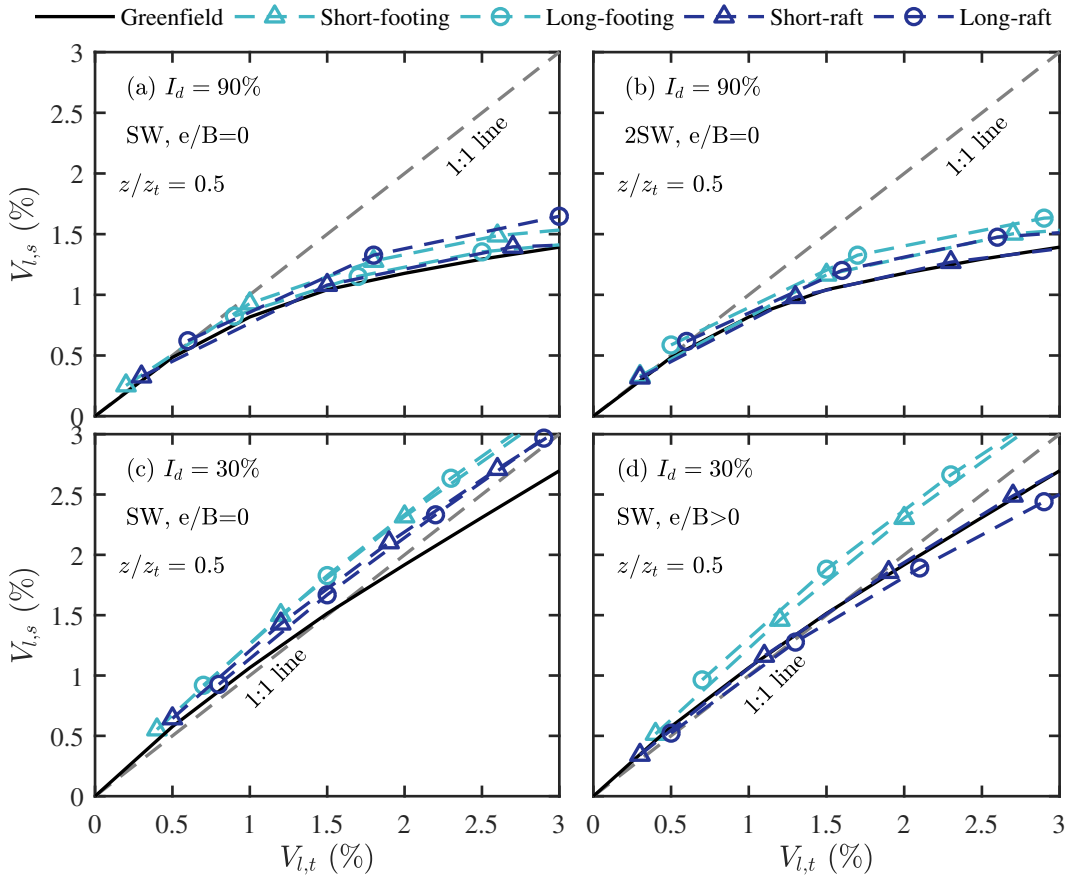


Fig. 5.10. Subsurface (z/z_t = 0.5) soil volume loss against tunnel volume loss: (a) central structures with self-weight SW in dense soil cases; (b) central structures with double self-weight 2SW in dense soil cases; (c) central structures with self-weight SW in loose soil cases; (d) eccentric structures with self-weight SW in loose soil cases

z/z_t = 0.5 are lower than at the surface z/z_t = 0 for all considered tests, indicating that the behaviour of the soil between z/z_t = 0 and 0.5 is overall contractive in both the loose and dense soil tests; subsurface soil volume losses $V_{l,s}$ at the depth of z/z_t = 0.5 are never greater than tunnel volume losses $V_{l,t}$ in the dense tests, whereas $V_{l,s} - V_{l,t}$ relationships of the loose soil tests are rather close to the 1:1 line.

5.5.2 Soil volume loss with varying depths

To better quantify the impact of the structure on the ground volumetric behaviour, subsurface values of $V_{l,s}$ at $V_{l,t}$ = 1 and 2% of the tests are shown, respectively, in Figures 5.11 and 5.12.

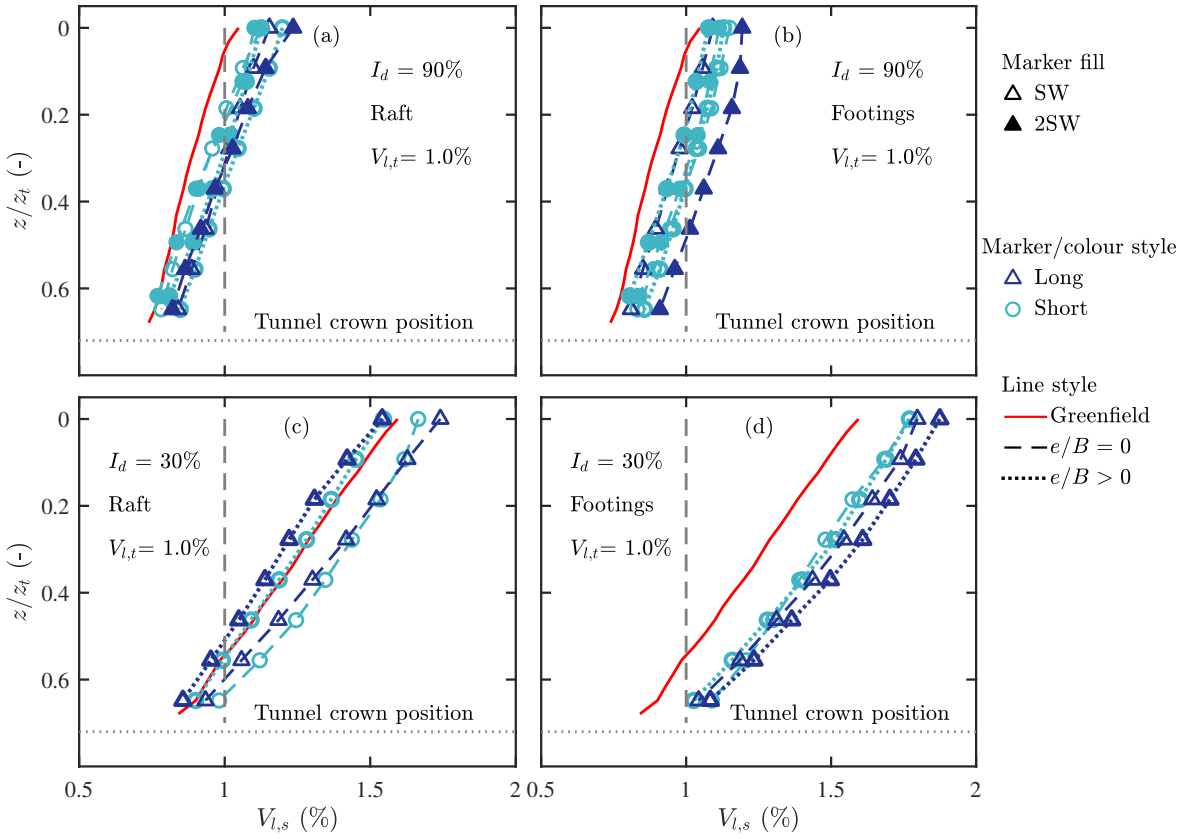


Fig. 5.11. Soil volume loss with varying depths at $V_{l,t} = 1.0\%$

For the loose soil tests, the increase of building eccentricity decreased the subsurface values of $V_{l,s}$ for the rafts, but affected marginally the $V_{l,s}$ for separate footings. Apart from this, results show that foundation configuration has a minor effect on the subsurface soil volume loss in other tests. Same with the raft foundation tests, the shift of the interaction curves in the tests involving separate footings, with respect to the greenfield data, towards greater $V_{l,s}$ values is also relatively constant with depth; this shift, due to soil contractive strains, is slightly greater in loose soil. This nearly uniform shift indicates that most of the change in the soil volumetric response (between greenfield and interaction tests) happened at $z/z_t \geq 0.7$, i.e. close to the tunnel. Also, the behaviour of the soil between the surface and the tunnel crown ($z/z_t = 0-0.7$) is overall contractive in both the raft and separate footings tests, with $V_{l,s}$ at $z/z_t = 0$ greater than $V_{l,t}$ when $V_{l,t} = 1.0\%$ for both soil density conditions (also $V_{l,t} = 2.0\%$ in loose soil tests), and $V_{l,s}$ at $z/z_t = 0.7$ less than $V_{l,t}$ for both $V_{l,t} = 1.0\%$ and $V_{l,t} = 2.0\%$ cases, hence the dilative

response (when present) happened close to the tunnel.

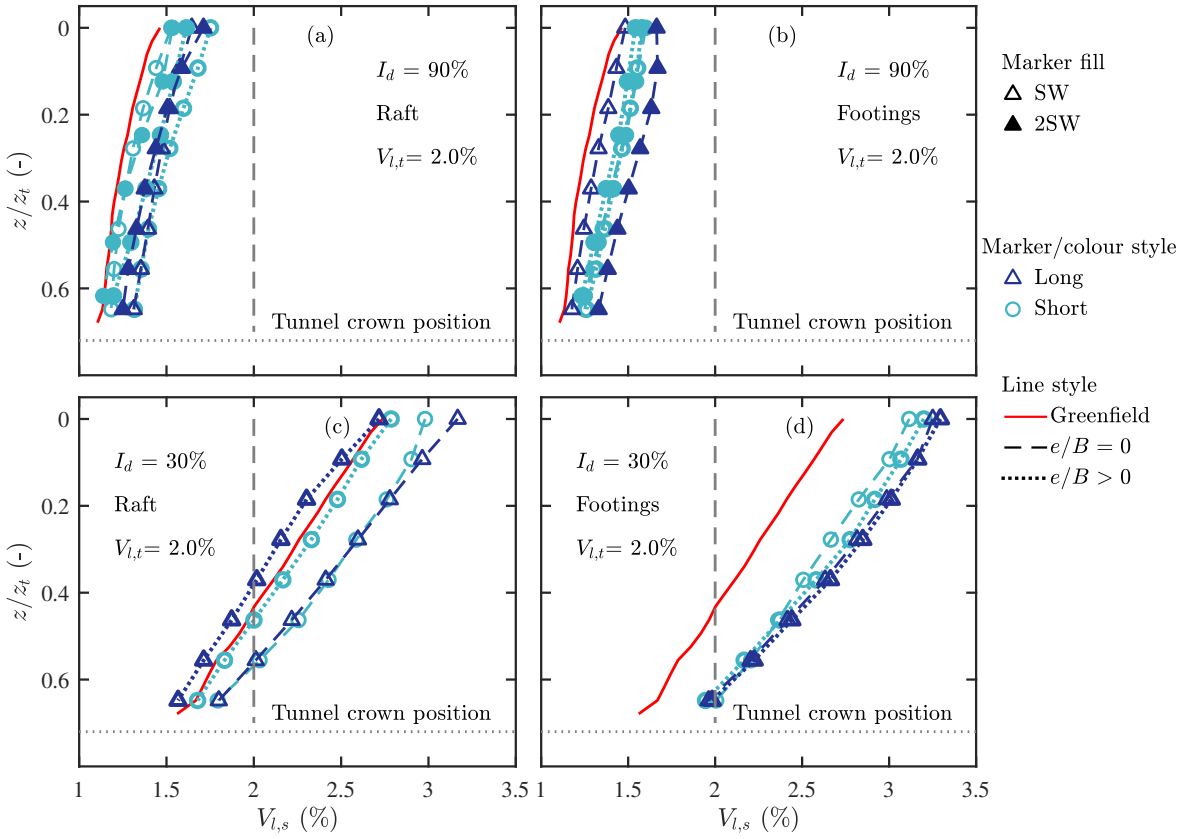


Fig. 5.12. Soil volume loss with varying depths at $V_{l,t}$ = 2.0%

5.6 Ground deformations affected by buildings

5.6.1 Comparison between rafts and separate footings

Figures 5.13 and 5.14 show the ground movements (horizontal U_x and vertical U_z) and strain (engineering shear γ_s and volumetric ϵ_v) contours for selected tests at a tunnel volume loss of $V_{l,t}$ = 2%. In Figures 5.13 and 5.14, positive horizontal and vertical displacements are oriented towards the right and downwards, respectively, while positive volumetric strains are contractive.

As discussed in Section 4.6, from Figure 5.13(a), the greenfield ground settlement shows a chimney-like pattern due to the low C/D_t value (Marshall et al., 2012; Franza et al., 2019),

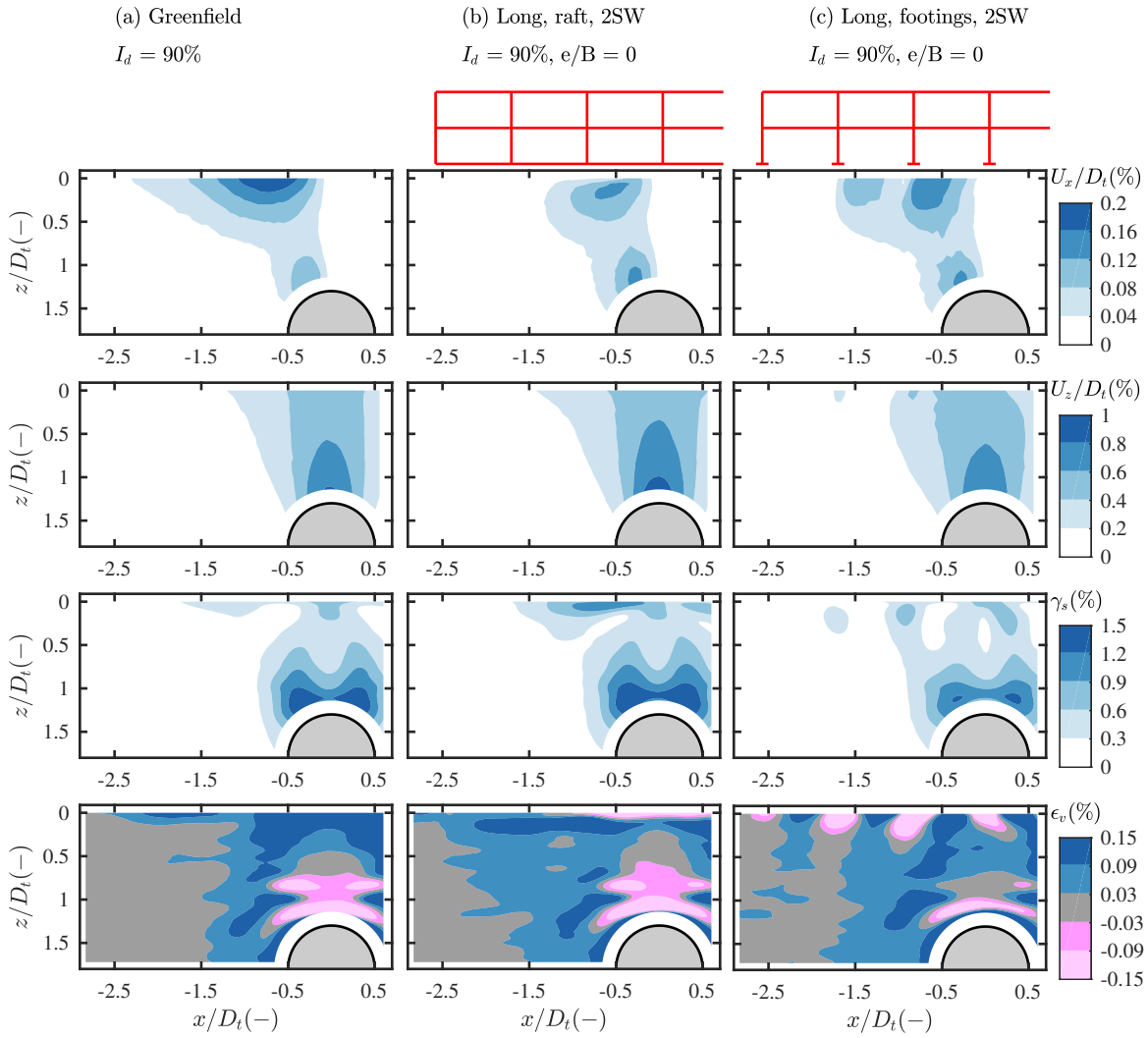


Fig. 5.13. Soil movements normalised by the tunnel diameter, engineering shear and volumetric strains ($\epsilon_v < 0$ indicates dilation) at $V_{l,t} = 2\%$: comparison between raft and separate footings foundations (data outside the contour thresholds were set equal to the closest limit value)

and large shear strains are observed at the tunnel shoulders. Soil directly above the tunnel crown experienced high levels of dilation, whereas the soil experienced intermediate levels of contraction within bands spanning from the tunnel springline to the surface. As discussed by Marshall et al. (2012), the zones of dilation and contraction correspond approximately to the areas of high and low shear strains, respectively. A zone of large contraction is noted centrally above the tunnel and near the surface; this zone is likely caused by the compressive action of the near-surface horizontal displacements on either side of the tunnel.

The effects, relative to the greenfield case, of the presence of framed buildings with raft foundations has also been discussed in Section 4.6. As shown in Figure 5.13(b), the horizontal displacements of the soil near the surface were largely restricted by the foundation roughness and building pressure towards the external part of the building, whereas the subsurface movements were marginally affected. Interestingly, the soil volumetric strain distribution near the surface was altered by the foundation axial action; this is consistent with the mechanism described by Ritter et al. (2017) that the foundation friction restricted the horizontal ground movements. The restriction of the horizontal soil movements resulted in a thin shear band at the soil-foundation interface with a decreased maximum contraction level and some areas of dilation now present. On the other hand, soil settlements increased throughout the ground, accommodated by a slight increase of shear strain at the tunnel shoulders.

For the central frames with doubled weight 2SW on separate footings, as displayed in Figure 5.13(c), the footings restricted horizontal soil displacements with a distinct change in magnitude at the location of the footings (compared to a more uniform distribution for the raft foundation). The vertical displacement of the soil directly above the tunnel decreased compared with the greenfield case and the raft foundation, accompanied by a decrease of the shear strain. However, localised zones of high shear strain are noted at the footing positions, with dilative response directly beneath the footings and contraction within the soil between footings.

5.6.2 Effects of building weight, width and soil density

The effect of the building weight is now discussed for separate footings. Comparing Figure 5.13(c) and Figure 5.14(a) shows that the increase of building weight slightly increased the settlement, shear and volumetric strains of the soil directly beneath the footings, but had a minor effect on the overall horizontal displacements.

The short eccentric frame with $e/B = 0.5$ in Figure 5.14(b) can be seen as half of the long frame in Figure 5.14(a). Therefore, data in these figures can be directly compared, with results showing that, because of the freedom to shift, the eccentric short frame in (b) increased the horizontal displacement of the soil near the surface compared with the long central frame in (a) (consistent with the raft foundation scenario in Section 4.6). At the same time, the action of the

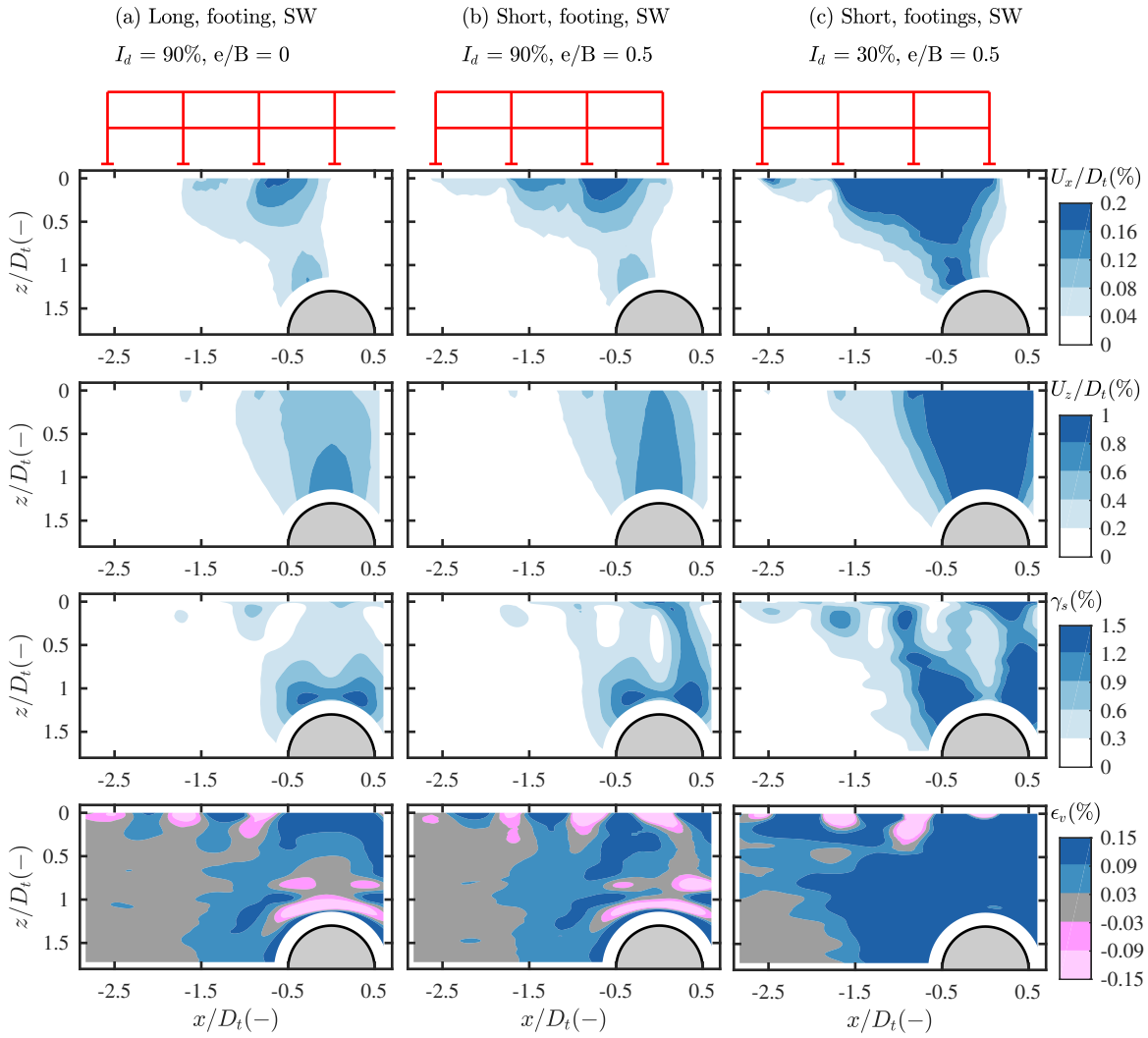


Fig. 5.14. Soil movements normalised by the tunnel diameter, engineering shear and volumetric strains ($\epsilon_v < 0$ indicates dilation) at $V_{l,t} = 2\%$ with varying length and soil density (data outside the contour thresholds were set equal to the closest limit value)

right-most footing (Foot-4) for $e/B = 0.5$ resulted in the soil chimney reaching the surface (i.e. larger soil settlements directly above the tunnel up to the surface), and the formation of a large shear band between Foot-4 and the right shoulder area of the tunnel (consistent with Ritter et al. (2017)).

Last, the effect of soil density is evaluated using data in Figure 5.14(b) for $I_d = 90\%$ and (c) for $I_d = 30\%$. The response of the loose soil in the $I_d = 30\%$ test is dominated by soil contraction (refer also to Figure 5.9). Consequently, the horizontal and vertical displacements, as well as

the shear strain, were significantly increased compared to the $I_d = 90\%$ test. Furthermore, the soil around the tunnel for the $I_d = 30\%$ test was observed to be in contraction (in contrast to all the $I_d = 90\%$ tests where dilation occurred). Interestingly, areas of dilation occurred around the footings for the $I_d = 30\%$ test. Due to the complex rotation/translation response of the footing, soil near the footings experienced high shear distortion. Based on the dilation index value presented in Figure 4.17, for soil with relative density of 30%, dilation of the soil occurs at high soil shear strain (Marshall et al., 2012; Zhao, 2008). Therefore, areas of dilation occurred around the footing, even for soil with relative density of 30%.

5.7 Superstructure deformation parameters

As discussed in Chapter 4, the shear strain or angular distortion of frame bays/panels provides a more direct estimation of framed building deformations than the deflection ratio (Boone, 1996). Figure 5.15 presents the variation of maximum shear strain γ (from all panels for frames on a raft; from upper panels for frames on footings) against tunnel volume loss $V_{l,t}$ for all presented tests. Results are categorised into four groups based on soil density, building weight, and eccentricity.

General trends for data in Figure 5.15 relating to raft foundations were reported in Chapter 4. The increase of building weight (subplots (a)-(b)) and the decrease of soil density (subplots (b)-(c)) increased building shear distortions for a given $V_{l,t}$, whereas the increase of building eccentricity (subplots (c)-(d)) decreased building distortions. On the other hand, there is little difference in shear distortion γ for separate footings compared to rafts (except for the eccentric long buildings in loose soil, for which the separate footings underwent larger settlements than the greenfield trough), despite the fact that the frames with a raft foundation have a greater structure stiffness than those with footings. This is likely due to the effect of two distinct phenomena affecting the two foundation types. For a given superstructure, the raft foundation contributed to increase the total stiffness of the frame, thereby reducing shear deformations, whereas for the separate footings (which do not contribute to the total frame stiffness), shear deformations were reduced by the effect of tunnelling-induced pressure redistribution beneath the footings, causing

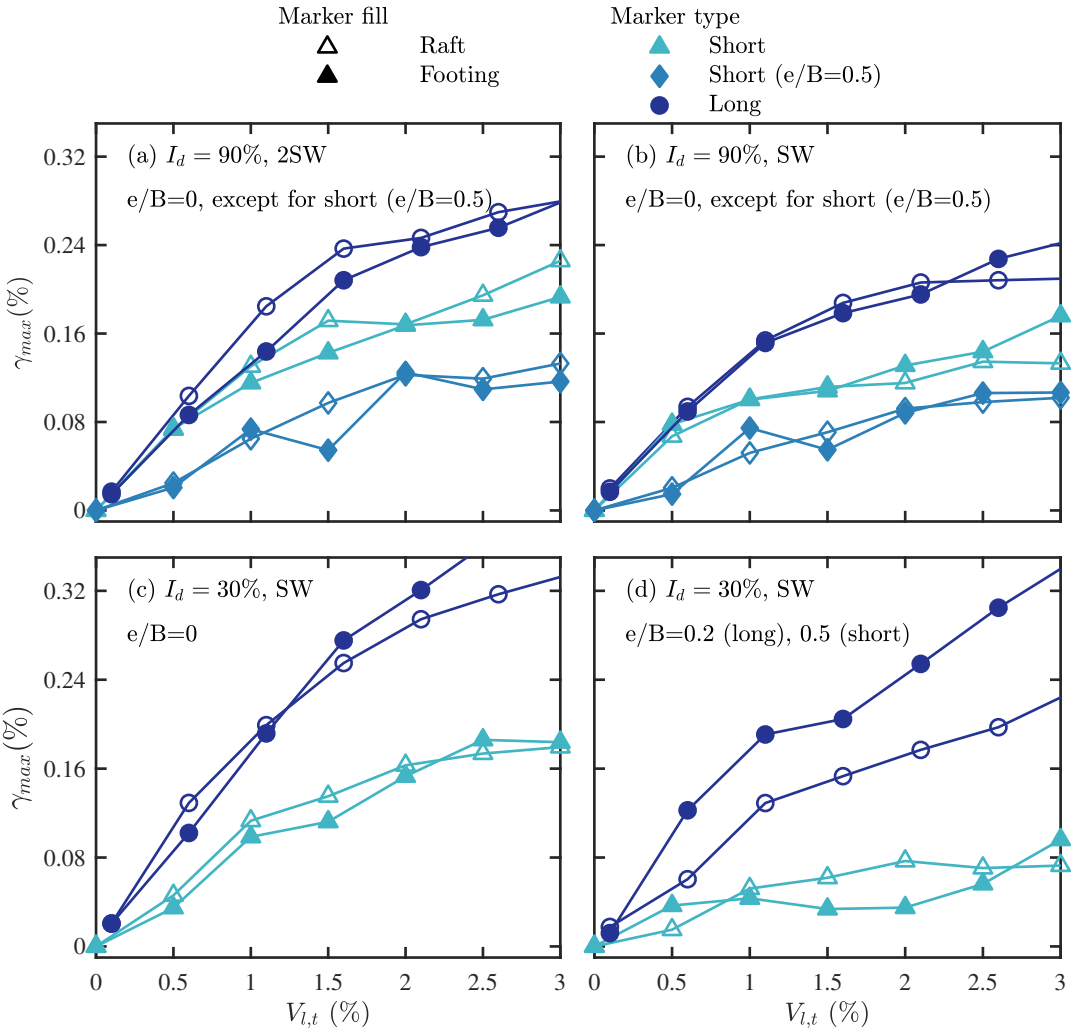


Fig. 5.15. Maximum shear distortion of the framed buildings with tunnel volume loss $V_{l,t}$

higher levels of shear strain within the soil around the footings and reducing the soil-foundation stiffness, resulting in greater structure embedment.

It is also of interest to compare building angular distortion γ for a given soil volume loss $V_{l,s}$ when considering the impact of soil density. Figure 5.16 presents the maximum γ for tests with $e/B = 0$ and SW. In Figures 5.16(a) and 4.27(c), the long frames with raft foundations show nearly identical γ values for loose and dense sand tests. Only the short frame (with the raft foundation) displayed greater shear distortion for dense sand at higher soil volume loss (for instance, when $V_{l,s}$ >1.0-1.5%). On the other hand, the γ values of the frames with separate footings for dense soil are always greater than for loose sand, regardless of their length. This

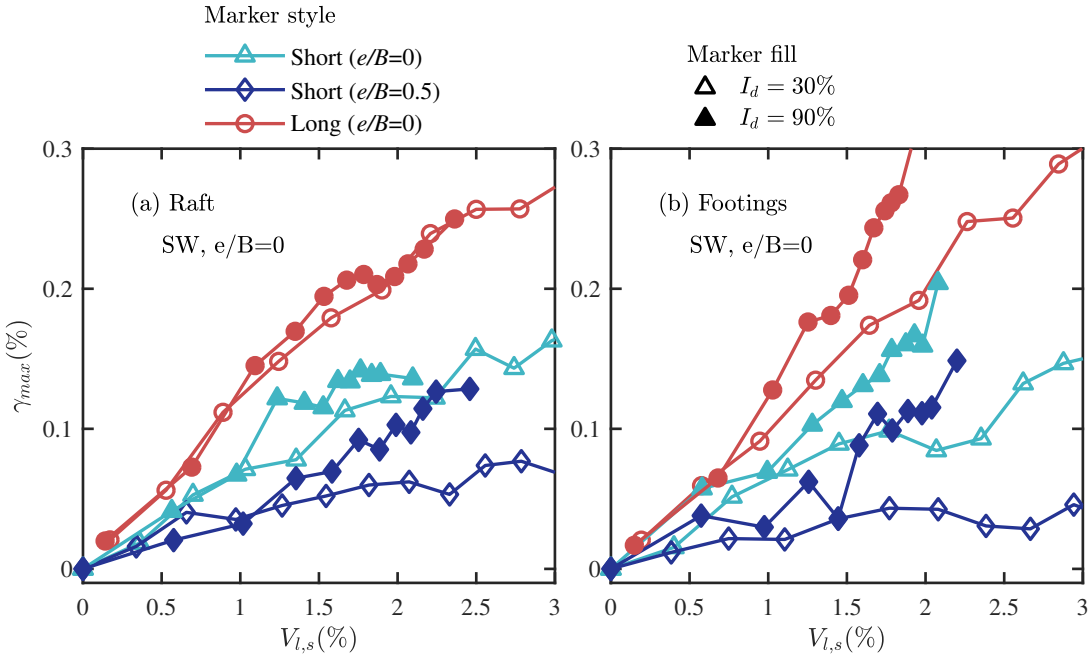


Fig. 5.16. Maximum shear distortion of the framed buildings with soil volume loss $V_{l,s}$: effect of soil density

indicates that the frame tested in loose soil can accommodate the ground differential settlements (reducing the distortion) by embedding the footings into the soil with a greater depth than the dense soil cases, whereas this effect is rather limited for the raft foundation.

5.8 Level of building damage

Figures 5.17 and 5.18 show the deformed shapes of the framed buildings and the ground surface movements for 11 of the centrifuge tests at $V_{l,t}$=1 and 2%, respectively. While in the previous section, the focus was on maximum bay distortions, this section considers the distribution of distortion within panels. To assess the distortion level of panels, indicators are used for the range of shear strain γ and the category of damage. Shear strains were inferred from the corner displacements of panels using the approach from Cook (1994), while the tensile strains $\epsilon_t = \gamma/2$ were computed from γ using a Mohr's circle of strain under plane-strain conditions while neglecting the horizontal strain of the panels (Son and Cording, 2005). The category of damage was obtained from the thresholds of Boscardin and Cording (1989), shown in Ta-

ble 2.4. A colour scheme was adopted to denote low (category 0-1); medium (category 2), and high (category 3+) levels of damage (see Table 2.4).

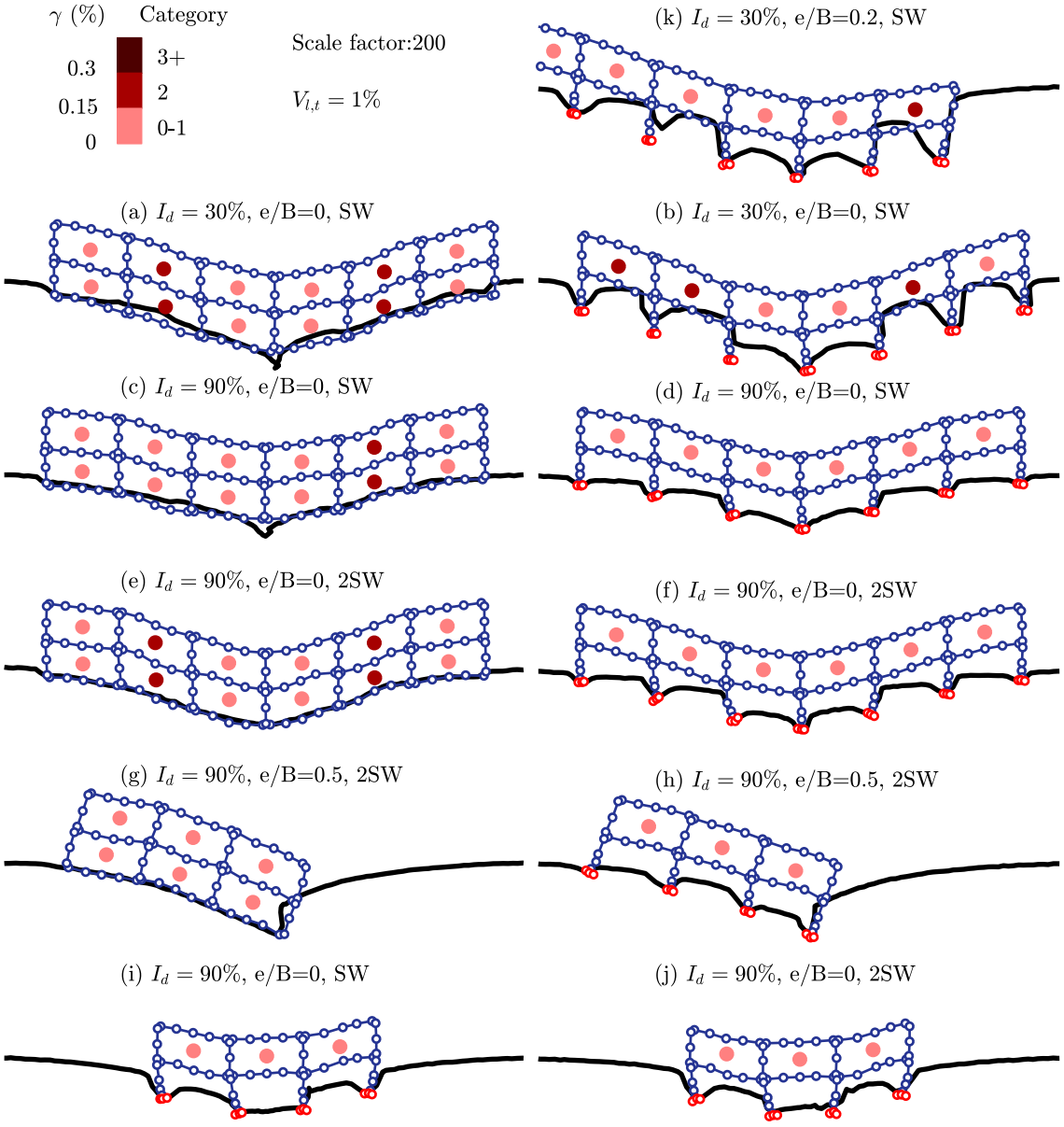


Fig. 5.17. Framed building deformed shapes and level of damage at $V_{l,t} = 1\%$ (scale factor: 200)

First, results at $V_{l,t} = 1\%$ in Figure 5.17 are considered. Overall, most panels of the frames in most tests underwent low levels of damage (negligible or very slight). The frame with separate footings in Figure 5.17 embedded more into the soil than the frame with raft foundations, while

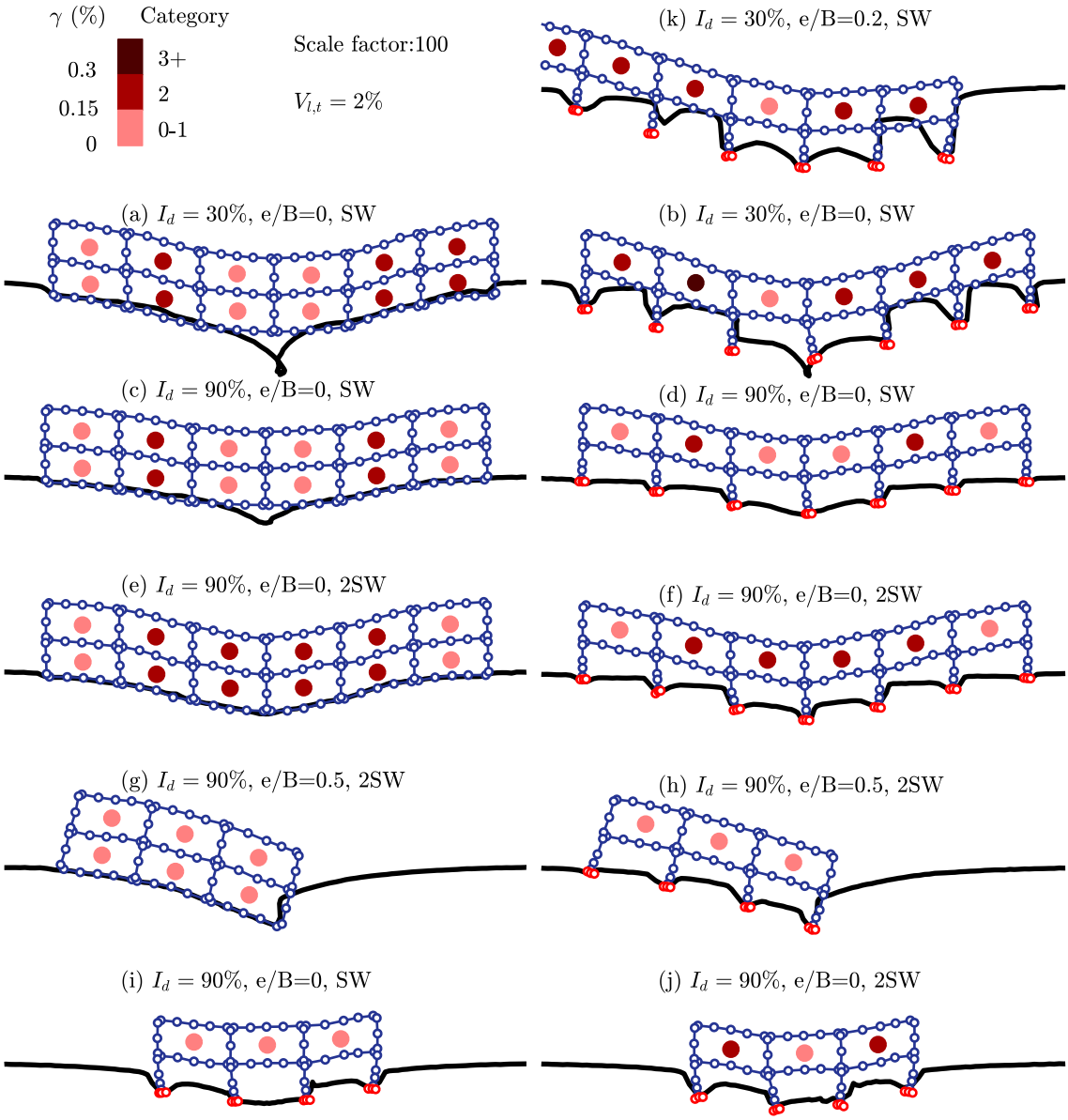


Fig. 5.18. Framed building deformed shapes and level of damage at $V_{l,t}$ = 2% (scale factor: 100)

columns underwent bending deflections (e.g. subplots (f) and (j)) due to the horizontal ground movements and the column head rotation at the first storey slab (caused by shear deflections of the frame). As expected, embedment was greater for the loose sand compared to the dense (compare subplot (b) to (d)), and for the double self-weight 2SW compared to the standard self-weight SW (compare subplot (d) to (f)). Despite the decreased total stiffness of the frame with

footings compared to the raft, only the distortion levels of the upper level panels in the loose soil (subplot (b)) are slightly higher than those in the raft (subplot (a)). For the dense soil cases (compare subplots (c)-(d) and (e)-(f)), the frames with rafts have larger deformations in specific panels compared to the footings. This indicates that the structure with separate footings is able to accommodate the differential ground settlement more readily than the raft, through the action of the footing embedment into the soil, thereby reducing the deformation of the structure.

Secondly, data presented in Figure 5.18 at $V_{l,t} = 2\%$ is discussed. The upper level of panels of long frames with both rafts and footings in dense soil (compare subplots (c) to (d) and (e) to (f)) have the same deformation mode and equivalent distributions of maximum damage level. Interestingly, the decrease of soil density (from $I_d = 90$ to 30%) tended to increase the distortion of external panels (panel-1 and 6) of long frames (from low to medium, compare subplot (a) to (c), and (b) to (d), except for panel-1 in (a) to (c)), while the increase of building weight increased the distortion of the internal panels (panel-3 and 4, from low to medium, compare subplot (c) to (e), and (d) to (f)).

Finally, consistent with the findings on raft foundations (see Chapter 4), results in Figure 5.18 confirm that the increase of building eccentricity (comparing (b) to (k), and (j) to (h)), as well as the decrease of the frame width (comparing (d) to (i), and (f) to (j)) decreased the deformation of the frame with separate footings. The short eccentric frame experienced lower levels of distortion than the long frame due to its freedom to tilt when subjected to tunnelling (see (e) to (g), and (f) to (h)).

5.9 Modification factor against relative soil-building stiffness

To link excavation-induced framed building angular distortion with relative soil-building stiffness, the use of the modification factor of angular distortion, M^{β} was proposed in Section 4.7.3.3 of Chapter 4. This modification factor $M^{\beta} = \beta_{max}/\overline{GS}_{max}$ is obtained through normalising the maximum angular distortion β_{max}, obtained using the equation of Son and Cording (2005), by the maximum average slope of the portion of the greenfield surface settlement trough spanning a bay width, $\overline{GS}_{max} = \Delta U_{z,gf,max}/b_{bay}$. The trends of M^{β} were related to the relative

soil-building shear stiffness $\kappa = (E_s B)/(GA_s^*) = (E_s BL)/(GA_s)$, where E_s is the representative Young's modulus of the soil (estimated using the approach described in Section 4.7.3.1), L is the length of the building in the longitudinal direction of the tunnel, $GA_s^* = GA_s/L$ is the building shear stiffness per meter run, and B is the building width.

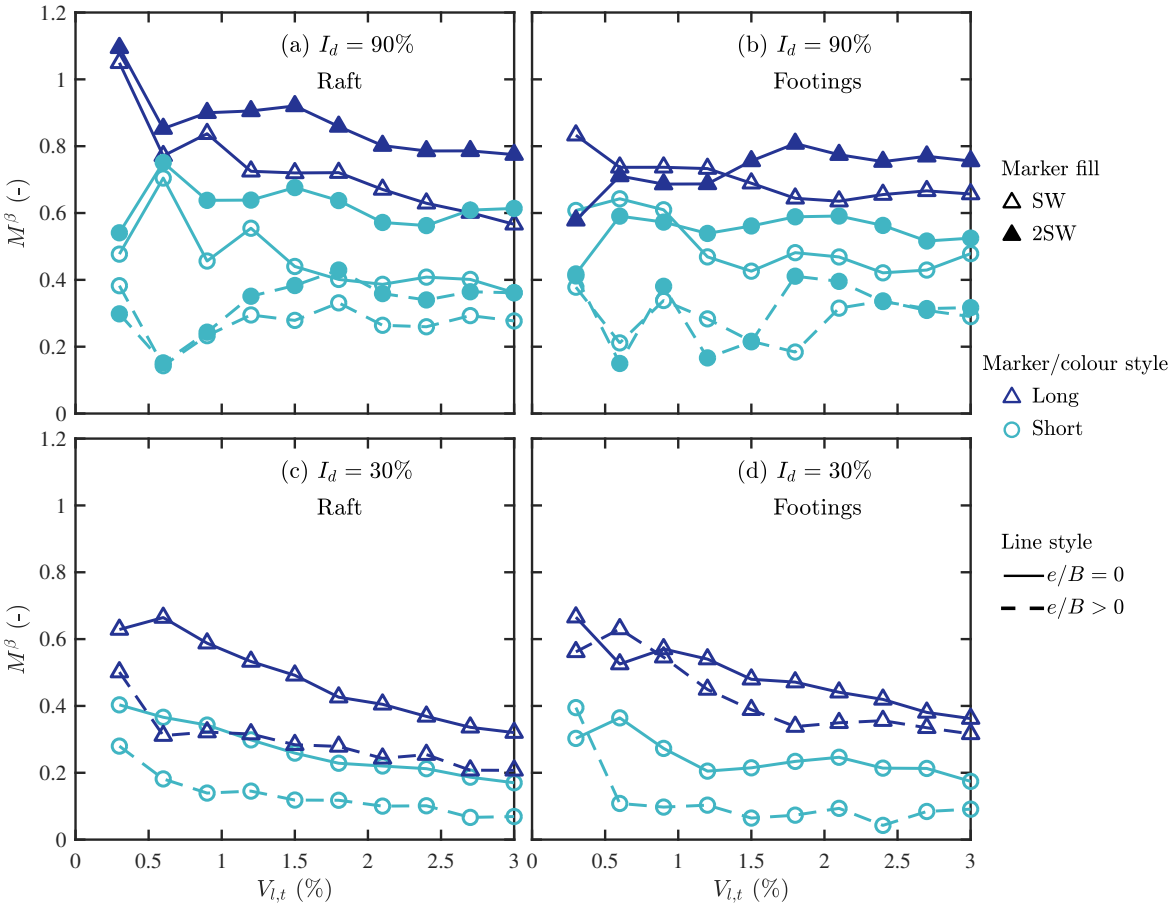


Fig. 5.19. Modification factors of β against tunnel volume loss $V_{l,t}$

First, the variation of the modification factor of angular distortion M^β with tunnel volume loss $V_{l,t}$ is discussed. Results in Figure 5.19 show that the M^β values for the raft tests are similar to those for the footing tests. Furthermore, consistent with the raft foundations, the M^β values for separate footings generally increase, increase and decrease, respectively, with the increase of building self-weight (from SW to 2SW), soil density (from I_d = 30 to 90%) and building eccentricity. Nevertheless, for the tests involving raft foundations (Figure 5.19(a) and (c)), most M^β trends (except for the eccentric short frame in the dense soil) are characterised by a steady

decrease with $V_{l,t}$; whereas for the separate footings tests, only the M^{β} trends in the loose soil tests (Figure 5.19(d)) follow the same principle. For the dense soil tests with separate footings (Figure 5.19(b)), the M^{β} trends are characterised by considerable fluctuations.

The mechanism behind this phenomenon (i.e. the fluctuation) is complex; it is probably due to the localised soil failure and slippage at the soil-foundation interface, caused by 1) structural load redistribution during tunnelling; and 2) footing column head rotation due to the structural distortion (causing the slippage at the footing bases). At a certain $V_{l,t}$, a mix of settlement, rotation and translation caused one or more footings to exceed their capacity. As a consequence, the bearing load of these footings suddenly decreased, whereas their settlements significantly increased (see the loading test results in Figure 5.3). Therefore, the structural differential settlements and distortion reduced, resulting in a sudden drop of M^{β} (see the fluctuations of the curves in Figure 5.15). After that, the structure gradually followed the ground movements, causing an increase of M^{β}. Therefore, the final $M^{\beta} - V_{l,t}$ trends of the frames with separate footings in the dense soil tests show a fluctuation. On the other hand, for the loose soil tests, footing bearing load always increases with settlement (see Figure 5.3), thus the fluctuation of the $M^{\beta} - V_{l,t}$ curves is not significant.

In Figure 5.20, M^{β} is plotted against relative soil-building shear stiffness κ for $V_{l,t} = 1$ and 2% (numbers beneath markers indicate $V_{l,t}$). To highlight the effects of normalised building transverse width and building position relative to the settlement trough on the soil-structure interaction, a colour scheme was adopted to distinguish between values of e/B and the ratio B/i, where i is the distance to the inflection point of the greenfield settlement trough.

As can be seen in Figure 5.20, envelopes for separate footings are suggested and compared with those for raft foundations from Chapter 4. For the central structures ($e/B = 0$) with separate footings, the upper envelope can be expressed as:

$$\begin{aligned} M^{\beta} &= 0 && \text{for } \kappa < 2.5 \\ M^{\beta} &= 0.56\log\kappa - 0.223 && \text{for } 2.5 \le \kappa \le 153 \\ M^{\beta} &= 1 && \text{for } \kappa > 153 \end{aligned} \tag{5.1}$$

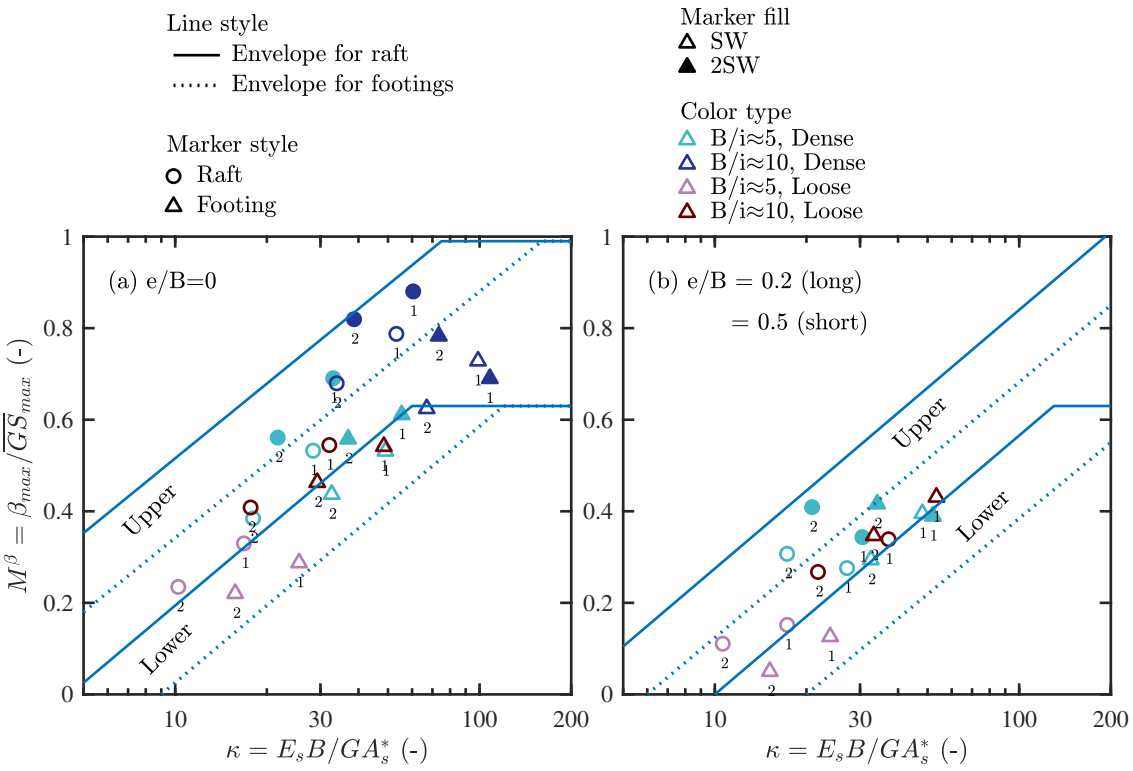


Fig. 5.20. Modification factors of β against relative soil-building shear stiffness at $V_{l,t}$ =1 and 2% ($V_{l,t}$ indicated by numbers below markers); (a) central structure cases; (b) eccentric structure cases

and the lower envelope can be expressed as:

$$\begin{aligned} M^\beta &= 0 && \text{for } \kappa < 9 \\ M^\beta &= 0.56\log\kappa - 0.5343 && \text{for } 9 \le \kappa \le 120 \\ M^\beta &= 0.63 && \text{for } \kappa > 120 \end{aligned} \tag{5.2}$$

For the eccentric scenarios ($e/B > 0$), the upper envelope can be expressed as:

$$\begin{aligned} M^\beta &= 0 && \text{for } \kappa < 6 \\ M^\beta &= 0.56\log\kappa - 0.4386 && \text{for } 6 \le \kappa \le 370 \\ M^\beta &= 1 && \text{for } \kappa > 370 \end{aligned} \tag{5.3}$$

and the lower envelope can be expressed as:

$$\begin{aligned} M^{\beta} &= 0 && \text{for } \kappa < 20 \\ M^{\beta} &= 0.56\log\kappa - 0.7336 && \text{for } 20 \leq \kappa \leq 272 \\ M^{\beta} &= 0.63 && \text{for } \kappa > 272 \end{aligned} \tag{5.4}$$

An approximately linear increase of M^{β} for separate footings is also observed in the semi-log scale with the relative soil-building stiffness. However, for a similar relative stiffness parameter κ, the frame on separate footings tends to have a smaller M^{β} value than the raft foundation. Additionally, this plot confirms that wider ($B/i \approx 10$) and heavier (2SW) frames, or structures with a smaller eccentricity e/B, tend to have a larger modification factor regardless of the foundation type (as also demonstrated in Figure 5.19). Finally, regarding the issue associated with the manufacturing process (i.e. the welding), although it was assumed to have negligible effects on the shear distortion of the structures, it still brings a certain level of uncertainty to the interpretation of the building distortion data. Therefore, numerical modelling based on the centrifuge results is currently undergoing to check the reliability of the proposed envelopes, with preliminary results demonstrating the reliability of the proposed envelopes (Boldini et al., 2020). The numerical results will also be used to investigate the uncertainties associated with the horizontal displacements of the footings caused by the manufacturing process.

5.10 Summary

This chapter presented a centrifuge study on soil-framed building interaction, with specific focus on the influence of foundation scheme. Tunnelling-induced displacements of the building and underlying soil were illustrated, and structural and ground deformations were analysed. The following conclusions can be drawn.

- In addition to the building weight and position (e.g. Ritter et al. (2017)), the foundation configuration (i.e. raft or separate footings) significantly affects the ground response and impacts the soil-structure interaction. The foundation type had an impact on both the vertical and

horizontal ground displacement fields as well as the shear and volumetric strain distributions. The action of the structure particularly affected the soil close to the foundation, with different trends depending on foundation type. Despite this and the differences in strain distributions, only marginal differences in the relationship between tunnel and soil volume loss was observed.

- Buildings with raft and separate footings acted to reduce flexural distortions caused by tunnelling in different ways; separate footings tended to embed into the soil in the areas where settlements were lowest, whereas raft foundations responded by uplifting the portion where settlements were greatest. Because of the embedment, the frame with separate footings settled significantly more than greenfield settlement at the corresponding location, as reported numerically by Elkayam and Klar (2019).

- In agreement with previous field (Goh and Mair, 2014) and modelling works (Fu et al., 2018; Franza and DeJong, 2019), it was confirmed experimentally that tunnelling-induced differential horizontal movements are significant for separate footings, whereas they are negligible for raft foundations.

- For the considered two-storey framed buildings, when only the foundation scheme was changed, the level of shear deformation of the building panels was similar because of two distinct mechanisms: for the raft, shear deformations were reduced because of the higher overall structure stiffness resulting from the raft; for the separate footings, shear deformations were reduced because of higher levels of shear strains in the soil around the footings, reducing the soil-foundation stiffness and causing greater building embedment. The trends highlighted in Chapter 4 for raft foundations were confirmed for separate footings: wider or heavier framed buildings display increased structural shear deformation, whereas building eccentricity reduces distortions for both foundation types.

- Different from the outcomes of the raft foundations, the trends of the modification factors of the frame angular distortions with tunnel volume loss for separate footings are characterised by significant fluctuations due to the localised soil failure and the slippage at the soil-footing interface; the modification factor was linked to the relative soil-building shear stiffness. It was

confirmed that the structural stiffness can play an important role in the soil-structure interaction of framed building configurations. With respect to raft foundations, frames on separate footings underwent slightly lower shear modification factors for a given relative stiffness; this is likely due to the fact that footings decreased the foundation footprint compared to rafts, which leads to greater flexibility of the soil-foundation system as well as higher levels of soil shearing (directly beneath the foundation, leading to greater stiffness degradation).

In this chapter, the considered scenarios were limited to a tunnel with constant cover-to-diameter ratio constructed beneath an elastic framed building with separate footings resting on the surface. Chapter 6 will study the roles of footing embedment and tunnel cover depth on tunnel foundation interaction.

Chapter 6

Influence of footing embedment and tunnel depth

When considering a building on shallow foundations subjected to tunnelling induced displacements, it is generally assumed that foundations rest directly on the surface, both in numerical (Goh and Mair, 2014; Fu et al., 2018) and experimental (Ritter, 2018) studies (also in Chapter 5). However, in reality, shallow foundations are usually buried at a certain depth. In the scenario of embedded footings, the response of footings and superstructures to ground displacements may differ from the cases in which the footings are assumed to rest on the surface, and thus uncertainties may arise in the risk assessment to the building damage. This aspect has been discussed for foundations that are continuous in the direction transverse to the tunnel by Losacco et al. (2014); Yiu et al. (2017) and Boldini et al. (2018), however, there is a lack of information for separate strip footings, for which embedment is arguably more important because of the potential for significant horizontal foundation displacements.

On the other hand, the cover depth of a tunnel affects the ground surface settlement trough, both in terms of magnitude (volume of the settlement trough) and trough width (Marshall et al., 2012; Franza et al., 2019), which could have a great impact on the structural distortion.

To evaluate the impacts of footing embedment and tunnel cover depth, this chapter presents results from 10 plane-strain geotechnical centrifuge tests of tunnelling in sand beneath a frame founded either on separate footings or a raft foundation. The foundation rests either on the

ground surface or is embedded within the soil, subjected to the ground movements caused by the excavation of a tunnel with a relative depth of C/D_t = either 1.3 or 2.0. The investigation aims to provide insights into the roles of the foundation embedment and tunnel cover depth on tunnel-foundation interaction, and provides experimental data which may serve as a benchmark for more exhaustive numerical analyses.

6.1 Considered tests

In this chapter, 10 centrifuge tests including 4 greenfield tunnelling and 6 tunnel-frame interaction tests ($e/B = 0$) are considered, as shown in Figure 6.1 and Table 6.1.

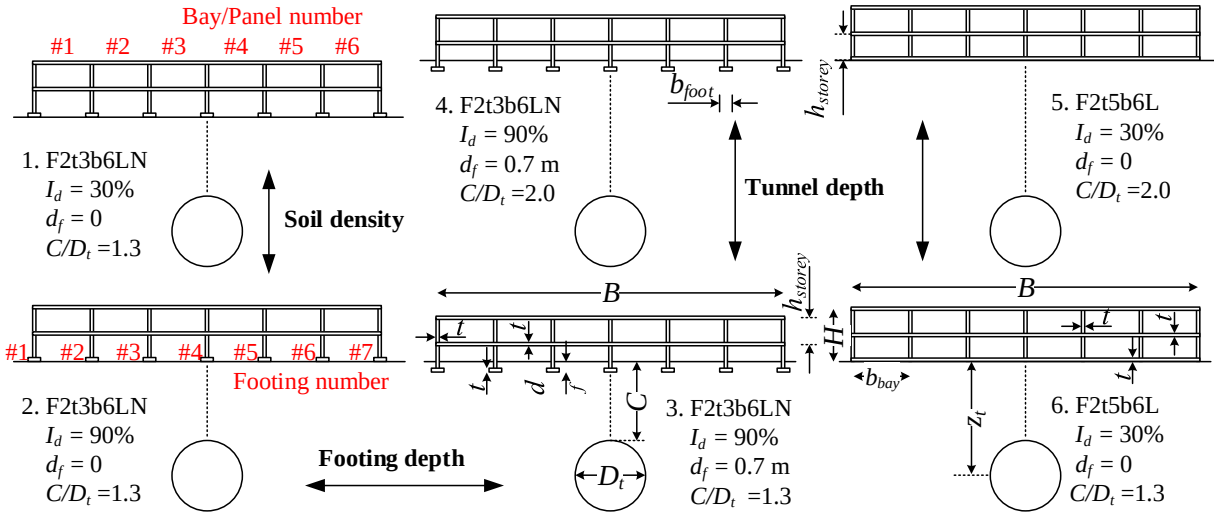


Fig. 6.1. Illustration of the considered centrifuge tests

Two framed building models are included, one frame on a raft foundation and one frame with separate footings. For the frame with separate footings, F2t3b6LN, 4 tests are considered: two tests involving a central tunnel with $C/D_t = 1.3$ beneath the frame with the footings resting on the ground surface in loose and dense soil, and two tests having a central tunnel with either $C/D_t = 1.3$ or 2.0 beneath the frame with the footings buried at a depth d_f of 10 mm (model scale, and 0.7 m in prototype scale) in dense soil. For the frame with the raft foundation, F2t5b6L, 2 tests involving a central tunnel with either $C/D_t = 1.3$ or 2.0 beneath the raft resting on the ground surface in loose soil are included. For each framed building model, building weight was always kept constant for different testing conditions.

This chapter studies the roles of footing embedment and tunnel cover depth on tunnel-foundation interaction. In Figure 6.1, tests 2 and 3 are used to investigate the role of footing embedment. Test 1 ($I_d = 30\%$, $d_f = 0$) was also included because, in Chapter 5, the horizontal displacements U_x of the footings were not considered due to the welding issue (refer to Section 3.7.2), and test 1 is used to study the effect of soil density on U_x of the footings due to tunnelling. The effect of tunnel cover depth on the response of framed buildings to tunnelling

Table 6.1. Considered centrifuge tests (model scale)

No.	Item	Foundation type	I_d (%)	D (mm)	C (mm)	C/D	d_f (mm)
1	Greenfield	-	30	90	117	1.3	-
2	Greenfield	-	90	90	117	1.3	-
3	Greenfield	-	30	90	180	2.0	-
4	Greenfield	-	90	90	180	2.0	-
5	F2t3b6LN	Footings	30	90	117	1.3	0
6	F2t3b6LN	Footings	90	90	117	1.3	0
7	F2t3b6LN	Footings	90	90	117	1.3	10
8	F2t3b6LN	Footings	90	90	180	2.0	10
9	F2t5b6L	Raft	30	90	117	1.3	0
10	F2t5b6L	Raft	30	90	180	2.0	0

is investigated using data from tests 3-6 (Figure 6.1).

6.2 Effects of footing embedment and soil density

6.2.1 Foundation and underlying soil displacements

The prototype scale settlement U_z and horizontal displacement U_x of the footings and underlying soil at soil volume loss $V_{l,s}$ = 1.5% are plotted in Figure 6.2, along with the greenfield soil displacements, to study the effects of footing embedment and soil density on soil-foundation interaction. First, the greenfield settlement troughs of soil equal volume ($V_{l,s}$ = 1.5%) were characterised by fitting modified Gaussian curves (Vorster et al., 2005) to the surface settlement data, as shown in Table 6.2. Note that for tunnel-frame interaction tests, the value of $V_{l,s}$ was directly obtained from the surface settlement trough. The characteristics of the greenfield settlement trough at the depth of 0.7 m for dense sand is also presented in Table 6.2. Results show that the greenfield settlement trough of the loose soil is slightly shallower (a smaller $U_{z,max}$) but wider (a larger i) than the dense soil. The greenfield settlements in dense sand at $z = 0$ and 0.7 m also do not differ drastically, with i = 2.9 m and $U_{z,max}$ = 31.4 mm at z = 0.7 m (narrower and deeper), compared to i = 3.4 m, $U_{z,max}$ = 29.7 mm at the surface.

Results of $V_{l,s}$ = 1.5% in Figure 6.2(a) show that the external footings (#1-2 and 6-7 from Figure 6.1) for I_d = 30% settled much more than for I_d = 90%; while the settlements of the central footings (#3-5) were similar for both cases. Consequently, the increase of soil density

Table 6.2. Greenfield settlement trough characteristics (prototype scale)

I_d (%)	$V_{l,t}$ (%)	z (m)	C/D_t	$V_{l,s}$ (%)	$U_{z,max}$ (mm)	i (m)	i/z_t (-)
30	0.9	0	1.3	1.5	28.4	3.8	0.35
90	2	0	1.3	1.5	29.7	3.4	0.31
90	2	0.7	1.3	1.4	31.4	2.9	0.27

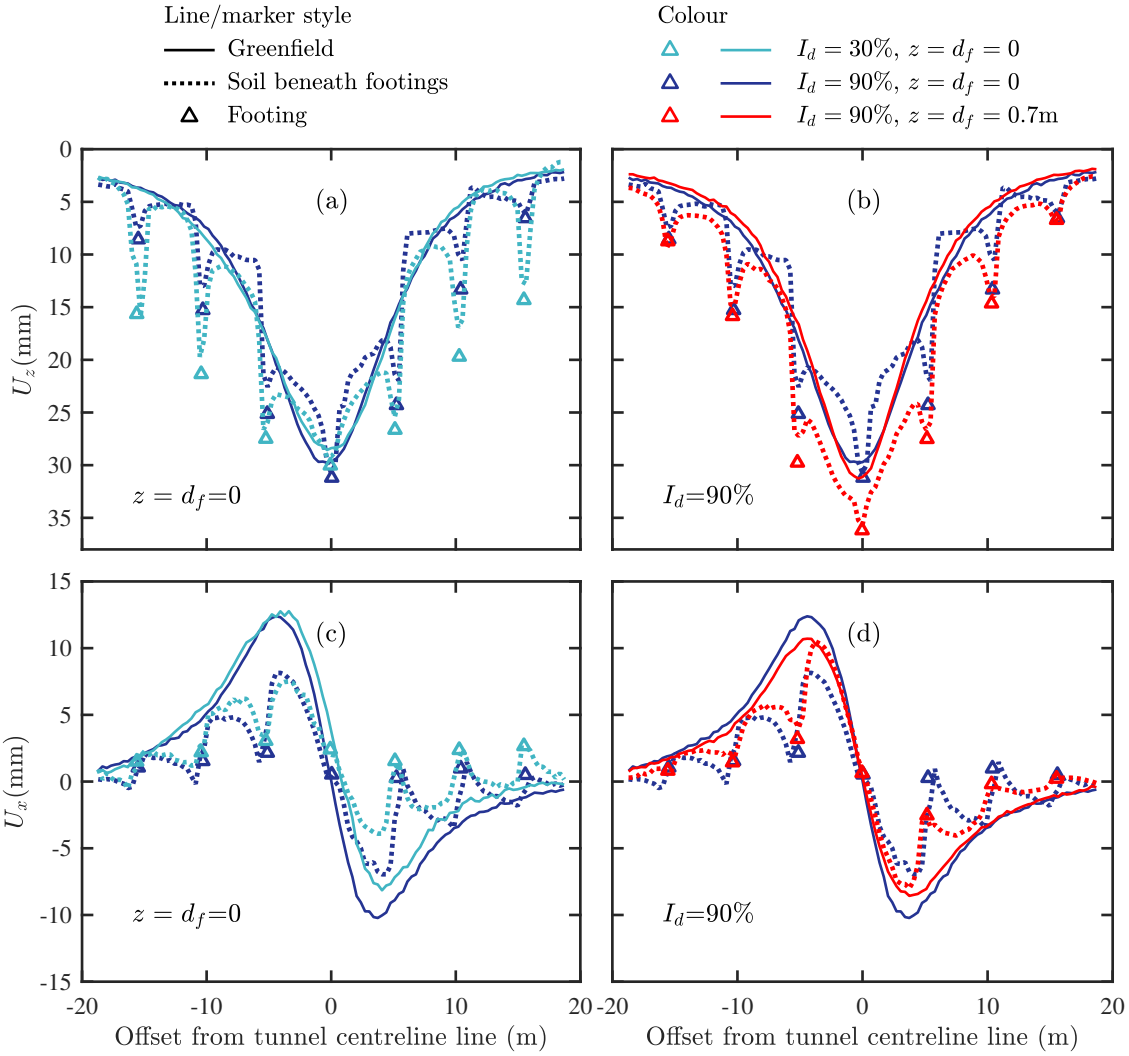


Fig. 6.2. Foundation and underlying soil displacements of frame F2t3b6LN at soil volume loss $V_{l,s}$ = 1.4-1.5%

(from I_d = 30 to 90%) increased the building differential settlements (when considering the surface settlement troughs of equal volume). Interestingly, results in Figure 6.2(b) show that the central footings (#3-5) for d_f =0.7 m settled more than for d_f =0; whereas the settlements of

the external footings were similar for both d_f values. Consequently, the footing embedment d_f also increased the building differential settlements. In the horizontal direction, Figure 6.2(c)-(d) shows that footings restricted (compared to greenfield displacements) the underlying soil horizontal displacements for all tests due to the stiffening action of the columns and the frictional interface between the soil and footings. The footing embedment d_f increased the level of differential horizontal displacements (therefore strains) between the footings, whereas the level of differential horizontal displacements between the footings tended to be smaller in loose sand than in dense sand.

To highlight the behaviour of the footings with tunnel ground losses, the settlements U_z of footings #1-4 (i.e. Foot-1 to -4), horizontal displacements U_x of footings #1-3 (Foot-1 to -3) and horizontal strains ϵ_h of bays #1-3 (i.e. Bay-1 to -3, refer to Figure 6.1) are plotted against tunnel volume loss $V_{l,t}$ up to 3% in Figures 6.3 (dense soil results) and 6.4 (loose soil data), along with greenfield displacements and nominal average horizontal strains (at bay locations).

First, the role of footing embedment is considered. For the footings resting on the ground surface, Figure 6.3(b) shows that the footings settled more than the greenfield displacements in (a) throughout the investigated tunnel volume loss range due to tunnelling-induced load redistribution, particularly for external footings (Foot-1 and -2). For instance, the settlement values of Foot-1 and -2 are approximately twice the corresponding greenfield displacements, whereas the vertical displacement for the central Foot-4 is similar to the corresponding greenfield result because of the reduction of its bearing load. On the other hand, for the footings embedded at a depth of $d_f = 0.7$ m in (c), the vertical displacements of internal footings (Foot-3 and -4) are greater than those in (b), with nearly identical settlements of Foot-1 and -2 in both d_f values.

In the horizontal direction, both the greenfield (at the Foot-3 location) and Foot-3 have the largest horizontal displacements in all tests. In the test with footings resting on the surface (Figure 6.3(b)), U_x of Foot-3 initially increased with $V_{l,t}$, but remained nearly constant after $V_{l,t}$ >1.5%. Surprisingly, Foot-1 and -2 first increased with the tunnel volume loss $V_{l,t}$, but decreased after approximately $V_{l,t} > 1\%$. This indicates that, apart from the ground displacements, the horizontal displacements of the footings are also affected by the structural distortion that results in the rotation of the footing column heads, as highlighted by Franza and DeJong

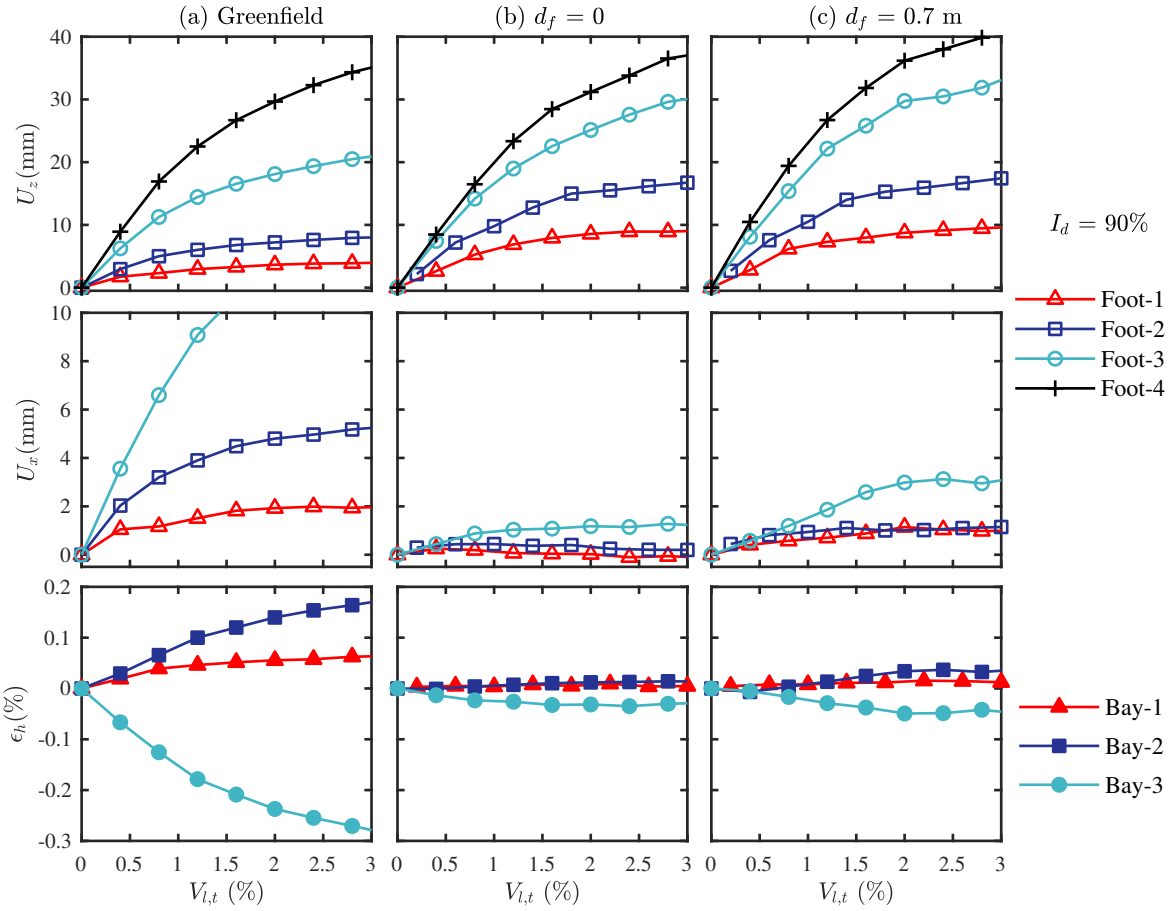


Fig. 6.3. Footing displacements and horizontal strains ($\epsilon_h > 0$ indicates tension) against tunnel volume loss in the dense soil ($I_d = 90\%$)

(2019). On the other hand, Figure 6.3(c) shows that, for the footings embedded at a depth of $d_f = 0.7$ m, the horizontal displacements U_x of Foot-1 to -3 increased significantly for a given tunnel volume loss $V_{l,t}$, compared with the surface footings in (b). Similar principles are also observed for the horizontal strains ϵ_h; the deformation modes between footings are consistent with the greenfield distortion modes, Bay-3 has the greatest absolute value of ϵ_h, and greater absolute values of ϵ_h (in both tension and compression modes) were obtained for the frame with embedded footings. Clearly, the footing embedment has the potential to increase the horizontal displacements and strains between footings, but overall, the values of U_x and ϵ_h are still much smaller than the greenfield case.

The impact of soil density is now considered using data in Figure 6.4 and Figure 6.3(b).

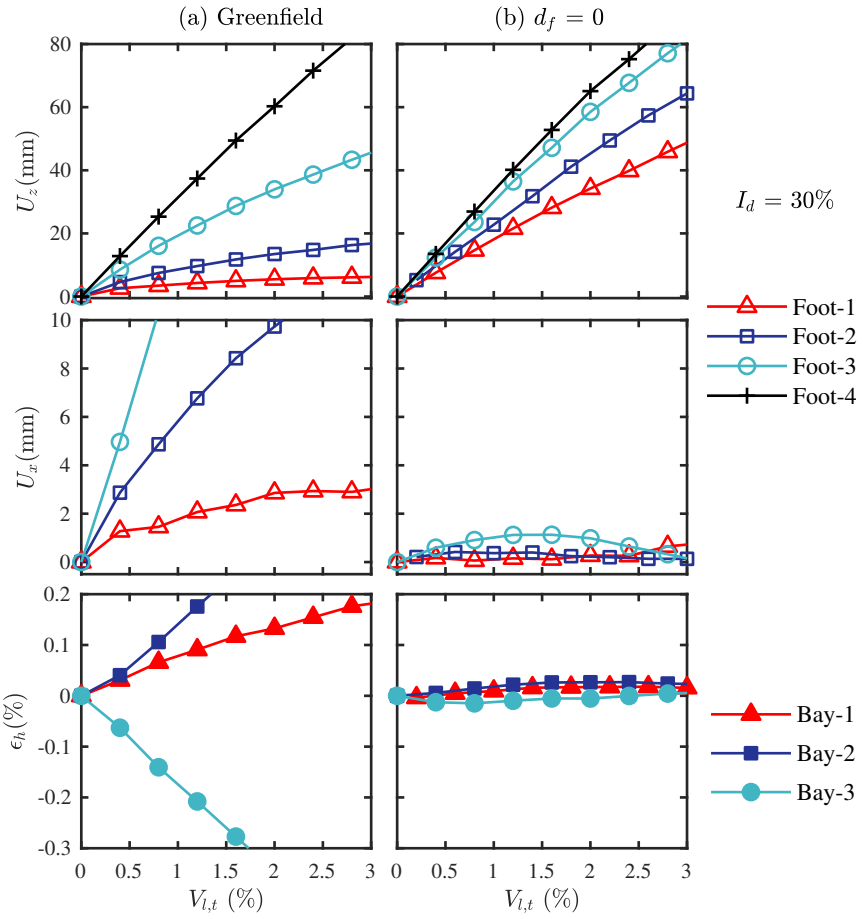


Fig. 6.4. Footing displacements and horizontal strains ($\epsilon_h > 0$ indicates tension) against tunnel volume loss in the loose soil ($I_d = 30\%$)

Compared with the dense soil results (Figure 6.3(b)), the external footings (Foot-1 and -2) in loose soil settled much more than the greenfield displacements (at the corresponding footing locations) and the footings in dense soil. The horizontal displacement U_x of Foot-3 in loose soil initially increased with tunnel volume loss $V_{l,t}$, but significantly decreased after $V_{l,t}$ >1.5%; similar with the dense soil results, the values of U_x of Foot-1 and -2 are minor. Interestingly, the horizontal strains ϵ_h between footings in all bays are in tensile mode (except that Bay-3 is in compression at lower $V_{l,t}$) with minor levels of strains. Therefore, in general, the decrease of the soil density (from I_d = 90 to 30%) increases the footing settlements but decreases the maximum footing horizontal displacements and the horizontal strains between footings; the deformation mode (tension or compression) between footings may also be altered.

6.2.2 Ground movements

Figure 6.5 presents contours of normalised ground horizontal (U_x/D_t) and vertical (U_z/D_t) displacements, along with engineering shear γ_s and volumetric ϵ_v strains of the soil at a tunnel volume loss of $V_{l,t} = 2.0\%$ in the greenfield tunnelling test, and two tunnel-frame interaction tests involving footings either resting on the surface or embedded at a depth of $d_f = 0.7$ m. All tests were in dense sand ($I_d = 90\%$). In Figure 6.5, positive horizontal and vertical displacements are oriented towards the right and downwards, respectively, while positive volumetric strains are contractive. Data outside the contour thresholds were set equal to the closest limit value.

In general, the greenfield results show: a chimney-like displacement pattern, as expected for the relatively low value of C/D_t (Marshall et al., 2012; Franza et al., 2019); large shear strain zones at the tunnel shoulders; high levels of soil dilation directly above the tunnel crown; and intermediate levels of contraction within bands spanning from the tunnel springline to the surface. Comparing the case of footings resting on the surface (b) to greenfield (a) (as discussed in Chapter 5): the footings restricted the horizontal displacements of the soil with a distinct change in magnitude at the footing locations; settlements and shear strains above the tunnel crown are slightly decreased; localised zones of high shear strain are noted at the footing positions due to the action of the footings, resulting in dilation beneath the footings and contraction of the soil between footings.

The role of footing embedment depth d_f is evaluated by comparing Figure 6.5(b)-(c). The embedded footings affected the displacements and strains of a much larger region of soil, with maximum soil displacements (both U_x and U_z) and engineering shear strains being greater for d_f =0.7 m compared to d_f =0. The pattern of horizontal displacements U_x in the region between Foot-1 and -2 is notable: for d_f =0, U_x was negligible due to the actions of the footings, whereas for d_f =0.7 m, U_x is similar to the greenfield values in (a). The embedded footings are also seen to drag down the soil above the depth of 0.7 m, with equal magnitude soil settlements above the footings.

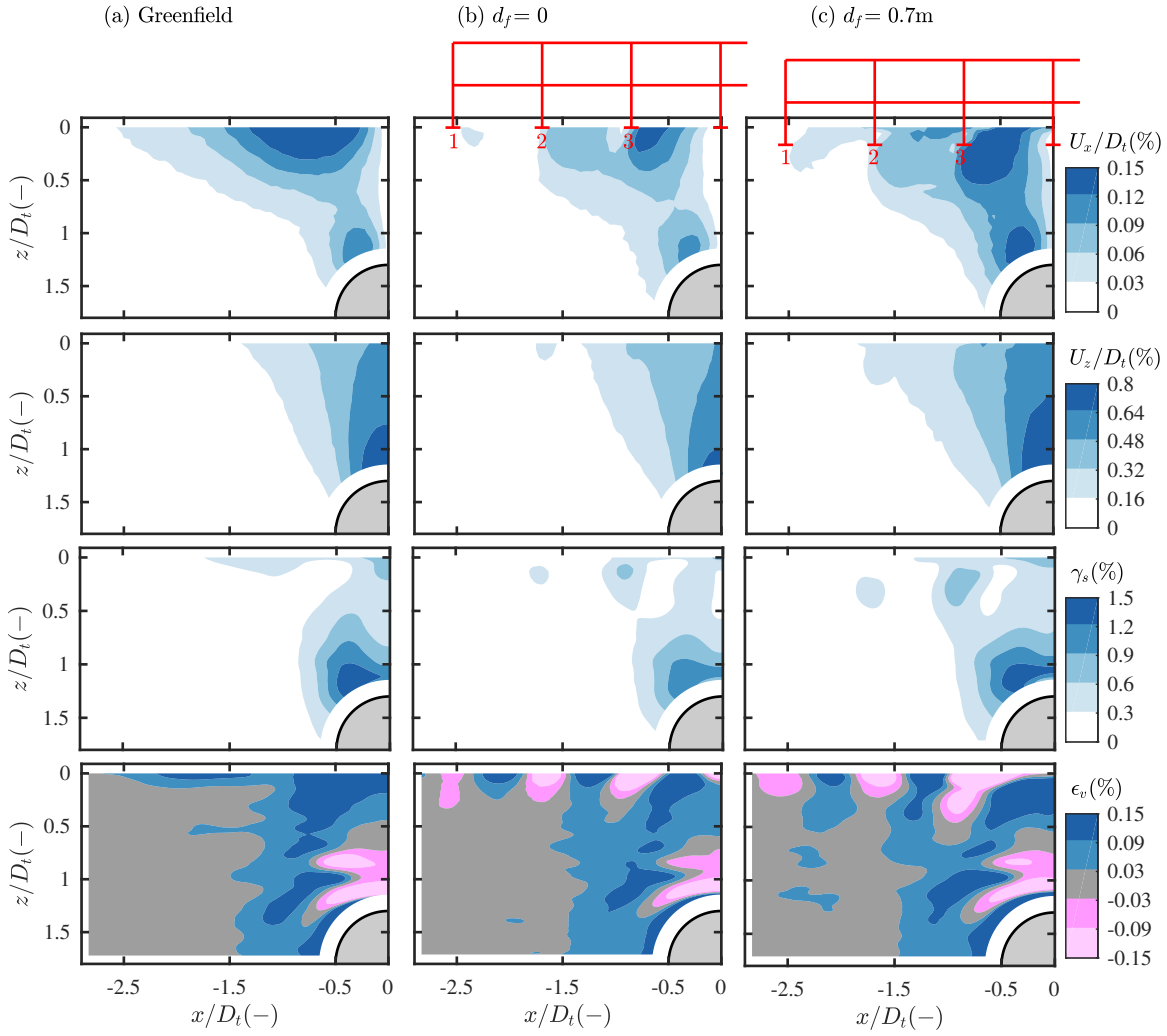


Fig. 6.5. Soil movements normalised by the tunnel diameter, engineering shear and volumetric strains at $V_{l,t} = 2.0\%$ of dense soil ($\epsilon_v < 0$ indicates dilation, data outside the contour thresholds were set equal to the closest limit value): effect of footing embedment depth

6.2.3 Structural distortion and modification factor

The shear deformations of the panels are now discussed. The maximum values of the building angular distortion β_{max} in upper panels are presented in Figure 6.6. In particular, Figure 6.6(a) presents β_{max} against tunnel volume loss $V_{l,t}$ for the dense soil tests to discuss the role of footing embedment, whereas Figure 6.6(b) displays β_{max} against soil volume loss $V_{l,s}$ for the tests with the footings resting on the surface to study the impact of soil density considering settlement troughs of equal volume. Figure 6.6(a) shows that the structure with embedded footings

(d_f =0.7 m) displayed a greater maximum distortion than the structure with the footings resting on the surface (d_f =0). Results in Figure 6.6(b) highlight that, consistent with the results in Chapter 5, the distortion of the framed building with separate footings can be much greater in dense soil than in loose soil for a given soil volume loss, and the higher the volume loss, the greater the difference.

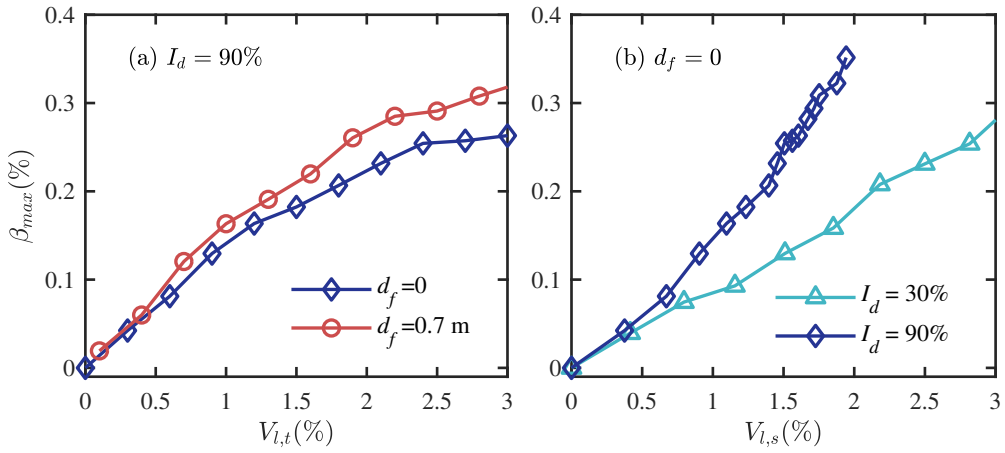


Fig. 6.6. Maximum frame angular distortion against (a) tunnel and (b) soil volume loss

To consider the distribution of distortion and level of damage within panels, the deformed shape of the frames at $V_{l,t}$ = 2% are presented in Figure 6.7. Indicators are used for the range of maximum tensile strain ϵ_{max} and the category of damage within upper and lower panels to assess the distortion levels of panels. Values of ϵ_{max} were computed using the method of Elkayam and Klar (2019) using displacements at the four corners of a panel (Equation 2.21), while the category of damage was obtained from the thresholds of Boscardin and Cording (1989) (Table 2.4). A colour scheme was adopted to denote low for category 0-1, medium for category 2 and high for category 3+.

For the frame with footings on the surface (d_f = 0), Figure 6.7(a) shows that, for the upper floor, only panel-2 and -5 underwent medium levels of damage, whereas all lower panels experienced medium damage levels due to the significant footing horizontal displacements (columns underwent bending deflections). For the embedded footings (d_f = 0.7 m) in (b), damage levels within both upper and lower level panels increased; for instance, all upper panels underwent medium levels of damage and the damage levels of the lower level panel-2 to -5 increased from

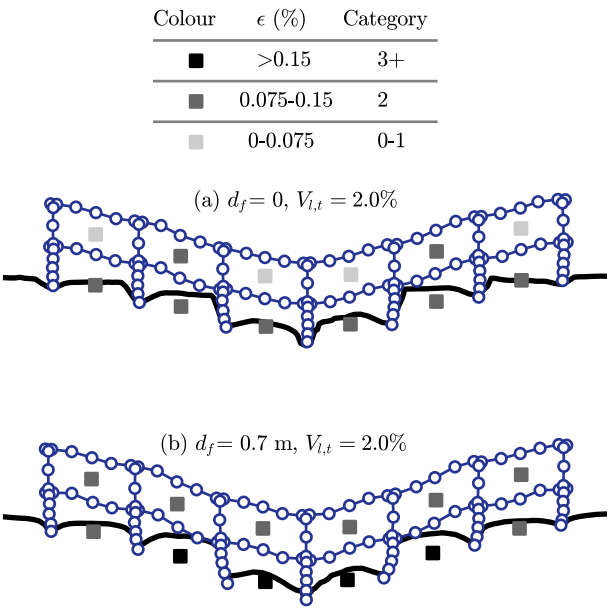


Fig. 6.7. Deformed shape and damage levels of the framed buildings at $V_{l,t}$ =2.0% (scale: 150)

medium to high. As illustrated in Figure 6.2, this is because the frame with embedded footings experienced greater differential settlements and horizontal displacements (larger bending deflections of columns) than the footings resting on the surface.

In practice, modification factor approaches are often used to predict tunnelling-induced structure distortion from greenfield displacements. Chapter 4 and Goh and Mair (2014) presented modification factors of angular distortion M^{β} and horizontal strains $M^{\epsilon,h}$, respectively.

For angular distortion, $M^{\beta} = \beta_{max}/\overline{GS}_{max}$ is obtained by normalising the maximum angular distortion within the structures (β_{max}) by the maximum (among all bay locations) average slope of the greenfield surface settlement trough (or the settlement at the foundation depth) spanning a bay width ($\overline{GS}_{max} = \Delta U_{z,gf,max}/b_{bay}$). The modification factor M^{β} was related to the relative soil-building shear stiffness $\kappa = (E_s B)/(GA_s^*)$. Similarly, $M^{\epsilon,h} = \epsilon_{h,bldg}/\epsilon_{h,gf}$ is given by the ratio of the maximum horizontal strains ($\epsilon_{h,bldg,max}$) among all bays at the foundation level, to the maximum average horizontal strains ($\epsilon_{h,gf,max}$) inferred from the greenfield displacements at the footing locations. Following the work of Franza et al. (2017), the dimensionless relative footing-soil stiffness α_f^* is defined by $\alpha_f^* = 1/(E_s L)\times 3K_b K_c/(h_{storey}^2(2K_b+3K_c))$ inferred from a one storey, single bay portal (Goh and Mair, 2014) (see Equation 2.43), where $K_b = \left(EI/b_{bay}\right)_b$

and $K_c = \left(EI/h_{storey}\right)_c$ are the average stiffness (per metre run) of the beam and footing column, respectively.

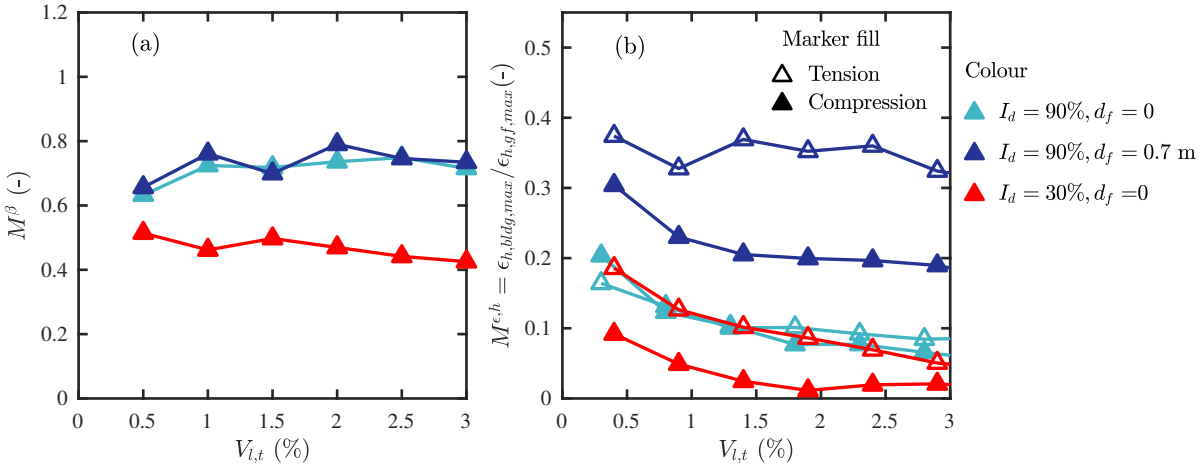


Fig. 6.8. Modification factors of (a) angular distortion and (b) horizontal strain against tunnel volume loss $V_{l,t}$

First, the variation of M^{β} and $M^{\epsilon,h}$ with tunnel volume loss $V_{l,t}$ is discussed. Results in Figure 6.8(a) shows that the trends of M^{β} in loose soil show a steady decrease, whereas the trends in the dense soil tests show a fluctuation within a certain range (consistent with the results in Chapter 5), accepting an overall increasing trend within the investigated tunnel volume loss range. The M^{β} value in loose soil is smaller than in dense soil, whereas the values of M^{β} are very similar for the embedded footings and the footings resting on the surface. Figure 6.8(b) presents the modification factors of maximum tensile and compressive strains (computed by Equation 2.34) against tunnel volume loss $V_{l,t}$. Generally, modification factor trends in all tests are characterised by a steady decrease with $V_{l,t}$ over the investigated range. Furthermore, the value of $M^{\epsilon,h}$ tended to be larger for tensile mode than for compression in all tests (not true for the footings resting on the surface in dense soil at lower $V_{l,t}$). Finally, compared with the scenario involving the footings resting on the surface of dense soil, the decrease of soil density (from $V_{l,t}$ = 90 to 30%) largely reduced the value of $M^{\epsilon,h}$ in the compressive mode, whereas the footing embedment (from d_f = 0 to 0.7 m) increased the modification factors for both deformation modes.

The modification factors are plotted against relative stiffness in Figure 6.9 for $V_{l,t}$ = 0.5, 1.0

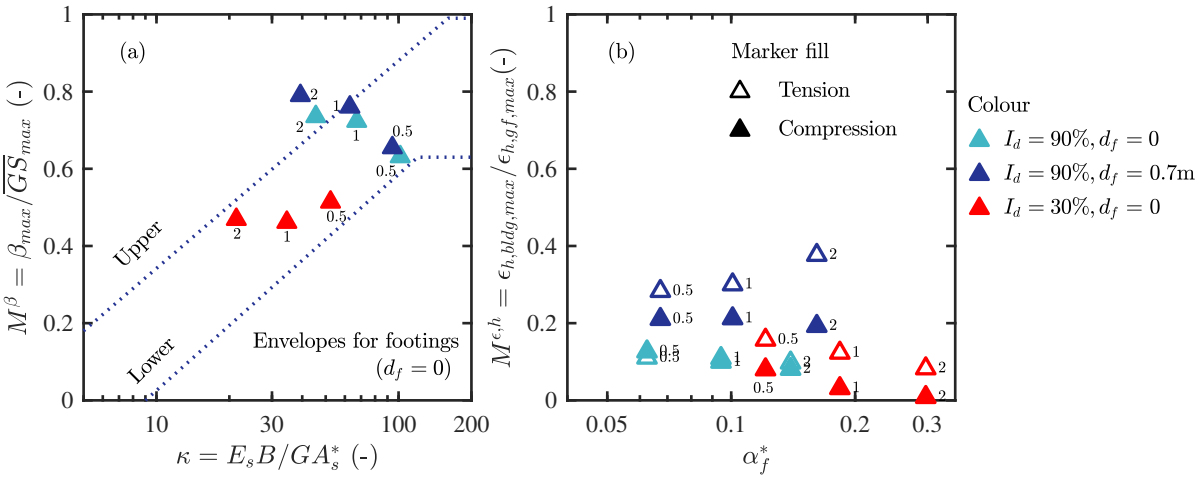


Fig. 6.9. Modification factors of (a) angular distortion and (b) horizontal strain against relative stiffness (numbers near markers indicate $V_{l,t}$)

and 2.0%. Figure 6.9(a) shows that the impact of footing embedment on the normalised maximum angular distortion is minor, with the experimental results (involving the tests with the footing resting on the surface) agreeing well with the empirical envelopes proposed in Chapter 5, which were based on centrifuge test data for frames with footings on the ground surface, i.e. $d_f = 0$. The frame with embedded footings displays slightly larger M^{β} values than the frame with footings on the surface, with the difference increasing with tunnel volume loss $V_{l,t}$.

Results in Figure 6.9(b) display an overall decreasing trend of $M^{\epsilon,h}$ with relative stiffness α_f^*. Figure 6.9(b) shows that the frame with embedded footings exhibited larger values of $M^{\epsilon,h}$ in both tensile and compressive deformation modes. Interestingly, results of the $d_f = 0$ and $I_d = 90\%$ test indicate that modification factors for the tensile and compressive strains were nearly identical, whereas for the tests involving either embedded footings or loose soil, larger values of $M^{\epsilon,h}$ were obtained for tension than for compression. The reason for this difference relates to a complex combination of mechanisms affecting the footing response, i.e. those related to the soil (e.g. shear resistance to sliding for the surface footings in dense sand versus 1) that in loose sand, and 2) a combination of shear resistance along the base and active/passive earth pressures acting on the sides of the embedded footings) and those related to the building (which would not be consistent for different levels of distortion). This can be illustrated using Figure 6.10.

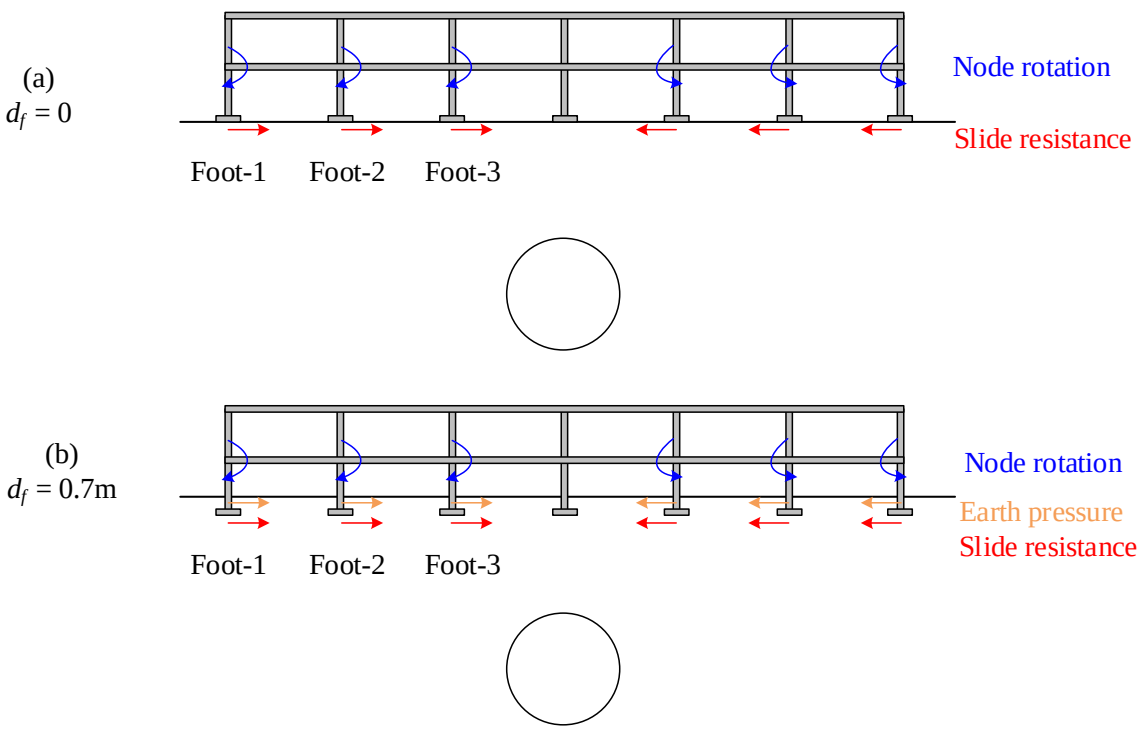


Fig. 6.10. Illustration of the horizontal displacements of the footings

Experimental (Figure 3.20) and numerical (Figure 3.21) loading test results have shown that when the framed building undergoes shear distortion, node rotation occurs, thereby causing the horizontal displacements of the footings. Interestingly, for the central building scenario, the movement direction of the footings caused by building shear distortion is opposite to the greenfield horizontal displacement direction. Therefore, the horizontal displacement of a given footing is either similar to the underlying soil horizontal displacement U_x before the slippage occurs, or smaller than the value of U_x of the underlying soil after the slippage (a reverse movement direction may also be possible when the building distortion is severe). The initiation of the slippage depends on the magnitude of the shear distortion/node rotation, the average pressure (determined by the building load redistribution) at the soil-footing interface, as well as the active/passive earth pressures (for the embedded footings). Finally, the deformation mode (i.e. tension or compression) between footings depends on the differential horizontal displacements of adjacent footings. Importantly, the change of either soil density and footing embedment non-linearly alters the mechanisms related to both the soil and building (distortion level/node rotation), thus resulting in a very complex change of deformation mode/magnitude,

as displayed in Figure 6.9(b).

6.3 Effect of tunnel cover depth

6.3.1 Foundation and underlying soil displacements

The prototype scale settlement U_z and horizontal displacement U_x of the foundations and underlying soil at $V_{l,t} = 2.0\%$ are plotted in Figure 6.11, along with greenfield soil displacements, to investigate the effect of tunnel cover depth on soil-structure interaction. To evaluate the soil-structure interaction for settlement troughs of equal volume (with different values of C/D_t), results are also compared for a given soil volume loss (at the foundation depth, $V_{l,s} = 2.8\%$ for $I_d = 30\%$, and $V_{l,s} = 1.4\%$ for $I_d = 90\%$) using data presented in Figure 6.12. First, the greenfield settlement troughs at $V_{l,t} = 2.0\%$, were characterised by fitting modified Gaussian curves (Vorster et al., 2005) to the surface settlement data, with the results summarised in Table 6.3. The greenfield settlement trough above the tunnel with a greater cover depth ($C/D_t = 2.0$) is much wider than for the tunnel with a smaller cover depth ($C/D_t = 1.3$) for both values of soil density, although the maximum settlement values are close (similar values of $U_{z,max}$). Furthermore, the values of settlement trough parameter K in $C/D_t = 2.0$ tests are also slightly greater than in $C/D_t = 1.3$ tests. The wider settlement trough for the $C/D_t = 2.0$ tests should result in lower differential settlements and distortion levels of a building than the $C/D_t = 1.3$ tests.

Table 6.3. Greenfield settlement trough characteristics (prototype scale)

I_d (%)	$V_{l,t}$ (%)	z (m)	C/D_t	$V_{l,s}$ (%)	$U_{z,max}$ (mm)	i (m)	$K = i/z_t$ (-)
30	2	0	1.3	2.8	60.3	3.4	0.31
30	1.3	0	2.0	2.8	41.6	5.6	0.37
30	2	0	2.0	4.0	62.5	5.1	0.34
90	2	0.7	1.3	1.4	31.4	2.9	0.27
90	1.2	0.7	2.0	1.4	21.5	5.3	0.34
90	2	0.7	2.0	1.9	29.3	4.7	0.31

Table 6.3 also presents the characteristics of greenfield settlement troughs of equal volume for the tests with different values of C/D_t ($V_{l,s} = 2.8\%$ for $I_d = 30\%$, and $V_{l,s} = 1.4\%$ for $I_d = 90\%$). As expected, for both $I_d = 30$ and 90%, the greenfield settlement troughs in

C/D_t = 2.0 tests are much wider and shallower than in C/D_t = 1.3. Therefore, when considering the settlement troughs of equal volume, the wider and shallower settlement trough for the C/D_t = 2.0 tests should also result in much lower differential settlements and distortion levels of a building than the C/D_t = 1.3 tests.

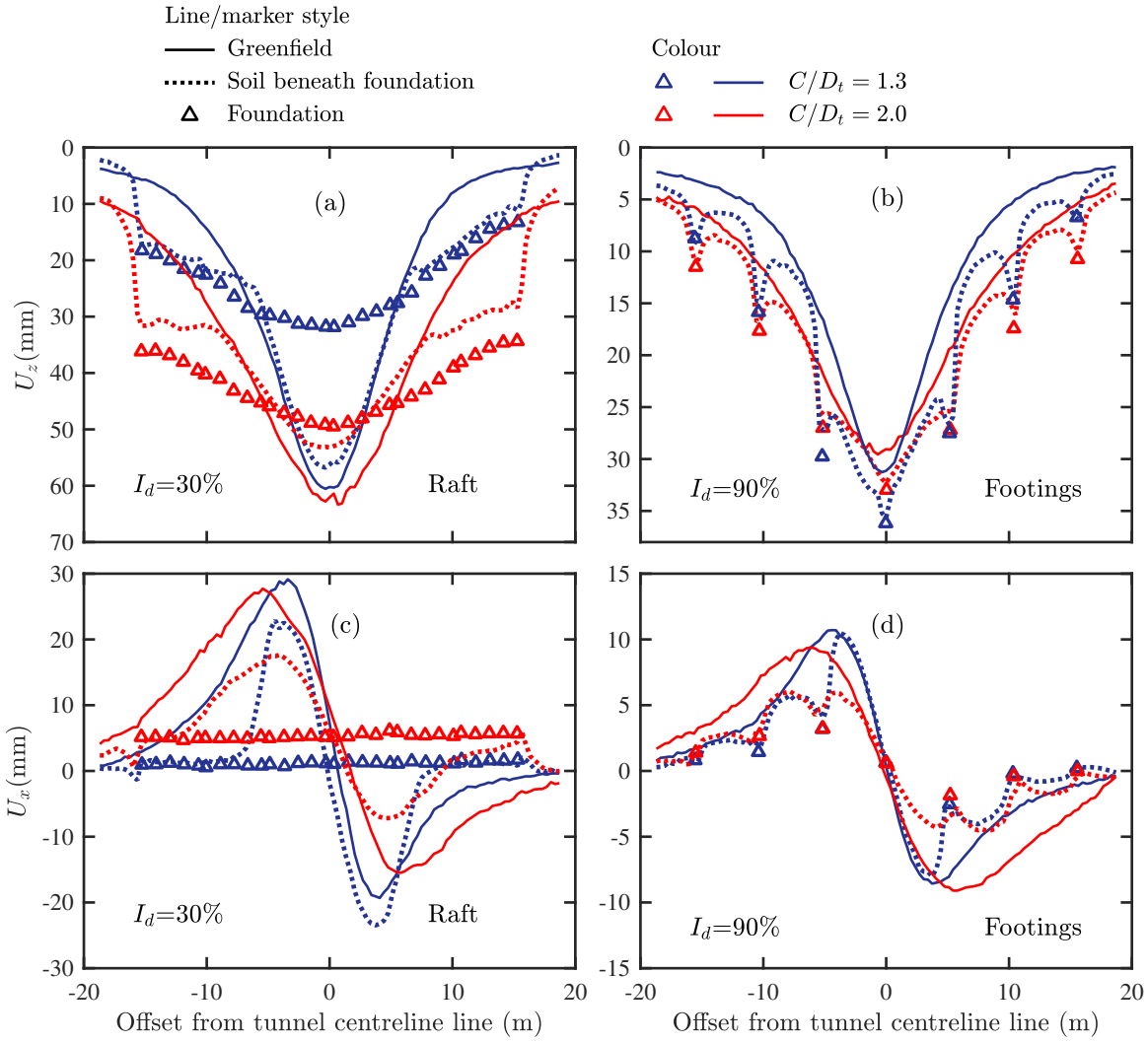


Fig. 6.11. Foundation and underlying soil displacements at $V_{l,t}$ = 2.0%: effect of tunnel cover depth

Figure 6.11(a) shows that in loose soil, the increase of tunnel cover depth (C/D_t from 1.3 to 2.0) resulted in a greater settlement level of the raft foundation, but the deflection ratio of the foundation tended to be smaller (the distortion will be quantified in the following section). The gap was formed for both testing conditions, with a greater magnitude of the gap in the shallower

tunnel test ($C/D_t = 1.3$). Due to the high axial stiffness of the raft, the differential horizontal displacements of the foundation in both tests are negligible.

Results of the footings in Figure 6.11(b) show that, in dense soil, the external footings (Foot-1 to -2, and -6 to -7) in $C/D_t = 1.3$ test settled more than in $C/D_t = 2.0$ case, while the central footings (Foot-3 to -5) had a smaller settlement level for $C/D_t = 1.3$ than for $C/D_t = 2.0$. Consequently, the increase of tunnel cover depth reduced the differential settlements of the footings, and thus decreased the structural distortion. In the horizontal direction, the horizontal displacements U_x of the external footings (Foot-1 to -2) in the deeper tunnel ($C/D_t = 2.0$) tended to be greater than in the shallower tunnel ($C/D_t = 1.3$), however the differential horizontal displacements decreased.

When considering the settlement troughs of equal volume, Figure 6.12(a)-(b) shows that the foundation differential settlements for $C/D_t = 2.0$ were lower than for $C/D_t = 1.3$. For the raft foundation (Figure 6.12(a)), a greater maximum settlement is observed in the $C/D_t = 2.0$ and $I_d = 30\%$ test, whereas for separate footings, a greater maximum settlement is observed in the $C/D_t = 1.3$ and $I_d = 90\%$ test. In the horizontal direction, the maximum horizontal displacements U_x of the soil in the greenfield and tunnel-frame interaction tests for $C/D_t = 2.0$ were smaller than for $C/D_t = 1.3$ (see Figure 6.12(c)-(d)). Consequently, the horizontal displacements of the footings also decreased in $C/D_t = 2.0$ compared $C/D_t = 1.3$.

Figure 6.13 presents the variation of the settlement U_z and horizontal displacements U_x of the footings and the horizontal strains ϵ_h between footings against tunnel volume loss $V_{l,t}$, along with the corresponding greenfield displacements and nominal average strains. Compared with the greenfield tunnelling for $C/D_t = 1.3$ in Figure 6.13(a), the surface soil at the Foot-1 to -3 locations had greater settlements for $C/D_t = 2.0$ throughout the investigated $V_{l,t}$ range, while the maximum settlement (at the Foot-4 location) was nearly identical (see Figure 6.13(d)). Consequently, the differential settlements (see the difference of the settlements between Foot-1 and -4) for both the greenfield test in (d) and the tunnel-frame interaction test in (c) were smaller than in (a) and (b).

A similar principle with U_z was also observed for the horizontal displacements U_x; the U_x of the ground surface at the locations of Foot-1 and -2 in the greenfield test were greater

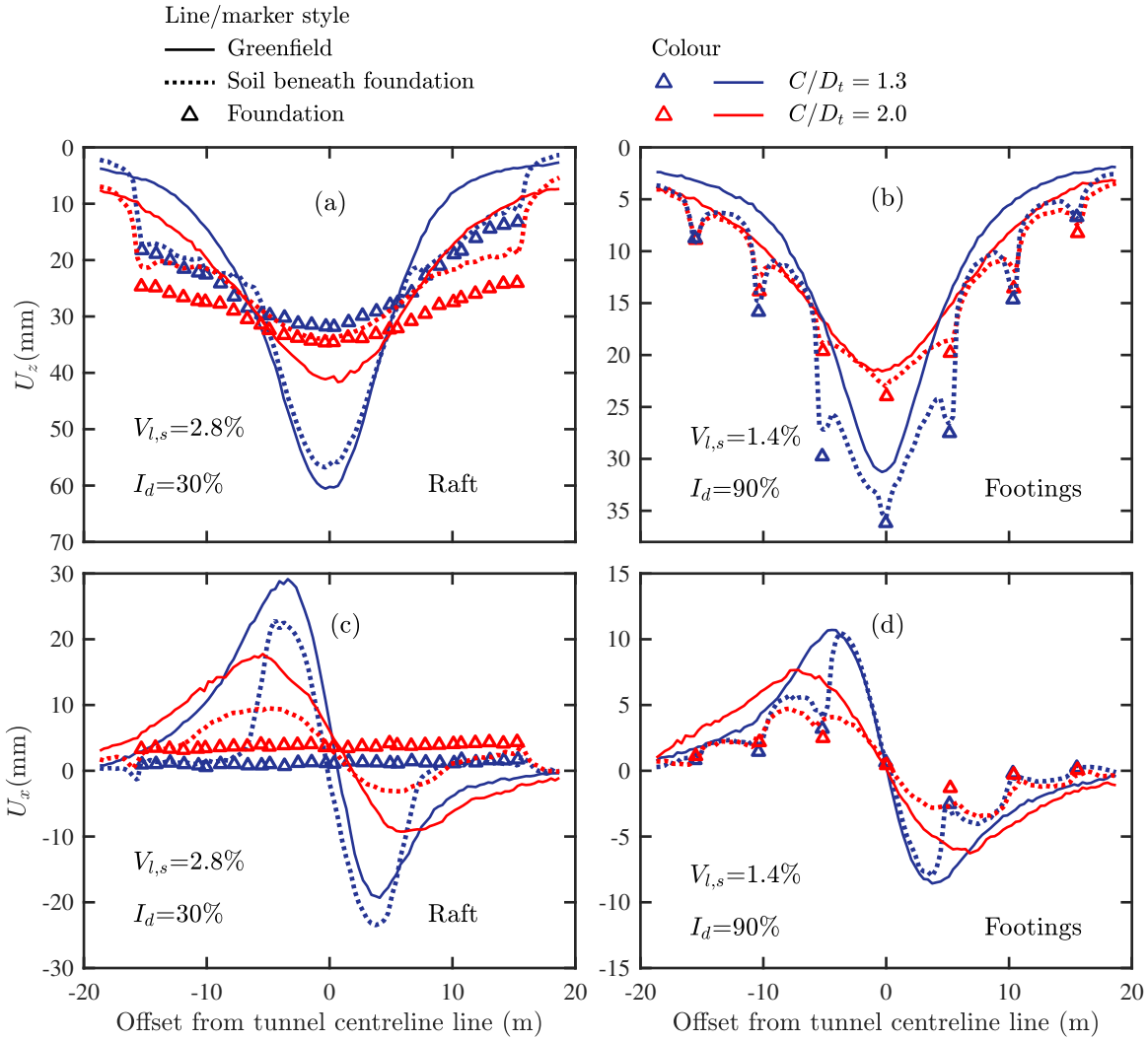


Fig. 6.12. Foundation and underlying soil displacements at identical soil volume loss ($V_{l,s}$ = 1.4% for I_d = 90% and $V_{l,s}$ = 2.8% for I_d = 30%): effect of tunnel cover depth

for C/D_t = 2.0 than for 1.3, resulting in greater values of U_x of Foot-1 and -2 (compare Figure 6.13(c) and (b)). Furthermore, in the greenfield tests, the nominal average tensile strain $\epsilon_{h,t}$ at Bay-1 and -2 locations increased and decreased, respectively, for C/D_t = 2.0 than for 1.3 (compare Figure 6.13(d) with (a)). As a result, the values of tensile strains $\epsilon_{h,t}$ of Bay-1 and -2 for C/D_t = 2.0 were also slightly greater and smaller, respectively, than those for C/D_t = 1.3. On the other hand, the nominal average compressive strains $\epsilon_{h,c}$ of Bay-3 in greenfield tests (Figure 6.13(a) and (d)) were nearly identical for C/D_t = 2.0 and 1.3, thus compressive strains $\epsilon_{h,c}$ of Bay-3 in the two tunnel-frame interaction tests were similar (see Figure 6.13(b) and (c)).

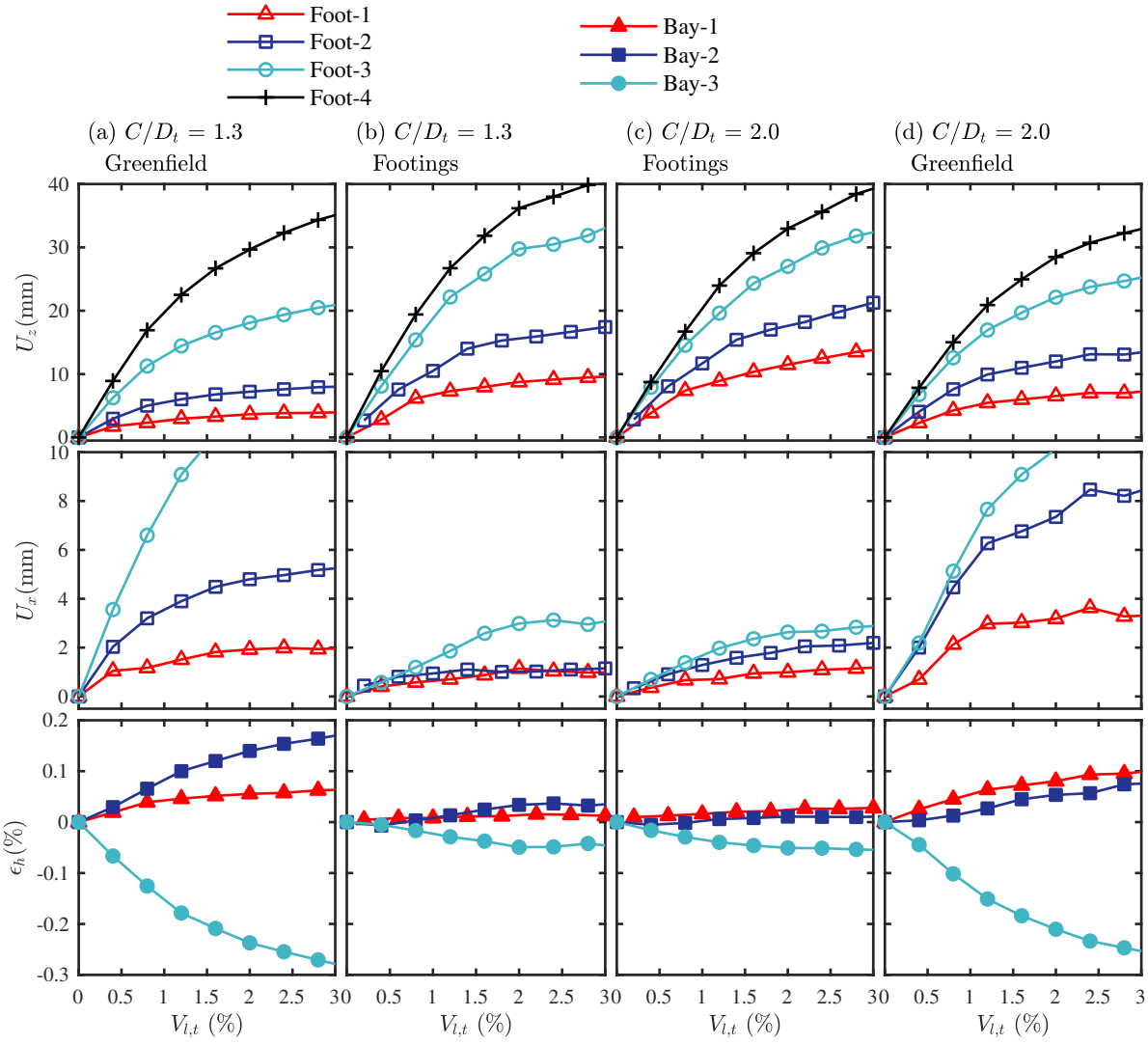


Fig. 6.13. Footing displacements and horizontal strains ($\epsilon_h > 0$ indicates tension) against tunnel volume loss in the dense soil ($I_d = 90\%$): effect of tunnel cover depth

6.3.2 Ground movements

Figure 6.14 presents contours of normalised ground horizontal (U_x/D_t) and vertical (U_z/D_t) displacements, along with engineering shear γ_s and volumetric ϵ_v stains of the soil at a tunnel volume loss of $V_{l,t} = 2.0\%$ in greenfield tunnelling test ($C/D_t = 2.0$), and two tunnel-frame interaction tests with either a shallower ($C/D_t = 1.3$) or relatively deeper ($C/D_t = 2.0$) tunnel. All tests were in dense sand ($I_d = 90\%$). In Figure 6.14, positive horizontal and vertical displacements are oriented towards the right and downwards, respectively, while positive volu-

metric strains are contractive. Data outside the contour thresholds were set equal to the closest limit value.

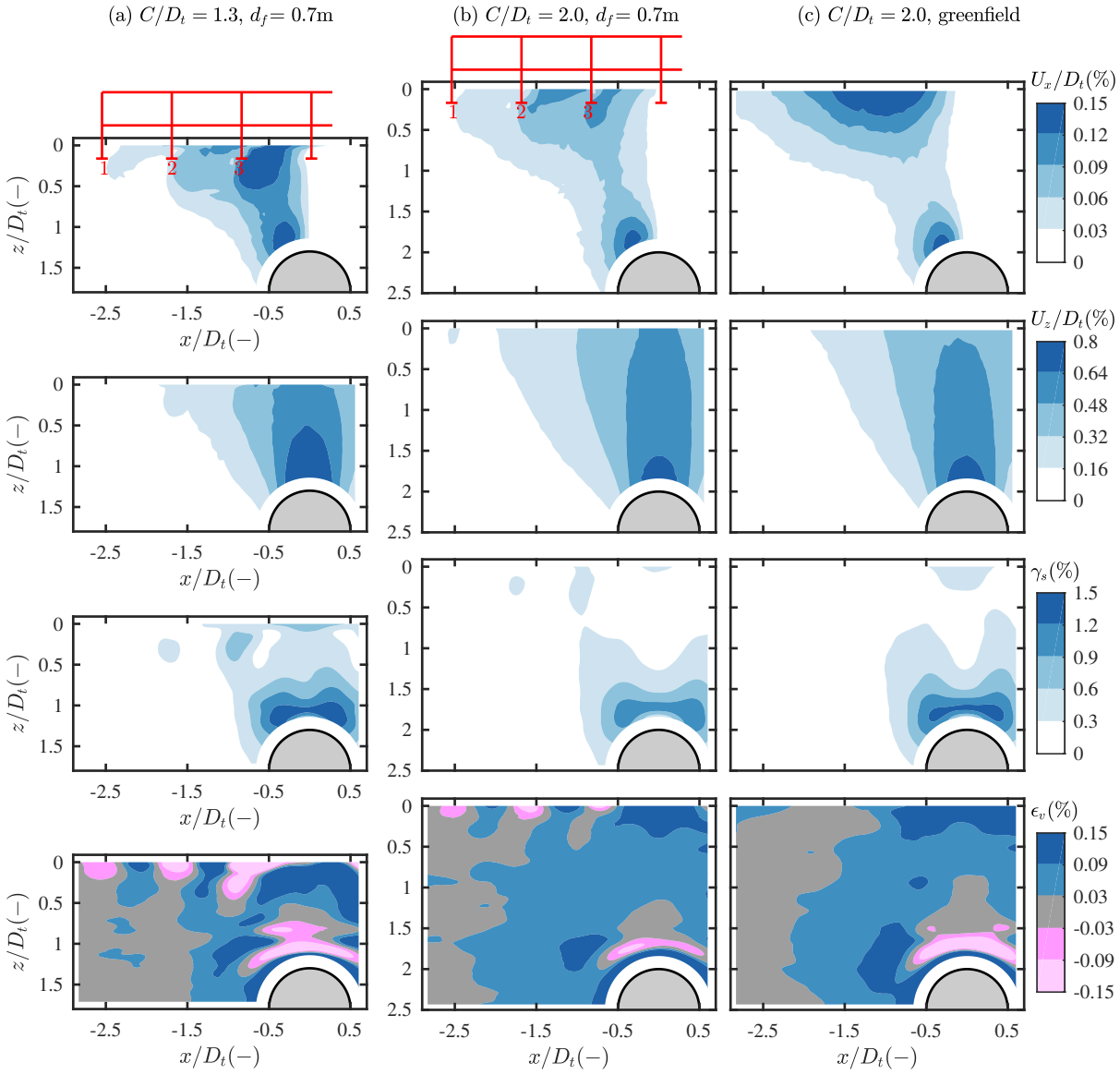


Fig. 6.14. Soil movements normalised by the tunnel diameter, engineering shear and volumetric strains at $V_{l,t} = 2.0\%$ ($\epsilon_v < 0$ indicates dilation, data outside the contour thresholds were set equal to the closest limit value): effect of tunnel cover depth

The effect of tunnel cover depth on the ground deformation is briefly discussed using data in Figure 6.14(a) and (b). Results show that the increase of tunnel cover depth ($C/D_t = 1.3$ to 2.0) primarily affected the magnitude of the displacements and strains; the higher the C/D_t,

the lower the levels of displacements and strains. The effect, relative to the greenfield case, of the presence of the building on tunnelling-induced ground deformation for $C/D_t = 2.0$ is identical to that for $C/D_t = 1.3$; the footings restricted the horizontal displacements of the soil with a distinct change in magnitude at the footing locations; shear and volumetric strains above the tunnel crown are slightly decreased; localised zones of high shear strain are noted at the footing positions due to the action of the footings, resulting in dilation beneath the footings and contraction of the soil between footings.

6.3.3 Soil volume losses

As discussed in Chapters 4 and 5, in drained soils, because of their contractive/dilative response to shearing, the relationship between soil volume loss $V_{l,s}$ (given by the integration of the soil settlements at a given depth) and tunnel volume loss $V_{l,t}$ (the ground loss at the tunnel boundary) is not 1:1 (as would be the case in undrained soils), which could also have an impact on the tunnel-framed building interaction behaviour. Engineers tasked with designing excavations need to predict/assume reasonable values of soil volume losses given an expected level of tunnel volume loss $V_{l,t}$ for the applied tunnelling operations (Franza et al., 2020b). Figure 6.15 presents the relationship between soil volume loss $V_{l,s}$ (given by the integration of the soil settlements at the foundation depth) and tunnel volume loss $V_{l,t}$.

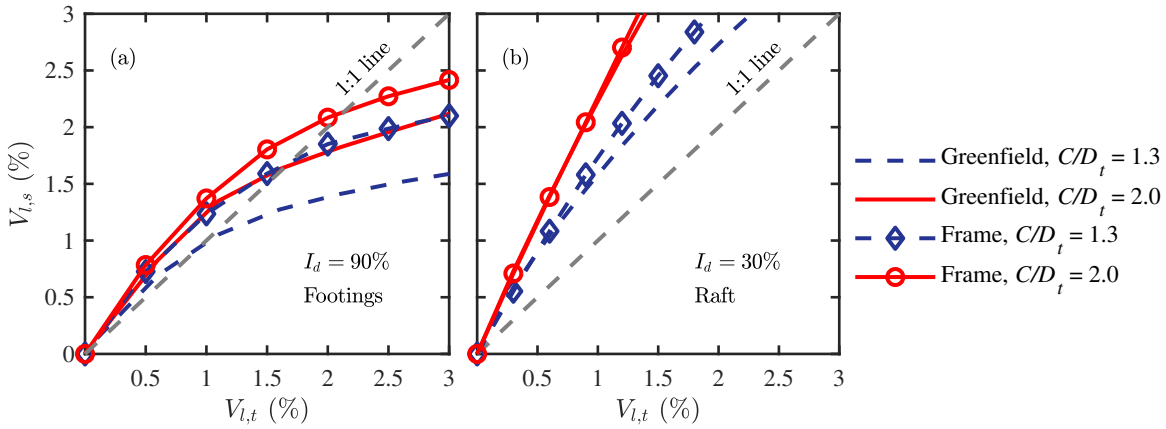


Fig. 6.15. Variation of soil volume loss with tunnel volume loss: effect of tunnel cover depth

Figure 6.15 shows that, consistent with Franza et al. (2019), the greater the tunnel cover

depth, the higher the soil volume loss in both greenfield and tunnel-structure interaction tests. Interestingly, for the dense soil tests involving the footings embedded at a depth of $d_f = 0.7$ m, Figure 6.15(a) shows that the presence of the building notably increased the soil volume loss $V_{l,s}$, compared with the greenfield scenario. This differs from the results for the cases with the footings resting on the surface presented in Chapter 5, indicating a more complex soil-footing interaction mechanism for the embedded foundation.

6.3.4 Structural distortion and modification factor

The effect of tunnel cover depth on the shear deformations of the panels is now discussed. First, the maximum values of the building angular distortion β_{max} in upper level panels are plotted against $V_{l,t}$ and $V_{l,s}$ in Figure 6.16(a) and (b), respectively. As expected, the values of β_{max} are smaller for $C/D_t = 2.0$ tests than for $C/D_t = 1.3$ cases, and the difference of the values of β_{max} between $C/D_t = 1.3$ and 2.0 for an identical $V_{l,s}$ tends to be greater than for an identical $V_{l,t}$.

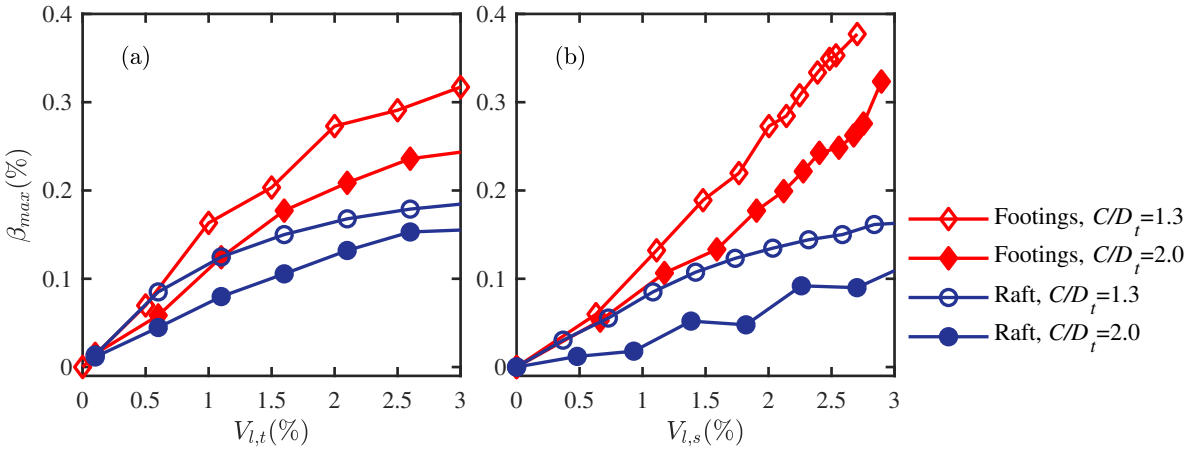


Fig. 6.16. Maximum building angular distortion against tunnel/soil volume loss: effect of tunnel cover depth

To consider the distribution of distortion and level of damage within the upper and lower level panels, the deformed shape of the framed buildings and the ground surface movements at $V_{l,t} = 2\%$ are presented in Figure 6.17. Indicators are used for the range of maximum tensile strain ϵ_{max} (computed using Equation 2.21) and the category of damage (obtained from the thresholds of Boscardin and Cording (1989), see Table 2.4) within upper and lower panels to

assess the distortion levels of panels. A colour scheme was adopted to denote low for category 0-1, medium for category 2 and high for category 3+.

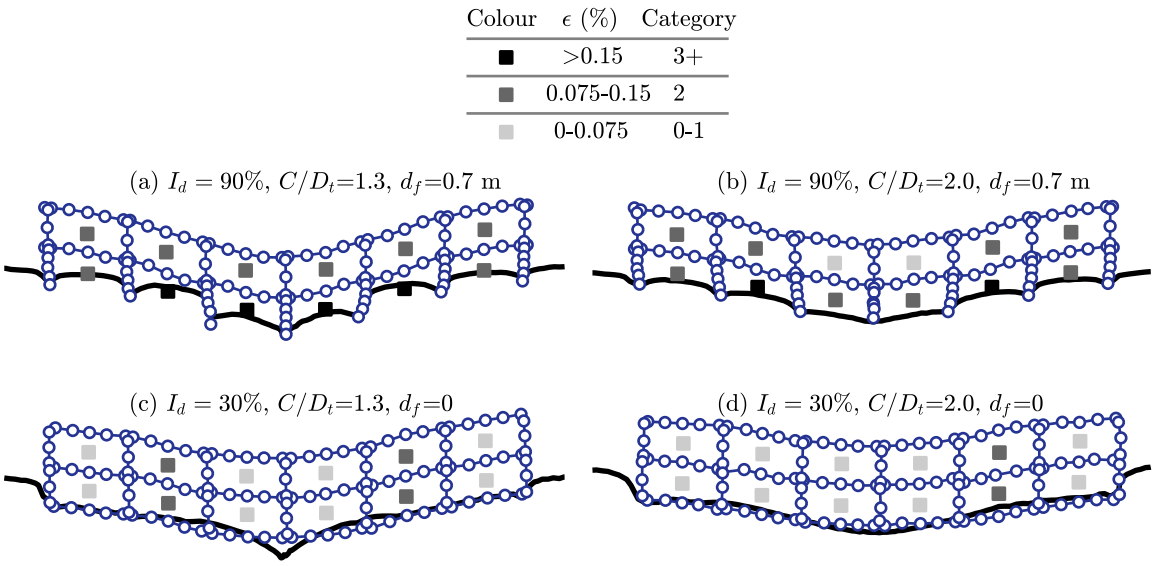


Fig. 6.17. Frame deformed shape and level of damage at tunnel volume loss $V_{l,t}$ = 2.0%: effect of tunnel cover depth

For the C/D_t = 1.3 test in Figure 6.17(a) (I_d = 90%, d_f = 0.7 m, and separate footings), all the upper level panels and lower level Panel-1 and -6 underwent medium levels of damage; whereas lower level Panel-2 to -5 experienced high levels of damage due to bending deflections of footing columns. For the scenario with a greater tunnel cover depth (C/D_t = 2.0), Figure 6.17(b) shows that the level of damage within the internal panels (Panel-3 to -4) decreased (from high to medium, or from medium to low). In Figure 6.17(c) (C/D_t = 1.3, I_d = 30%, and the raft foundation), Panel-2 and -5 underwent medium damage levels, and the level of distortion for Panel-2 decreased to low damage level for C/D_t = 2.0 in Figure 6.17(d).

In practice, modification factor approaches are often used to predict tunnelling-induced structure distortion from greenfield displacements. First, the variation of M^{β} and $M^{\epsilon,h}$ with tunnel volume loss $V_{l,t}$ is discussed. Results in Figure 6.18(a) shows that the trends of M^{β} in loose soil show a steady decrease, whereas the trends in the dense soil tests show a fluctuation within a certain range (consistent with the results in Chapter 5). The increase of tunnel cover depth (from C/D_t = 1.3 to 2.0) tended to increase the values of M^{β}. Figure 6.18(b) also dis-

plays a decreasing trend of $M^{\epsilon,h}$ with $V_{l,t}$, with a greater rate for the loose soil tests, and the value of $M^{\epsilon,h}$ in tension mode was greater than in compression mode for both tests. Furthermore, the values of $M^{\epsilon,h}$ tended to be greater for a deeper (C/D_t = 2.0) tunnel test (not true for $M^{\epsilon,h}$ at high $V_{l,t}$), however their difference is rather limited. Note that Figure 6.18 presents the variation of modification factors with tunnel volume loss $V_{l,t}$. For a given $V_{l,t}$, the soil volume loss $V_{l,s}$ is greater for C/D_t = 2.0 than for 1.3 (refer to Figure 6.15). Therefore, when plotting the modification factor against soil volume loss $V_{l,s}$, the curves of C/D_t = 2.0 in Figure 6.18 should shift toward the right, and thus similar findings as those from Figure 6.18 (described above) will be obtained when considering the identical soil volume loss $V_{l,s}$.

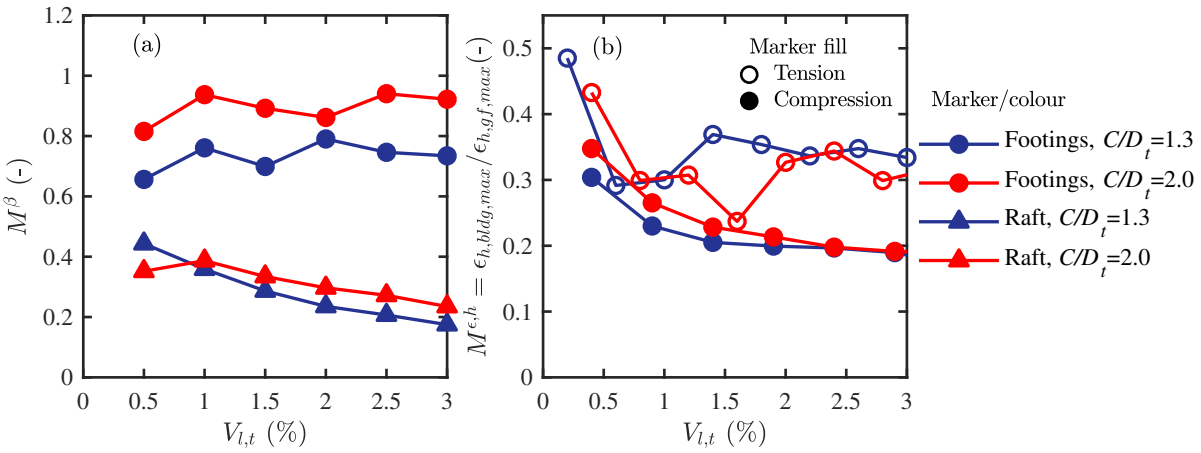


Fig. 6.18. Modification factors of (a) angular distortion and (b) horizontal strain against tunnel volume loss: effect of tunnel cover depth

The modification factors (M^{β} and $M^{\epsilon,h}$) are plotted against relative stiffness in Figure 6.19 for $V_{l,t}$ = 0.5, 1.0 and 2.0%. Envelopes for the raft and separate footings proposed, respectively, in Chapters 4 and 5 based on centrifuge testing data for frames with foundations on the ground surface (C/D_t = 1.3), are also included in Figure 6.19(a). Results show that, for the frame on raft foundation resting on the ground surface, experimental results agree well with the empirical envelopes for the raft. On the other hand, data points of M^{β} for the frames with embedded footings do not entirely agree with the empirical envelopes for the footings resting on the surface, with a greater value of M^{β} than the predicted maximum data for a given relative stiffness value. Interestingly, results of M^{β} for the embedded footings agree well with the empirical envelopes

for the raft, suggesting that the envelopes for the raft could be applicable for the frame with embedded footings (more work is needed to support this conclusion). In Figure 6.19(b), a decreasing trend of $M^{\epsilon,h}$ tends to be observed. The value of $M^{\epsilon,h}$ for tension is greater than for compression at high tunnel volume loss $V_{l,t}$ = 2.0%.

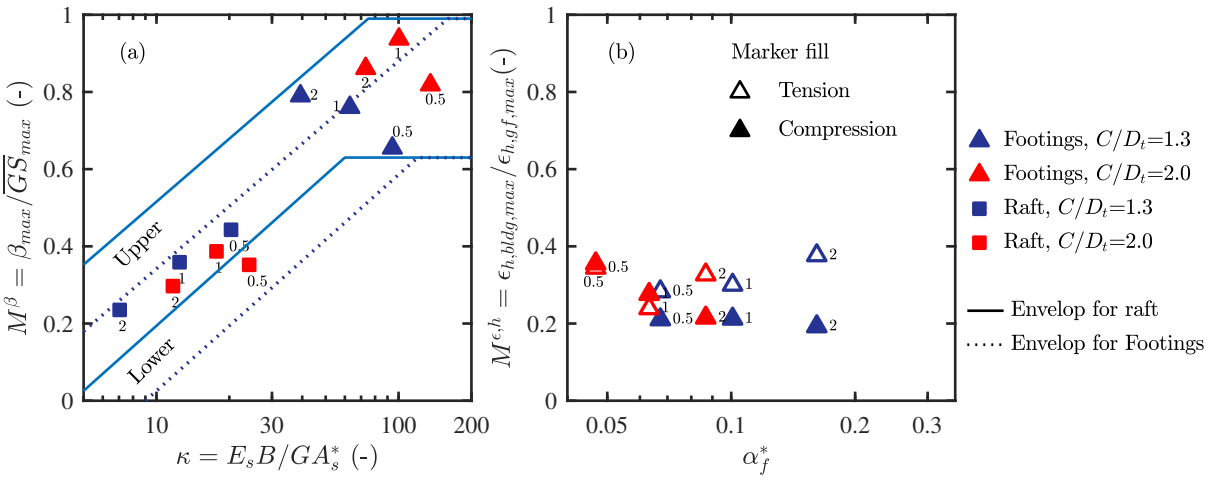


Fig. 6.19. Modification factors of (a) angular distortion and (b) horizontal strain against relative stiffness (numbers near markers indicate $V_{l,t}$): effect of tunnel cover depth

6.4 Summary

This chapter presented results from a centrifuge study of the effects of foundation embedment and tunnel cover depth on tunnelling-induced deformations of a framed building resting on the shallow foundation (raft or separate footings). Results illustrated that the embedment slightly increased the ground deformations, the soil volume losses, the foundation differential settlements and the building (shear) angular distortions. On the other hand, the increase in tunnelling-induced horizontal displacements and strains at the foundation was notable, particularly at high tunnel volume losses. The increase of tunnel cover depth decreased the differential settlements and structural distortion, as well as the level of ground deformations (displacements and strains). Results were also used to evaluate frame modification factors, normalising the building maximum angular distortion and maximum horizontal strains by the greenfield deformation levels. For modification factors of the building maximum angular distortions M^{β}, results of M^{β} of the

frame with embedded footings do not entirely agree with the empirical envelopes, whereas an increasing trend of modification factors of maximum horizontal strains with relative stiffness is obtained.

The presented results indicate that, in practice, engineers should consider that the embedment of separate footings could increase tunnelling-induced distress of buildings with respect to predictions obtained by assuming footings rest directly on the ground surface, particularly if the building is susceptible to the actions of horizontal ground deformations (as for separate footings).

Chapter 7

Conclusions and Recommendations

In the urban environment, tunnels are often constructed to satisfy the need for the improvement of infrastructure. In increasingly congested cities, tunnelling is gradually taking place in close proximity to buried and surface structures. To mitigate tunnelling-induced damage of nearby structures, engineers are tasked with the understanding of the complex soil-structure interaction mechanisms caused by tunnel excavation.

When considering the response of surface buildings to tunnel construction, extensive studies have simplified the building as an equivalent plate/beam (Franzius et al., 2006; Pickhaver et al., 2010; Maleki et al., 2011; Namazi and Mohamad, 2013; Farrell et al., 2014; Bilotta et al., 2017; Franza and Marshall, 2018). This simplification involves uncertainties that have not yet been sufficiently investigated for realistic buildings. For instance, when estimating the total structure stiffness, most researchers have adopted a pure bending stiffness (Franzius et al., 2006; Goh and Mair, 2014; Haji et al., 2018) despite the evidence that shear flexibility can have an important role (Potts and Addenbrooke, 1997; Finno et al., 2005; Franza et al., 2020a). Furthermore, the local deformations of infill walls in frames is potentially not well described by equivalent beams or plates (Goh and Mair, 2014; Boldini et al., 2018).

This thesis addressed the issue of the response of framed buildings, resting on either raft foundations or separate strip footings, to tunnelling in sandy ground. Geotechnical centrifuge testing of scaled physical models was the main tool to provide reliable and valuable data for this research. This chapter first summarises the most significant findings of the study within

the previous chapters (Chapters 4, 5 and 6); then areas of interest related to the topic of this research that deserve further study are suggested.

7.1 Conclusions

A comprehensive experimental study on the response of framed buildings on either raft foundations or separate strip footings to tunnelling in sandy ground was presented in this thesis, including data from a unique set of centrifuge tests (44 in total). The research considered 8 elastic framed building models with varying configuration and foundation type, with tunnelling- and structure-related parameters (soil density, tunnel cover depth, foundation embedment depth, building eccentricity) varied during tests. The tunnelling-induced displacements of the framed buildings and the underlying soil were analysed; the tunnelling-induced ground movements affected by the presence of the buildings were presented and discussed; the framed structure deformations were studied using deflection ratios, angular distortions, and strain-based damage categories. The response of the frames on raft foundations was also contrasted against the results obtained in the scenario in which an equivalent isotropic plate was adopted (Farrell, 2010).

To the knowledge of the author, this research, in the first time, provides the centrifuge data related to the tunnel-framed building interaction problem. Experimental results confirmed that the bending and shear stiffness of framed buildings can be directly estimated by modelling load-deflection tests, with framed structures (without infill shear wall) primary exhibiting shear behaviour. Therefore, it was found that angular/shear distortions within each bay or panel are more appropriate for quantifying framed building distortions than deflection ratios. A new modification factor approach was proposed to relate maximum angular distortions to the slope of the greenfield settlement profile. Upper and lower empirical envelopes for preliminary damage assessment considering building eccentricity and foundation configuration were suggested. The following detailed conclusions can be drawn from the work.

7.1.1 The response of framed buildings on raft foundations

The response of framed buildings on raft foundations to tunnel construction was discussed in Chapter 4. Five framed building models were considered and the influence of building configuration, weight, eccentricity, and soil density were evaluated. Soil and foundation displacements,

soil engineering shear and volumetric strains, frame deformed shape, maximum structure deformation parameters (deflection ratios and angular distortions), and associated modification factors are illustrated.

First, the response of raft foundations to tunnelling was compared against the results of equivalent isotropic plates (Farrell, 2010). Comparison of settlement profiles demonstrated that the settlements of equivalent isotropic plate models (with a bending dominated deformation mode) do not always adequately match those from framed building models, missing important features mainly with respect to the shape of the foundation settlement; the raft foundations primarily exhibited shear behaviour and underwent a semi-flexible response with both sagging and hogging deformation modes, whereas the equivalent isotropic plates mainly displayed sagging zones (also observed in numerical studies (Boldini et al., 2018)). This mechanism is likely due to the role of the shear flexibility being negligible for the equivalent isotropic plates, as well as the non-uniform contact pressure associated with the frame geometry (for instance, the contact pressure beneath the column is greater than other portions of the foundation).

Generally, building width, location, stiffness and weight significantly affected the response of the framed buildings to tunnel construction. Results showed that, for both loose and dense soil, a greater transverse width increased the tunnelling-induced framed building distortions, whereas a larger building eccentricity (facilitating building tilt) tended to reduce frame distortions. The structure self-weight and stiffness also played a role, particularly in relation to the formation of a gap beneath the building; the greater the weight, or the smaller the stiffness, the smaller the gap formed beneath the foundation.

Soil relative density affected the soil shear and volumetric behaviour and dominated the $V_{l,s} - V_{l,t}$ relationship for all centrifuge tests, which impacted the overall structure settlement level (consequently, the distortions of the frames), whereas the presence of the surface building had a minor effect; for the loose soil tests, the loose sand always exhibited an overall contractive response, whereas the dense soil transitioned from contractive at lower values of tunnel volume loss $V_{l,t} < 1\%$ towards dilative at higher tunnel volume losses. Therefore, loose sands had greater potential for building distortions than dense sands at a given tunnel volume loss. On the contrary, for a given soil volume loss at the ground surface (equal volume of the surface

settlement trough), buildings experienced greater levels of settlement and smaller distortion for loose sand tests, and the smaller the area of the foundation (for instance, from long to short rafts), the greater the influence.

The presence of the framed buildings on raft foundations had a great impact on the tunnelling-induced ground movements. For the central long structures, or the long buildings with limited eccentricity (for instance, $e/B = 0.2$ in this thesis), the horizontal displacements of the soil near the surface were largely restricted by the foundation roughness and building pressure towards the external part of the building (consistent with Ritter (2018)); the smaller the gap formed at the soil-foundation interface, or the heavier the structure, the greater the restriction to the horizontal displacements of the soil. For the short structure, the eccentric ($e/B = 0.5$) building increased the horizontal displacements of the soil near the surface because of the freedom to shift, compared with the central short frame. The influence of the building on the ground settlement field was minor for relatively light structures, whereas a heavy building tended to widen the soil vertical displacement field, particularly for the loose sand. The restriction of the foundation to the soil horizontal movements generally resulted in a thin shear band at the soil-foundation interface with a decreased maximum contraction level and some areas of dilation present; the overall level of the shear strains depended on the magnitude of the soil vertical displacements, which were somewhat affected by the presence of the buildings. For a given tunnel volume loss, soil density mainly affected the magnitude of the displacements; due to the fact that the response of the loose soil is dominated by contraction, soil horizontal and vertical displacements, as well as the shear strain, were significantly increased compared with the dense soil test. However, settlements and shear strains of the loose soil were smaller than those of the dense soil for a similar soil volume loss.

The framed structure deformations were studied using deflection ratios and angular distortions. The obtained building deformed shapes indicated that angular/shear distortions within each bay or panel are more appropriate for quantifying framed building distortions than deflection ratios; the maximum shear distortion of the frames was generally observed at the bays or panels where the maximum slope of the ground settlement trough occurred, whereas in the portion of building subjected the largest relative deflections (associated with deflection ratio),

building distortions were relatively small. Based on this, a new modification factor approach was proposed to relate maximum angular distortions to the slope of the greenfield settlement profile; the trends of angular distortion modification factors were found to be characterised by a steady decrease with tunnel volume loss over the investigated range, and a greater rate of decrease was obtained for the loose soil (consistent with the trend of deflection ratio modification factors). Furthermore, the modification factor of angular distortion was linked to a relative shear stiffness parameter, in which linear trends of modification factors with relative stiffness (in semi-log scale) were observed. Upper and lower empirical envelopes for preliminary damage assessment considering building eccentricity were suggested for raft foundations. On the other hand, experimental data of deflection ratio modification factors agreed with existing charts when the equivalent bending stiffness of the building was decreased to account for the shear flexibility from the actual bending stiffness; in particular, experimental results confirmed that the bending and shear stiffness of framed buildings may be directly estimated by modelling load-deflection tests.

7.1.2 Comparison between raft foundations and separate footings

The response of framed buildings on raft foundations to tunnelling was compared against the results of separate footings in Chapter 5. First, framed building stiffness and footing bearing capacity were evaluated experimentally. Tunnelling-induced soil movements and deformation fields, framed building displacements and structure shear distortions (with associated modification factors) are illustrated. In addition, the effects of building width, weight and eccentricity (with respect to the tunnel) on foundation settlements and structural distortions are quantified for separate footings and contrasted against results for raft foundations.

Results showed that, in addition to the building weight and position (e.g. Ritter et al. (2017)), the foundation configuration (i.e. raft or separate footings) significantly affects the ground response and impacts the soil-structure interaction. The foundation type had an impact on both the vertical and horizontal ground displacement fields as well as the shear and volumetric strain distributions. The action of the structure particularly affected the soil close to the foundation, with different trends depending on foundation type; for instance, the footings restricted hori-

zontal soil displacements with a distinct change in magnitude at the location of the footings, compared to a more uniform distribution for the raft foundation. Consequently, localised zones of high shear strain were noted at the footing positions, with dilative response directly beneath the footings and contraction within the soil between footings. Despite this and the differences in strain distributions, only marginal differences in the relationship between tunnel and soil volume loss were observed.

Buildings with raft and separate footings acted to reduce flexural distortions caused by tunnelling in different ways; separate footings tended to embed into the soil in the areas where soil settlements were lowest, whereas raft foundations responded by uplifting the portion where settlements were greatest. Because of the embedment, the frame with separate footings settled significantly more than greenfield settlement at the corresponding location, as reported numerically by Elkayam and Klar (2019). On the other hand, in agreement with previous field (Goh and Mair, 2014) and modelling works (Fu et al., 2018; Franza and DeJong, 2019), it was experimentally confirmed that tunnelling-induced differential horizontal movements are significant for separate footings, whereas they are negligible for raft foundations.

For the considered two-storey framed buildings, when only the foundation scheme was changed, the level of shear deformation of the building panels was similar because of two distinct mechanisms: for the raft, shear deformations were reduced because of the higher overall structure stiffness resulting from the raft; for the separate footings, shear deformations were reduced because of higher levels of shear strains in the soil around the footings, reducing the soil-foundation shear stiffness and causing greater building embedment. The trends highlighted for raft foundations were confirmed for separate footings: wider or heavier framed buildings display increased structural shear deformation, whereas building eccentricity reduces distortions for both foundation types.

Different from the outcomes of the raft foundations, the trends of angular distortion modification factors with tunnel volume loss for separate footings are characterised by significant fluctuations due to the localised soil failure and the slippage at the soil-footing interface. The modification factor of angular distortion of the framed building with separate footings was linked to the relative soil-building shear stiffness; it was confirmed that the structural stiffness

can play an important role in the soil-structure interaction of framed building configurations. Furthermore, with respect to raft foundations, frames on separate footings underwent slightly lower angular distortion modification factors for a given relative stiffness; this is likely due to the fact that footings decreased the foundation footprint compared to rafts, which leads to greater flexibility of the soil-foundation system as well as higher levels of soil shearing (directly beneath the foundation, leading to greater stiffness degradation). Finally, upper and lower empirical envelopes for preliminary damage assessment considering building eccentricity were also suggested for separate footings.

7.1.3 The roles of footing embedement and tunnel cover depth

In tunnel-structure interaction problem, tunnel cover depth affects the characteristics (including maximum settlement and trough width) of the surface settlement trough, thereby impacting the structural response to excavation. Furthermore, the embedment depth of the foundation (separate footings in particular) may also play an important role in the horizontal response of the footings to ground movements, because of the potential for significant horizontal foundation displacements. Chapter 6 discussed these two aspects using the data from a selection of centrifuge tests.

Results illustrated that the foundation embedment slightly increased the ground deformations, the soil volume losses, the foundation differential settlements and the building angular distortions. On the other hand, the increase in tunnelling-induced horizontal displacements and strains at the foundation for embedded footings was notable, particularly at high tunnel volume losses ($V_{l,t} > 2.0\%$). The increase of tunnel cover depth decreased the differential settlements and structural distortion, as well as the overall level of ground deformations (including displacements and strains) caused by tunnelling. Results were also used to evaluate frame modification factors, normalising the building maximum angular distortion and maximum horizontal strains by the greenfield deformation levels. For modification factors of the building maximum angular distortions, results of the frame with embedded footings do not entirely agree with the empirical envelopes proposed in Chapter 5, with the values of modification factors for embedded footings greater than the predicted range using the same relative stiffness value. On the other hand, an

overall decreasing trend of modification factors of maximum horizontal strains with relative stiffness was obtained.

7.1.4 Implications for engineering practice

Several key aspects were highlighted from the work which have implications for engineering practice. First, the need to monitor/evaluate framed building displacements at multiple elevations to better estimate deformations and damage was confirmed; foundation level deformations may be greater than within the superstructure. Framed buildings on raft foundations will likely have a shear dominated deformation mode; therefore, the use of equivalent isotropic plates (dominated by bending behaviour) to represent the framed structures may lead to significant errors for some tunnel-building interaction cases. Framed structures centrally located above a tunnel will have the greatest potential for distortions compared to eccentric cases. The maximum shear distortion of the frames was generally observed at the bays or panels where the maximum slope of the ground settlement trough occurs. When possible, to better estimate the distortions of frames, shear strains should be evaluated using the displacements of the corners of bays/panels rather than using a deflection ratio based evaluation.

The presented results also indicate that, in practice, engineers should consider that the embedment of separate footings could increase tunnelling-induced distress of buildings with respect to predictions obtained by assuming footings rest directly on the ground surface, particularly if the building is susceptible to the actions of horizontal ground deformations (as for separate footings). Finally, upper and lower empirical envelopes (see Equations 4.6-4.9, 5.1-5.4) considering building eccentricity and foundation configuration were suggested for preliminary damage assessment of a real tunnelling project.

7.2 Recommendations for further research

7.2.1 Limitations of the research

In this thesis, upper and lower empirical envelopes considering building eccentricity and foundation configuration were suggested for the preliminary damage assessment of a real tunnelling project. However, because of the limited number of considered scenarios in this study (for instance, the scenarios with stiffer structures, or long frames with a greater eccentricity (larger than 0.2) could be tested), and given that the envelopes are based solely on the experimental results, care should be taken when the suggested empirical envelopes are referenced in real tunnelling projects. The proposed empirical envelopes also need to be verified by data from field testing studies or numerical models. On the other hand, the issue associated with the manufacturing process (i.e. the welding), which in particular affects the horizontal response of separate footings, is also one aspect that could be addressed in future research. Therefore, the numerical modelling based on the centrifuge results is currently being conducted to 1) investigate the uncertainties associated with the horizontal displacements of the footings caused by the manufacturing process, and 2) to further explore the problem by considering more tunnel-frame interaction scenarios.

7.2.2 Recommendations for further research

In this thesis, the response of framed building on either raft foundations or separate footings to tunnelling was investigated using data obtained from comprehensive centrifuge tests. The research considered the effects of the tunnelling- and structure-related parameters on tunnel-building interaction, including building configuration (number of storeys, building transverse width, the thickness of structural element and bay width), weight, eccentricity, soil density, foundation type, tunnel cover depth, and foundation embedment. Nevertheless, there are certain areas of interest that are worthy of further investigation. They are listed in the following.

- **Structural property:** Building stiffness and configuration play an important role in soil-structure interaction. This research studied the response of an elastic bare framed building

model to tunnel construction. It would be interesting to consider the non-linear behaviour or even damage of a framed structure. Furthermore, the presence of infill walls can significantly affect the mechanical behaviour (shear- or bending-dominated) of the structure. Therefore, the effect of the presence of infill (shear) walls on the response of a framed building to tunnelling is also worthy of investigation.

- **Building position:** As discussed in Chapter 4, building eccentricity reduced structural distortion because of the freedom to tilt for the eccentric structure. However, in this thesis, the considered scenario was limited to a relatively short structure with an eccentricity of $e/B = 0.5$, or a long building with a limited value of eccentricity $e/B = 0.2$. As discussed in Haji et al. (2018), for the long buildings with an eccentricity of $e/B = 0.5$, the building tilt at the external edge is restricted by the portion of the building located outside the settlement trough influence zone. In this case, building eccentricity may not be able to reduce structural distortion; this aspect could be experimentally studied in the future.

- **Building skew:** In this thesis, the considered building was placed along the transverse direction of the tunnel (i.e. the orthogonal tunnel case). In reality, this orthogonality is not always the case. Instead, a skew angle between the structure and the tunnel often exists (i.e. the skew tunnel case), which results in the twist deformation of a structure (as observed in Franzius et al. (2005)). Therefore, centrifuge tests involving a skew tunnel should also be performed.

- **Foundation:** This thesis considered framed buildings resting on either raft foundations or separate footings. For the tests with embedded footings, the embedment depth was limited to a certain value (0.7 m). Foundations with a greater embedded depth could also be tested. Furthermore, tunnelling beneath framed buildings with deep foundations (for instance, piled foundations) could certainly be studied.

- **3D tunnelling:** In reality, the soil-structure interaction problem caused by tunnel excavation is a three-dimensional problem. This thesis only considered the effect of transverse ground deformation on framed buildings. However, the progressive longitudinal ground settlement during tunnel construction could also damage structures. The response of framed buildings to longitudinal ground settlement is also an area of interest for future research.

- **Ground condition:** In this research, dry silica sand was used for the ground. However, the ground condition of a real tunnelling project is more complicated involving saturated sand, clay, gravels, or even a mixture of these types of soil. Future research could start with the saturated sand, clay, and then moving to the layered ground of different soil types.

References

Adrian, R. J. (1991). Particle-Imaging Techniques for Experimental Fluid Mechanics. *Annual Review of Fluid Mechanics*, 23(1):261–304.

Attewell, P. B. and Woodman, J. P. (1982). Predicting the dynamics of ground settlement and its derivatives caused by tunnelling in soil. *Ground Engineering*, 15(8):13–22 and 36.

Attewell, P. B., Yeates, J., and Selby, A. R. (1986). *Soil movements induced by tunnelling and their effects on pipelines and structures*. Blackie and Son Ltd, UK.

Attewell, P. B. and Yeates, J. O. H. N. (1984). Tunnelling in soil. *Ground movements and their effects on structures*, pages 132– 215.

Bilotta, E. (2008). Use of diaphragm walls to mitigate ground movements induced by tunnelling. *Géotechnique*, 58(2):143–155.

Bilotta, E., Paolillo, A., Russo, G., and Aversa, S. (2017). Displacements induced by tunnelling under a historical building. *Tunnelling and Underground Space Technology*, 61:221–232.

Bilotta, E. and Russo, G. (2011). Use of a line of piles to prevent damages induced by tunnel excavation. *Journal of Geotechnical and Geoenvironmental Engineering*, 137(3):254–262.

Boldini, D., Losacco, N., Bertolin, S., and Amorosi, A. (2018). Finite Element modelling of tunnelling-induced displacements on framed structures. *Tunnelling and Underground Space Technology*, 80(April):222–231.

Boldini, D., Losacco, N., Franza, A., J, D. M., Xu, J., and Marshall, A. M. (2020). Tunnelling induced deformation of framed structures: a numerical study. *Submitted to Journal of Geotechnical and Geoenviromental Engineering*.

Bolton, M. D. (1986). The strength and dilatancy of sands. *Géotechnique*, 36(1):65–78.

Boone, S. J. (1996). Ground-Movement-Related Building Damage. *Journal of Geotechnical Engineering*, 122:886–896.

Boscardin, M. D. and Cording, E. J. (1989). Building response to excavation-induced settlement. *Journal of Geotechnical Engineering*, 115(1):1–21.

Burland, J. B., Broms, B. B., and De Mello, V. F. B. (1977). Behaviour of foundations and structures. In *Proceedings of the 9th International Conference on Soil Mechanics and Foundations Engineering*, volume 2, pages 495–546, Tokyo.

Burland, J. B. and Wroth, C. P. (1974). Settlement of buildings and associated damage. In *Conference on the Settlement of Structures*.

Celestino, T. B., Gomes, R. A. M. P., and Bortolucci, A. A. (2000). Errors in ground distortions due to settlement trough adjustment. *Tunnelling and Underground Space Technology*, 15(1):97–100.

Clarke, J. A. and Laefer, D. F. (2014). Evaluation of risk assessment procedures for buildings adjacent to tunnelling works. *Tunnelling and Underground Space Technology*, 40:333–342.

Clough, W. and Schmidt, B. (1981). Design and performance of excavations and tunnels in soft clay. *Soft Clay Engineering*, pages 567–634.

Cook, D. (1994). Studies of settlement and crack damage in old and new facades. In *Proc., 3rd Int. Masonry Conference., London, England*, volume 6, pages 203–211.

Cording, E. J. (1991). Control of ground movements around tunnels in soil. In *Proceeding of the 9th Pan-American Conference on Soil Mechanics and Foundation Engineering*, volume 4, pages 2195–2244.

Cording, E. J. and Hansmire, W. H. (1975). Displacements around soft ground tunnels. In *Proceeding of the 5th Panamerican conference on soil mechanics and foundation engineering*, pages 571–632.

Deck, O. and Singh, A. (2012). Analytical model for the prediction of building deflections induced by ground movements. *International Journal for Numerical and Analytical Methods in Geomechanics*, 36(1):62–84.

Dimmock, P. S. and Mair, R. J. (2008). Effect of building stiffness on tunnelling-induced ground movement. *Tunnelling and Underground Space Technology*, 23(4):438–450.

Dyer, M., Hutchinson, M., and Evans, N. (1996). Sudden valley sewer: a case history. In *International symposium on geotechnical aspects of underground construction in soft ground*, pages 671–676, London.

Elkayam, I. and Klar, A. (2019). Nonlinear elasto-plastic formulation for tunneling effects on superstructures. *Canadian Geotechnical Journal*, 56(7):956–969.

Ellis, E., Cox, C., Yu, H. S., Ainsworth, A., and Baker, N. (2006). A new geotechnical centrifuge at the University of Nottingham, UK. In Ng, Zhang, and Wang, editors, *6th International Conference of Physical Modelling in Geotechnics: ICPMG'06*, pages 129–133, Hong Kong. Taylor & Francis Group, London.

Fargnoli, V., Gragnano, C. G., Boldini, D., and Amorosi, A. (2015). 3D numerical modelling of soil–structure interaction during EPB tunnelling. *Géotechnique*, 65(1):23–37.

Farrell, R. (2010). Tunnelling in sands and the response of buildings. *Ph.D. Thesis, Cambridge University*.

Farrell, R., Mair, R., Sciotti, A., and Pigorini, A. (2014). Building response to tunnelling. *Soils and Foundations*, 54(3):269–279.

Farrell, R. P. (2015). Tunnelling and compensation grouting at bond street, london. *Proceedings of the Institution of Civil Engineers-Geotechnical Engineering*, 168(6):471–482.

Finno, R. J., Voss, F. T., Rossow, E., and Blackburn, J. T. (2005). Evaluating Damage Potential in Buildings Affected by Excavations. *Journal of Geotechnical and Geoenvironmental Engineering*, 131(10):1199–1210.

Franza, A. (2016). *Tunnelling and its effects on piles and piled structures*. PhD thesis, University of Nottingham.

Franza, A., Acikgoz, S., and DeJong, M. J. (2020a). Timoshenko beam models for the coupled analysis of building response to tunnelling. *Tunnelling and Underground Space Technology*, 96:103160.

Franza, A. and Dejong, M. J. (2018). Discussion of " A cantilever approach to estimate bending sti ff ness of buildings a ff ected by tunnelling " by Twana Kamal Haji , Alec M . Marshall , and Walid Tizani. *Tunnelling and Underground Space Technology*, 77(February):314–315.

Franza, A. and DeJong, M. J. (2019). Elastoplastic solutions to predict tunneling-induced load redistribution and deformation of surface structures. *Journal of Geotechnical and Geoenvironmental Engineering*, 145(4):04019007.

Franza, A. and Marshall, A. M. (2018). Centrifuge Modeling Study of the Response of Piled Structures to Tunneling. *Journal of Geotechnical and Geoenvironmental Engineering*, 144(2):04017109.

Franza, A. and Marshall, A. M. (2019a). Centrifuge and real-time hybrid testing of tunneling beneath piles and piled buildings. *Journal of Geotechnical and Geoenvironmental Engineering*, 145(3):04018110.

Franza, A. and Marshall, A. M. (2019b). Empirical and semi-analytical methods for evaluating tunnelling-induced ground movements in sands. *Tunnelling and Underground Space Technology*, 88:47–62.

Franza, A., Marshall, A. M., Haji, T., Abdelatif, A. O., Carbonari, S., and Morici, M. (2017). A simplified elastic analysis of tunnel-piled structure interaction. *Tunnelling and Underground Space Technology*, 61:104–121.

Franza, A., Marshall, A. M., and Zhou, B. (2019). Greenfield tunnelling in sands: the effects of soil density and relative depth. *Géotechnique*, 69:297–307.

Franza, A., Marshall, A. M., Zhou, B., Shirlaw, N., Boone, S., Shirlaw, C. N., and Boone, S. (2020b). Discussion: Greenfield tunnelling in sands : the effects of soil density and relative depth. *Géotechnique*.

Franza, A., Ritter, S., and Dejong, M. J. (2020c). Continuum solutions for tunnel–building interaction and a modified framework for deformation prediction. *Géotechnique*, 70(2):108–122.

Franzius, J., Potts, D., and Burland, J. (2005). Twist behaviour of buildings due to tunnel induced ground movement. In *Geotechnical Aspects of Underground Construction in Soft Ground: Proceedings of the 5th International Symposium TC28. Amsterdam, the Netherlands, 15-17 June 2005*, page 107. CRC Press.

Franzius, J. N. (2003). Behaviour of buildings due to tunnelling induced subsidence. *Ph.D thesis, Imperial College of London*.

Franzius, J. N., Potts, D. M., Addenbrooke, T. I., and Burland, J. B. (2004). The influence of building weight on tunnelling-induced ground and building deformation. *Soils and Foundations*, 44(1):25–38.

Franzius, J. N., Potts, D. M., and Burland, J. B. (2006). The response of surface structures to tunnel construction. *Proceedings of the ICE - Geotechnical Engineering*, 159(1):3–17.

Fu, J., Yu, Z., Wang, S., and Yang, J. (2018). Numerical analysis of framed building response to tunnelling induced ground movements. *Engineering Structures*, 158:43–66.

Fuglsang, L. (1988). The application of the theory of modelling to centrifuge studies. *Centrifuges in soil mechanics*, pages 119–138.

Geddes, J. D. (1991). Discussion of "building response to excavation-induced settlement" by marco d. boscardin and edward j. cording (january, 1989, vol. 115, no. 1). *Journal of Geotechnical Engineering*, 117(8):1276–1278.

Goh, K. H. and Mair, R. J. (2011). Building damage assessment for deep excavations in Singapore and the influence of building stiffness. *Geotechnical Engineering Journal of the SEAGS & AGSSEA*, 42(3):1–12.

Goh, K. H. and Mair, R. J. (2014). Response of framed buildings to excavation-induced movements. *Soils and Foundations*, 54(3):250–268.

Grant, R. J. and Taylor, R. N. (2000). Tunnelling-induced ground movements in clay. *Proceedings of the ICE - Geotechnical Engineering*, 143(1):43–55.

Haji, T. K., Marshall, A. M., and Tizani, W. (2018). A cantilever approach to estimate bending stiffness of buildings affected by tunnelling. *Tunnelling and Underground Space Technology*, 71:47–61.

Hardin, B. O. and Richart, F. (1963). Elastic wave velocities in granular soils. *Journal of Soil Mechanics & Foundations Div*, 89(Proc. Paper 3407).

Hwang, R., Fan, C., and Yang, G. (1995). Consolidation settlements due to tunnelling. In *Proceedings of South East Asian Symposium on Tunneling and Underground Space Development, Bangkok, Thailand*, pages 79–86.

Iglesia, G. R., Einstein, H. H., and Whitman, R. V. (2014). Investigation of soil arching with centrifuge tests. *Journal of Geotechnical and Geoenvironmental Engineering*, 140(2):04013005.

Jacobsz, S. W. (2002). The effects of tunnelling on piled foundations. *Ph.D. Thesis, Cambridge University*.

Jacobsz, S. W., Standing, J. R., Mair, R. J., Hagiwara, T., and Sugiyama, T. (2004). Centrifuge modelling of tunnelling near driven piles. *Soils and Foundations*, 44(1):49–56.

Jones, B. D. (2010). Low-volume-loss tunnelling for London ring main extension. *Proceedings of the Institution of Civil Engineers - Geotechnical Engineering*, 163(3):167–185.

Kutter, B., Chang, J., and Davis, B. (1994). Collapse of cavities in sand and particle size effects. In C. F. Leung, F. Lee, and T. Tan, editor, *Proceedings of International Conference Centrifuge '94*, pages 809–815, Singapore. Balkema.

Laefer, D. F., Ceribasi, S., Long, J. H., and Cording, E. J. (2009). Predicting RC frame response to excavation-induced settlement. *Journal of geotechnical and geoenvironmental engineering*, 135(11):1605–1619.

Lambe, T. W. (1973). Predictions in soil engineering. *Géotechnique*, 23(2):151–202.

Lanzano, G., Visone, C., Bilotta, E., and Santucci de Magistris, F. (2016). Experimental Assessment of the Stress Strain Behaviour of Leighton Buzzard Sand for the Calibration of a Constitutive Model. *Geotechnical and Geological Engineering*, 34(4):991–1012.

Lau, C. K. and Bolton, M. D. (2011). The bearing capacity of footings on granular soils. II: Experimental evidence. *Geotechnique*, 61(8):639–650.

Ledesma, A. and Alonso, E. (2017). Protecting sensitive constructions from tunnelling: the case of world heritage buildings in barcelona. *Géotechnique*, 67(10):914–925.

Lee, C.-J., Wu, B.-R., and Chiou, S.-Y. (1999). Soil movements around a tunnel in soft soils. *Proceedings of the National Science Council, Republic of China, Part A: Physical Science and Engineering*, 23(2):235–247.

Lee, S.-W. (2002). The use of compensation grouting in tunnelling: a case study. *Proceedings of the Institution of Civil Engineers-Geotechnical Engineering*, 155(2):101–109.

Lehane, B. and Cosgrove, E. (2000). Applying triaxial compression stiffness data to settlement prediction of shallow foundations on cohesionless soil. *Proceedings of the ICE - Geotechnical Engineering*, 143(4):191–200.

Loganathan, N. and Poulos, H. G. (1998). Analytical prediction for tunneling-induced ground movements in clays. *Journal of Geotechnical and Geoenvironmental Engineering*, 124(9):846–856.

Losacco, N., Burghignoli, A., and Callisto, L. (2014). Uncoupled evaluation of the structural damage induced by tunnelling. *Géotechnique*, 64(8):646–656.

Losacco, N., Callisto, L., and Burghignoli, A. (2016). Soil-structure interaction due to tunnelling in soft ground, an equivalent solid approach. In Van Balen, K. and Verstrynge, E., editors, *Structural Analysis of Historical Constructions*, pages 495–501. CRC Press.

Mair, R. (2013). Tunnelling and deep excavations: ground movements and their effects. In Anagnostopoulos, A., Pachakis, M., and Tsatsanifos, C., editors, *Proceedings of the 15th European Conference on Soil Mechanics and Geotechnical Engineering - Geotechnics of Hard Soils - Weak Rocks (Part 4)*, pages 39 – 70, Amsterdam, the Netherlands. IOS Press.

Mair, R., Gunn, M., and O'Reilly, M. (1981). Ground movements around shallow tunnels in soft clay. In *Proceedings of the 10th international conference on soil mechanics and foundation engineering*, pages 323–328. ISSMFE: International Society for Soil Mechanics and Foundation Engineering.

Mair, R. J. and Taylor, R. N. (1997). Theme lecture: Bored tunnelling in the urban environment. In *14th International conference on soil mechanics and foundation engineering*, pages 2353–2385, Hamburg. Balkema.

Mair, R. J., Taylor, R. N., and Bracegirdle, A. (1993). Subsurface settlement profiles above tunnels in clay. *Géotechnique*, 43(2):315–320.

Mair, R. J., Taylor, R. N., and Burland, J. B. (1996). Prediction of ground movements and assessment of risk of building damage due to bored tunnelling. In Mair, R. J. and Taylor, R. N., editors, *Proceedings of the International Symposium on Geotechnical Aspects of Underground Construction in Soft Ground*, pages 713–718, London, United Kingdom. Balkema, Rotterdam.

Maleki, M., Sereshteh, H., Mousivand, M., and Bayat, M. (2011). An equivalent beam model for the analysis of tunnel-building interaction. *Tunnelling and Underground Space Technology*, 26(4):524–533.

Marshall, A. M. (2009). Tunnelling in sand and its effect on pipelines and piles. *Ph.D. Thesis, Cambridge University*.

Marshall, A. M., Elkayam, I., and Klar, A. (2009). Ground behaviour above tunnels in sand-dem simulations versus centrifuge test results. In *Euro: Tun 2009, Proceedings of the 2nd International Conference on Computational Methods in Tunnelling, Bochum, Germany*, pages 9–11. Aedificatio Verlag, Bochum, Germany.

Marshall, A. M., Farrell, R., Klar, A., and Mair, R. (2012). Tunnels in sands: the effect of size, depth and volume loss on greenfield displacements. *Géotechnique*, 62(5):385–399.

Melis, M. J. and Rodriguez Ortiz, J. M. (2001). Consideration of the stiffness of buildings in the estimation of subsidence damage by EPB tunnelling in the Madrid subway. In *Proceedings of international conference: response of buildings to excavation induced ground movements, London*, pages 87–394, London, UK. Ciria Special Publication 201.

Meyerhof, G. (1953). *Some recent foundation research and its application to design*. The Structural Engineer.

Moh, Z. C., Ju, D. H., and Hwang, R. N. (1996). Ground movements around tunnels in soft ground. In *Proceedings International Symposium on Geotechnical Aspects of Underground Construction in Soft Ground*, volume 730, pages 725–730.

Namazi, E. and Mohamad, H. (2013). Assessment of Building Damage Induced by Three-Dimensional Ground Movements. *Journal of Geotechnical and Geoenvironmental Engineering*, 139(4):608–618.

New, B. and O'Reilly, M. (1991). Tunnelling induced ground movements; predicting their magnitude and effects. In *Proceeding of the 4th International Conference on Ground Movements and Structures, Jul 8-11*, pages 671–697, Cardiff, Wales. Pentench Press Ltd.

O'Reilly, M. and New, B. (1982). Settlements above tunnels in the United Kingdom - their magnitude and prediction. *Tunnelling '82: Proceedings of the 3rd International Symposium*, pages 173–181.

Peck, R. B. (1969). Deep excavations and tunnelling in soft ground. In *Proceedings of the 7th International Conference on Soil Mechanics and Foundation Engineering*, pages 225–290, Mexico City, Mexico.

Pickhaver, J., Burd, H., and Houlsby, G. (2010). An equivalent beam method to model masonry buildings in 3D finite element analysis. *Computers & Structures*, 88(19):1049–1063.

Polshin, D. E. and Tokar, R. A. (1957). Maximum allowable non-uniform settlement of structures. *Proceedings of the 4th International Conference on Soil Mechanics and Foundation Engineering*, 1:402–405.

Potts, D. M. and Addenbrooke, T. I. (1997). A structure's influence on tunnelling-induced ground movements. *Proceedings of the ICE - Geotechnical Engineering*, 125(2):109–125.

Rankin, W. (1988). Ground movements resulting from urban tunnelling: predictions and effects. *Geological Society, London, Engineering Geology Special Publications*, 5(1):79–92.

Ritter, S. (2018). Experiments in tunnel-soil-structure interaction. *Ph.D. thesis, Cambridge University*.

Ritter, S., Giardina, G., DeJong, M. J., and Mair, R. J. (2017). Influence of building characteristics on tunnelling-induced ground movements. *Géotechnique*, 67(10):926–937.

Ritter, S., Giardina, G., DeJong, M. J., and Mair, R. J. (2018). Centrifuge modelling of building response to tunnel excavation. *International Journal of Physical Modelling in Geotechnics*, 18(3):146–161.

Ritter, S., Giardina, G., Franza, A., Dejong, M. J., and Asce, A. M. (2020). Building Deformation Caused by Tunneling : Centrifuge Modeling. *Journal of Geotechnical and Geoenvironmental Engineering*, 146(5):1–17.

Skempton, A. W. and MacDonald, D. H. (1956). The allowable settlements of buildings. *Proceedings of the ICE*, 5(6):727–768.

Son, M. (2015). Response analysis of nearby structures to tunneling-induced ground movements in sandy soils. *Tunnelling and Underground Space Technology*, 48:156–169.

Son, M. and Cording, E. J. (2005). Estimation of Building Damage Due to Excavation-Induced Ground Movements. *Journal of Geotechnical and Geoenvironmental Engineering*, 131(2):162–177.

Son, M. and Cording, E. J. (2007). Evaluation of Building Stiffness for Building Response Analysis to Excavation-Induced Ground Movements. *Journal of Geotechnical and Geoenvironmental Engineering*, 133(8):995–1002.

Song, G. (2019). The use of protective structures to reduce tunnelling induced damage to buildings. *Ph.D. Thesis, University of Nottingham*.

Song, G. and Marshall, A. M. (2020). Centrifuge modelling of tunnelling induced ground displacements: pressure and displacement control tunnels. *Tunnelling and Underground Space Technology*, 103:103461.

Stanier, S. A., Blaber, J., Take, W. A., and White, D. J. (2016). Improved image-based deformation measurement for geotechnical applications. *Canadian Geotechnical Journal*, 53:727–739.

Sugiyama, T., Hagiwara, T., Nomoto, T., Nomoto, M., Ano, Y., Mair, R., Bolton, M., and Soga, K. (1999). Observations of ground movements during tunnel construction by slurry shield method at the Docklands Light Railway Lewisham Extension-East London. *Soils and Foundations*, 39(3):99–112.

Taylor, R. N. (1995a). *Geotechnial centrifuge technology*. Blackie Academic & Professional, London.

Taylor, R. N. (1995b). Tunnelling in soft ground in the UK. In *Underground construction in soft ground*, pages 123–126, Balkema.

Timoshenko, S. P. (1957). *Strength of Materials: Part 1*. Van Nostrand Reinhold Company.

Torp-Petersen, G. E. and Black, M. G. (2001). Geotechnical investigation and assessment of potential building damage arising from ground movements: CrossRail. *Proceedings of the ICE - Transport*, 147(2):107–119.

Vesic, A. S. (1963). Bearing Capacity of Deep Foundations in Sand. *Highway Research Record*, 39:112–153.

Vorster, T. E. B., Klar, A., Soga, K., and Mair, R. J. (2005). Estimating the Effects of Tunneling on Existing Pipelines. *Journal of Geotechnical and Geoenviromental Engineering*, 131(11):1399–1410.

White, D., Take, W., and Bolton, M. (2003). Soil deformation measurement using particle image velocimetry (PIV) and photogrammetry. *Géotechnique*, 53(7):619–631.

Xu, J., Franza, A., and Marshall, A. M. (2020a). The response of framed building on raft foundations to tunnelling. *Journal of Geotechnical and Geoenviromental Engineering (in press, doi: 10.1061/(ASCE)GT.1943-5606.0002376)*.

Xu, J., Franza, A., Marshall, A. M., Losacco, N., and Boldini, D. (2020b). Tunnel-framed building interaction: comparison between raft and separate footing foundations. *Géotechnique (in press, doi: 10.1680/jgeot.19.P.393)*.

Xu, J., Marshall, M. A., Franza, A., Boldini, D., Amorosi, A., and DeJong, J. M. (2019). The response of framed buildings on raft foundations to tunnelling: a centrifuge and numerical modelling study. In *17th European Conference on Soil Mechanics and Geotechnical Engineering, Reykjavik, Iceland*, volume 1, pages 1–8.

Yiu, W., Burd, H., and Martin, C. (2017). Finite-element modelling for the assessment of tunnel-induced damage to a masonry building. *Géotechnique*, 67(9):780–794.

Zhao, Y. (2008). In situ soil testing for foundation performance prediction. *Ph.D. Thesis, Cambridge University*.

Zhou, B. (2014). Tunnelling-induced ground displacements in sand. *Ph.D. Thesis, University of Nottingham*.

Appendix A

A1 Optimisation of the welding parameter

To optimise the welding parameters while achieving the rigid connection between angles, a series of stress analysis tests were conducted in Autodesk Inventor 2018. The bottom plate (raft foundation), side wall and angles were created and assembled to obtain the designed framed building model (having an identical configuration and dimension with frame F5t5b6L). Note that to consider the realistic welding process and depth (2 mm for the contact surface of angles A and B in Figure A1(a)), the outer corner of the angles (for instance, angle A) were cut off to fill in the welding parts (see Figure A1(b)). On the other hand, the right angle (for instance, the corner formed by angles B and C) was filled by an isosceles right triangle (3 mm side length) shaped welding part.

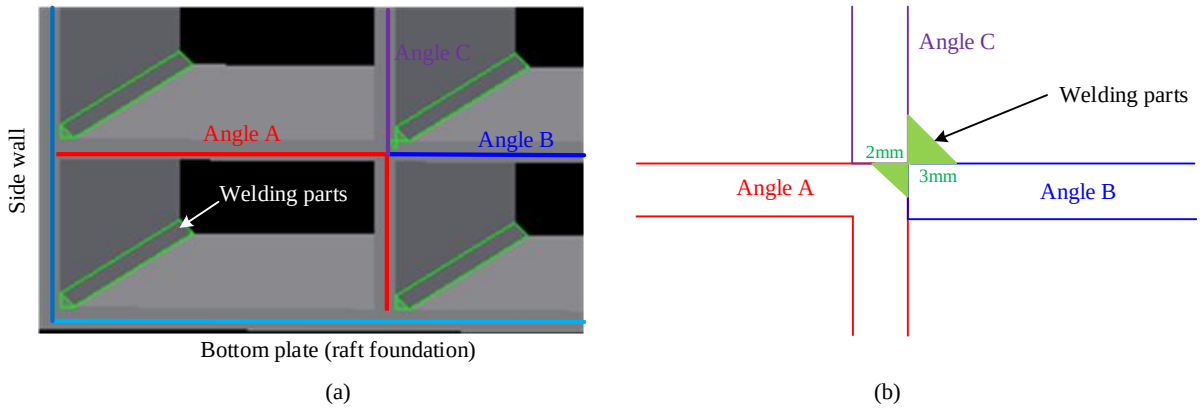
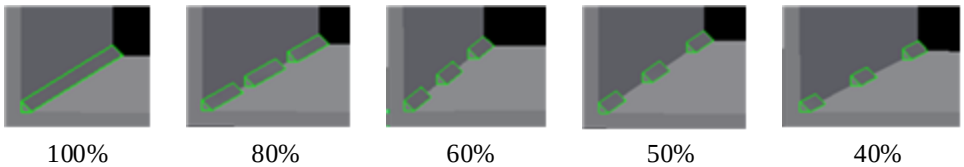


Fig. A1. Illustration of the welding parts

Importantly, when welding the entire length of the frame, significant distortion of the foundation may be induced, resulting in non-uniform pressure distribution at the soil-foundation

interface when the building model was placed at the soil surface. This is not ideal for the subsequent tunnel-frame interaction tests. Therefore, an optimisation of the welding parameters (the percentage of welding length and the distribution of welding parts) is needed. The considered welding schemes for the parametric study are presented in Figure A2 (take frame F5t5b6L as the example). In particular, Figure A2(a) presents the considered percentage of the welding length, while Figure A2(b) shows the possible distribution of welding parts in the manufacturing process of the frame. To simplify the problem, the length of each welding part for a given model is identical.



(a) Percentage of welding length



(b) Distribution of welding parts

Fig. A2. Illustration of the considered welding plan (example of frame F5t5b6L)

The total stiffness (P/Δ) of the frame was evaluated using cantilever loading tests (one side was fixed while the load was imposed to another side, see Figure 3.18(c)). Results are normalised by the value of the stiffness of the frame in the full welding scenario (100% in Figure A2(a)), as shown in Figures A3 and A4.

Figure A3 shows that, as expected, the greater the welding percentage, the larger the total stiffness of the frame. Note that, a significant drop of the stiffness is observed when the welding percentage decreased from 60 to 50%. On the other hand, for both 60 and 80% of the welding percentage, the second type of the distribution of the welding parts tended to give a slightly larger total stiffness. Therefore, in this research, 60% welding with the distribution type of D2 (see Figure A2(b)) was adopted.

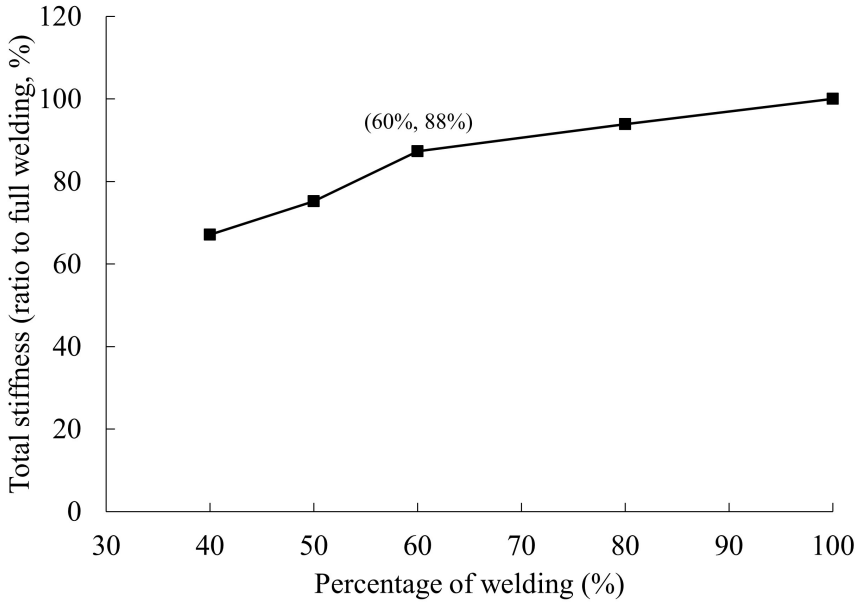


Fig. A3. The effect of the welding percentage on the frame total stiffness

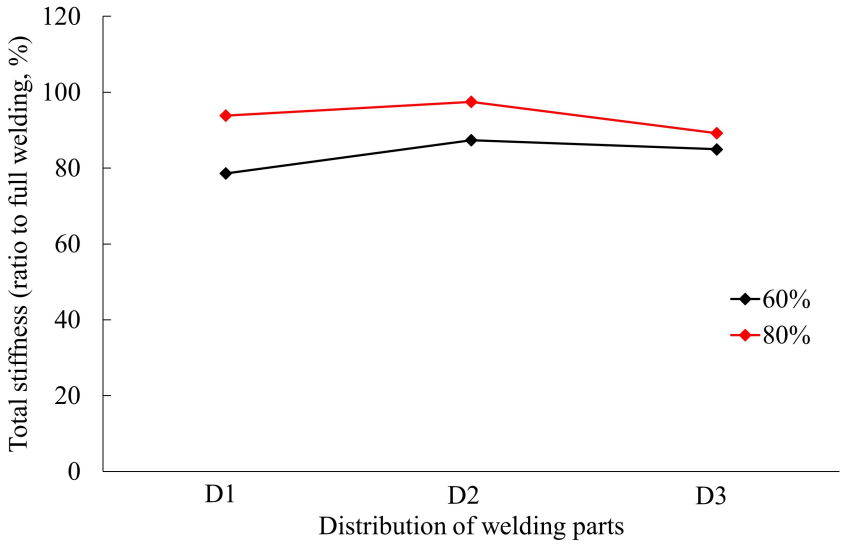


Fig. A4. The effect of the distribution of welding parts on the frame total stiffness

A2 Instrumentation details

The National Instruments interface and modules were used for the data acquisition (16-bit reading at 50Hz sampling rate) and control systems. The connected modules of the instruments are summarised in Table A1.

Table A1. The module for each sensor/device

Instrument	NI modulus
L03 MecVel ball Servo motor control	NI9505
Solonide valve and servo motor break control	NI9474
Data acquisition (LVDT, PPT, Load cell)	NI9205
Stepper motor control	NI9403

The instrument/sensor specifications are summarised in the following tables.

Table A2. Servo motor (Linear Actuator L03 DC) specification

Parameter	Value
Basic information	Permanent magnet motor Planetary gearbox Acme lead screw (VRS) Chrome plated steel push rod Permanent grease lubrication IP 65 (rule CEI EN 60529) Intermittent duty S3 30% (5 min) a 30°C
Temperature range	-10 to +60°C
Max force	5000 N
Max speed	30 mm/s
Voltage	12-24 Vdc

Table A3. Hydraulic piston (SMC CP96SDB50-320C) specification

Parameter	Value
Brand	SMC
Type	Standard
Series	CP96
Connection diameter	G1/4 in
Action	Double acting single rod
Switch	Auto switch (Built-in magnet)
Mounting type	Basic
Bore size	50 mm
Cylinder stroke	320 mm
Working pressure	0.05-1MPa

Table A4. LVDT specification

Parameter	AS/15	AS/50
Measurement range	± 15	± 50
Pre-travel ± 0.5mm	5	5
Linearity (% FSO)	<0.2	<0.2
Resolution	<0.2μm	<0.5μm
Temperature Coefficients (%FSO/°C)	<0.01	<0.01
Body Diameter	19 mm	19 mm
Case Material	300 Series Stainless Steel	
Core Material	Nickel	Iron
Tip Force (±20%)	1.2 N	2.1 N
Cable Type	FEP	FEP
Standard Cable Length	3 m	3 m
Standard Cable Style	B	B
Nominal Mass	92 g	153 g
Nominal Mass of Core	6.8 g	9.1 g
Temperature	-40 to +120°C	-40 to +120°C
Storage Temperature	0 to +65°C	0 to +65°C
Sealing	IP65	IP65
Vibration Random	DO160F Curve D	
Shock	1m onto hard surface	
Energising Voltage	1-10 (Vrms)	1-10 (Vrms)
Energising Current at 5 kHz	1.5mA/V	0.6mA/V
Sensitivity at 5 kHz ±10% mV/V/mm	60	15

Table A5. Load cell specification

Parameter	Value
Standard Ranges	0 to 5 kN
Excitation Voltage	10V (normal), 15V (max) DC
Sensitivity	2.0 mV/V (nominal)
Non-Linearity	0.29% of F.R.O or Better
Hysteresis	0.29% of F.R.O or Better
Zero Balance	0.5% of F.R.O or Better
Bridge Resistance	350 Ohm Bridge
Over Load Characteristics	125% with no loss in Calibration 150% with no structural failure
Insulation Resistance	> 2000M Ohm
Storage Temp	40 to +70°C
Operating Temp	-20 to +70°C
Compensated Temp	+20 to +70°C
Electrical Connections	2m Integral Screened Cable
Thermal Sensitivity	0.005% of F.R.O/C or better

Table A6. Druck UNIK 5000 Pressure Sensor specification

Parameter	Value
Place of Origin	United Kingdom
Brand Name	Druck
Model Number	PDCR 5011-TA-A1-CB-H0-PA
S/N	3664288
Supply	7 to 12 Vdc
Output signal	0 to 100mV
Temperature Compensation	10 to +50°C
Accuracy	Industrial accuracy
Pressure Connection	Female
Material	Stainless Steel
Pressure type	Gage
Range	0 to 10 bar (1000 kPa)

Table A7. Stepper motro specification

Parameter	Value
Step angle	1.8° ±5%
No. of phases	2
Rated voltage	1.72V
Rated current	4.2A
Resistance	0.41 ohm±10% at 25°C
Inductance	1.3 mH±20% at 1kHz, 1Vrms
Holding torque	1.22Nm
Dielectric strength	500V A.C
Insulation Resistance	Min. 100 MΩ
Insulation class	Class B
Temperature rise	Max. 80K
Rotor Inertia	245g. cm^2
Weight	Approx. 1.1kg
Allowable thrust load	36N
Allowable radial load	120N (on the shaft end)
Operation ambient temp	0 to +50°C
Operation ambient hum	20 to 90%
Life	5000 hours

A3 Effect of centrifuge radius on the gravity field

The gravity field in the centrifuge is not parallel because the gravity direction of any point in the centrifuge is always orthogonal to its rotation direction (i.e. point towards the reverse direction of the centre of the rotation). Therefore, apart from the points at the centreline of the model, all the parts of the model would suffer a horizontal acceleration component, and the larger the distance of the point of interest to the centre of the model, the greater the horizontal acceleration, as shown in Figure A5. Consequently, this non-uniform gravity field inevitably affects the behaviour of the model (both the soil sample and the model tunnel filled with liquid) during centrifuge spinning up and tests.

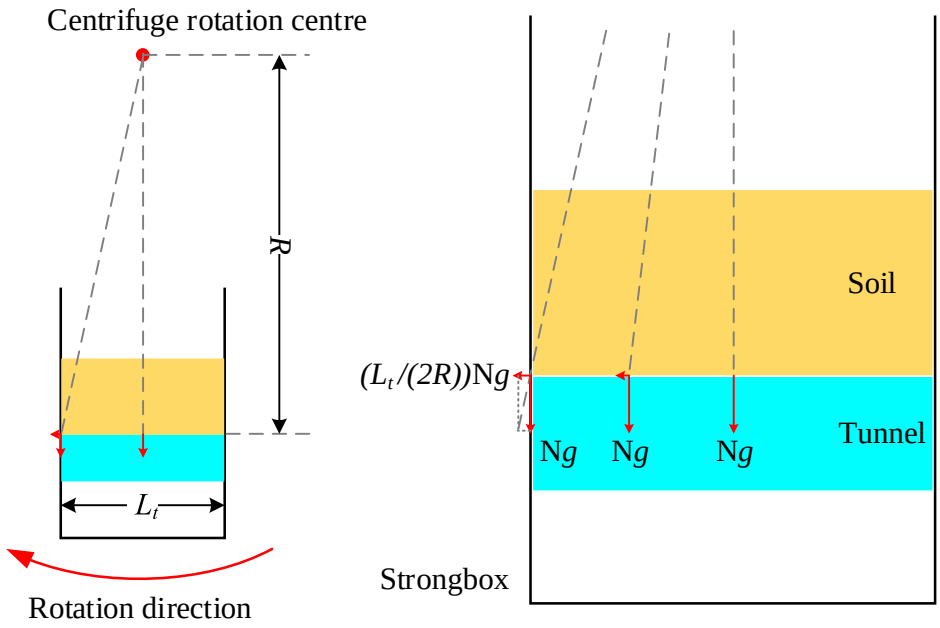


Fig. A5. Illustration of the gravity field in the centrifuge

For a plain strain condition model, the displacements of the model are often measured using particle image velocimetry technique through a transparent wall. The boundary of the model would suffer the effect of the non-uniformity of the gravity field. In the model of this study, if the longitudinal length of the model tunnel is L_t, and the distance of the point of interest to the centrifuge rotation centre is R, the horizontal acceleration component at the model boundary can be expressed as $(L_t/(2R))Ng$, which is determined by both the centrifuge radius and the

longitudinal length of the model tunnel, i.e. the ratio of L_t/R. It should be noted that the radii of the centrifuges at the Nottingham and Cambridge are 2 and 5 m, respectively, while the longitudinal lengths of the model tunnels are 260 and 150 mm. Consequently, the values of L_t/R for Nottingham and Cambridge centrifuges are 0.13 and 0.03, respectively. This indicates that the great difference of the values of L_t/R between experiment setups may have different effects on the model behaviour. This aspect should be particularly noted when comparing the results obtained from two different experiment setups. Nevertheless, at the investigated range of tunnel volume loss (1-3%), the difference between two greenfield displacements is small. Hence, the results of the framed buildings in this study and those from Farrell (2010) are still comparable.

A4 Soil movements after centrifuge spin-up

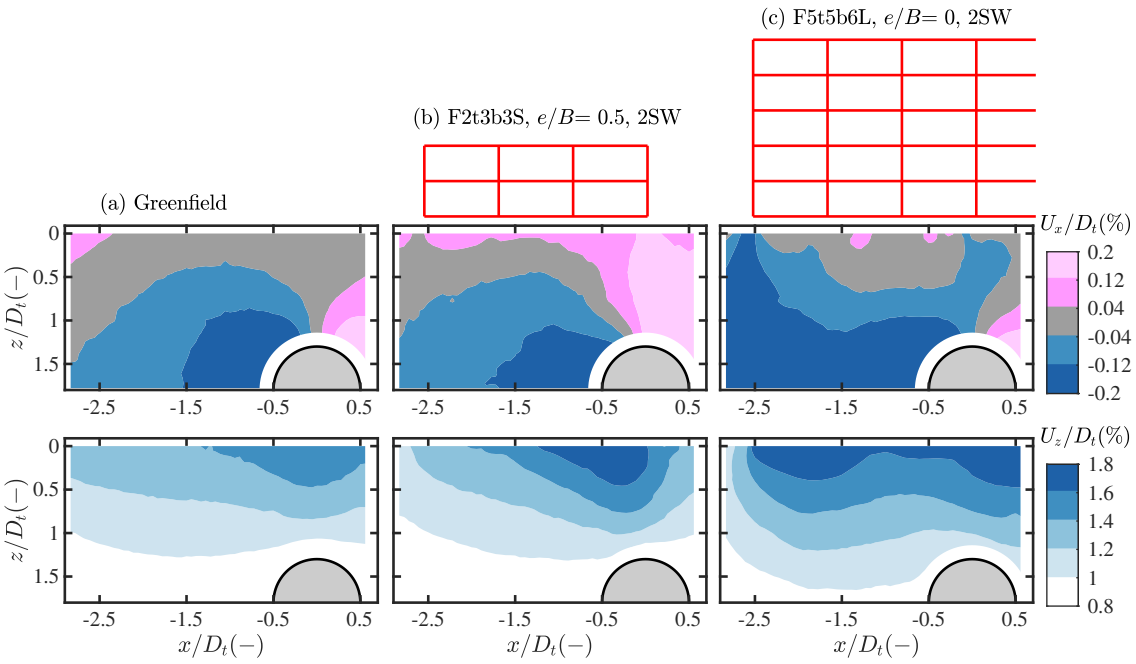


Fig. A6. Horizontal U_x and vertical U_z displacements of the dense (I_d = 90%) soil in selected tests (2SW) after centrifuge spin-up (data outside the contour thresholds were set equal to the closest limit value)

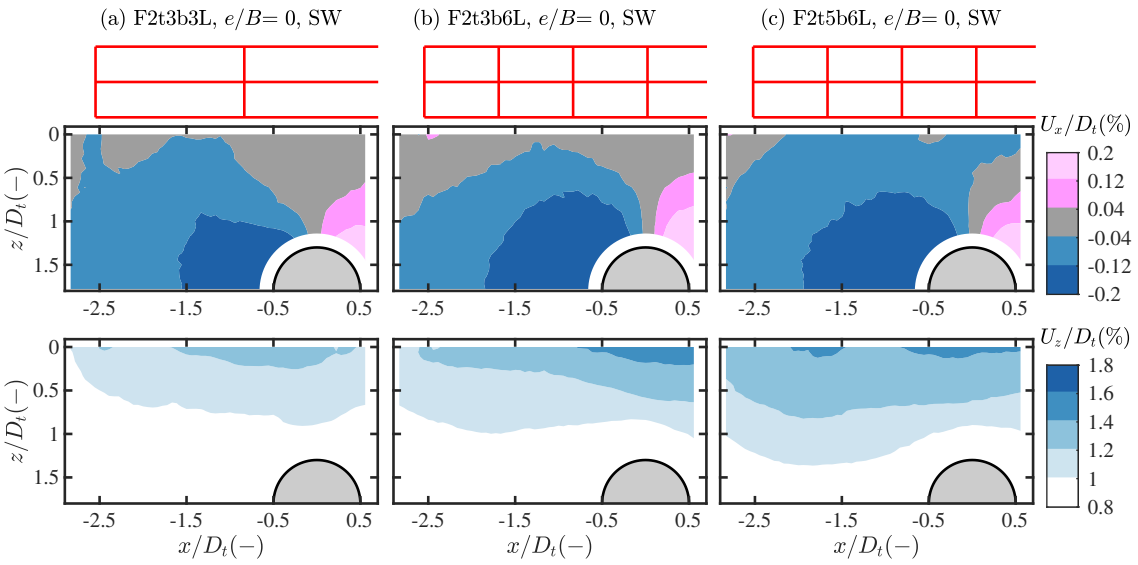


Fig. A7. Horizontal U_x and vertical U_z displacements of the dense (I_d = 90%) soil in selected tests (2-storey, e/B =0, SW) after centrifuge spin-up (data outside the contour thresholds were set equal to the closest limit value)

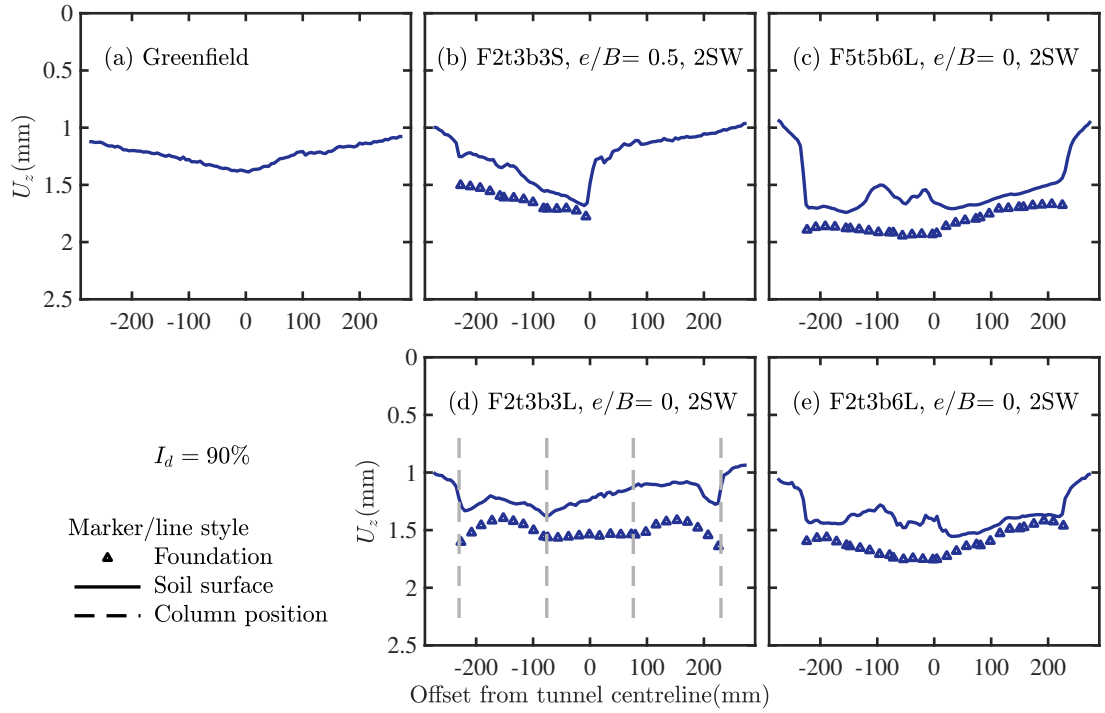


Fig. A8. Settlements of the rafts and surface soil in selected tests (2SW) during centrifuge spin-up from 1 to 68 g

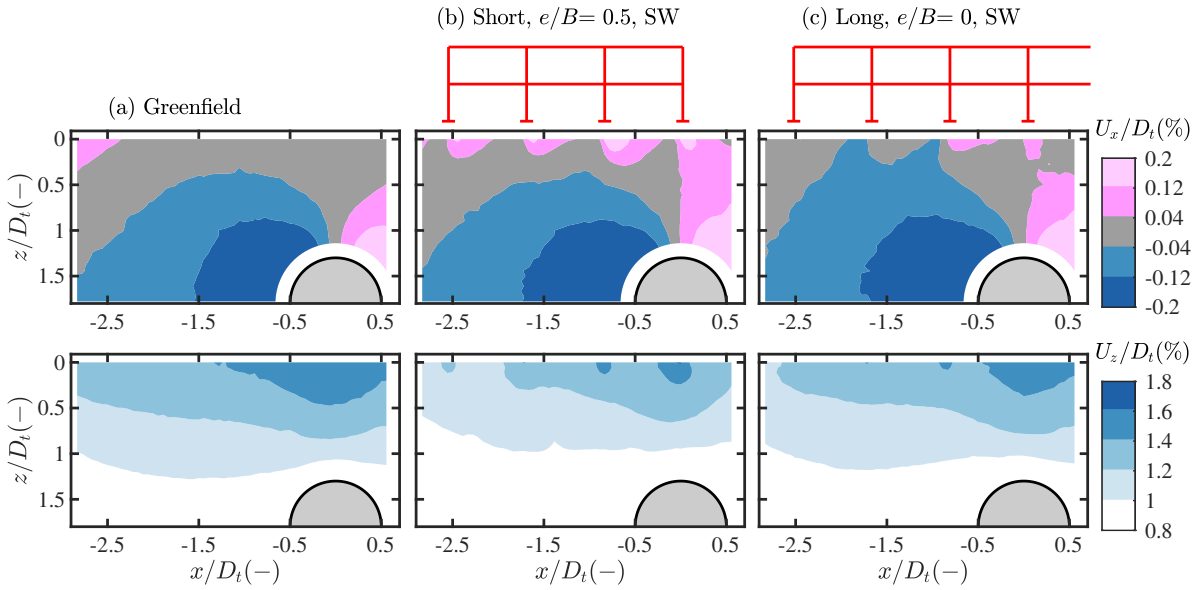


Fig. A9. Horizontal and vertical displacements (normalised by the tunnel diameter D_t) of the dense (I_d = 90%, SW) soil in selected footing tests during centrifuge spin-up from 1 to 68 g (data outside the contour thresholds were set equal to the closest limit value)

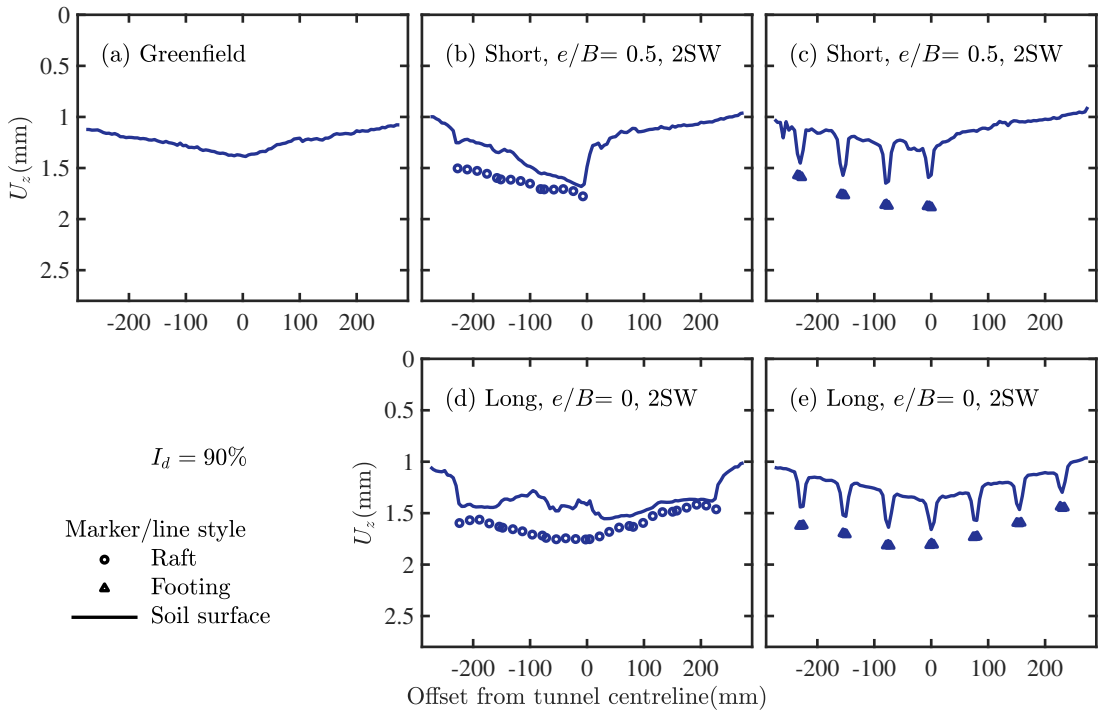


Fig. A10. Settlements of the foundations and surface soil in selected tests (2SW) during spin-up: comparison between rafts and separate footings

A5 Foundation and underlying soil displacements at $V_{l,t}$ =1%

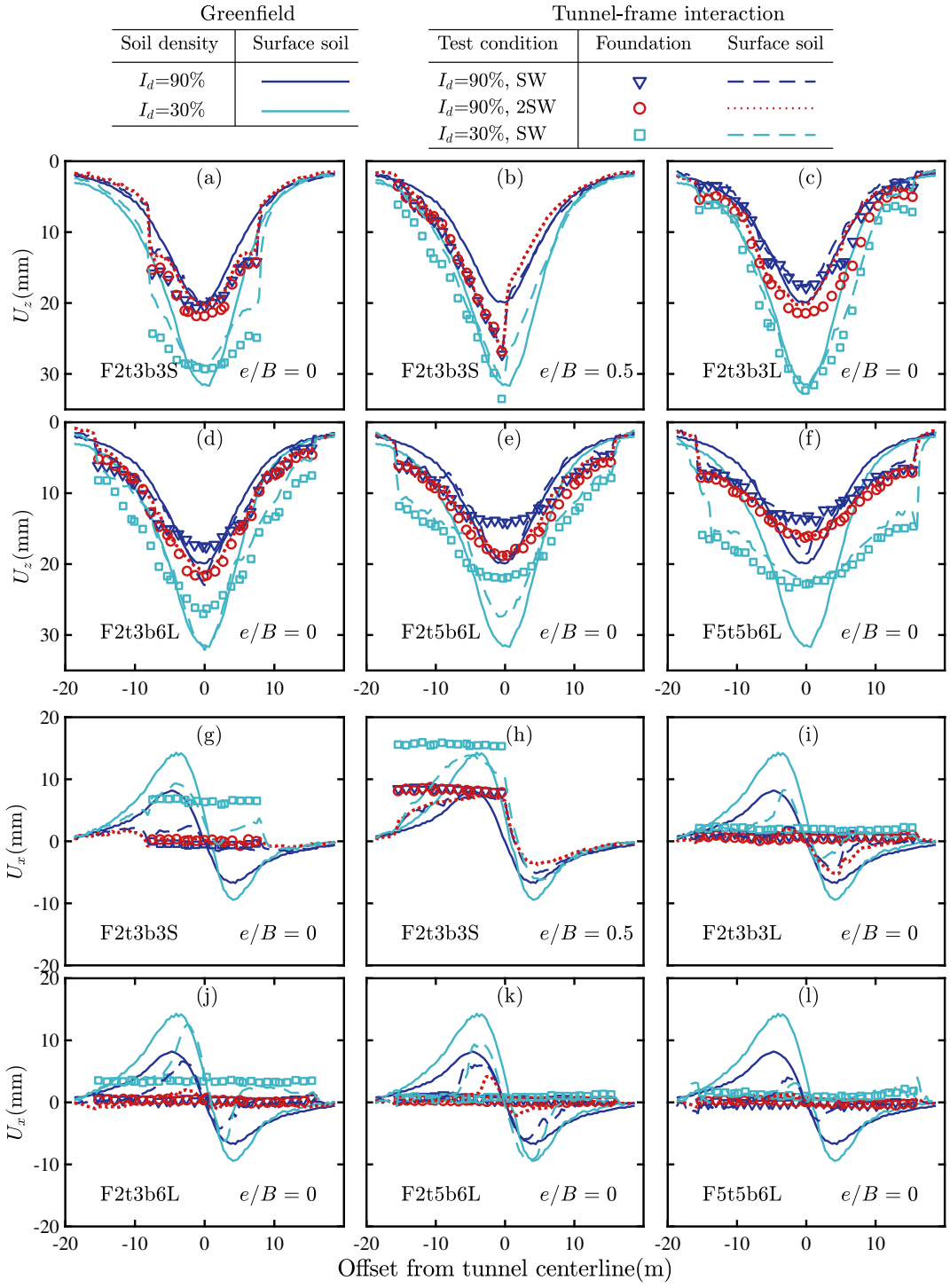


Fig. A11. Displacement of model frame foundations and underlying soil at $V_{l,t}$ =1 %

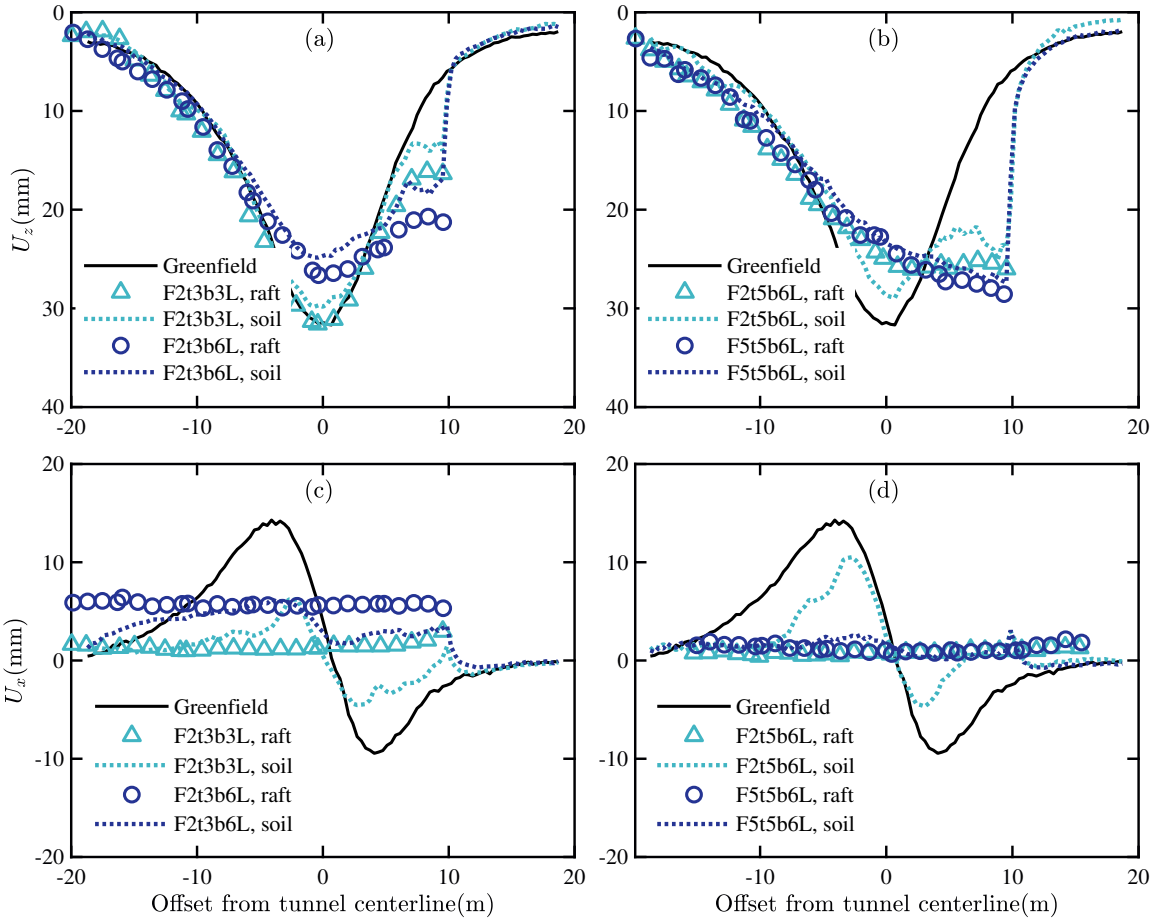


Fig. A12. Displacement of model frame foundations and underlying soil at $V_{l,t}$ = 1% with e/B = 0.2 in loose soil

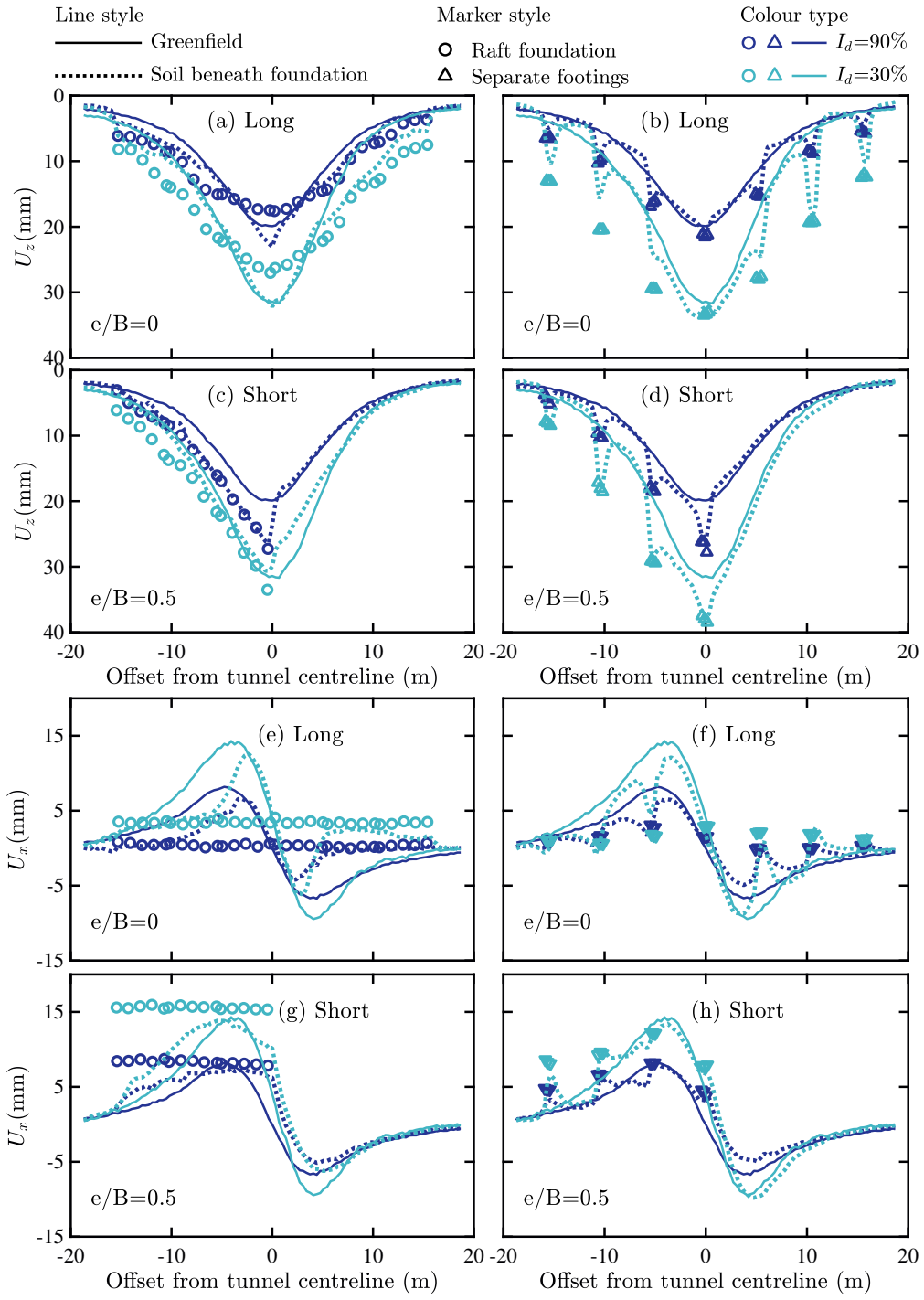


Fig. A13. Foundation and underlying soil displacements for loose and dense soil at $V_{l,t}$ = 1% (SW)

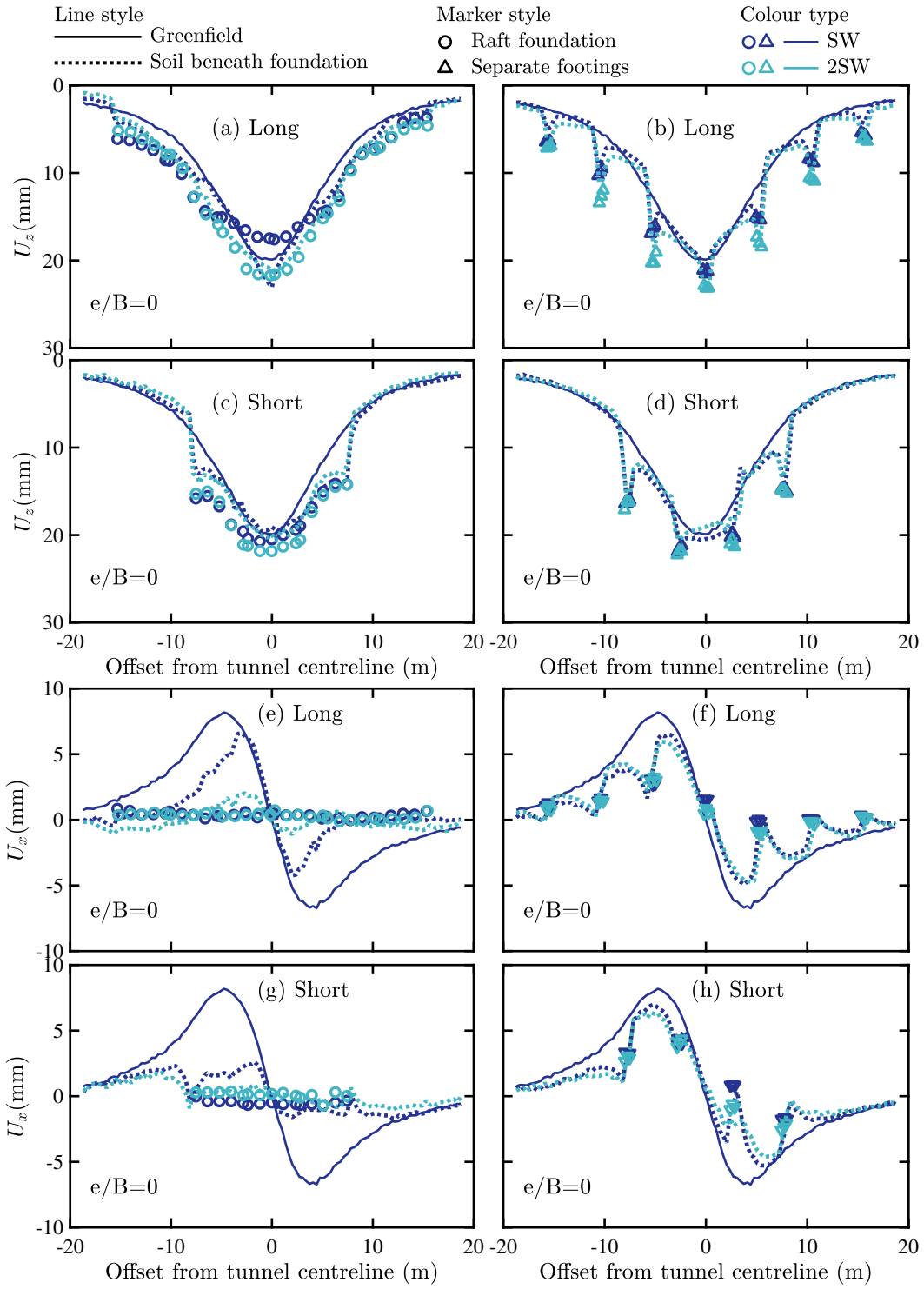


Fig. A14. Foundation and underlying soil displacements with different building weights for dense soil at $V_{l,t} = 1\%$ ($I_d = 90\%$)

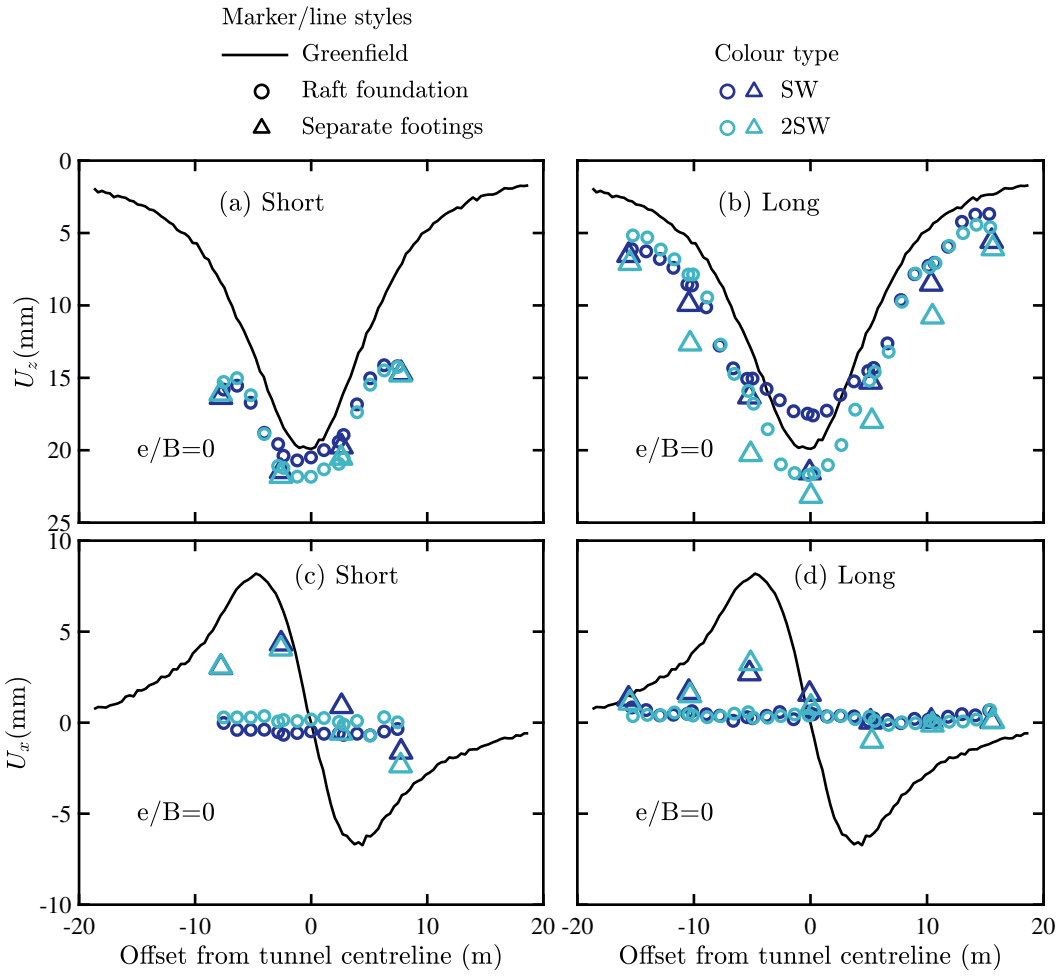


Fig. A15. Foundation displacements for central buildings founded on dense soil at $V_{l,t} = 1\%$